UNIVERSIDADE
FEDERAL DO CEARÁ

CENTRO DE CIÊNCIAS
DEPARTAMENTO DE FÍSICA
PROGRAMA DE PÓS-GRADUAÇÃO EM FÍSICA

Universiteit
Antwerpen

FACULTEIT WETENSCHAPPEN
DEPARTEMENT FYSICA

Plasmons e transporte eletrônico em materiais bidimensionais

Plasmons and electronic transport in two-dimensional materials

---

Plasmonen en elektronisch transport in tweedimensionale materialen

Thesis submitted for the degree of Doctor in Physics at the University of Antwerp (Belgium) and Universidade Federal do Ceará (Brazil) to be defended by:

ÍCARO RODRIGUES LAVOR

Fortaleza
2021

Ícaro Rodrigues Lavor

Plasmons e propriedades de transporte em sistemas bidimensionais

---

Plasmons and transport properties in two-dimensional systems

Plasmonen en transport eigenschappen in tweedimensionale systemen

Thesis submitted for the degree of Doctor in Physics at the University of Antwerp (Belgium) and Universidade Federal do Ceará (Brazil).

Advisors
Prof. Dr. Andrey Chaves
Prof. Dr. François M. Peeters

Co-advisors
Prof. Dr. Diego Rabelo da Costa
Dr. Ben Van Duppen

Fortaleza - Brazil
29 de julho de 2021

ÍCARO RODRIGUES LAVOR

Plasmons e propriedades de transporte em sistemas bidimensionais

---

Plasmons and transport properties in two-dimensional systems

Plasmonen en transport eigenschappen in tweedimensionalesystemen

Thesis submitted for the degree of Doctor in Physics at the University of Antwerp (Belgium) and Universidade Federal do Ceará (Brazil).

Approved in: 29/07/2021.

Composition of the PhD Jury

Prof. François Maria Leopold Peeters (Supervisor)
University of Antwerp (Belgium)

Prof. Dr. Andrey Chaves (Supervisor)
Universidade Federal do Ceará (Brazil)

Prof. Dr. Diego Rabelo da Costa (Co - supervisor)
Universidade Federal do Ceará (Brazil)

Prof. Dr. João Milton Pereira Junior
Universidade Federal do Ceará (Brazil)

Prof. Dr. André Jorge Carvalho Chaves
Instituto Tecnológico de Aeronáutica (Brazil)

In memoriam of
my grandfather,
Antônio Rodrigues.

Acknowledgement

First of all, I would specially like to express my gratitude to my parents *Franciso de Assis* and *Jacinta Rodrigues*, who, with love, intelligence, humility and wisdom, taught me to live wisely.

To my brothers *Ítalo* and *Írvile*, for all moments that they were patient with my attitudes and for the countless times that they contributed, by supporting and encouraging me, with my Dreams.

I would also like to thank my wife, *Mayara Barbosa*, for her love, affection and friendship, fully reciprocated. Her support was and is essential. Thanks for being a part of my dreams.

To my family, in which I always found support and strength in every moment I needed it.

To Prof. *Ricardo César* and Prof. *Célio Rodrigues*, for awakening my passion for Physics.

Not least, to my promoter, Prof. *Andrey Chaves*, for his competence, patience, and dedication during my scientific career, since the time of my scientific initiation, exactly 10 years ago, until today, as well as for the teachings, which I will take for the rest of my life. I will be eternally grateful for everything.

To the professors of the Department of Physics of the UFC, especially the professors *Raimundo Nogueira*, *José Ramos*, *Ascanio Araújo*, *Josué Mendes Filho*, *Renan Landim*, *Marcos Antônio*, *Nildo Loiola*, *João Milton*, *João Milton*, *Saulo D. Reis* and *Wandember Paiva*.

To my colleagues of the Department of Physics, *João Paulo Nogueira*, *Danilo Borges*, *Ravenna Rodrigues*. As well as everyone else I've lived with all this time. I thank *Luan Vieira*, *Gabriel Oliveira*, *Duarte José*, *Lucas Sami* , friends who share the same space with me every day and who are always willing to help. To all students and teachers who make up the Condensed Matter Theory Group - GTMC.

I also thank Prof. *Silvia Helena*, who indirectly encouraged me with the development of a part of this work. To Prof. *Diego Rabelo* for your patience and demonstration of love for what you do (without a doubt, you are the north for many people).

To my colleagues at the Federal Institute of Education, Science and Technology do Maranhão - IFMA/Campus Pinheiro, where I am a Professor, in particular to *Silvestre Jesus*, *Ana Gabriela*, *Marina*, *César Henrique*, *Higo*, *Victor Hugo*, *Jhose Ariam*, *Ermerson Ney*,*Jully Helen*, *Vandemberg Araújo*, *Luzimar Aroucha*, *Danielle Santos*, *Stefan*, *Saulo* and *Vicente*, as well as the others I didn't mention, for their companionship and welcome.

Not least, I will be eternally grateful for the lessons I learned during my visit, for almost two years, to the CMT group at the University of Antwerp. During that time, I had the honor of had Prof. Francois Peeters as my promoter. In addition to discussions about physics, I was able to learn a lot about society from my co-supervisor, Dr. Ben. "It will never just be about physics..." I hope we can keep working together. Also thank you Véronique, for the dozens of emails that were always promptly answered.

To CMT colleagues, which before COVID-19, I was able to teach them a little how to play football (it is a joke, I know!). These were moments of joy that will remain forever in my memory. Furthermore, Antwerp gave me a person who became very important: Raí. Thank you for your friendship.

I would like to thank all the agencies that gave me financial support for carrying out my projects and also for presenting them at conferences: National Council for Scientific and Technological Development (CNPq); Federal Institute of Education, Science and Technology of Maranhão (IFMA); Phantoms Foundations; Flemish Science Foundation (FWO); Universidade Federal do Ceará (UFC); University of Antwerpen (UA).

Finally, I want to thank the jury and my collaborators on these projects, without whom this work could never have been done.

This study was supported by the Coordenação de Aperfeiçoamento de Pessoal de Nível Superior - Brasil (CAPES) - Finance Code 001.

I hope you will enjoy the work.

Ícaro Rodrigues Lavor Fortaleza, June 2021

"Voici mon secret. Il est très simple: on ne voit bien qu'avec le coeur.
L'essentiel est invisible pour les yeux."
"Aqui está meu segredo. É muito simples: só se vê bem com o coração.
O essencial é invisível aos olhos."

Le Petit Prince, Antoine de Saint-Exupéry

Resumo

Esta tese apresenta, em sua primeira parte, uma investigação sobre *zitterbewegung* (ZBW), um movimento trêmulo de pacotes de onda eletrônicos, em multicamadas de grafeno, bem como o ZBW de excitons de moiré em heterostruturas formadas por uma bicamada de MoS_2/WSe_2 rotacionada. Nas últimas décadas, a dinâmica dos pacotes de ondas tem sido objeto de muitos estudos teóricos e experimentais em vários tipos de sistemas, tais como: semicondutores, supercondutores, sólidos cristalinos e átomos frios. Assim, com a descoberta do grafeno e dos excitons de moiré em hetero-bicamadas, agora surgem dois novos sistemas para a comunidade científica investigar a evolução temporal dos pacotes de ondas e possivelmente observar o fenômeno *zitterbewegung*. Esse movimento trêmulo foi teoricamente previsto pela primeira vez por Schrödinger para pacotes de ondas que descrevem partículas que obedecem à equação de Dirac. Este é exatamente o caso dos elétrons de baixa energia no grafeno, bem como dos excitons de moiré em MoS_2/WSe_2 rotacionados sob um campo eletromagnético externo aplicado.

No caso do ZBW em multicamadas de grafeno, foi desenvolvido um estudo analítico e computacional, através do método da função de Green e da técnica do *split-operator*, respectivamente. Neste sistema, verificou-se que os pacotes de ondas dependem não apenas da largura do pacote de ondas inicial e da polarização inicial do pseudopin, mas também do número de camadas. Além disso, os métodos analíticos e numéricos propostos aqui permitem investigar a dinâmica de pacotes de ondas em sistemas de grafeno com um número arbitrário de camadas e com potenciais arbitrários.

Para o exciton de moiré, é mostrado que, analogamente a outras partículas de Dirac, este sistema também exibe ZBW quando está sob um campo elétrico externo aplicado perpendicularmente. Neste caso, o ZBW apresenta longas escalas de tempo compatíveis com as técnicas experimentais atuais para dinâmica de excitons. Isso promove o estudo da dinâmica de excitons de moiré em heteroestruturas de van der Waals como uma plataforma de estado sólido vantajosa para sondar ZBW, amplamente ajustável por tensão eletrostática e ângulo de rotação entre camadas.

Na segunda parte desta tese, um estudo sobre plasmons em grafeno, combinado em heteroestruturas de van der Waals, é tratado através da teoria da resposta linear, dentro da aproximação de fase aleatória (do inglês *random phase approximation* ou simplesmente RPA), com suporte da heteroestrutura eletrostática quântica (do inglês *quantum electrostatic heterostructure* (QEH)), um método computacional baseado em teoria do funcional da densidade (do inglês, *density functional theory*, DFT). Uma vez que os plasmons de Dirac no grafeno são muito sensíveis às propriedades dielétricas do ambiente, é possível explorar tal propriedade para sondar a estrutura e composição das heteroestruturas de van der Waals colocadas embaixo de uma única camada de grafeno. Desta forma, pode-se diferenciar, utilizando os plasmons no grafeno, a diferença entre números de camadas, isto é, é possível identificar se uma estrutura possui uma ou duas camadas, por exemplo, quando essa é composta apenas por um único material, bem como diferenciar entre diferentes dicalcogenetos de metais de transição para heteroestruturas que apresentam mais do que 2 camadas (heterostruturas formadas por mais de um material). Como consequência do estudo inicial em plasmons, a hibridização de plasmons de Dirac em grafeno com fônons de dicalcogenetos de metais de transição também é estudado, quando estes são combinados nas chamadas heteroestruturas de van der Waals. Verificou-se que é possível alcançar regimes de acoplamento fortes e ultra-fortes, ajustando a energia de Fermi do grafeno e alterando o número da camada dicalcogenetos de metais de transição.

Abstract

This thesis presents, in its first part, an investigation on the trembling motion of wave packets known as zitterbewegung (ZBW), in multilayer graphene, as well as in moiré excitons in twisted MoS_2/WSe_2 hetero-bilayers. In the last few decades, the dynamics of wave packets has been subject of many theoretical and experimental studies in various types of systems such as semiconductors, superconductors, crystalline solids and cold atoms. The discovery of graphene and moiré excitons in twisted hetero-bilayers, brought two new platforms for the investigation on time evolution of wave packets and possible observation of ZBW. This trembling motion was first theoretically predicted by Schrödinger for wave packets describing particles that obey the Dirac equation. This is exactly the case of low energy electrons in graphene, as well as of moiré exciton in twisted MoS_2/WSe_2 under an external applied electromagnetic field.

ZBW in multilayer graphene was studied both analytically and computationally, respectively, through the Green's function and *split-operator* methods. In this system, it is found that ZBW depends not only on the wave packet width and initial pseudospin polarization, but also on the number of layers. Furthermore, the analytical and numerical methods proposed here allow to investigate wave packet dynamics in graphene systems with an arbitrary number of layers and arbitrary potential landscapes.

For moiré excitons in twisted MoS_2/WSe_2 hetero-bilayers, it is shown that, analogously to other Dirac-like particles, this system also exhibits ZBW when under a perpendicular applied field. In this case, the ZBW presents long timescales that are compatible with current experimental techniques for exciton dynamics. This promotes the study of the dynamics of moiré excitons in van der Waals heterostructures as an advantageous solid-state platform to probe zitterbewegung, broadly tunable by gating and inter-layer twist angle.

In the second part of this thesis, a study into graphene plasmonic in van der Waals heterostructure (vdWhs) are treated in a linear response framework within the *Random Phase Approximation* and with support of the *quantum electrostatic heterostructure* (QEH), a DFT-based method. Since Dirac plasmons in graphene are very sensitive to the dielectric properties of the environment, it is possible to explore this property to probe the structure and composition of van der Waals heterostructures (vdWh) placed underneath a single graphene layer. In this way, one can achieve a layer sensitivity of a single layer and differentiate between different TMDs for heterostructures thicker than 2 layers. As a consequence of this, study, the hybridization of Dirac plasmons in graphene with phonons of transition metal dichalcogenides (TMDs), when the materials are combined in so-called van der Waals heterostructures (vdWh) forming surface plasmon-phonon polaritons (SPPPs) are also investigated. It was found that it is possible to realize both strong and ultrastrong coupling regimes by tuning graphene's Fermi energy and changing TMD layer number.

Abstract

In deze thesis stellen we als eerste een onderzoek voor naar de trillende beweging van golfpakketjes, de zogenaamde *Zitterbewegung* (ZBW), van eleketronen in multilaag grafeen en moire excitonren in hetero-bilagen van verdraaid MoS2/WSe2. In de laatste decennia, de dynamica van golfpakketjes is het onderwerp geweest van vele theoretische en experimentele studies in halfgeleiders, supergeleiders, crystallen en koude atomen. De ontdekking van grafeen en moire excitonen hebben hieraan twee nieuwe platformen toegevoegd. De ZBW zelf was eerst theoretisch voorspeld door Schrodinger voor deeltjes die de Dirac bewegingsvergelijkingen volgen. Het zijn immers ook deze vergelijkingen die grafeen elektronen en excitonen in verdraaide MoS2/WSe2 bilagen onder een extern elektromagnetisch veld beschrijven.

ZBW in multilaag grafeen is zowel analytisch als computationeel bestudeerd, respectievelijk door de Greense functie- en de split-operatormethode. In dit systeem vonden we dat ZBW niet enkel afhangt van de pakketbreedte en de initiele pseudospin polarisatie, maar ook van het aantal lagen. Verder lieten de analytische en numerieke methoden toe om golfpakketdynamica te bestuderen in systemen met een arbitrair aantal lagen en voor arbitraire potentiaaloppervlakken.

Voor moiré excitonen in verdraaid MoS_2/WSe_2 heterobilagen, tonen we analoog aan andere Diracachtige deeltjes, dat dit systeem ook ZBW vertoont, wanneer het onderworpen wordt aan een extern elektromagnetisch veld. In dit geval komt ZBW naar boven op lange tijdsschalen die compatibel zijn met hedendaagse technieken voor exciton dynamica. Dit laat toe om de dynamica van excitonen in van der Waals heterostructuren te bestuderen en dit systeem te beschouwen als voordelig vastestof platform om ZBW te bestuderen door de elektrische potentiaal en inter-laag verdraaiingshoek te variëren.

In het tweede deel van deze thesis wordt een studie van grafeen plasmonen in van der Waals heterostructuren voorgesteld. De plasmonen worden berekend binnen een raamwerk van de zogenaamde 'willekeurige fase benadering' en ondersteund door het 'kwantum elektrostatisch heterostuctuur' model, een methode die gebaseerd is op dichtsheidsfunctionaaltheorie (DFT). Aangezien Dirac plasmonen zeer gevoelig zijn door de dielektrische eigenschappen van de omgeving, is het mogelijk om de structuur en compositie van van der Waals heterostructuur lagen onder een grafeen laag te ontdekken door plasmonen te onderzoeken. Op deze manier kunnen we een laag-gevoeligheid bereiken van een enkele laag en tussen verschillende transitiemetaaldichalchegonides (TMD) differentieren vanaf twee lagen. Verder onderzoeken we ook hoe plasmonen hybridiseren met optische phononen die ook aanwezig zijn in de TMD's. Deze hybride deeltjes, de zogenaamde oppervlakte plasmon-phonon polaritonen (SPPPs), worden ook onderzocht. Hierbij is gevonden dat op deze manier zowel sterke als ultrasterke koppelingsregimes bereikt kunnen worden door het Fermi niveau van grafeen te veranderen of door het aantal lagen van de TMD's aan te passen.

Contents

List of publications

During the course of my PhD project, I had the chance to work on different topics on graphene. I was also honored to work with different researchers. Here, I list the works I worked on that are so far submitted or published.

1. **I. R. Lavor**, L. S. R. Cavalcante, Andrey Chaves, F. M. Peeters and B. Van Duppen: *Probing the structure and composition of van der Waals heterostructures using the nonlocality of Dirac plasmons in the terahertz regime.* 2D Materials, **8** 015014 (2020).
2. **I. R. Lavor**, D. R. da Costa, L. Covaci, M. V. Milošević, F. M. Peeters and Andrey Chaves: *Zitterbewegung of moiré excitons in twisted* MoS_2/WSe_2 *hetero-bilayers.* Manuscript accepted: Physical Review Letters.
3. **I. R. Lavor**, D. R. da Costa, Andrey Chaves, S. H. R. Sena, G. A. Farias, B. Van Duppen and F. M. Peeters: *Effect of zitterbewegung on the propagation of wave packets in ABC-stacked multilayer graphene: an analytical and computational approach.* Journal Physics: Condensed Matter, **33**, 095503 (2020).
4. **I. R. Lavor**, Andrey Chaves, F. M. Peeters and B. Van Duppen: *Strong and ultra-strong plasmon-phonon coupling regime in graphene-based van der Waals heterostructures in the THz spectral range.* (Manuscript submitted. For an arXiv version click here).
5. **I. R. Lavor**, D. R. da Costa, Andrey Chaves, G. A. Farias, R. Macêdo and F. M. Peeters: *Magnetic field induced vortices in graphene quantum dots.* Journal Physics: Condensed Matter, **32**, 155501 (2020)

List of Figures

List of Tables

List of Abbreviations

$0D$	Zero-dimensional
$1D$	One-dimensional
$2D$	Two-dimensional
$3D$	Three-dimensional
AFM	Atomic force microscopy
STM	scanning tunneling microscope
FLG	Few-layers graphene
MLG	Multilayer graphen
BLG	Bilayer graphene
TLG	Trilayer graphene
CNTs	Carbon nanotubes
CVD	Chemical vapor deposition
LPE	Liquid phase exfoliation
2DLMs	2D layered nano-materials
TMDs	transition metal dichalcogenides
h-BN	Hexagonal boron nitride
SiO_2	Silicon dioxide
MoS_2	Molybdenum disulfide
$MoSe_2$	Molybdenum diselenide
WS_2	Tungsten disulfide
WSe_2	Tungsten diselenide
vdWhs	van der Waals heterostructures
CMOS	Complementary metal-oxide-semiconductor
FET	Field effect transistor transistor
LED	Light-emitting diode
MOSFET	Metal oxide semiconductor field effect transistor
CCD	Charge-coupled device

BPRs	Biphenylene ribbons
AGNR	Armchair graphene
ZBW	Zitterbewegung
SOT	Split-operator technique
ILE	Inter-layer excitons
RPA	Random phase approximation
(s-)SNOM	(Scattering-type) Scanning near-field optical microscope
DFT	Density functional theory
QEH	Quantum electrostatic heterostructure model
TO	Transverse optical
RS	Reststrahlen bands
SP^2	Surface plasmon-polariton
SP^3	Surface plasmon-phonon-polariton mode
HP^2	Hyperbolic phonon polaritons
HP^3	Hyperbolic plasmon-polariton
SPPPs	Surface plasmon-phonon polaritons
IR	Infrared
WC	Weak coupling
SC	Strong coupling
USC	Ultra-strong coupling
DSC	Deep-strong coupling

List of Nomenclatures

v_f	Fermi velocity
τ, γ_i, $t_{A(B)}$	Hopping parameters
$\Psi_A(\Psi_B)$	The probability of finding the electron on sublattice A and B
$\Psi_i\left(\boldsymbol{r},t\right)$	Time-dependent (pseudospin-) wave function
$\Psi\left(\boldsymbol{r},t+\Delta t\right)$	Propagated wave function after a time step Δt
$\varepsilon_{\lambda\mathbf{k}}$	Graphene eigenenergies
$\lambda=\pm 1$	Indicate the conduction $+1$ and valence (-1) bands
$\boldsymbol{a}_i$	Real lattice vector i
$\boldsymbol{b}_i$	Reciprocal lattice vector i
$\hat{a}_i^\dagger$	Creation operator of electrons on the site i of the subllatice A
$\hat{a}_i$	Annihilation operator of electrons on the site i of the subllatice A
$\hat{b}_i^\dagger$	Creation operator of electrons on the site i of the subllatice B
$\hat{b}_i$	Annihilation operator of electrons on the site i of the subllatice B
K	Dirac cone K
K'	Dirac cone K'
ϵ_i	Self-energy on site i
d	Width of initial gaussian wave packet
k	The modulus of the wave vector
Γ	Gamma point, center of first Brillouin zone
H_{TB}	Tight-binding Hamiltonian
$H_{mo}^{\pm}$	Monolayer graphene Hamiltonian
$H_{bi}^{\pm}$	Bilayer graphene Hamiltonian
$H_n^{\pm}$	N-ABC-stacked multilayer graphene Hamiltonian
$G_{\mu v}\left(\boldsymbol{r},\boldsymbol{r}',t\right)$	Green's functions coefficients
$\mathbb{1}$	Identity matrix
$J_n\left(z\right)$	Bessel functions of the n-th order
$\langle\boldsymbol{r}\left(t\right)\rangle$	Time-dependent expectation value of the position operator

$(\mathscr{F}^{-1})$ $\mathscr{F}$	(inverse) Fourier transform operator
$\rho\,(\boldsymbol{r},t)$	Electronic probability density
$[\mathrm{C}_1\ \mathrm{C}_2]^T$	Initial pseudospin polarization
σ_i	Pauli matrices
$E_g(\boldsymbol{r}_0)$	Inter-layer excitons bandgap
ϵ	Applied electric field (in the context of moiré exciton)
H_{mex}	Exciton Hamiltonian
ω_{ZB}	Zitterbewegung frequency (from Dirac equation)
R_h^μ	R-type stacking in twisted $\mathrm{MoS}_2/\mathrm{WSe}_2$ hetero-bilayers
$\epsilon^{RPA}(q,\omega)$	Dynamical RPA dielectric function
ϵ_{env}	Effective dielectric function of the environment
$\bar{\epsilon}$	Average dielectric function between two mediums
$\epsilon_{\mathrm{sub}}\,(\omega)$	Frequency-dependent dielectric function of the environment
$\hat{U}(t,t_0)$	Unitary time-evolution operator
$\hat{A}_{\alpha\beta}$, $\hat{B}_{\alpha\beta}$	Matrix elements of the single particle operators $\hat{A}$ and $\hat{B}$
$\chi_{AB}(\tau)$	Retarded linear response function
$\chi_{AB}^{(0)}(\tau)$	Non-interacting response function
$\chi_{nn}^{(0)}(q,\omega)$	Density-density response function
$\chi_{nn}^{(0)}(q,\omega)$	Non-interacting density-density response function
$\chi_{nn}^{RPA}(\mathbf{q},\omega)$	RPA density-density response function
k_F	Fermi wave vector
E_F	Fermi energy
$\Theta(\tau)$	Heaviside step function
α_{ee}	Graphene fine-structure constant
ω_{pl}	Plasmon frequency
ω_{ph}	Phonon frequency
$v_{\boldsymbol{q}}$	2D Fourier transform of the Coulomb interaction
$\mathcal{D}$	Drude weight
$\hbar$	Plank constant
$\lambda(\omega;\bar{\epsilon},E_{\mathrm{F}})$	Plasmon wavelength ($q \to 0$ limit)
$\epsilon_{\parallel}^{\infty}$	In-plane high-frequency dielectric constant
$\omega_{\mathrm{TO},n}$	Frequency of the n-th TO surface phonon mode
$L(q,\omega)$	Loss function
V_{p} $(\mathsf{V}_{\mathrm{g}})$	Phase (group) velocity
E'' (A_2'')	(Out-) In-plane vibrational phonon mode
Γ	Plasmon-phonon coupling strength
η	Normalized plasmon-phonon coupling strength
H_{pl}	Plasmon Hamiltonian
H_{ph}	Phonon Hamiltonian
$H_{\mathrm{pl-ph}}$	Plasmon-phonon interaction Hamiltonian

1

Introduction

1.1 Motivations for the study of graphene

In December 1959, physicist Richard Feynman[1] gave a lecture at the California Institute of Technology that would come to be considered the starting point of nanotechnology[2], although he did not use this term during the meeting. In his lecture, entitled *There's Plenty of Room at the Botton*, Feynman suggested that atoms could be manipulated and organized individually, as needed, giving rise to new materials with properties entirely different from those existing [1].

The nanotechnology, in a simple and direct way, can be understood as the study of matter on an atomic and molecular scale, with the ability to create new useful objects using specific techniques and tools. The development of nanotechnology took a very important step in 1981, when Gerd Binning and Heinrich Roher, from the IBM laboratory in Zurich, developed the scanning tunneling microscope - STM), allowing for nanometric manipulations. This achievement earned G. Binning and H. Rober, together with Ernst Ruska, the 1986 Nobel Prize in Physics. Over the years, other microscopes have been developed, such as: scanning probe microscope (SPM), near field microscope (NFM) and atomic force microscope (AFM).

In 1985, a group of researchers discovered a series of compounds entirely made out of carbon: the fullerenes [2]. Feynman's dream was beginning to come true: the carbon atoms of fullerene have sp^2 hybridization, making them more reactive molecules than common aromatic systems. This allows the addition of functional groups to fullerenes, giving rise to new structures (fullerenes).

The discovery of fullerenes left the scientific community enthusiastic, so that in 1991 Sumio Iijima discovered and characterized for the first time the nanotubes of carbon [3],

---

[1] Richard Philips Feynman (New York, May 11, 1918 — Los Angeles, February 15, 1988) was a renowned 20th century American physicist, one of pioneers of quantum electrodynamics and the 1965 Nobel Prize in Physics.

[2] The term nanotechnology was coined for the first time by Norio Taniguchi in 1959, to describe the technologies that allowed the construction of materials on a scale of $1nm$.

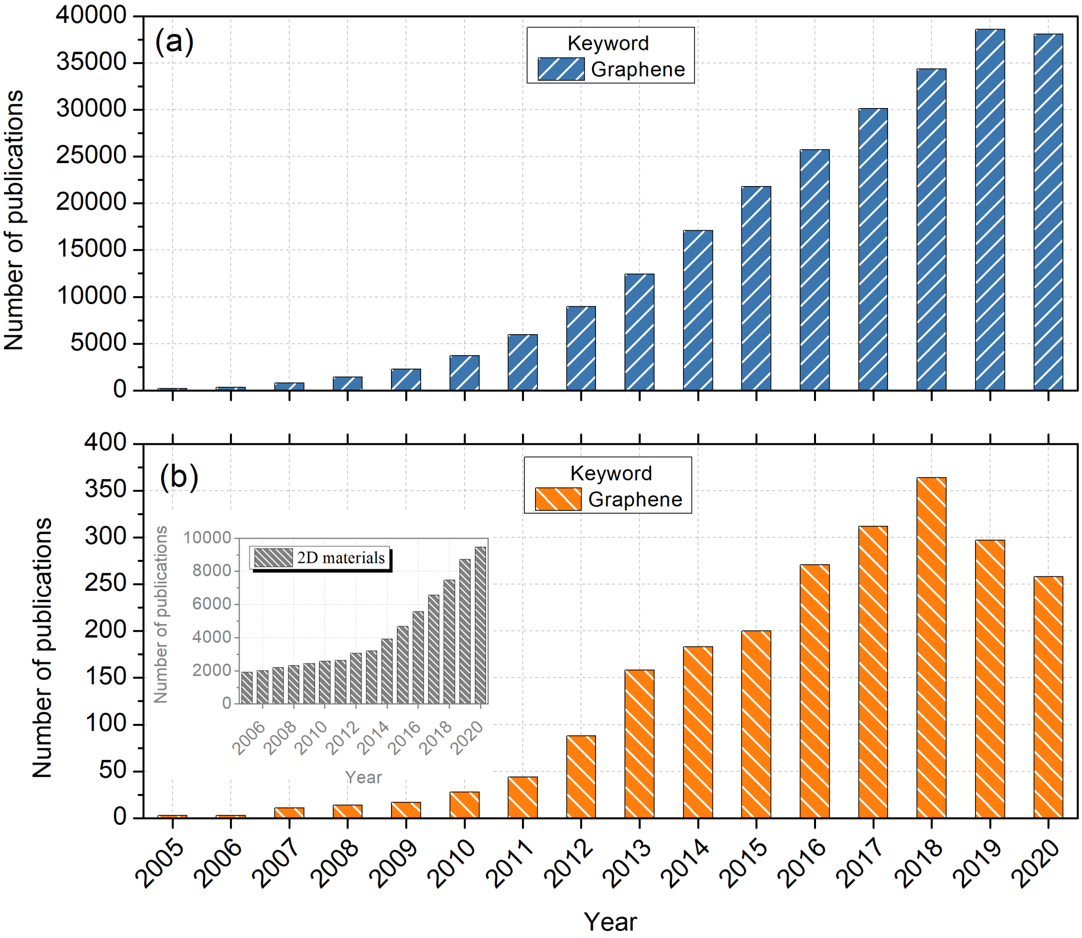

Figure 1.1: Number of publications including the keyword (a) "graphene" and (b) "graphene + plasmons". Inset in panel (b) represents the number of publications using the keyword "2D materials". Data obtained from the *web of science* from 2005 to 2020.

one-dimensional (1D) structures with unique characteristics. Until then, structures exclusively made by carbon with zero-dimensional (0D) (Fullerenes) and three-dimensional (3D) (Graphite and Diamond) were already known.

For a long time, it was believed that two-dimensional (2D) dimensional material was not feasible due to thermodynamic instability. [4–6].

However, on October 5, 2010, Konstantin Novoselov and Andre Geim[3] would win the Nobel Prize in Physics for the pioneering study of the electronic properties of the graphene (2D structures, in the form of a honeycomb, or, simply, a monolayer graphite) [8]. Using an experimental technique known as micromechanical cleavage, Novoselov and Geim, together with their group, managed to obtain a single layer of graphite. Theoretically, it all started in 1947 when Canadian physicist Philip Richard Wallace (1915-2006) studied the band structure of graphite [9]. The importance of this material is due to the fact that

---

[3] Andre Geim, was the first scientist to win both the IgNobel [7] award, awarded to the year's strangest discoveries, and the Nobel.

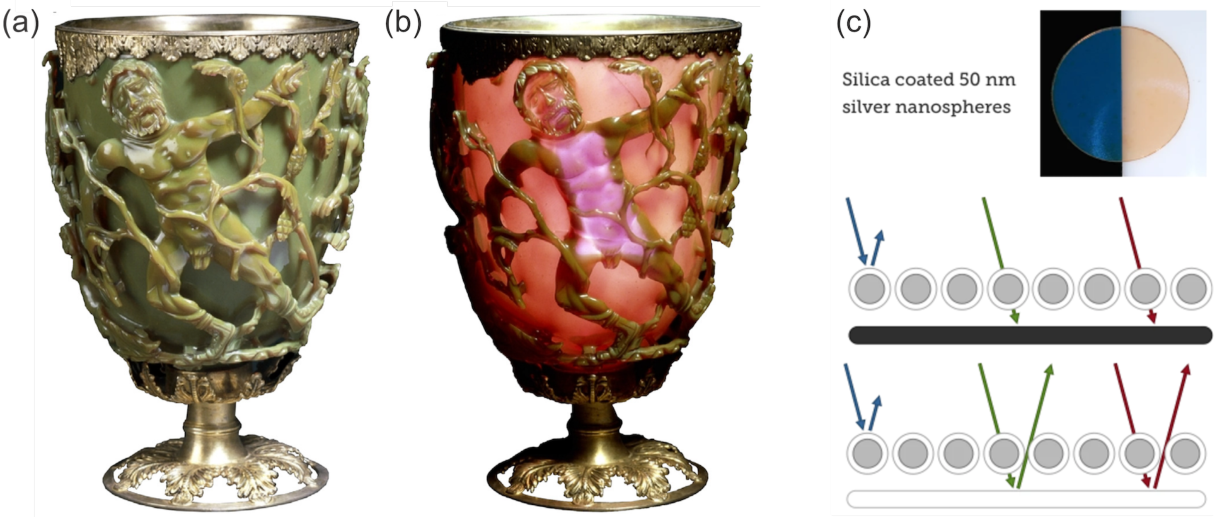

Figure 1.2: Illustration of the dichroism property of the Lycurgus cup. (a) When the light source is located outside the glass looks green, on the other hand, (b) when the light source is located inside the cup looks red. (c) Schematic representation of an incident light in a silica coated 50 nm silver nanospheres material that showing dichroism. When the background is black (white) the reflect color is blue (brown). This property of the same material showing different colors depending on the position of the light is called dichroism. Adapted from Refs. [10, 11].

graphene has unique electronic, mechanical, optical, thermal and chemical properties, making it extremely promising for industrial applications.

Since the discovery of the graphene in 2004, there has been a significant increase in the number of publications related to this material, as verified by hatched blue color bars in Fig. 1.1. Since graphene can support plasmons, which will be discussed later in this thesis, the interest of the scientific community on graphene plasmons also increased significantly, as shown by orange bars in Fig. 1.1, making this subject a hot topic until nowadays. Although *zitterbewegung* is also a subject of this thesis, as it is a very specific subject, the number of annual publications is restricted to a few publications, so it was omitted from Fig. 1.1.

1.2 Plasmons in graphene-based systems

One of the oldest examples of interaction between light and matter is an extraordinary work with glass made by the Romans in the fifth century AD known as Lycurgus cup[4], Fig. 1.2(a)-(b). Surprisingly, when the light source is located outside, Fig. 1.2(a), the glass looks green. On the other hand, when the light source is located inside, the cup looks red. However, it was only in 1990 that it was possible to explain this phenomenon.

---

[4] The Lycurgus cup, which is part of the collection of the British Museum, shows King Lycurgus being dragged to the underworld by Ambrosia. It is one of the oldest synthetic nanocomposites [12].

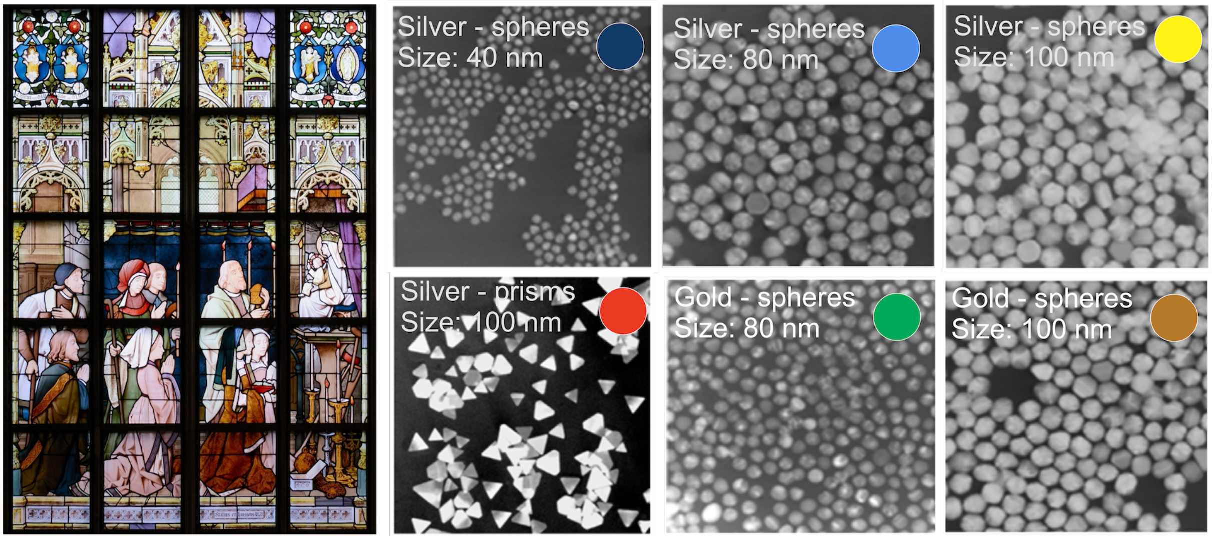

Figure 1.3: Illustration of the dichroism property in a stained glass window of the Antwerp's cathedral (left). Controlling the size and shape (prism and sphere, for example) of gold and silver nanoparticles allows to obtain different colours (right). Adapted from Ref. [15].

Using AFM [13], scientists observed the presence of nanoparticles: 66.2 % silver, 31.2 % gold and 2.5 % silver [14]. The light scattered by colloids of silver nanoparticles with size $>$ 40 nm gives rise to the green color, Fig. 1.3(a). On the other hand, the red color is originated when the light is absorbed by gold particles, while the purple color, which can be seen in the body of King Lycurgus, is due to the absorption of large particles, Figs. 1.3(b). Figure 1.2(c) presents a schematic illustration of an incident light in a silica coated 50 nm silver nanospheres, a typical material that presents the dichroism property, i.e a same material can exhibit different colors depending on the position of the light.

The use of nanoparticles in the medieval age can also be seen in the stained glass windows of Gothic churches, where the use of metallic gold and silver particles was normally used to create different colors, as can be seen in Fig. 1.3.

But, what is the relation between those two examples and plasmons? The answer is simple: plasmons arise due to the interaction between light and free-electron in conductive materials. [16–18]. To be more precise, plasmon are collective density oscillations of the electron liquid in conductive materials, that arise as response of the electron-electron interaction in the material, to an external electromagnetic field [16–19], as illustrated in Fig. 1.4(a). On the other hand, when a plasmon wave is restrict to the surface of the metallic material, these plasmons are called as Surface Plasmon-Polaritons (SPPs). The SPPs are defined as a propagating electromagnetic surface wave coupled to collective charge excitations of the conduction electrons, that propagates along the interface between a dielectric and a conductor [16–18]. Figure 1.4(b) illustrates one of the first experimental setups to detect SPPs in graphene (the substrate is SiO_2) [20]. Using a ultrafast laser coupled to an AFM tip to stimulate SPPs, Fig. 1.4(b), allowed them to visualize the

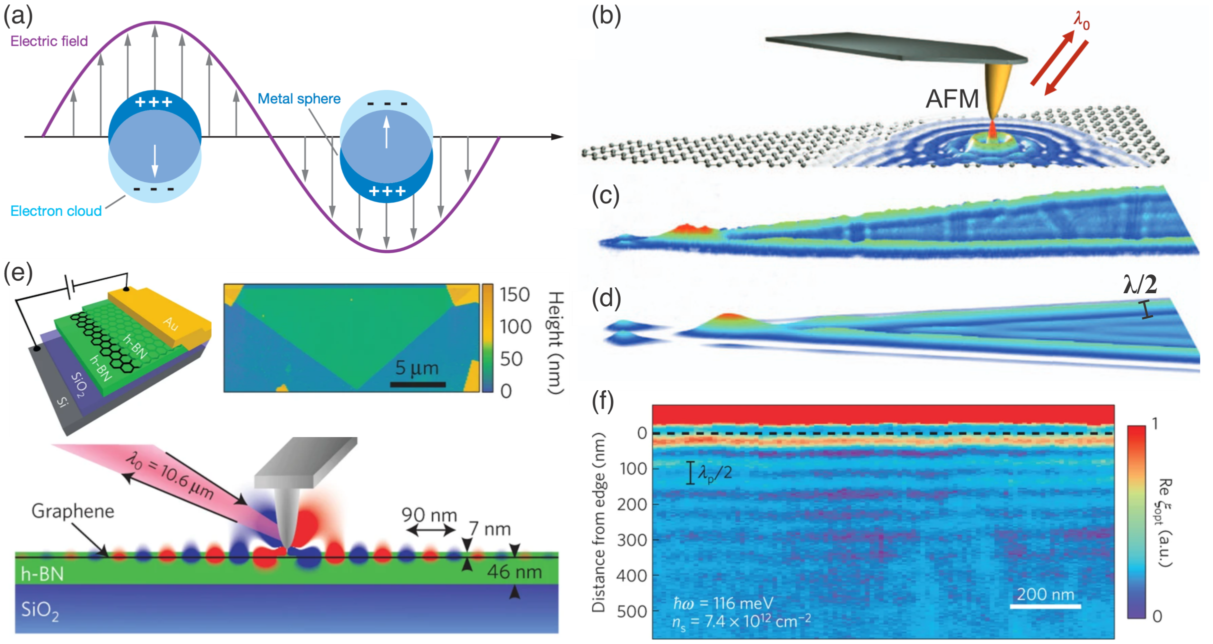

Figure 1.4: (a) Illustration of a localized surface plasmon excited by an electric field, adapted from Ref. [19]. (b) Diagram of the first experimental setup to detect propagating surface waves in graphene monolayer. (c) Visualization of the propagating and localized graphene plasmon in real space by scattering-type scanning near-field optical microscopy (s-SNOM). (d) Results obtained computationally using local density of optical states (LDOS). λ is the plasmon wavelength. (e)-(f) Experimental setup of graphene encapsulated by hexagonal boron nitride (hBN) and experimental image obtained from s-SNOM. Plasmons in such heterostructure are extremely confined to the graphene monolayer. Adapted from references [20] and [21], respectively to (b)-(d) and (e)-(f).

propagating and localized plasmon wave in real space by scattering-type scanning near-field optical microscopy (s-SNOM), Fig. 1.4(c). Their results were confirmed by local density of optical states (LDOS) simulations, Fig. 1.4(d) (λ is the plasmon wavelength). Other significant progress was taken in 2014 by A. Woessner et. al [21], when the plasmon life time was increased 10 times, when compared to the results of Ref. [20]. To do so, they encapsulated graphene in between hBN layers, as represented in Fig. 1.4(e). Figure 1.4(f) represents the visualization of the SPPs in such structure obtained experimentally using also s-SNOM, as mentioned before.

In this thesis we used the sensitivity of Dirac plasmons (SPPs in a graphene monolayer) to study the structure and composition of van der Waals heterostructures and to investigate how these plasmons can couple to phonons in these heterostructures.

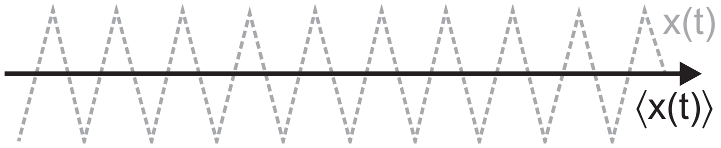

Figure 1.5: Illustration of the Zitterbewegung for an simple one-particle picture. The position $x(t)$ (dashed gray line) performs a ZBW around the mean (classical) trajectory $\langle x(t) \rangle$ (solid black line). Adapted from Ref. [22].

1.3 Wave packet dynamics and zitterbewegung of electrons in graphene and of moiré excitons

The *zitterbewegung* (ZBW) (trembling motion, from German) was first described in 1930 by Erwin Schrödinger [23]. Schrödinger used the Dirac equation to study relativistic electrons in a vacuum and realized that the spin operators ($\vec{\sigma}$) corresponding to the velocity component did not commute with the Hamiltonian. As a consequence, the electron velocity is not a constant of motion, and that is a purely quantum phenomenon, since it violates Newton's first law of classical mechanics[5]. Schrödinger calculated the average velocity and position (see illustration in Fig. 1.5) of the electron in vacuum as a function of time and concluded that, in addition to their classic motion, these particles exhibit very rapid oscillations, which he called *zitterbewegung*. The frequency of oscillation ($\hbar\omega_z \simeq 2m_0c^2 \simeq 1$ MeV) predicted by Schrödinger is determined by the gap due to interference between the positive and negative energy states that compose the initial wave packet and the oscillation amplitude is in the order of the Compton length ($\lambda_c = \hbar/m_0c \simeq 3.86 \times 10^{-3}$ Å) [26].

In the last few decades, the study of the dynamics of wave packets, as well as the study of the ZBW, has been the subject of numerous theoretical studies e.g. in ultracold atoms [27, 28], semiconductors [29–34], carbon nanotubes [35], topological insulators [36], crystalline solids [37, 38] and other systems [39–42]. Although ZBW was theoretically found using a quantum simulation of the Dirac equation for trapped ions [43], Bose–Einstein condensates [44–46] and, most recently, an optical simulation [47], up to now, no direct experimental observations have been carried out. The reason is that the Dirac equation predicts ZBW with amplitude of the order of the Compton wavelength (10^{-2} Å) and a frequency of $\omega_{ZB} \approx 10^{21}$ Hz, which are not accessible with current experimental techniques.

With the advent of graphene, a new system has now emerged for the scientific community to investigate the evolution of the dynamics of wave packet and the presence of the ZBW phenomenon, since electrons in graphene behave as massless relativistic particles

---

[5] Perhaps the reader concludes that because it is a study of electron dynamics, it was expected that the ZBW was of a quantum nature. However, we must not forget that Quantum Mechanics was a novelty at that time, since the equation of Schrödinger was published in 1926 and the Waa Dirac in 1928 [24, 25].

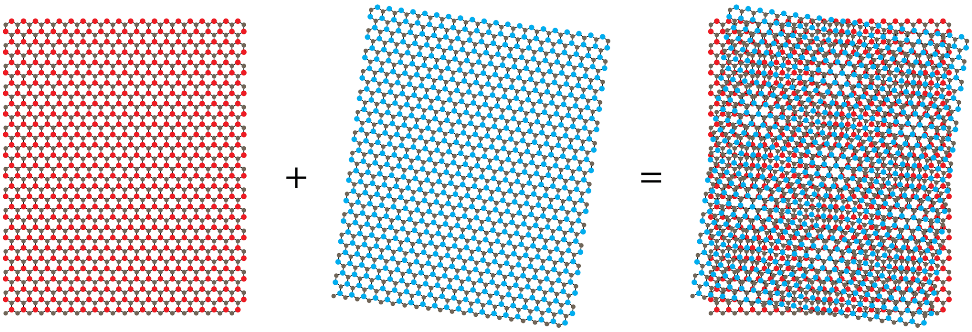

Figure 1.6: Illustration of a top view of a moiré pattern (right) originated by stacking two rotated monolayers (left) with honeycomb lattice. Adapted from Ref. [54].

that are governed by the Dirac equation. Inspired by this properties, in 2008 and 2010, respectively, Maksimova et al. [48] and Chaves A. et al [49], investigated the dynamics of charged particles described by a Gaussian wave packet in graphene monolayer analytically and computationally, respectively. As studies analogous to the aforementioned ones had not yet been developed for more than one layer of graphene, it was pertinent to study the dynamics of wave packet in multilayer graphene, in order to verify how is the evolution of a Gaussian wave packet when there is more than one graphene layer and, in addition, verify the existence of the ZBW.

Most recently, advances in the isolation of monolayer semiconductors and their stacking as van der Waals heterostructures (vdWhs) opened a new field of study of artificial 2D hybrid materials [50, 51]. Combining two monolayers of semiconducting transition-metal dichalcogenides (TMDs) in a vdWhs with an inter-layer twist introduces an in-plane moiré pattern [52], as illustrated in Fig. 1.6. This pattern is associated with an in-plane modulation of the conduction and valence band edges, thus presenting new possibilities to engineer the electronic band structure, quasi-particle confinement, and optical properties of the system. Applying a perpendicular electric field, the moiré exciton band structure acquires a massless Dirac fermion character, similar to low-energy electrons in graphene. The combination of the long lifetime and bright luminescence [53] of ILE, along with their Dirac-like dispersion tunable by the twist angle and applied fields, makes twisted vdWhs a strong candidate for experimental detection of ZBW of moiré excitons, motivating us to study, theoretically, such a possibility.

1.4 Structure of the thesis

This thesis is divided in two different subjects. After presenting a general introduction to both subjects and to the main properties of graphene, the ZBW phenomena, within the time evolution of a 2D Gaussian wave packet, for low-energy electrons in ABC-stacked n-layer graphene (ABC-NLG) and also for moiré excitons in twisted MoS_2/WSe_2 hetero-bilayers, is investigated in the first part of this thesis. In the second part, the plasmonic properties of graphene is used to probe the structure and composition of van der Waals heterostructures. Also, a detailed study of how Dirac plasmons couple to the phonons of transition metal dichalcogenides is presented.

Below, a summary of the content in each chapter is provided.

- In Chapter 2, I present the types of orbital hybridization and the allotropes of carbon. Then, the techniques for obtaining graphene, its main characteristics and applications are presented. At the end of this Chapter, we introduce the novel two-dimensional materials that rise after graphene and are inspired by it;

- In Chapter 3, we develop the *tight-binding* model for graphene monolayer and bilayer, generalizing it later to the N-ABC-stacked multilayer graphene case;

- In Chapter 4, the effect of *zitterbewegung* on the propagation of wave packets in ABC-stacked multilayer graphene, within an analytical and computational approach, is investigated. The aim of this is to answer the following question: **How is the *zitterbewegung* affected by changing the number of graphene layers?**

- Chapter 5 shows that, analogously to other Dirac-like particles, moiré excitons exhibit trembling motion, also known as zitterbewegung, whose long timescales are compatible with current experimental techniques for exciton dynamics. In this Chapter, the following question is answered: **Is it possible to use moiré excitons in van der Waals heterostructures as an advantageous solid-state platform to directly probe the *zitterbewegung* phenomena and its Dirac-like nature?**

- As a second subject of this thesis, in Chapter 6, the theoretical tools to study graphene plasmonics are introduced, from a brief introduction to the linear response theory and to the random phase approximation.

- In Chapter 7, a study of Dirac plasmons in van der Waals heterostructures is presented. Since graphene plasmons are very sensitive to the electrical surrounding environment, two important questions are answered: **Can Dirac plasmons, excited from terahertz to mid-infrared regime, be used to probe the structure and composition of van der Waals heterostructure?**

- In Chapter 8, the coupling strength between plasmons and the different vibrational phonon modes of the transition metal dichalcogenides (TMDs) are studied. The extend to which these modes are coupled depends on the TMD composition and structure, but also on the plasmons' properties. In this Chapter, the following question is answered: **How strong is the coupling of terahertz Dirac plasmons to phonons in transition metal dicalchogenide-based van der Waals heterostructures, and how the tuning of the Fermi energy can be used to increase the coupling strength?**

- In Chapter 9, the conclusions and outlook are presented.

2

Carbon: from graphite to graphene and beyond

In this chapter, the different forms of hybridization that the atom carbon atom can assume are presented along with its main allotropes, among them graphene, the object of study of this thesis. Next, the main techniques for obtaining graphene, its characteristics, and applications of graphene are shown. In the last section of this chapter, the new two-dimensional materials that raised after graphene are discussed.

2.1 The carbon atom

Carbon, the name given by Lavoisier in 1789, derives from Latin, which means coal. It is a chemical element whose symbol is C, has an atomic number 6 (6 protons and 6 electrons), mass of 12 u and is solid at room temperature. In the periodic table, it is located in the second period of the 4A family, being between metals and non-metals, as presented in Fig. 2.1. Carbon is responsible for the existence of a variety of organic and inorganic compounds. Due to its atomic structure, carbon can come together in different ways, giving rise to other substances exclusively made by carbon atoms, i.e., carbon allotropes.

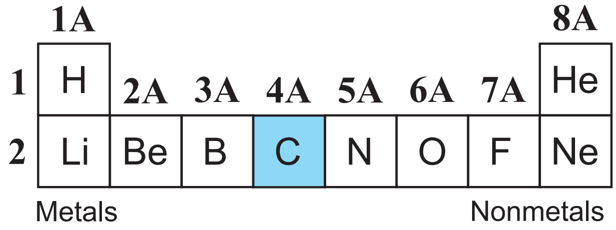

Figure 2.1: Illustration of the position of the carbon atom (C) in the table periodic.

The carbon atom, due to its six electrons, has its configuration for the lowest energy state, also called the ground state, given by $1s^2 2s^2 2p^2$. Electrons in an atom can be divided into valence electrons, defined as electrons that are orbiting the nucleus in the outermost atomic shell of an atom, and those electrons that are closer to the nucleus with filled orbitals, the so-called core electrons. The valence electrons are responsible for the

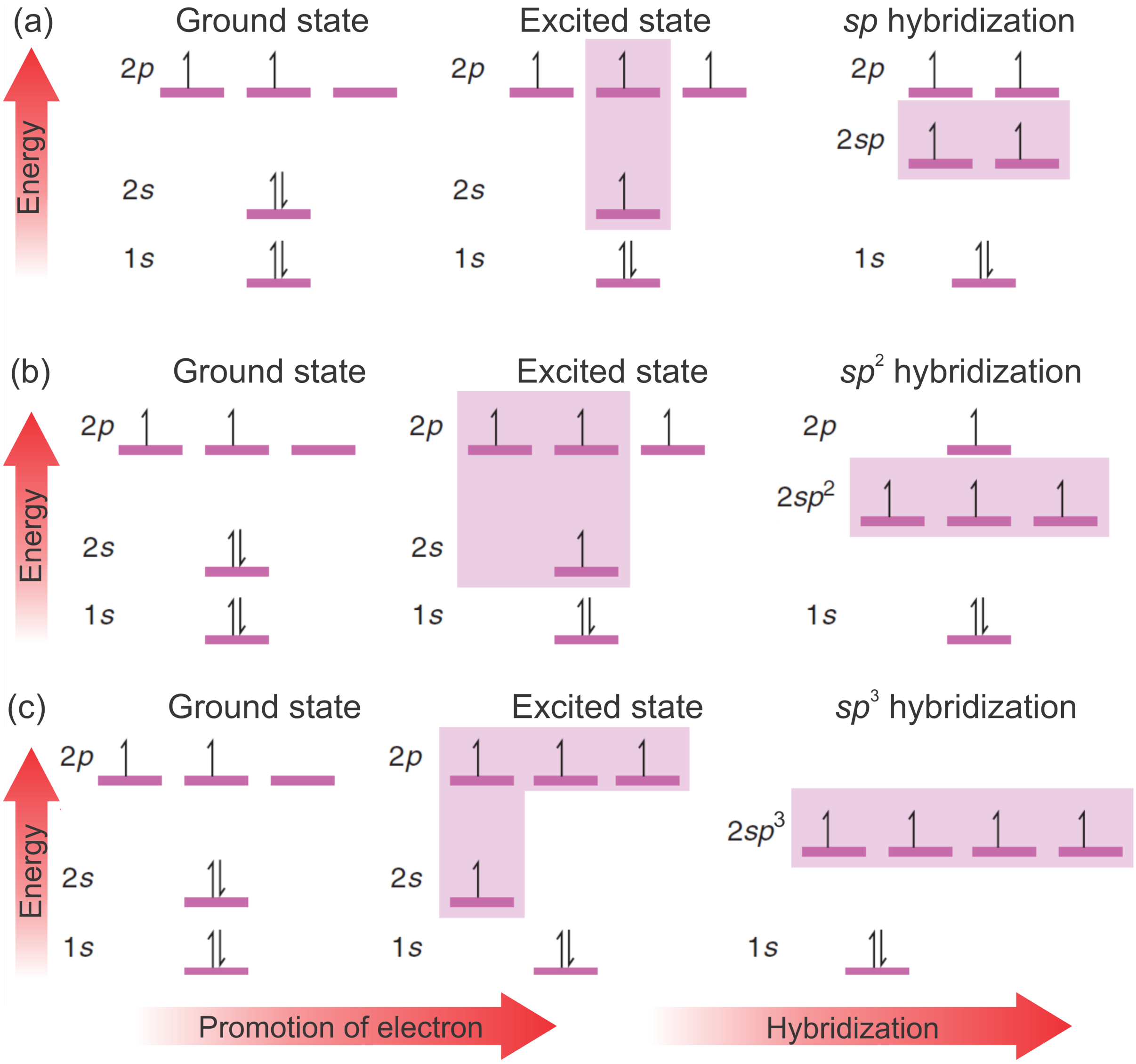

Figure 2.2: Electronic configuration for the ground and excited state of the carbon atom. Adapted from Ref. [55].

chemical properties of the atom, because it is the loss, gain, or rearrangement of these that determine the chemical reactions, while the core electrons do not contribute to chemical reactions [56]. Thus, in the graphene case, the four atoms that occupy the $2s^2$ and $2p^2$ are the valence electrons. Thereby, the wave functions of the last four electrons can recombine with each other, changing the occupation of the $2s$ and $2p$ orbitals originating hybrid orbitals[1] [57]. These hybrid orbitals are defined as σ or π. The σ bond is formed due to the overlap of two hybrid atomic orbitals and is cylindrically symmetric. That is, the electrons in the bond are symmetrically distributed around an imaginary line connecting the centers of atoms joined by the bond. On the other hand, the π link is due to the overlap of two p orbitals side by side.

---

[1] The concept of combining orbitals, called hybridization of orbitals, was proposed by first time by Linus Pauling (1901-1994) in 1931.

Table 2.1: Representation of the arrangement of the hybrid orbitals, geometry and examples for the types of sp, sp^2 and sp^3 hybridization, respectively, of the carbon atom. Adapted from references [58], [59] and [60].

Hybrid orbital	Geometry	Arrangement of hybrid orbitals	Example
a) 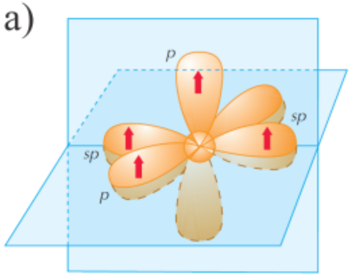 Hybridization *sp*	b)  Linear	c) 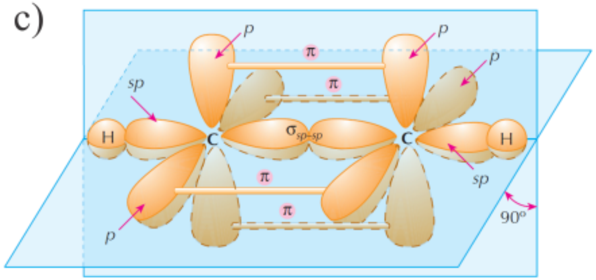 Ethine	d) 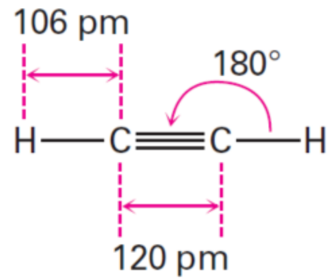 Ethine
e) 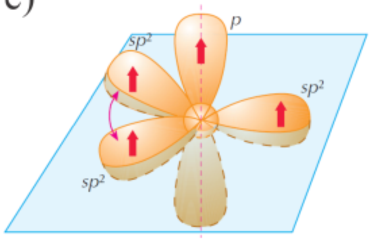 Hybridization *sp²*	f) 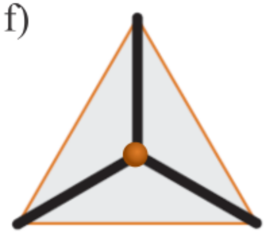 Trigonal planar	g) 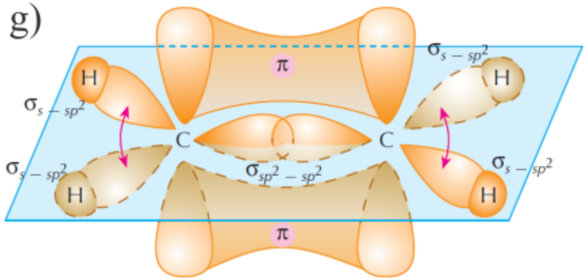 Ethene	h) 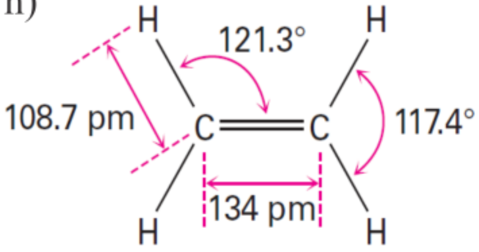 Ethene
i) 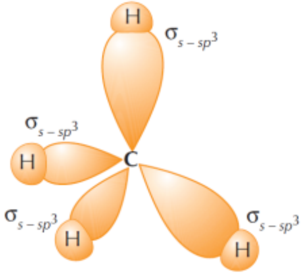 Hybridization *sp³*	j) 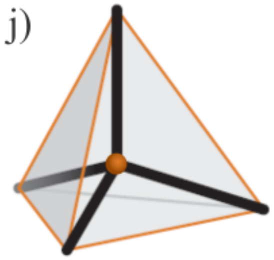 Tetrahedral	l) 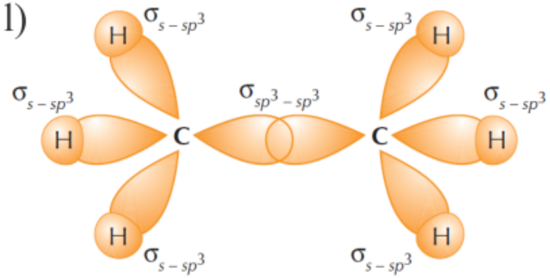 Ethane	m) 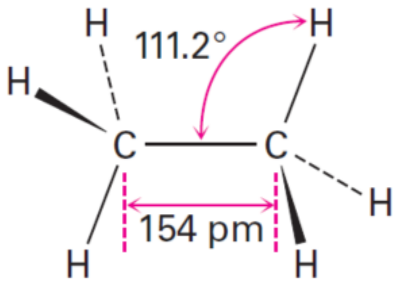 Ethane

2.1.1 *sp* hybridization

In this type of hybridization, one electron from the 2*s* layer and another one from the 2*p* layer of the carbon atom are hybridized to form two *sp* orbitals, equivalent to each other, Fig. 2.2(a). The remaining orbitals (2*p*) are not hybridized and are perpendicular to each other and to the *sp* orbitals. On the other hand, the two hybridized orbitals are located on the same line and opposite to each other, to minimize electronic repulsion, forming an angle of 180º in relation to each other, as illustrated in Tab. 2.1(a)). That is the reason why the geometry of *sp* hybridization is called linear, as can be seen in Tab. 2.1(b).

To illustrate the *sp* hybridization, the ethyne ($HC\equiv CH$), illustrated in Tab. 2.1(c)-(d), also known as acetylene, can be considered. The hybrid molecular orbitals of ethyne are formed as follows: (i) two carbon atoms overlap the *sp* orbitals to form a σ_{sp-sp} bond between them (this is just one bond of the triple bond, CC); (ii) the remaining two *sp* orbitals, one from each carbon atom, overlap with the *s* orbitals of hydrogen atoms to form two σ bonds ($C-H$); (iii) the two *p* orbitals of each carbon atom join laterally to form two π bonds (these are the other two bonds of the triple bond); these two π bonds, which determine two nodal planes that pass through the two nuclei, is the reason of the ethyne to have circular symmetry along the triple bond. Consequently, if a rotation occur, any new compound will not be formed. The Tab. 2.1(c) shows the final configuration after these three steps.

2.1.2 sp^2 hybridization

In this case, three electrons from the carbon valence layer (layers 2*s* and 2*p*), as shown in Fig. 2.2(b), rearrange, giving rise to three hybrid orbitals called sp^2. These hybrid orbitals, located on the same plane, are equivalent to each other and are separated by an angle of 120º, which is the reason why its hybridization is called planar trigonal, see Tab. 2.1(e)-(f). The remaining electron remains in the *p* orbital, perpendicular to the plane of the three hybrid orbitals.

Taking the ethane ($H_2C=CH_2$), whose molecular structure is illustrated in panel Tab. 2.1(g), as an example, the hybrid molecular orbitals are formed as follows: (i) a sp^2 orbital of each carbon atom overlaps each other forming a $\sigma_{sp^2-sp^2}$ molecular orbital ($C=C$); (ii) the other sp^2 orbitals of carbon atoms overlap with the 1*s* orbitals of hydrogen atoms forming bonds σ_{s-sp^2} (CH); (iii) the remaining two electrons are located in the *p* orbitals of each carbon atom, thus the lateral overlap of these two orbitals results in a π bond. The π orbital resembles an electronic cloud, located in the regions above and below the plane determined by the double bonds. Table 2.1(g) shows the final configuration after these three steps.

Unlike ethyne, the $C=C$ double bond in ethane has no rotational symmetry with respect to the axis that joins the two carbon atoms. This is due to the fact that the overlap will be maximum between the p orbitals of a π bond when the axes of the p orbitals are parallel, so, rotating the double bonded carbon atom to 90^{o} will break the π bond.

2.1.3 sp^3 hybridization

Finally, the sp^3 hybridization occurs when one electron from the $2s$ layer and three from the $2p$ layer of the carbon atom rearrange, giving rise to four hybrid sp^3 orbitals, as shown in Fig. 2.2(c). These four hybrid orbitals are equivalent to each other and oriented towards the vertices of a tetrahedron, hence the origin of the name of the hybridization geometry sp^3, see Tab. 2.1(i)-(j). The hybridized orbitals attract s orbitals of the hydrogen atom until they form σ_{s-sp^3} (C——H) molecular orbitals.

As a last example, ethane (H_3C——CH_3), can be used to illustrate this type of hybridization, (see Tab. 2.1(l)-(m)). In this case, the formation of atomic orbitals occurs as follows: (i) first, the formation of the bond σ_{s-sp^3} between the carbon atom and the hydrogen atom, occurs as previously described; (ii) the frontal overlap of the sp^3 orbitals of the two carbons, forming a link $\sigma_{sp^3-sp^3}$. The final configuration can be seen in Tab. 2.1(l).

Since the $\sigma_{sp^3-sp^3}$ bond has cylindrical symmetry along the connection axis (or rotational symmetry, as long as the central axis that joins the two carbon atoms is used as a reference), the rotation of the single bond does not require a large amount of energy. Therefore, atoms groups united by a simple bond turn relatively free in relation to each other.

2.2 Allotropic forms of carbon

Due to the forms of hybridization of the carbon atom, a series of other compounds formed exclusively by carbon can be obtained (found in nature or synthesized in the laboratory). Table 2.2 classifies the five allotropes described in this section according to their dimensionality, also providing information about hybridization, density, bond length and electronic properties [55, 61].

2.2.1 Graphite and diamond

The two most stable and well-known carbon allotropes are graphite and diamond, whose crystal structures are illustrated in Figs. 2.3(a)-(b), respectively [62]. Graphite crystallizes in a regular hexagonal system with dihexagonal dipyramidal symmetry, composed of several layers of atoms with symmetry sp^2. It is due to this form of hybridization that graphite conducts electricity. Another characteristic worth mentioning is the fact that the parallel planes in a crystal of graphite are connected by a π bond. As the planar interaction is weak, it is possible to isolate a single layer of graphite, obtaining one of the most important materials synthesized in recent years: graphene.

Unlike graphite, the diamond presents hybrid sp^3 orbitals. The diamond-shaped crystal structure, illustrated in Fig. 2.3(b), consists of a Bravais lattice of face-centered cubic system and a base with two identical atoms, one at the origin and another at 1/4 from the diagonal of the cube [63]. Note also that each atom is in the center of a tetrahedron formed by four nearest neighbors, typical of the sp^3 hybridization. On the Mohs scale[2], the diamond is the hardest natural material presenting a value equal to 10, on a scale ranging from 0 to 10.

2.2.2 Fullerenes

In 1985, Harold. W. Kroto, Robert F. Curl and Richard E. Smalley, obtained a series of chemical structures formed exclusively by carbons, which would later be called

Table 2.2: Carbon allotropes in terms of their dimensionality, as well as some characteristics of them. Since the electrical conductivity in graphite depends on the position, then "*" indicates the "a" direction and "**" indicates the "c"direction. Adapted from Refs. [55, 61].

	0D	1D	2D	3D
Allotrope	Fullerene C_{60}	Nanotube	Graphene	Graphite; Diamond
Hybridization	sp^2	sp^2	sp^2	$sp^2;sp^3$
Density (g/cm^3)	1.72	1.20	2.26	~2,1;3.52
Tenacity	Flexible; Elastic	Flexible; Elastic	Elastic	Flexible; Inelastic; N/a
Electric conductivity (S/cm)	10^{-10}	Depends on the structure	~2.000	~2.5x10^{4*} and $6^{**;}$ N/a

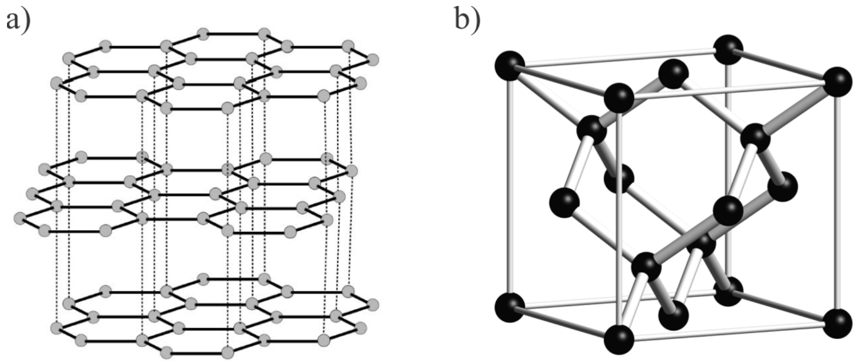

Figure 2.3: Illustration of the crystal structure of (a) graphite and (b) diamond.

---

[2] The Mohs scale quantifies the hardness of minerals through the ability of harder material to scratch a softer material and goes from 0 to 10.

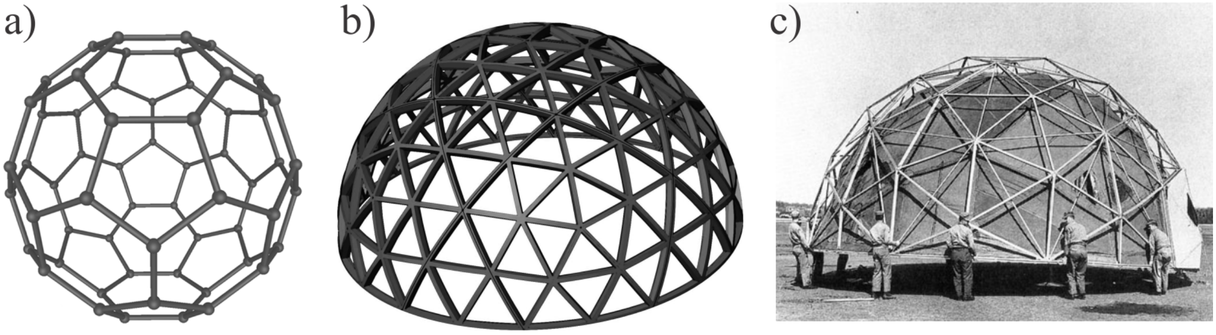

Figure 2.4: (a) Schematic representation of the fullerene C_{60}, (b) the geodesic dome and (c) the idealized construction of B. Fuller.

fullerenes [64]. According to the literature, Kroto and his team were trying to understand the mechanisms for the formation of long carbon chains observed in interstellar space. The experiment consisted in the vaporization of rotating graphite disks punctually by irradiating high-energy lasers, in a helium atmosphere, in high-temperature [65]. The obtained samples were analyzed using a mass spectrometer, allowing the detection of carbon clusters with different quantity of atoms. However, the most stable structure of fullerene is made up of 60 carbon atoms (C_{60}).

Those carbon samples present a geometrical shape similar to that of a geodesic dome illustrated in Fig. 2.4, therefore, those carbon clusters were labeled fullerenes, honoring one of the greatest architects of the 20th century, the North American Buckminster Fuller[3], mentor of the geodesic domes [66]. That was the first new allotropic form of carbon discovered in the 20th century, wich earned H. 1996 Kroto, R, Curl and R. Smalley the 1996 Nobel Prize in Chemistry.

2.2.3 Carbon nanotubes

The frontier of carbon physics would be expanded again in 1991, when Sumio Iijima discovered the carbon nanotubes (CNTs), illustrated in Fig. 2.5. CNTs are made up of hexagonal carbon arrays that give rise to small cylinders, Fig. 2.5(a). Typically, they have a diameter range from a few angstroms to tens of nanometers and can be over several centimeters in length [67].

Figure 2.5 illustrates the geometry of the CNTs [68]. Structurally, CNTs can be seen as a graphite sheet rolled into a cylindrical shape, with two distinct types: single-walled (SWCNTs) and multiple-walled (MWCNTs). When two crystallographically equivalent sites coincide on a rolled graphite network, we have an SWCNTs. The *chiral* vector $\boldsymbol{C}$ defines the relative position of two sites and is defined by two integers (n, m), and by the unit vectors $\hat{a}_1$ and $\hat{a}_2$ ($\vec{C} = n\hat{a}_1 + m\hat{a}_2$) of the hexagonal lattice, as show in Fig. 2.5(d). The values of (n, m) determine the class of CNTs, which can be: armchair, when $n = m$

---

[3] Richard Buckminster Fuller (1895 - 1983) was a visionary, designer, architect, inventor and American writer.

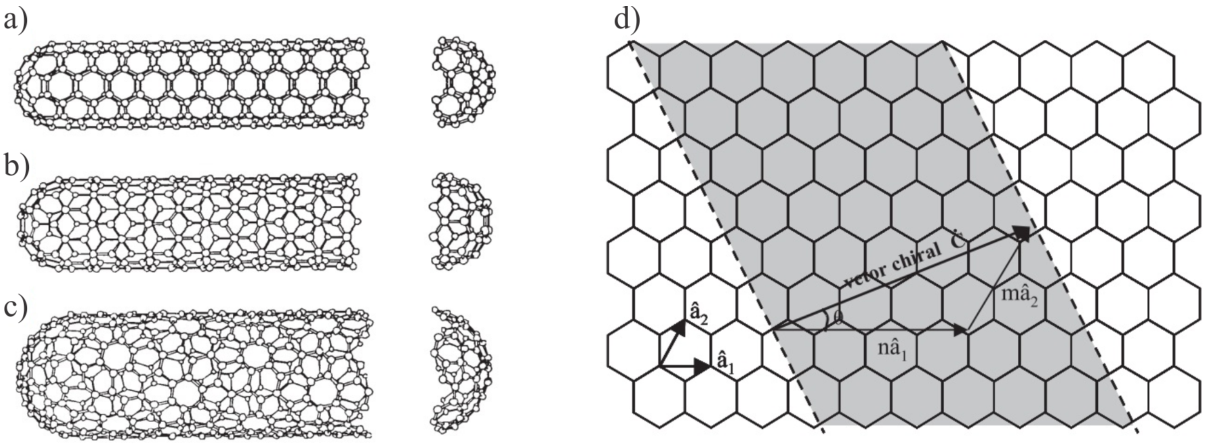

Figure 2.5: CNTs geometries: (a) armchair, (b) zig-zag, (c) chiral. The schematic structure of unrolled CNT is shown in (d).

and $\varphi = 30°$, zig-zag, $n = m = 0$ e $\varphi = 30°$, or chiral, $n \neq m \neq 0$ and $0 < \varphi < 30°$, respectively represented in Figs. 2.5(a)-(c).

2.2.4 Carbon nanofoam

In 2002, a team of physicists from Greece, Australia and Russia, led by Andrei V. Rode, discovered carbon nanofoams [69, 70]. Carbon nanofoam is considered the fifth allotrope of carbon and presents carbons with sp^2 and sp^3 hybridization. Figure 2.6(a)-(b), respectively, shows an image using transmission electron microscopy (TEM) and scanning electron microscopy (SEM) [71]. This new material, a highly porous, amorphous carbon nanomaterial, is a cluster of randomly interconnected carbons with average diameters between 6 and 9 nanometers [72, 73]. Among the solids, it has the lowest known density (only two milligrams per cubic centimeter), low electrical conductivity and is the first allotropic form of carbon to exhibit ferromagnetism properties, although temporary, at room temperature [71–73].

2.2.5 Graphene

Graphene, the last allotropic form of carbon discovered, was obtained in 2004. Figure 2.10 illustrates a timeline of events from graphite to the preparation and characterization of graphene made by Geim, Novosolev and collaborators in 2004 [8, 74]. The technique used by the team of scientists to obtain graphene is relatively simple and consists of using a specific type of scotch tape, to separate layers from graphite, until a monolayer graphene is obtained, as shown in Fig. 2.7.

The use of animal or vegetable glues to connect interfaces dates back to the prehistory [75, 76]. In Ancient Greece, the phenomenon of adhesion that allows the geckos to settle and move quickly on ceilings and walls caught Aristotle's attention. Only with the aid of the SEM was it possible to unravel the physical phenomenon behind the enormous

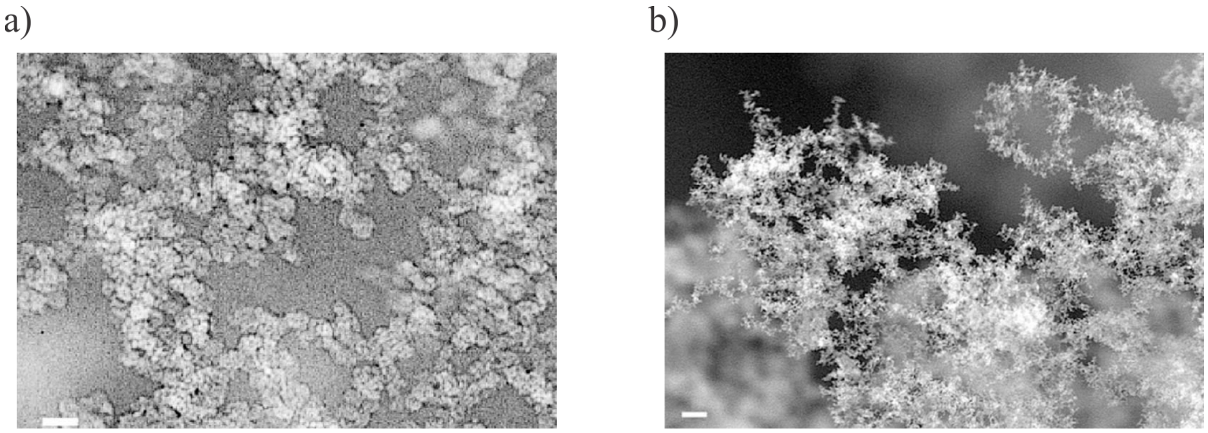

Figure 2.6: Image of a carbon nano-foam using (a) transmission electron microscopy (TEM) and (b) scanning electron microscopy (SEM). Adapted from Ref. [71].

ability of the geckos' feet to adhere: the sole of the gecko's paw is made up of micrometric "hairs" that adhere to surfaces by non-directional van der Waals-London interactions, as illustrated in Fig. 2.8. Considering only one micro "hair", the force supported is small, $\sim 10^{-7}$ N). On the other hand, millions of these hairs produce an adhesion of the order of 10 $\mathrm{N/cm^2}$ due to the van der Waals-London forces [77]. Geim, Irina V. Grigorieva (Geim's wife), Novoselov, S. V. Dubonos, A. A. Zhukov and S. Yu. Shapoval, in 2003, developed biomimetic microphytes that played the role of the geckos feet [78]. This was, undoubtedly, one of the main steps taken by the research team in the search of the graphene monolayer.

Geim and his team, exfoliated layers of a graphite crystal with the adhesive tape developed by them, managing to obtain flakes formed from some layers of graphite and then deposited them on a SiO_2 substrate with thickness of 315 nm. For graphite films with thicknesses of the order of 50 nm, it is necessary to add an optical path to produce different interference patterns on the SiO_2 substrate to define the region where the monolayer can

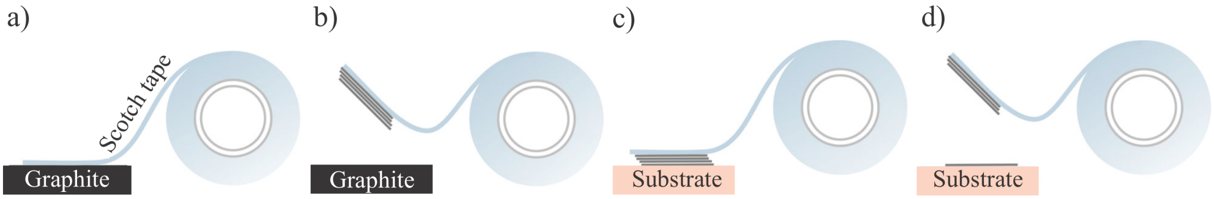

Figure 2.7: Pictorial illustration of the micromechanical cleavage technique to obtain graphene. First, (a) a special type of scotch tape is placed on top of a graphite crystal, (b) in order to obtain some layers of graphene. Then, (c) the graphene layers are pressed onto a substrate, normally is used a silicon dioxide SiO_2 substrate. After removing the tape (d) some layers remain on the substrate, making it possible to localize a graphene monolayer through some experimental techniques, such as scanning electron microscopy, for example. Adapted from Ref. [74].

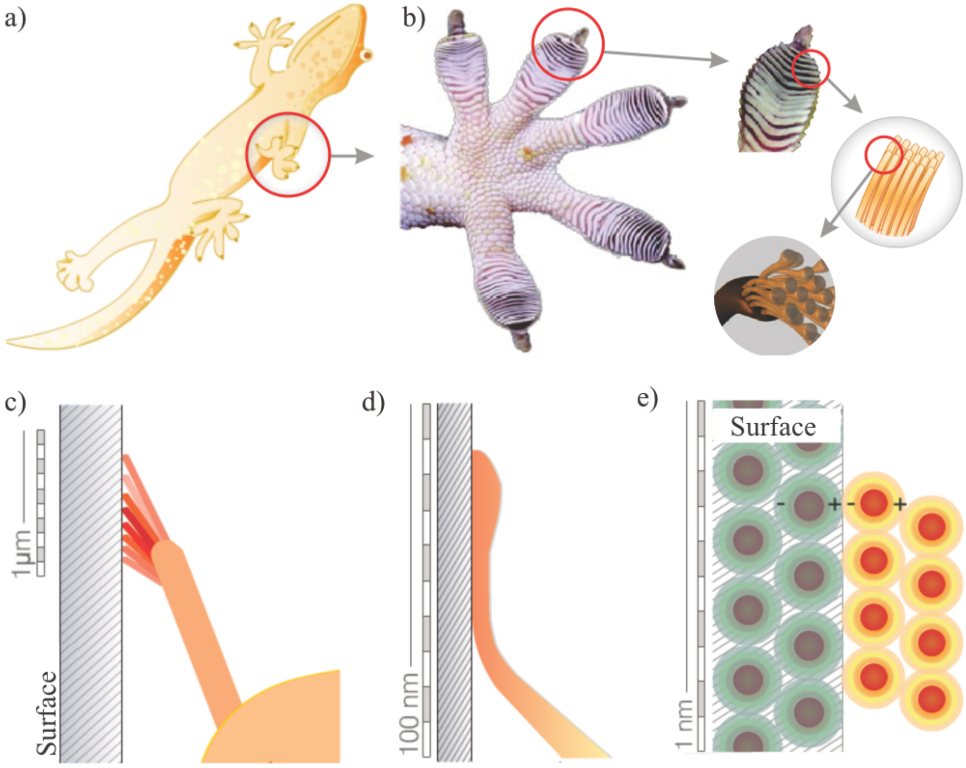

Figure 2.8: Illustration of the adhesion of the geckos'keratinized hair: (a) sole of the gecko's paw, (b) blades of the tips of the feet with a zoom showing the lamellae and the micrometric hairs, (c, d) micrometric hairs touching the surface and (e) illustration of van der Waals-London's strength. Adapted from Ref. [79].

be found using atomic force microscopy (AFM), since a graphite flake with this thickness is semi-transparent. However, it was not possible to observe changes in the interference pattern for films with thicknesses ∼1.5 nm. Thus, it is possible to classify the films into two classes: few-layers graphene (FLG), up to a thickness of approximately 10 layers, and multilayer graphene (MLG), for more than 10 layers [80]. Finally, Geim and his team, using SEM, were able to identify the monolayer graphene from samples containing FLG [8]. An adaptation of the images obtained by the group of researchers mentioned here are illustrated in Fig. 2.9.

Once the researchers were able to obtain graphene using mechanical exfoliation, it was obtained by scientists from around the world using different experimental techniques already known to the scientific community. In the next section, we will describe some of the most common and important methods to obtaining graphene.

2.3 Techniques for obtaining graphene

The most important factor for any new product to be commercially viable, as well as for it to be produced on a large scale, is its cost of production and its quality. For graphene, the method adopted to produce it plays a fundamental role in the properties

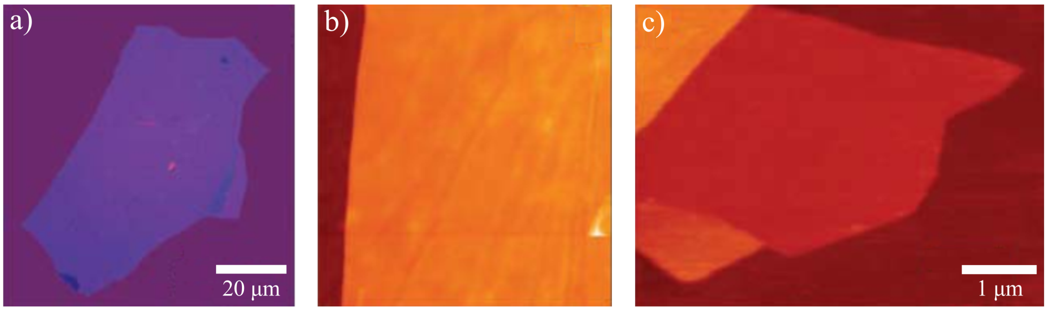

Figure 2.9: Graphene films: (a) image of a relatively large graphene multilayer with thickness 3 nm over SiO_2, (b) AFM image of a graphene area of $4\mu m^2$ close to its border (SiO_2 is represented by the brown region) and (c) graphene image obtained by AFM. Adapted from Ref. [8].

of the final product.

In this section, some quantitative aspects of graphene production methods are discussed, including the procedure used by Geim et. al [8]. Table 2.3 summarizes the advantages and disadvantages for producing graphene using the four methods described here.

2.3.1 Mechanical exfoliation

Mechanical exfoliation, also known as micromechanical cleavage, is a method that has been used for decades by scientists in the field of crystallography [84, 85]. In 1999, this method was applied to graphite where scientists were able to obtain some layers of graphene that were proven through SEM and AFM [86]. In Fig. 2.11(a), a diagram classifies this method according to the quality of the graphene obtained, cost, scalability, purity and production.

As previously described, the micromechanical cleavage is a simple method, which consists of using an adhesive tape to reduce the number of layers of the graphite, using SiO_2 as a substrate, Fig. 2.11(e). Although this technique is not feasible for large-scale application, it is still the method for obtaining graphene with the best level of quality, being widely used for fundamental studies and for technological prototypes.

2.3.2 Liquid phase exfoliation

Liquid phase exfoliation (LPE) is another technique for obtaining graphene. It consists of exfoliating the graphite in solutions that can be aqueous or not [87–92]. In the first step, the graphite is placed in the solution to reduce the force of the van der Waals interactions between the graphene layers. Then, ultrasonic waves or electric fields are used to maximize the process of exfoliating a graphite crystal [93].

Unfortunately, this technique ends up leaving an amount of graphite that was not ex-

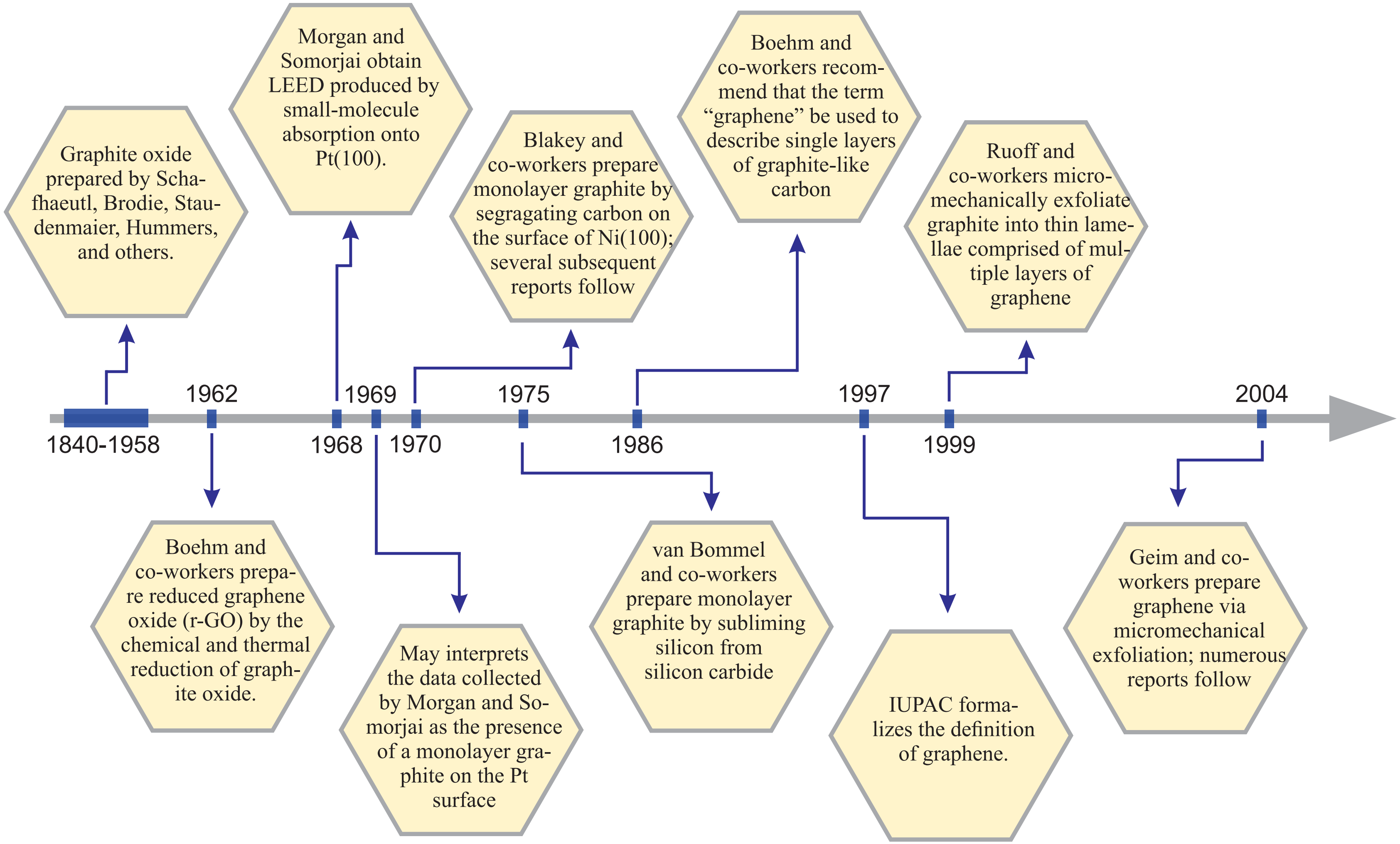

Figure 2.10: Timeline from graphite to the preparation and obtaining of Graphene by Gaim and his team. Adapted from Ref. [81].

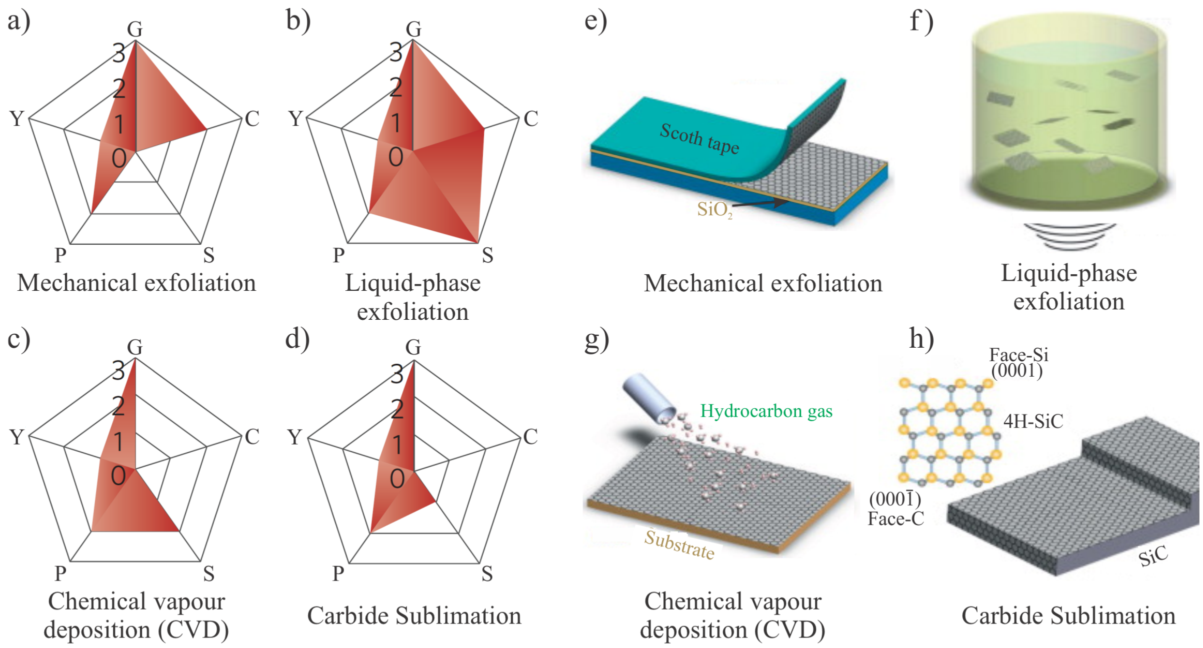

Figure 2.11: Most common forms of graphene production. On the left side, panels (a)-(d), is presented a diagram illustrating the quality of graphene (G), cost (C) (lower values correspond to higher production costs), scalability (S), purity (P) and production (Y) for four different methods to produce graphene. On the right side, panels from (e) to (g), is show a scheme for each type of process of production. Adapted from Refs. [82, 83].

foliated. This excess needs to be removed later [94]. However, due to the high scalability and low cost, this technique eventually became suitable for large-scale graphene production [95]. Figures 2.11(g) and (b) illustrate this process and provide the main information related to this technique, respectively.

2.3.3 Chemical vapor deposition

In this method, abbreviated by CVD, a silicon substrate with a metal layer is used, once copper or nickel is usually used due to low carbon solubility [96–98]. A hydrocarbon gas (methane) is used in a hydrogen atmosphere. As the temperature rises, the methane molecule breaks down and the atom carbons is adhered to the substrate, forming graphene layers, as shown in Fig. 2.11(f). Then, the graphene is transferred to a substrate.

The result is a high-quality graphene without impurities. Although large-scale production is viable, the cost of this technique is high, as shown in Fig. 2.11(c).

2.3.4 Carbide sublimation

Graphite production from SiC was reported for the first time in 1896 by Acheson for lubricant applications [99]. It is common to find in the literature the term "epitaxial growth" for this method [100]. Figure 2.11(d) shows a schematic representation of some aspects of this technique.

The sublimation of carbides consists of using some carbide, normally silicon carbide (SiC), where this material is heat treated in a vacuum or in an inert atmosphere. The objective is to make the sublimation of the material bounded to the carbon atoms, giving origin to graphene [101–103], as shown in Fig. 2.11(h). Growth can be done on both sides of the carbon and silicon. The advantage of this technique is due to the fact that there is no need to transfer the graphene to a substrate. However, the negative aspect is due to the formation of zones with different number of graphene layers, i.e., the number of layers to be obtained is not yet controlled and mobility becomes less if growth occurs on the silicon side [104, 105].

2.4 Graphene's properties

2.4.1 Electronic properties

In 2005, Novoselov and his group demonstrated that the charge carriers of graphene can behave continuously like electrons and holes in concentrations in the order of 10^{13} cm^{-2} with a mobility μ that can exceed the 15.000 cm^2/volts even at room temperature ($\sim$ 300 K) [107]. However, the dependence on graphene's electronic mobility is limited by impurities. Thus, in clean samples μ can reach values in the order of 100.000 cm^2/volts,

Technique	Advantages	Disadvantages
Mec. exfoliation	✓ Excellent electronic quality; ✓ Flat surface.	✗ Small size; ✗ Not scalable.
Liquid phase exfoliation	✓ Low cost; ✓ It can be produced on a large scale.	✗ Small overlapping fragments; ✗ Low quality electronics.
Chemical vapor deposition	✓ Graphene monolayer; ✓ Excellent electronic quality; ✓ Large graphene areas; ✓ Easy to transfer to other substrates; ✓ Can be reproduced on a large scale.	✗ No need for high Cu vapor; ✗ Rough surface; ✗ It needs to be transferred to a substrate; ✗ Requires a cleaning step; ✗ Large difference in expansion coefficient with the substrate.
Carbide sublimation	✓ Excellent electronic quality; ✓ Flat surface; ✓ It does not need to be transferred to another substrate;	✗ Process takes place at high temperatures; ✗ Areas limited according to the size of the silicon carbide.

Table 2.3: Advantages and disadvantages for producing graphene from mechanical exfoliation, chemical exfoliation in liquid phase, chemical deposition in vapor phase and carbide sublimation. Adapted from Ref [55, 106].

surpassing some semiconductors, such as the indium antimony (InSb), which has a mobility approximately given by $\mu \approx 77.000$ cm^2/volt at room temperature [77].

In chapter 3, the electronic band structure of graphene is calculated, analytically, showing that low-energy electrons in graphene behave like massless quasi-relativistic particles with spin 1/2. This allows one to describe these electrons through a Dirac-like equation for massless particles. This intrinsic electrons behavior in graphene, perhaps the most notable one, was observed by Novoselov and his group, as reported in Ref. [8]. In that case, they found that the charge carriers in graphene present high velocity, in the order of the Fermi velocity, i.e., 10^6 m/s, and low scattering, characterizing a ballistic transport. Thus, the treatment of electrons in graphene could no longer be treated by the Schrödinger equation, but by the Dirac equation. For this reason, graphene can be used for many experimental observations of quantum mechanics, such as the quantum Hall effect (QHE) [8], the Berry phase [108], Klein tunneling [109], and also for a wide range of industrial applications.

2.4.2 Mechanical properties

In 2008, researchers Changgu Lee, Xiaoding Wei, Jeffrey W. Kysar and James Hone, studied the elastic properties of graphene using the instrumented indentation technique[4] through an AFM [110]. To do so, the group placed graphene flakes on a silicon substrate with circular wells, Fig. 2.12(a), with diameters between 1 μm and 1.5 μm, both with depth of 500 nm, separated by 5 nm from each other. On top of the substrate, they placed a very thin layer of SiO$_2$ with a thickness 300 nm thick. Using an optical microscopy, the group

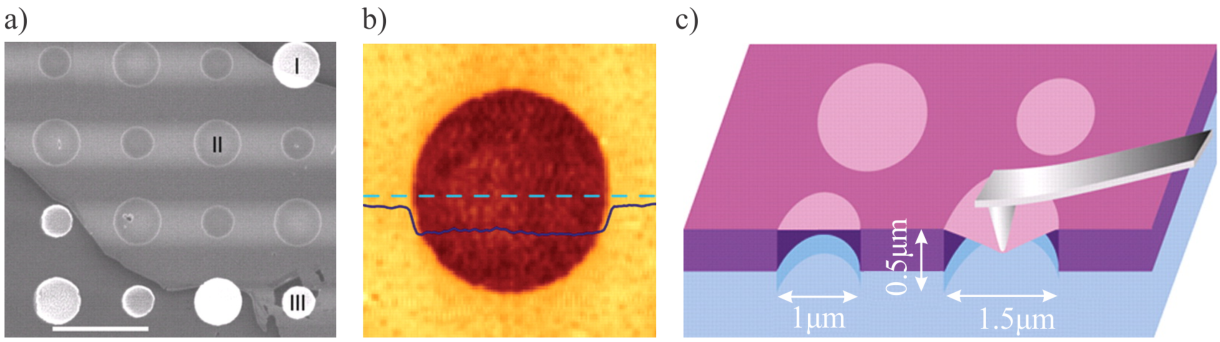

Figure 2.12: Images of suspended graphene membranes. (a) electron micrograph images of a graphene flake on top of a SiO$_2$ substrate with holes. Regions I and II show pores partially and totally covered by graphene, respectively, and region III shows a fracture due to indentation. (b) Image of the pore yet to be drilled. The continuous line represents the height profile of the dashed line, which is about 2.5 nm. (c) Schematic view of the nanoindentation procedure and the graphene membrane. Adapted from reference [110].

---

[4] Also known as nanoindentation. With this technique it is possible to measure the hardness (H) and the modulus of elasticity (E). To do so, is applied a force perpendicular to the sample using a tip with a specific shape allowing to measure the hardness and also the elasticity of the sample.

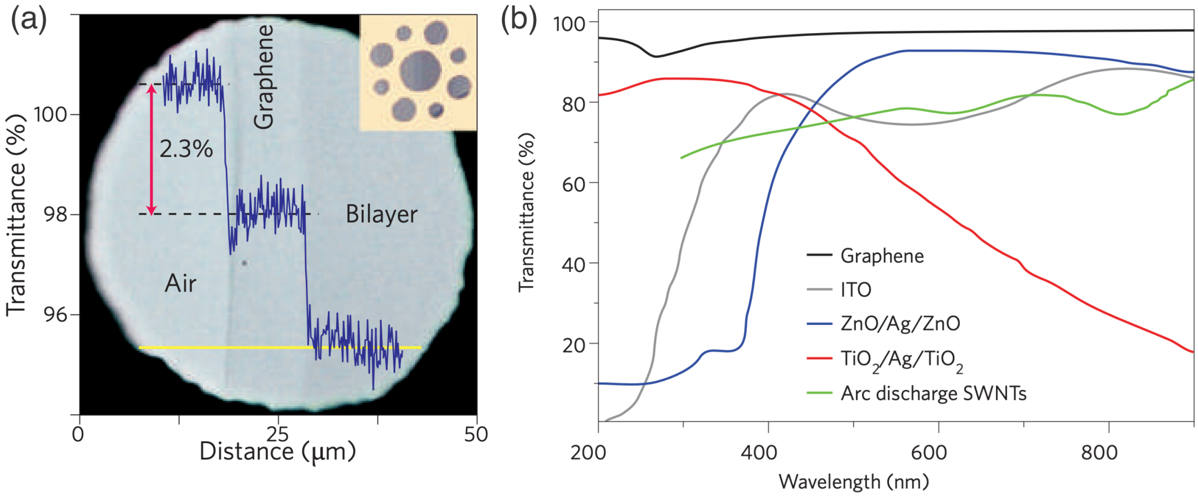

Figure 2.13: (a) Transmittance of graphene from a monolayer to a bilayer graphene. Note that a single layer absorbs only 2.3 % of the incident light, while a bilayer absorbs twice this value. (b) Transmittance of graphene as a function of the wavelengths (in nm) compared to other compounds, like: ITO, ZnO/Ag/ZnO, TiO_2/Ag/TiO_2 and single-walled carbon nanotubes (SWNTs). Adapted from Ref. [111].

located a region with only one graphene monolayer. Then, using Raman microscopy it was possible confirm that was, in fact, a single graphene layer. Finally, a force was applied to the graphene membrane until the limit of its rupture. Figure 2.12 shows some images of the experiment.

As an outstanding result, the experimental value found by the researchers for the breaking point was 42 N/m, about 10 times higher than steel, a value higher than any other existing material until that date.

2.4.3 Optical properties

In addition to the properties already mentioned here, graphene has optical properties that make it a special material, when compared to any other existing. In terms of optical properties, a single layer graphene absorbs only 2.3 % of the incident light, as shown in Fig. 2.13, making it a practically transparent material [112]. The light absorption by a graphene monolayer grows linearly, thus it is possible to obtain the fine structure constant α experimentally. This is possible due to the fact that $\pi\alpha$, which is the same as $\pi e^2/\hbar c$, is approximately equal to 2.3 %.

2.5 Graphene applications

Due to its remarkable properties, graphene is one of the most promising materials of the last years. The idealization of its applications is quite vast and applies from genetic engineering to the aerospace industry. In this section, we will make a brief qualitative explanation of the possible applications of graphene in some areas.

2.5.1 Graphene-based transistors

As the progress of integrated circuits is based on reducing the scale of CMOS devices[5] and, parallel to this, through the relationship between low voltage, low power and high performance, graphene emerges as a great candidate for composing microchips in the post-silicon era. Since miniaturization allows a larger number of transistors to be used to form a particular electronic component, today it is quite common for personal computer processors to have two billion MOSFET transistors[6], with approximately 30 nm.

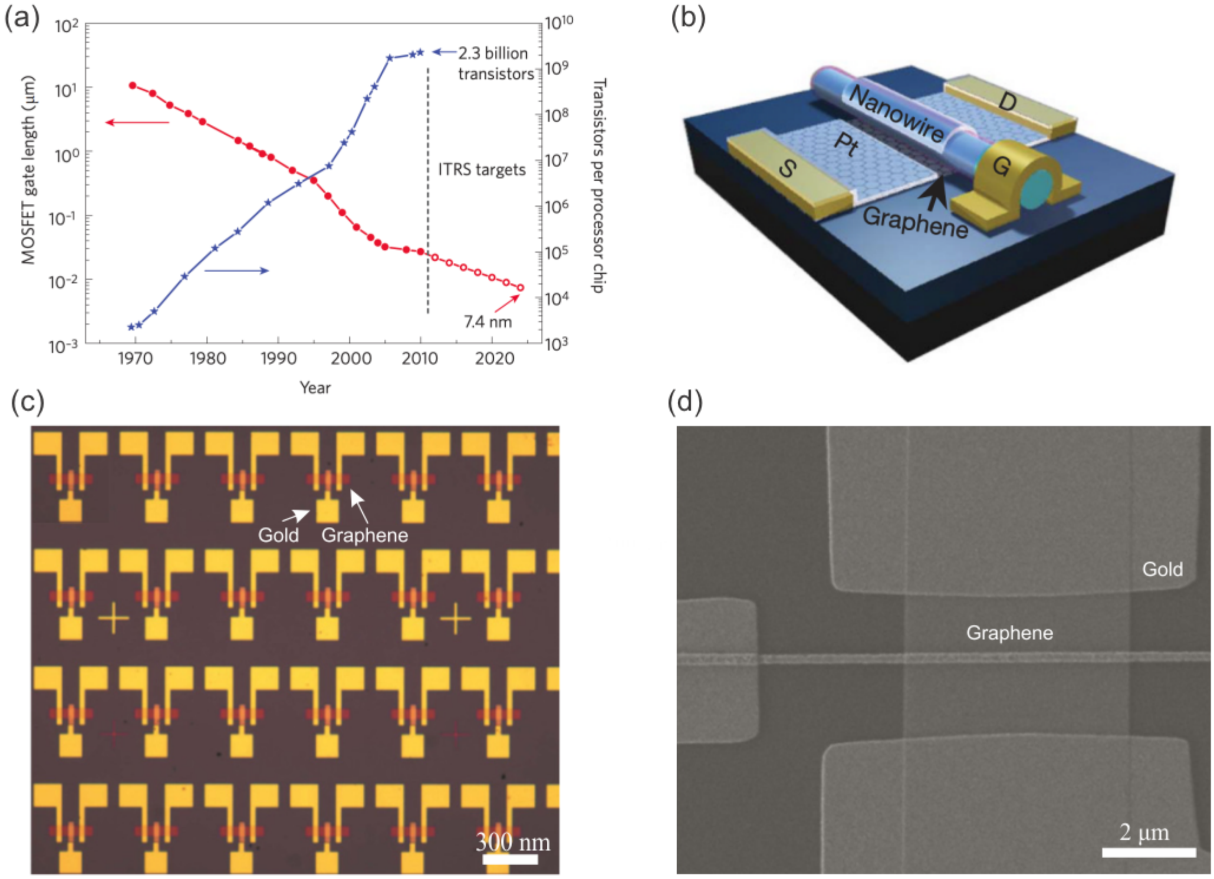

Figure 2.14: (a) Evolution of the size of MOSFET transistors (empty red circles are projections) over the years. (b) Schematic representation of a high-speed self-aligned graphene transistor. (c) and (d) represents a magnification of a self-aligned graphene-based transistor. Adapted from Refs. [113–115].

---

[5] CMOS, complementary metal-oxide-semiconductor, is a type of metal–oxide–semiconductor field-effect transistor (MOSFET) commonly used in the manufacture of integrated circuits, such as logic gates, microprocessors and microcontrollers.

[6] The metal oxide semiconductor field effect transistor (MOSFET), is the most common type of field effect transistor used in digital and analog circuits.

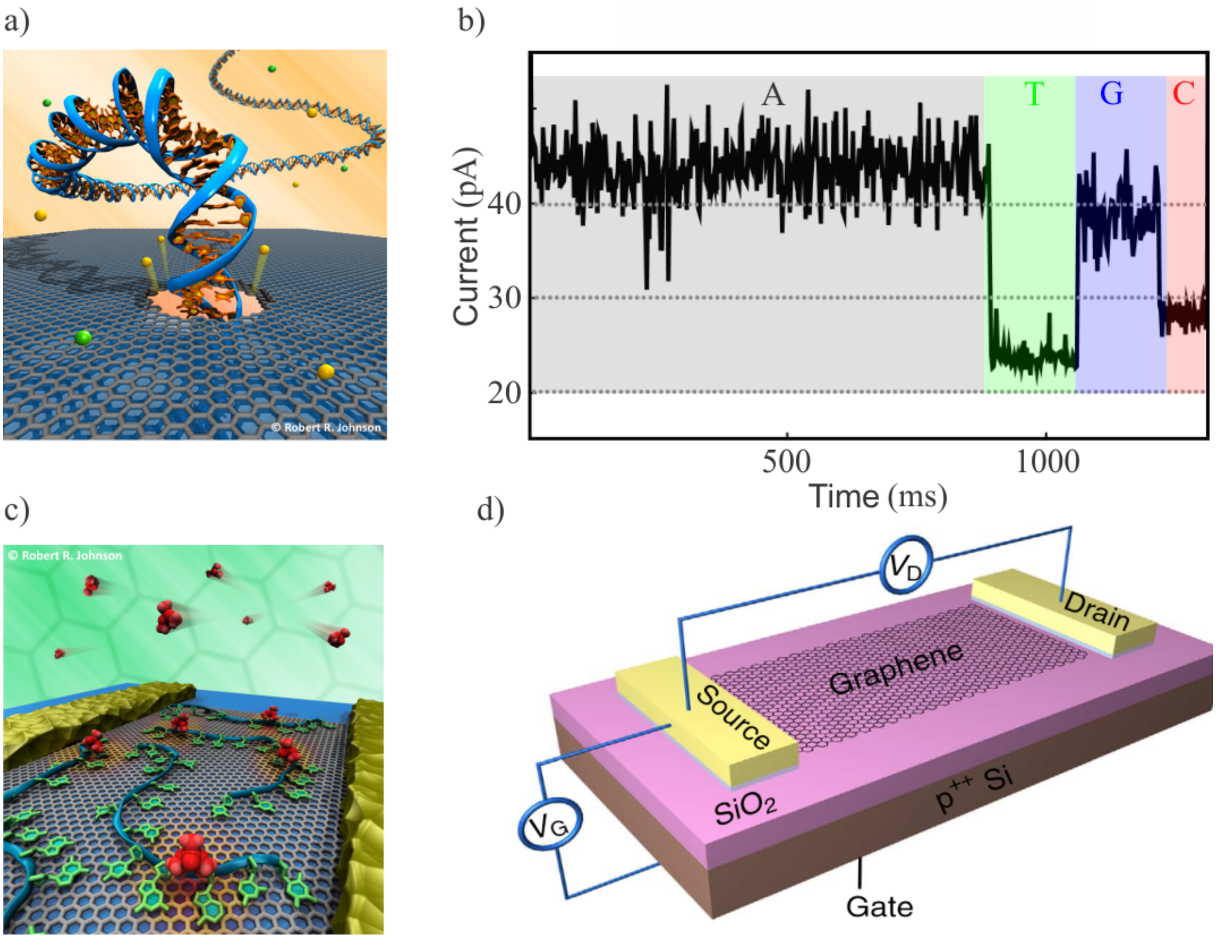

Figure 2.15: (a) Schematic illustration of a DNA molecule passing through a nanopore of a graphene monolayer. (b) Current variation as a function of time for a molecule that passes through a nanopore (A- adenine, T-thymine, G-guanine and C-cytosine). (c) Representation of a graphene-based biosensor and (d) graphene-based photosensors. Adapted from Refs. [120–123].

Figure 2.14(a) illustrates the evolution of the MOSFET size over the years, adapted from Ref. [113].

As an example of the properties of graphene applied to transistors, Fig. 2.14(b), researchers have shown that it is possible to achieve high frequencies with graphene, reaching 427 GHz [114–119], for example. Figures 2.14(c)-(d) represents a magnification of a self-aligned graphene-based transistor.

2.5.2 Graphene-based sensors

Nowadays, electronic sensors are quite common in our lives. They can be used to detect smoke, light, and others. Currently, studies using graphene as a sensor are increasing in many fields, such as electrochemistry, biology and photonics.

As a result of the high sensitivity to external ambient, such as molecules, electric fields, magnetic fields, graphene-based sensors are capable of detecting minimal variations of the current. For example, researchers have developed a promising technique to make genetic sequencing of DNA molecules [124–127]. Using a graphene monolayer, the researchers passed an individual DNA molecule through a small hole (called nanopore) in the graphene monolayer, as illustrated in Fig. 2.15(a). As the DNA molecule slid through the nanopore, a current is induced making possible its detection. With this information, it is possible to do the genetic mapping, as shown in Fig. 2.15(b). As one can see in Fig. 2.15(b), the adenine, thymine, guanine and cytosine, represented by A, T, G and C, respectively, induce different current values, making it possible to distinguish such molecules and, consequently, probe the genetic sequencing [120].

As another example, graphene can also be used to create biosensors capable of identifying toxic substances[128–132], for example, as illustrated in Fig. 2.15(c). Also, Fig. 2.15(d) represents a graphene-based photosensor developed to be used in digital cameras, presenting a sensitivity considerably higher (thousands of time) than the the conventional CCDs[7] and current CMOS, that also allows to capture images in a wider range of the electromagnetic spectrum [121].

2.5.3 Graphene-based flexible panels

As a last example of graphene application, is it possible to combine the excellent optical and electronic graphene properties with its flexibility, to develop new touchscreen displays/panels, replacing the commonly used Indium Tin Oxide[8] (ITO) used in cell phone screens and TV's. In Fig. 2.16(a) a thin graphene film, measuring approximately 30 inches, ideal for use in next generation televisions, is illustrates [134].

Graphene can also be applied to create a smart window to display information, as shown in Fig. 2.16(b). Once the graphene-based panel is turned off, the window is transparent [111, 135], Fig. 2.16(c). Figure 2.16(d) illustrates the flexibility that graphene-based displays have [136].

Recently, the company 2D Carbon Tech started producing graphene to be used in smartphones touch screen displays. Figure 2.16(e) depicts (on the left side) a graphene-based conductive film (measuring about 20×20 cm^2)) produced by 2D Carbon Tech and (on the right side) a prototype of a smartphone already using the graphene-based touch screen display [137].

As a last example, as illustrated in Fig 2.16(f), graphene can also be used in photovoltaic cell modules, that can be also flexible. Research shows that graphene is one of the materials with the highest potential for this purpose [139–144].

---

[7] CCD, charge-coupled device, is a semiconductor sensor for capturing images used in digital cameras.

[8] Indium tin oxide is one of the most widely used transparent conducting oxides due to its electrical conductivity and optical transparency, as well as the ease with which it can be deposited as a thin film [133]

Figure 2.16: (a) Graphene-based display. A transparent smart window that can displaying information, when it is turn on, (b) or not (c), when is off. (d) Illustration of a thin graphene display emphasizing its flexibility. (e) Another example of a thin graphene-based conductive display (touch screen display) produced by the company 2D Carbon Tech (left) and its use as a prototype of smartphone display (right). (f) Illustration of a flexible photovoltaic cell modules. Adapted from Refs. [111, 134, 136–138]

2.6 Beyond graphene: the rise of novel ultrathin 2D-nanomaterials

With the advent of graphene and its unique characteristics, starting a new era of 2D materials and creating a new field in the physics of condensed matter, other 2D materials have been emerging over time. Although graphene presents many extraordinary properties, as discussed in Sec. 2.4, with the advent of novel ultrathin 2D layered nanomaterials (2DLMs), new unique properties in the low-dimensional physics can be reached when these materials are combined. As illustrated in Fig. 2.17, these new 2DLMs, such as h-BN, transition metal dichalcogenides (TMDs; e.g., MoS_2, WS_2, TiS_2, $MoSe_2$, *etc.*), layered metal oxides, black phosphorus, oxides, *etc*, present also outstanding properties due their unique structural features.

Figure 2.18 summarize some of these important 2DLMs, classifying them by stability as: stable monolayer at room temperature (blue shaded), stable in air (shaded green), unstable in air but may be stable in special conditions (pink). The compounds that can be exfoliated down to monolayer are represented by gray shadow [146].

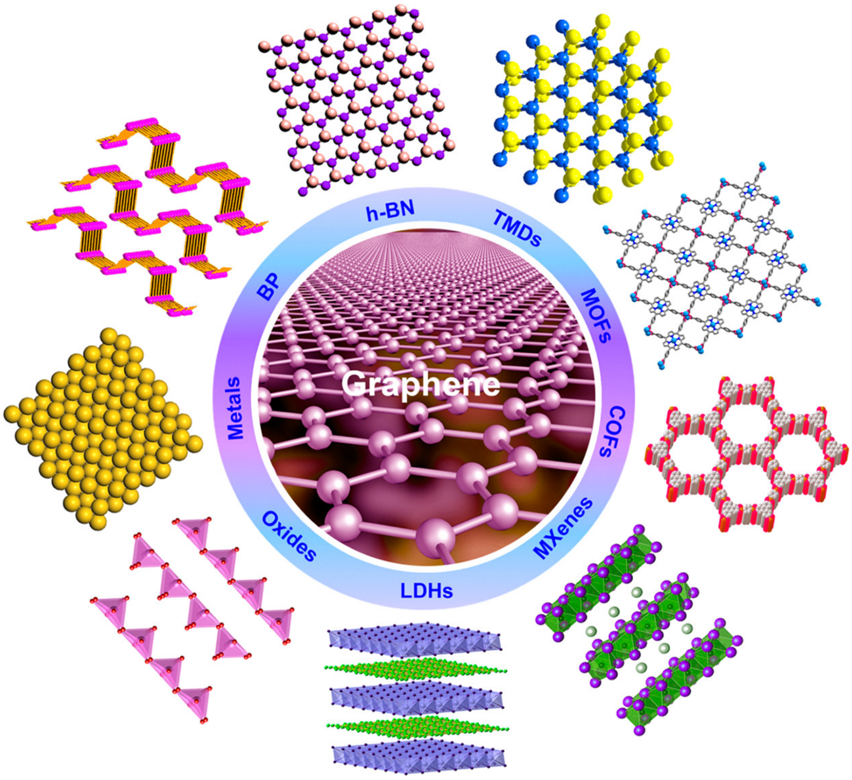

Figure 2.17: Schematic illustration of different kinds of typical ultrathin 2D nanomaterials, such as graphene, h-BN, TMDs, MOFs, COFs, MXenes, LDHs, oxides, metals, and BP. Adapted from Ref. [145].

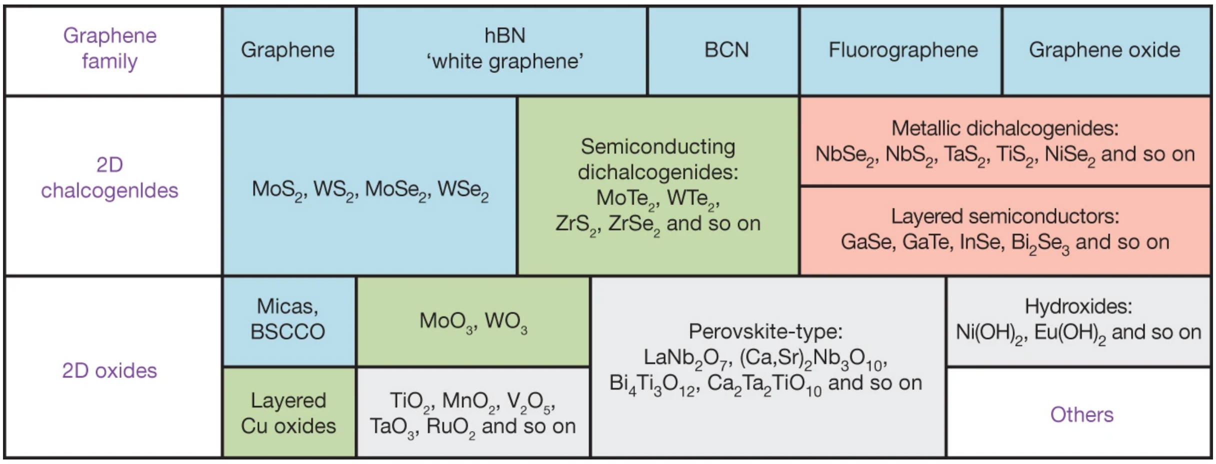
<table>
<tr><td>Graphene family</td><td>Graphene</td><td>hBN
'white graphene'</td><td>BCN</td><td>Fluorographene</td><td>Graphene oxide</td></tr>
<tr><td rowspan="2">2D chalcogenides</td><td colspan="2" rowspan="2">MoS_2, WS_2, $MoSe_2$, WSe_2</td><td rowspan="2">Semiconducting dichalcogenides: $MoTe_2$, WTe_2, ZrS_2, $ZrSe_2$ and so on</td><td colspan="2">Metallic dichalcogenides: $NbSe_2$, NbS_2, TaS_2, TiS_2, $NiSe_2$ and so on</td></tr>
<tr><td colspan="2">Layered semiconductors: GaSe, GaTe, InSe, Bi_2Se_3 and so on</td></tr>
<tr><td rowspan="2">2D oxides</td><td>Micas, BSCCO</td><td>MoO_3, WO_3</td><td colspan="2" rowspan="2">Perovskite-type: $LaNb_2O_7$, $(Ca,Sr)_2Nb_3O_{10}$, $Bi_4Ti_3O_{12}$, $Ca_2Ta_2TiO_{10}$ and so on</td><td>Hydroxides: $Ni(OH)_2$, $Eu(OH)_2$ and so on</td></tr>
<tr><td>Layered Cu oxides</td><td>TiO_2, MnO_2, V_2O_5, TaO_3, RuO_2 and so on</td><td>Others</td></tr>
</table>

Figure 2.18: Important ultrathin 2D layered nanomaterials and compounds. Blue shaded represents stable monolayer at room temperature, green represents monolayer stable in air and pink represents monolayers that are unstable in air but may be stable in special conditions. The compounds that that can be exfoliated down to monolayer are represented by gray shadow. Adapted from Ref. [146].

2.6.1 Transition metal dichalcogenides[9]

Transition metal dichalcogenides (TMDs) are semiconductors of the type MX_2, consisting of an atomic layer of transition metal atoms, represent by M (such as molybdenum

---

[9] Although a vast variety of new 2DLMs has emerged, on this thesis, beside graphene, the other

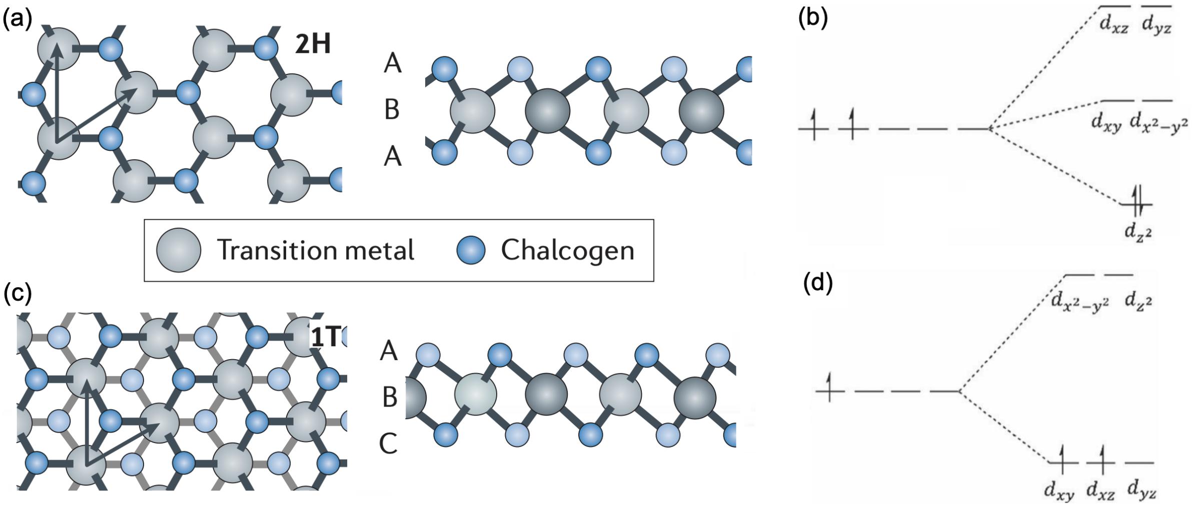

Figure 2.19: (a) Top and lateral view of the atomic structure of 2H-TMDs monolayer and (b) the splitting diagram and occupation of orbitals by d electrons in group VI TMDs for 2H phase. (c)-(d) The same as in (a) and (b) but now for the distorted octahedral (1T) phase. Adapted from Refs. [147, 148, 150]

.

(Mo) or tungsten (W), *etc.*), in between two atomic layers of chalcogen atoms, X (for example, disulfide (S), diselenide (Se), *etc.*) [147].

Basically, TMDs present two main phases: trigonal prismatic (2H) and octahedral (1T) [147, 148]. The first one, i.e., 2H, belongs to the hexagonal crystal group with a metal atom organized in a trigonal prismatic geometry, as illustrated in Fig. 2.19(a). Also, this structural phase correspond to an ABA stacking with the chalcogen atom occupying position A, in different atomic planes and on top of each other perpendicular to the layer, along the periodic chain. On the other hand, the metal atom are located on the position B (see Fig. 2.19(a)). 2H-TMDs from Group VI of the periodic table[10] are semiconducting, due to the fact that the lowest energy orbital d_{z^2} is completely filled [147, 148], as illustrated in Fig. 2.19(b). As a second example, the 1T phase, Fig. 2.19(c), presents two chalcogen atoms in the unit cell, while 2H phase presents only one. In addition, 2T phase are characterized by an ABC stacking order, Fig. 2.19(c), right panel. 1T-TMDs, made by Group IV, such as 1T-MoS_2 and 1T-WS_2, are metallic due to the partial filling of the degenerate orbitals d_{xy}, d_{xz} and d_{yz} as a consequence of the octahedral coordination [147, 148], Fig. 2.19(d).

---

main materials used to develop this thesis are the molybdenum disulfide (MoS_2), molybdenum diselenide ($MoSe_2$), tungsten disulfide (WS_2) and tungsten diselenide (WSe_2). Thus, in this section, is emphasized the basic features of these four materials.

[10] In the last page of this thesis is provide a periodic table of elements obtained from Ref. [149].

2.6.1.1 TMDs electronic band structure

A consequence of the TMDs phases, in combination with their different chemical composition, is the rise of vast range of different electronic properties. Since the main studies of this thesis on TMDs were obtained considering materials formed by Group IV transition metal[11] Mo and W combined with S and Se, here, the basic features of the their band structure are discussed. Figure 2.20(a) presents the MoS_2 band structure for different thickness, from bulk to monolayer, calculated by density functional theory (DFT) [147, 151]. As can be seen from Fig. 2.20(a), decreasing thickness results in a change of the indirect bandgap of the semiconductor bulk material into a direct bandgap semiconductor monolayer [147, 152–154]. Figure 2.20(b) shows an overview of the bandgap for some important 2D layered materials, from zero bandgap, represented by graphene (white color) to wide gap materials such as hBN. Furthermore, Fig. 2.20(b) illustrates the corresponding wavelength of bandgap, also separating in materials with direct and indirect bandgap, represented as black name or a golden name, respectively. Finally, other important properties of these materials is their valley-dependence. As illustrated in Fig. 2.20(c), the conduction band minimum and the valence band maximum are located at the two nonequivalent high-symmetry points K and K′, similar to graphene. These two nonequivalent points correspond to the corners of the hexagonal Brillouin zone[12], Fig. 2.20(c).

2.6.2 van der Waals heterostructures

After the quick growth of the 2D layered nanomaterials family over the last decade, presenting material with a wide range of electrical, chemical, optical and mechanical properties, a new field of research has been gaining strength based on stacking different 2D crystals on top of each other. As illustrated in Fig. 2.21, the procedure consist, first, isolating a monolayer and then putting it on top of another monolayer or few-layer crystal, creating a van der Waals heterostructure (vdWhs), analogous to LEGO blocks [156, 157]. This new vdWhs represents an artificial material with novel hybrid properties [20, 145, 146, 158–165]. The possibility of obtaining these mixed materials from mono- or few layers is due to the fact that while strong covalent bonds provide in-plane stability of the 2D crystals, inter-plane van der Waals-like forces, relatively weak, are sufficient to keep the layers together [156, 157]. This is exactly the reason that such materials are called van der Waals heterostructures, since the atomically thin layers are not mixed through a chemical reaction but rather attached to each other via a weak inter-plane van der Waals interaction.

---

[11] That is, formed by MX_2, where M is molybdenum (Mo) or tungsten (W) and X is disulfide (S) or diselenide (Se).

[12] Brillouin zone is a uniquely defined primitive cell in reciprocal space[155].

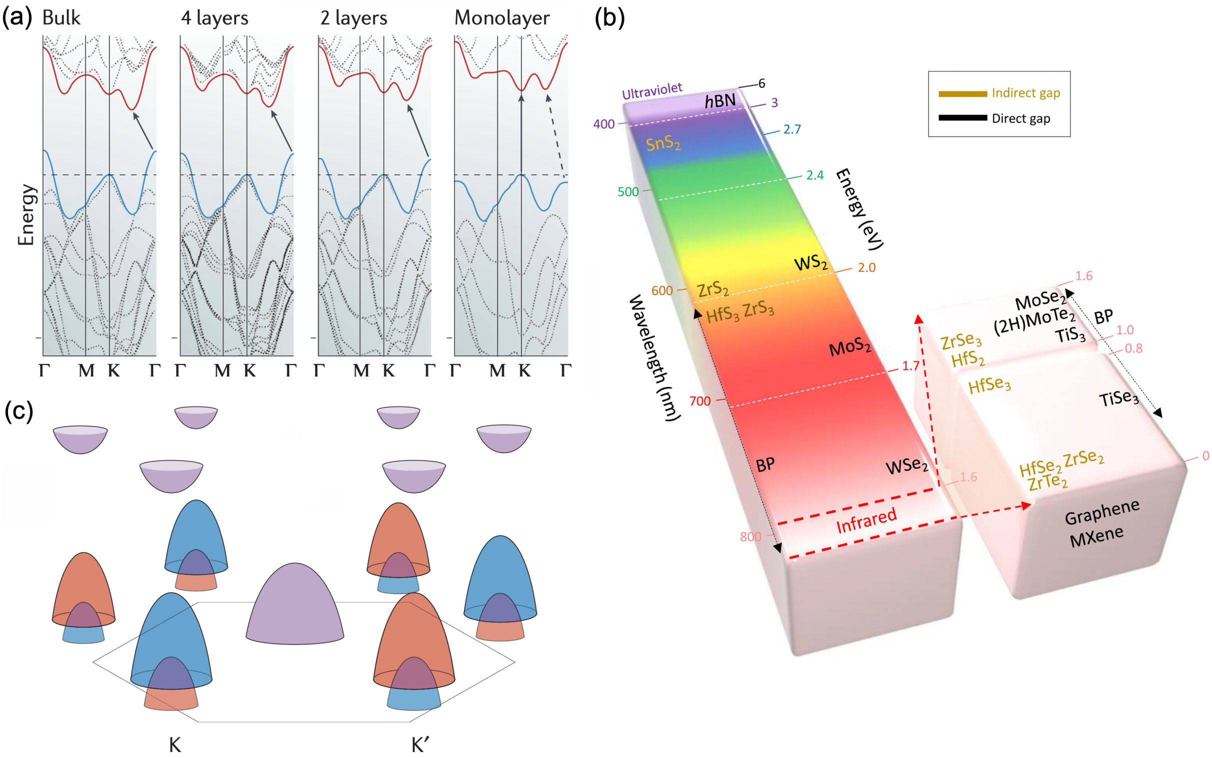

Figure 2.20: (a) Band structure for different thickness of 2H-MoS_2. (b) Bandgap and the correspondent wavelength of different 2D materials varying from zero band gap of graphene (white color) to wide bandgap of hBN. On the left (right) are the 2D materials with an indirect (direct) bandgap. (d) Representation of the conduction band minimum and the valence band maximum located at the two nonequivalent high-symmetry points K and K, similar to graphene. Adapted from Refs. [147, 150]

.

2.6.3 Synthesis and assembly of vdWHs

As in the case of graphene, obtained from micromechanical exfoliation, Subsec. 2.3.1, this strategy has been also applied to many other 2DLMs found in 3D layered forms, such as MoS_2, naturally obtained from molybdenite [156], and black phosphorus, from an artificially synthesized bulk crystal [51, 166, 167]. Thus, most of the techniques to obtain graphene as discussed in Sec. 2.3 can be also applied to obtain 2DLMs, such as: chemical intercalation, mechanical sonification, similar to the liquid phase exfoliation and CVD processes [166, 168–170].

In a second step, after obtaining the atomic layers, the challenge is in stacking the individual layers to create the desired vdWhs. Similar to the synthesis of individual atomic layers, the creation of a vdWhs follows two strategies: the top-down and bottom-up approaches. Figure 2.22(a) illustrates the state-of-the-art transfer methods to create complex vdWhs [166]. To do so, wet and dry transfer process are used to attach the individual sheet onto a transparent stamp material (for example, poly(dimethyl siloxane) (PMDS)). Thus, after attaching the stamp to a glass, with the help of a microscope stage

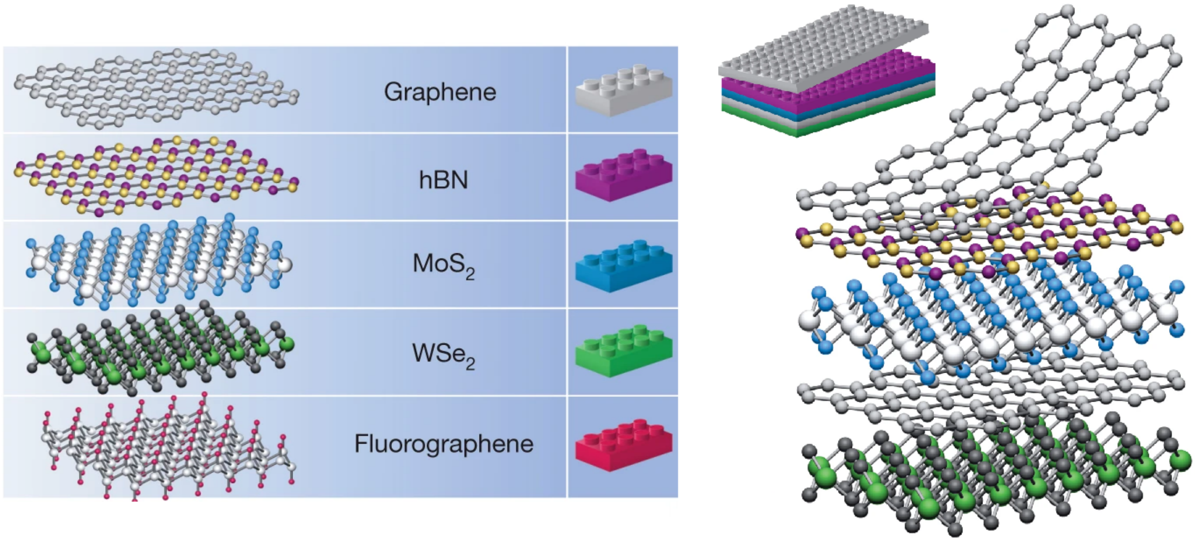

Figure 2.21: (left) Some example of 2D layered nanomaterials and (right) creation of van der Waals heterostructure stacking different 2D crystals on top of each other, analogous to LEGO blocks. Addapted from Ref. [146].

equipped with micro-manipulators, it is possible to align the sheets. To isolate the vdWhs, it is possible to dissolve the stamp chemically (direct dissolution), mechanically peel off or even pick up the entire stack for further transfer steps [166]. With the help of a high-resolution STM image, the cross-section can then be verified. For example, Fig. 2.22(b) shows a high-resolution cross-sectional STM image of the graphene-hBN vdWh (left) and a schematic representation (right). Figures 2.22(c)-(d) displays a moiré pattern of graphene on hBN for two different pattern sizes.

Recently, significant advances have been made to obtain and manufacture such nanostructures [107, 145–147, 157, 158, 171–177].

2.6.4 Some aspects on vdWhs

First of all, the monolayer and bilayer of these vdWhs-based 2DLMs presents completely different[13] properties [147, 148, 150, 152, 178, 179], as also discussed, in terms of the bandgap, in Subsec. 2.6.1.1. TMDs undergo a direct-to-indirect bandgap transition from mono- to multilayers [148]. In addition, black phosphorous has a layer dependent, tunable bandgap [180]. As an example of a vdWhs composed by two different materials, one of the first studies about stacking layers of different materials was the placement of graphene on top of hBN [181]. In this case, the use of the hBN decreases the undesired substrate effects on graphene. In this same line of reasoning, graphene encapsulated by hBN is also protected by surrounding environmental, such as adsorbed chemicals on the graphene surface. As a consequence, the carrier mobility can be improved [166]. Since the

---

[13] Indeed, is exactly this high electronic sensitivity of vdWhs that is explored in the study on plasmons developed in this thesis.

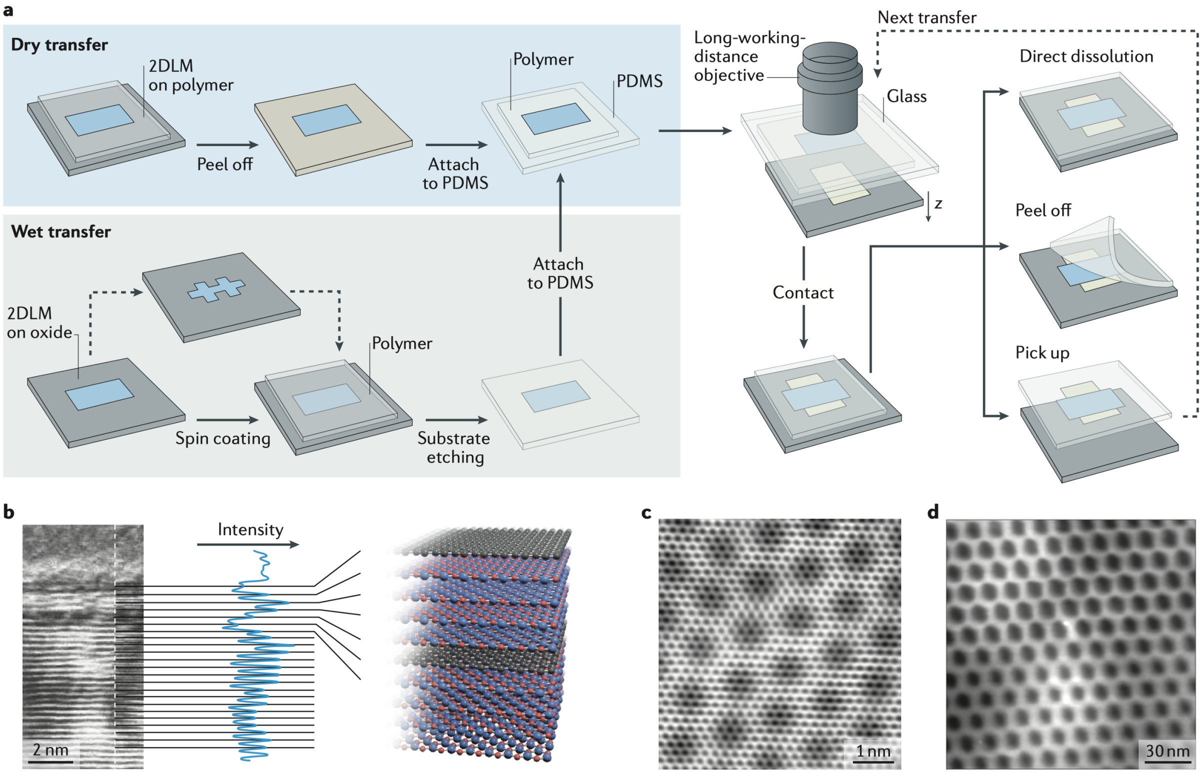

Figure 2.22: (a) Schematic illustration of the state-of-the-art transfer methods to create complex van der Waals heterostructure (vdWhs). Wet and dry transfer process are used to attach the individual sheet onto a transparent stamp material (for example, poly(dimethyl siloxane) (PMDS)). Thus, after attached the stamp to a glass, with the help of a microscope stage equipped with micro-manipulators, is possible align the sheets. To isolate the vdWhs, is possible dissolve the stamp chemically (direct dissolution), mechanically peel off or even used to pick up the entire stack for further transfer steps. (b) shows a high-resolution cross-sectional STM image of the graphene-hBN vdWh (left) and a schematic representation (right). (c)-(d) Displays a Moiré pattern of graphene on hBN for two different pattern size. Reproduced from Ref. [51].

electronic and optoelectronic properties of vdWhs depend on the material that composes it, their properties are a consequence of how these different materials are combine.

2.6.5 vdWhs applications

With unique electronic and optoelectronic properties, new vdWhs-based devices have been significantly attracting attention of the scientific community [20, 145, 146, 158–165]. As an example of vdWhs-based electronic device, Fig. 2.23(a) illustrates a planar 2D transistor[14] with coplanar contacts [166]. In this case, the gate and the graphene contact electrodes are on the same side of the 2D-semiconductor (2DSC). On the other hand,

---

[14] A transistor is a semiconductor-based component used to amplify or switch electronic signals and electrical power in a device.

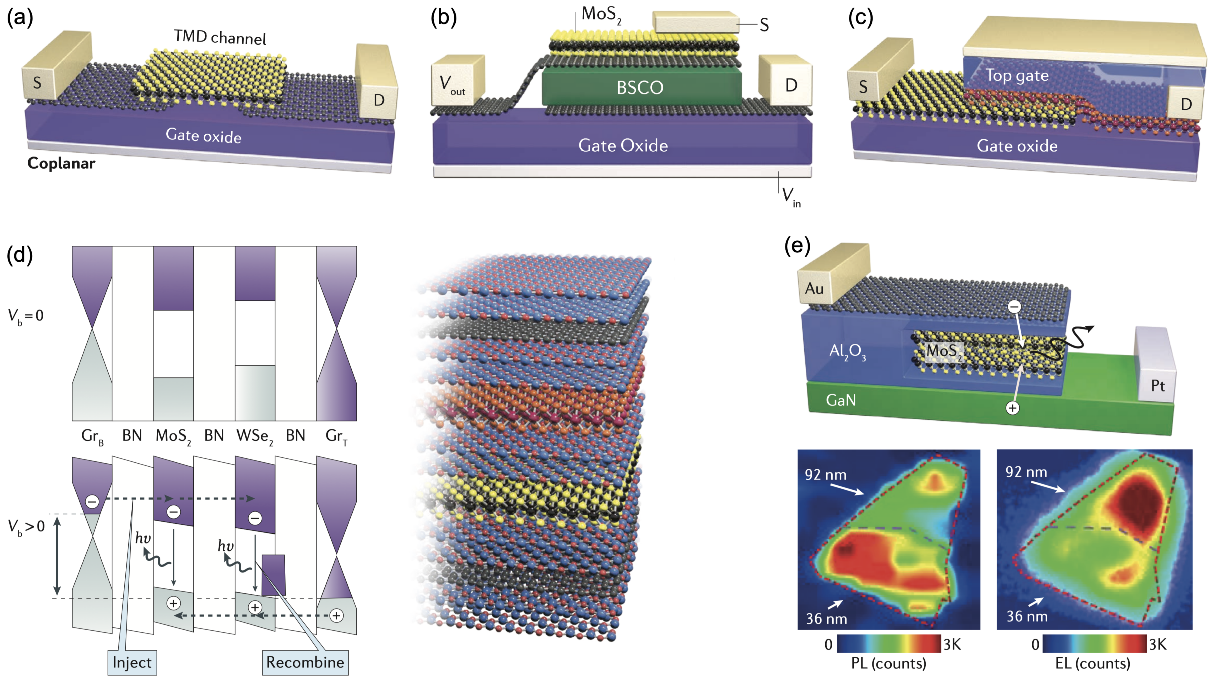

Figure 2.23: (a) Planar 2D transistor with the gate and graphene contact electrodes on the same side of the 2D-semiconductor (2DSC). (b) Vertical p- and n-type field effect transistor transistor (FET), where the position of the source (S) and drain (D) are located vertically to create a logic inverter with voltage gain. (c) A non-graphene-based device presenting a dual-gate structure. In this vdWhs, the electrostatic potential and carrier density of the two layers (p and n) is controlled individually by a top and a bottom gate electrodes reducing the lateral series resistance. (d) (left) Band diagram of a graphene electron- and hole-injection electrodes and (right) a schematic illustration of a heterostructure device of a multiple BN-2DSC-BN quantum-wells. (e) Schematic vdWhs of a light-emitting device based on a multilayer MoS_2, with a p-type GaN as the hole injector and a monolayer graphene as the electron injector. At the bottom of panel (e), are displayed a (left) photoluminescence and (rigth) electroluminescence mapping image of a MoS_2 region. Adapted from Ref. [51]

Fig. 2.23(b) illustrates a vertical p- and n-type field effect transistor (FET). One of the main differences is the position of the source (S) and drain (D), now displayed vertically to create a logic inverter with voltage gain. Since this strategy of multiple vertical transistor can be extended to form a 3D device, this idea can open a new direction of 3D-devices.

As an example of a non-graphene-based device, Fig. 2.23(c) presents a dual-gate structure. In this vdWhs, the electrostatic potential and carrier density of the two layers (p and n) is controlled individually by top and bottom gate electrodes reducing the lateral series resistance.

Figure 2.23(d) presents (left) a band diagram of a graphene electron- and hole-injection electrodes and (right) a schematic illustration of a heterostructure device of multiple BN-2DSC-BN quantum-wells. The main idea of this vdWhs is to create a light-emitting device. To do so, the electrons and holes are injected from the bottom monolayer graphene into the 2DSC layers and recombine to produce a photon emission, similar to a light-emitting diode (LED)[15] [166]. This type of LED, when combined to multiple repeated units of 2DSC-BN stacks, minimizing the current leakage and ensure efficient electron-to-photon conversion, is $\sim 10\%$ more efficient when compare to the current organic LED (OLED) and the state-of-the-art quantum-dot LEDs [166, 182, 183]. Figure 2.23(e), (top) shows a schematic vdWhs for a light-emitting device based on a multilayer MoS_2, with a p-type GaN as the hole injector and a monolayer graphene as the electron injector. At the bottom of Fig. 2.23(e), are displayed a (left) photoluminescence and (rigth) electroluminescence mapping image of a MoS_2 region.

---

[15] LED is a semiconductor light source that emits light when current flows through it.

3

Elementary properties of graphene

In this chapter, the structural and electronic characteristics of graphene monolayer are introduced. Furthermore, the Hamiltonian for monolayer and bilayer graphene are obtained from the tight-binding model (TB), which will also set the foundations for our calculations on few-layer graphene in the following chapters.

3.1 Electronic properties of graphene

3.1.1 Crystalline structure

Structurally, graphene is defined as a monolayer of carbon atoms organized in a honeycomb-like lattice. The unit cell of graphene, illustrated in Fig. 3.1(a), is not a Bravais lattice, but two interpenetrated triangular lattices A and B, where the lattice vectors are defined as [184]:

$$\boldsymbol{a}_1 = \frac{a}{2}\left(3, \sqrt{3}\right) \quad \text{and} \quad \boldsymbol{a}_2 = \frac{a}{2}\left(3, -\sqrt{3}\right), \tag{3.1}$$

where $a = 1.42\,\text{Å}$ is the distance between carbon atoms in the graphene lattice. As can be seen from Fig. 3.1(a), each atom of sublattice A are surrounded by three nearest-neighbors of sublattice B and vice-versa. The vectors that connect a specific site to the nearest-neighbors are given by [184]:

$$\boldsymbol{\delta}_1 = \frac{a}{2}\left(1, \sqrt{3}\right), \quad \boldsymbol{\delta}_2 = \frac{a}{2}\left(1, -\sqrt{3}\right) \quad \text{and} \quad \boldsymbol{\delta}_3 = a\left(-1, 0\right). \tag{3.2}$$

The vectors that define the reciprocal lattice, shown in Fig. 3.1(b), are given by [184]:

$$\boldsymbol{b}_1 = \frac{2\pi}{3a}\left(1, \sqrt{3}\right) \quad \text{and} \quad \boldsymbol{b}_2 = \frac{2\pi}{3a}\left(1, -\sqrt{3}\right), \tag{3.3}$$

The contour of the first Brillouin zone of graphene, Fig. 3.1(b), has six important points and, due to their symmetry, only two of them are inequivalent, denominated as K

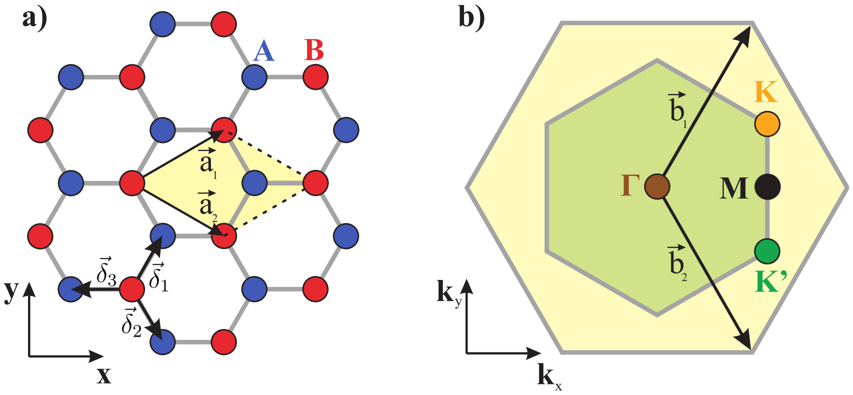

Figure 3.1: (a) Lattice structure of graphene formed by two interpenetrated triangular sublattice A and B. The unit vectors are defined by $\boldsymbol{a}_1$ and $\boldsymbol{a}_2$. The nearest-neighbors are located by $\boldsymbol{\delta}_i$ $(i = 1, 2,)$ and the distance between the carbon-carbon atoms is given by 1.42 Å. (b) First Brillouin zone. The Dirac cones are located at the points K and $K^{'}$.

and $K^{'}$. These points are extremely important for graphene, as we will see later. The positions of K and $K^{'}$ in reciprocal space are given by [184]:

$$\boldsymbol{K} = \left(\frac{2\pi}{3a}, -\frac{2\pi}{3\sqrt{3}a}\right) \quad \text{e} \quad \boldsymbol{K}' = \left(\frac{2\pi}{3a}, \frac{2\pi}{3\sqrt{3}a}\right) . \tag{3.4}$$

3.1.2 Tight-binding model for monolayer graphene

Considering only the hopping between the nearest-neighbors, the tight-binding Hamiltonian for graphene, in the second quantization formalism, can be written as [184]:

$$H_{TB} = -\tau \sum_{i,j} (\hat{a}_i^\dagger \hat{b}_j + \hat{b}_j^\dagger \hat{a}_i) \ , \tag{3.5}$$

where $\tau \approx 2.8$ eV is the hopping parameter associated with the transition of electrons between the nearest-neighbors. $\hat{a}_i$ $(\hat{a}_i^\dagger)$ and $\hat{b}_i$ $(\hat{b}_i^\dagger)$ annihilate (create) an electron at the i-th site of sublattices A and B, respectively. Such operators satisfy the fermion anticommutation rules [185]: $\left\{\hat{a}_i, \hat{a}_j^\dagger\right\} = \delta_{i,j}$, $\{\hat{a}_i, \hat{a}_j\} = \left\{\hat{a}_i^\dagger, \hat{a}_j^\dagger\right\} = 0$ e $\left\{\hat{b}_i, \hat{b}_j^\dagger\right\} = \delta_{i,j}$, $\left\{\hat{b}_i, \hat{b}_j\right\} = \left\{\hat{b}_i^\dagger, \hat{b}_j^\dagger\right\} = 0, \forall ij$.

A Fourier transform of the creation and annihilation operators is taken

$$\hat{a}_j = \frac{1}{\sqrt{N}} \sum_k e^{i\boldsymbol{k}\cdot\boldsymbol{r}_i} \hat{a}_k, \qquad \hat{a}_j^\dagger = \frac{1}{\sqrt{N}} \sum_k e^{-i\boldsymbol{k}\cdot\boldsymbol{r}_i} \hat{a}_k^\dagger, \tag{3.6}$$

$$\hat{b}_j = \frac{1}{\sqrt{N}} \sum_{k'} e^{i\boldsymbol{k}'\cdot\boldsymbol{r}_j} \hat{b}_{k'} \quad \text{e} \quad \hat{b}_j^\dagger = \frac{1}{\sqrt{N}} \sum_{k'} e^{-i\boldsymbol{k}'\cdot\boldsymbol{r}_j} \hat{b}_{k'}^\dagger . \tag{3.7}$$

where $\boldsymbol{k} = (k_x, k_y)$ and N is the number of unit cells.

Replacing Eq's. (3.6) and (3.7) into the Hamiltonian defined in Eq. (3.5), yields:

$$\begin{aligned} H_{TB} = -\tau \sum_{i,j} \Bigg[& \left(\frac{1}{\sqrt{N}} \sum_{k} e^{-i\boldsymbol{k}\cdot\boldsymbol{r}_i} \hat{a}_k^{\dagger} \right) \left(\frac{1}{\sqrt{N}} \sum_{k'} e^{i\boldsymbol{k}'\cdot\boldsymbol{r}_j} \hat{b}_{k'} \right) \\ & + \left(\frac{1}{\sqrt{N}} \sum_{k'} e^{-i\boldsymbol{k}'\cdot\boldsymbol{r}_j} \hat{b}_{k'}^{\dagger} \right) \left(\frac{1}{\sqrt{N}} \sum_{k} e^{i\boldsymbol{k}\cdot\boldsymbol{r}_i} \hat{a}_k \right) \Bigg], \end{aligned} \tag{3.8}$$

$$H_{TB} = -\frac{\tau}{N} \sum_{i,j} \sum_{k,k'} \left[\left(e^{-i\boldsymbol{k}\cdot\boldsymbol{r}_i} \cdot e^{i\boldsymbol{k}'\cdot\boldsymbol{r}_j} \right) \left(\hat{a}_k^{\dagger} \hat{b}_{k'} \right) + \left(e^{-i\boldsymbol{k}'\cdot\boldsymbol{r}_j} \cdot e^{i\boldsymbol{k}\cdot\boldsymbol{r}_i} \right) \left(\hat{b}_{k'}^{\dagger} \hat{a}_k \right) \right], \tag{3.9}$$

which is equivalent to

$$\begin{aligned} H_{TB} = -\frac{\tau}{N} \sum_{i,j} \sum_{k,k'} \Bigg[& \left(e^{i(\boldsymbol{k}'-\boldsymbol{k})\boldsymbol{r}_j} \cdot e^{-i\boldsymbol{k}(\boldsymbol{r}_i-\boldsymbol{r}_j)} \right) \left(\hat{a}_k^{\dagger} \hat{b}_{k'} \right) \\ & + \left(e^{-i(\boldsymbol{k}'-\boldsymbol{k})\boldsymbol{r}_j} \cdot e^{i\boldsymbol{k}(\boldsymbol{r}_i-\boldsymbol{r}_j)} \right) \left(\hat{b}_{k'}^{\dagger} \hat{a}_k \right) \Bigg]. \end{aligned} \tag{3.10}$$

As previously explained, each atom has three nearest neighbors, thus, considering that the origin is located at any site i and making j vary over the first three neighbors, located by Eq. (3.6), we obtain:

$$\begin{aligned} H_{TB} = -\frac{\tau}{N} \sum_{j} \sum_{k,k'} \Bigg\{ \Bigg[& e^{i(\boldsymbol{k}'-\boldsymbol{k})\boldsymbol{r}_j} \left(e^{-ik_x(a/2)} e^{-ik_y\left(a\sqrt{3}/2\right)} + e^{-ik_x(a/2)} e^{-ik_y\left(-a\sqrt{3}/2\right)} \right. \\ & \left. + e^{-ik_x(-a)} \right) \Bigg] \hat{a}_k^{\dagger} \hat{b}_{k'} + \Bigg[e^{-i(\boldsymbol{k}'-\boldsymbol{k})\boldsymbol{r}_j} \left(e^{ik'_x(a/2)} e^{ik'_y\left(a\sqrt{3}/2\right)} \right. \\ & \left. + e^{ik'_x(a/2)} e^{ik'_y\left(-a\sqrt{3}/2\right)} + e^{ik'_x(-a)} \right) \Bigg] \hat{b}_{k'}^{\dagger} \hat{a}_k \Bigg\} , \end{aligned} \tag{3.11}$$

$$\begin{aligned} H_{TB} = -\frac{\tau}{N} \sum_{j} \sum_{k,k'} \Bigg[& e^{i(\boldsymbol{k}'-\boldsymbol{k})\boldsymbol{r}_j} \left(e^{-ik_xa/2} e^{-ik_ya\sqrt{3}/2} + e^{-ik_xa/2} e^{ik_ya\sqrt{3}/2} + e^{ik_xa} \right) \hat{a}_k^{\dagger} \hat{b}_{k'} \\ & + e^{-i(\boldsymbol{k}'-\boldsymbol{k})\boldsymbol{r}_j} \left(e^{ik'_xa/2} e^{ik'_ya\sqrt{3}/2} + e^{ik'_xa/2} e^{-ik'_ya\sqrt{3}/2} + e^{-ik'_xa} \right) \hat{b}_{k'}^{\dagger} \hat{a}_k \Bigg] . \end{aligned} \tag{3.12}$$

Now, using the property of the Dirac delta function, defined as [186]

$$\frac{1}{N} \sum_{j} e^{i(\boldsymbol{k}'-\boldsymbol{k})\boldsymbol{r}_j} = \delta\left(\boldsymbol{k} - \boldsymbol{k}'\right), \tag{3.13}$$

in Eq. (3.12), yields

$$\begin{aligned} H_{TB} = -\tau \sum_{k} \Bigg[& \left(e^{-ik_xa/2} e^{-ik_ya\sqrt{3}/2} + e^{-ik_xa/2} e^{ik_ya\sqrt{3}/2} + e^{ik_xa} \right) \hat{a}_k^{\dagger} \hat{b}_k \\ & + \left(e^{ik_xa/2} e^{ik_ya\sqrt{3}/2} + e^{ik_xa/2} e^{-ik_ya\sqrt{3}/2} + e^{-ik_xa} \right) \hat{b}_{k'}^{\dagger} \hat{a}_k \Bigg] . \end{aligned} \tag{3.14}$$

From the relation $\cos(\theta) = \left(e^{i\theta} + e^{-i\theta}\right)/2$, we can rewrite Eq. (3.14) as

$$\begin{aligned} H_{TB} = -\tau \sum_{k} \Bigg\{ & \left[2\cos\left(k_ya\sqrt{3}/2\right) e^{-ik_xa/2} + e^{ik_xa} \right] \hat{a}_k^{\dagger} \hat{b}_k \\ & + \left[2\cos\left(k_ya\sqrt{3}/2\right) e^{ik_xa/2} + e^{-ik_xa} \right] \hat{b}_{k'}^{\dagger} \hat{a}_k \Bigg\}, \end{aligned} \tag{3.15}$$

$$H_{TB} = -\tau \sum_{k} \left[g\left(\boldsymbol{k}\right) \hat{a}_{k}^{\dagger} \hat{b}_{k} + g^{*}\left(\boldsymbol{k}\right) \hat{b}_{k'}^{\dagger} \hat{a}_{k} \right], \tag{3.16}$$

with the crystal lattice structure factor defined as

$$g\left(\boldsymbol{k}\right) = 2\cos\left(k_{y} a\sqrt{3}/2\right) e^{-ik_{x}a/2} + e^{ik_{x}a} . \tag{3.17}$$

The Hamiltonian given by Eq. (3.16) allows us to write Schrödinger equation as

$$H_{TB} \left|\psi\left(\boldsymbol{k}\right)\right\rangle = \varepsilon\left(\boldsymbol{k}\right) \left|\psi\left(\boldsymbol{k}\right)\right\rangle . \tag{3.18}$$

Therefore, from Eq's. (3.16) and (3.17), and using the fermionic anticommutation relations, we obtain two equations which can be written in matrix form, such as:

$$\begin{pmatrix} 0 & -\tau g\left(\boldsymbol{k}\right) \\ -\tau g^{*}\left(\boldsymbol{k}\right) & 0 \end{pmatrix} \begin{pmatrix} \psi_{A}\left(\boldsymbol{k}\right) \\ \psi_{B}\left(\boldsymbol{k}\right) \end{pmatrix} = \varepsilon\left(\boldsymbol{k}\right) \begin{pmatrix} \psi_{A}\left(\boldsymbol{k}\right) \\ \psi_{B}\left(\boldsymbol{k}\right) \end{pmatrix} , \tag{3.19}$$

where the wave function was rewritten as two-components pseudo-spinor given by $\psi\left(\boldsymbol{k}\right) = \left[\psi_{A}\left(\boldsymbol{k}\right) \quad \psi_{B}\left(\boldsymbol{k}\right)\right]^{T}$. The subscript A and B represents the probability of finds the electron on the sublattice A or B, which are chemically equivalent, also presenting the same on-site energy and equal to the energy of the π orbital. Thus, diagonalizing the Hamiltonian

$$H_{k} = \begin{pmatrix} 0 & -\tau g\left(\boldsymbol{k}\right) \\ -\tau g^{*}\left(\boldsymbol{k}\right) & 0 \end{pmatrix}, \tag{3.20}$$

the eigenenergies associated to $\psi\left(\boldsymbol{k}\right)$ are obtained:

$$\varepsilon_{\lambda\mathbf{k}} = \lambda\tau \left|g\left(\boldsymbol{k}\right)\right| = \pm\tau\sqrt{3 + f\left(\boldsymbol{k}\right)}, \tag{3.21}$$

with $f\left(\boldsymbol{k}\right) = 4\cos\left(3k_{x}a/2\right)\cos\left(3k_{y}a/2\right) + 2\cos\left(3k_{y}a/2\right)$ and $\lambda = \pm 1$ indicate the conduction $+1$ and valence -1 bands [187].

Figure 3.2(a) shows the six high symmetry points located at the vertices of the first Brillouin zone, where the valence band ($\varepsilon < 0$) touches the conduction band ($\varepsilon > 0$) when $E = 0$ [184, 188]. At these points, i.e K and K', known as Dirac points, the gap is null and the band structure exhibits a conical (linear, when projected at k_x or k_y) dispersion for small values of $|E|$. Figure 3.2(b) presents the band structure, across the high symmetry points (Γ-K-M-Γ), while the inset in Fig. 3.2(b) shows the result obtained experimentally by angle-resolved photoemission spectroscopy (ARPES) [189, 190].

3.1.3 Continuum approximation for monolayer graphene

To demonstrate that the low-energy electron in graphene behaves as a massless Dirac quasi-particle, we can start expanding the structure factor $g(\boldsymbol{k})$, Eq. (3.17), around $\boldsymbol{K}$, Eq. (3.4). To do so, only the terms up to the first order in $\boldsymbol{K'}$ are kept [184, 191], thus:

$$g(\delta\boldsymbol{k}) \approx g(\boldsymbol{K}) + \left.\frac{\partial g}{\partial k_{x}}\right|_{\boldsymbol{k}=\boldsymbol{K}} (k_{x} - K'_{x}) + \left.\frac{\partial g}{\partial k_{y}}\right|_{\boldsymbol{k}=\boldsymbol{K}} (k_{y} - K'_{y}), \tag{3.22}$$

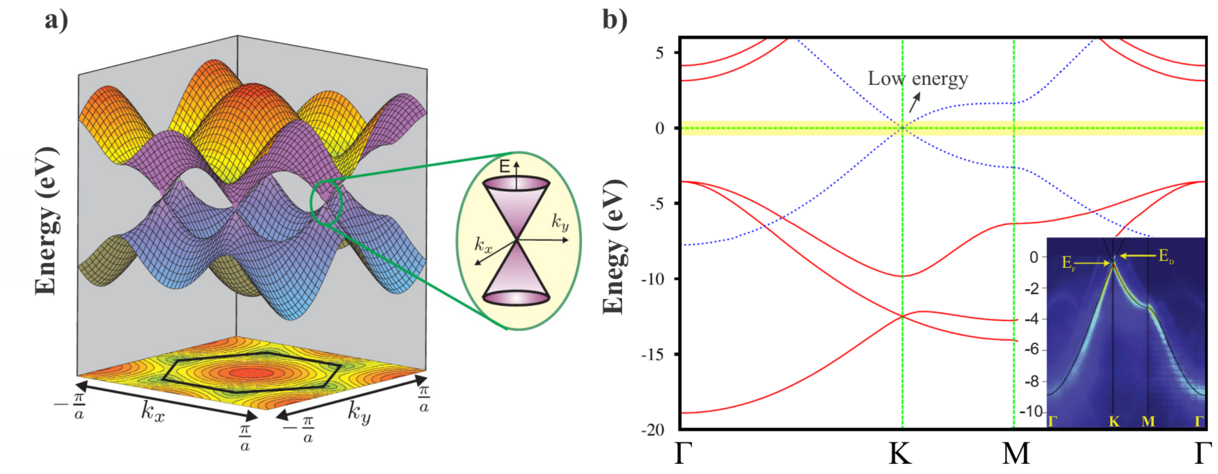

Figure 3.2: (a) Electronic band structure of graphene emphasizing one of the six Dirac points. (b) Band structure in relation to the high symmetry points (Γ-K-M-Γ) illustrates in Fig. 3.1. The inset in (b) shows the result obtained experimentally by angle-resolved photoemission spectroscopy (ARPES). The yellow region correspond to the low energy, where at the K point graphene presents a linear dispersion. Adapted from Refs. [188–190].

with $\delta\boldsymbol{k} = \boldsymbol{K} - \boldsymbol{k}$. After calculate the derivative of $g(\boldsymbol{k})$ at $\boldsymbol{k} = \boldsymbol{K}$, we obtain

$$g(\delta\boldsymbol{k}) \approx \frac{3a}{2}\left(-\frac{\sqrt{3}}{2} + i\frac{1}{2}\right)k'_x - \frac{3a}{2}\left(-\frac{\sqrt{3}}{2} + i\frac{1}{2}\right)ik'_y, \tag{3.23}$$

or

$$g(\delta\boldsymbol{k}) \approx \frac{3a}{2}(k'_x - ik'_y)e^{i5\pi/6}. \tag{3.24}$$

Analogously, the same procedure for $\boldsymbol{K}'$ can be done, resulting in:

$$g(\delta\boldsymbol{k}) \approx \frac{3a}{2}(-k'_x - ik'_y)e^{i5\pi/6}. \tag{3.25}$$

It is important to mention that the complex exponentials in Eq's. (3.24) and (3.24) can be included in the wave functions without any changes to the physical system, once that the quadratic norms of these terms are 1. Comparing Eq's. (3.24) and (3.25), we can see that they are not equivalent due to the signs + and − in the variable k_x. Thus, replacing Eq's. (3.24) and (3.25) in the Hamiltonian defined by Eq. 3.20, we obtain the well known Hamiltonian for a graphene monolayer:

$$H^{\pm}_{mo} = \hbar v_f \begin{pmatrix} 0 & (\pm k'_x - ik'_y) \\ (\pm k'_x + ik'_y) & 0 \end{pmatrix}. \tag{3.26}$$

In Eq. (3.26) $v_f = 3a\tau/2\hbar$ is the Fermi velocity and the signs + and − represent low-energy electrons for the valleys K and K', respectively. Note that the Hamiltonian defied in Eq. (3.26) is similar to the Dirac equation, except due to the Fermi velocity (v_f)

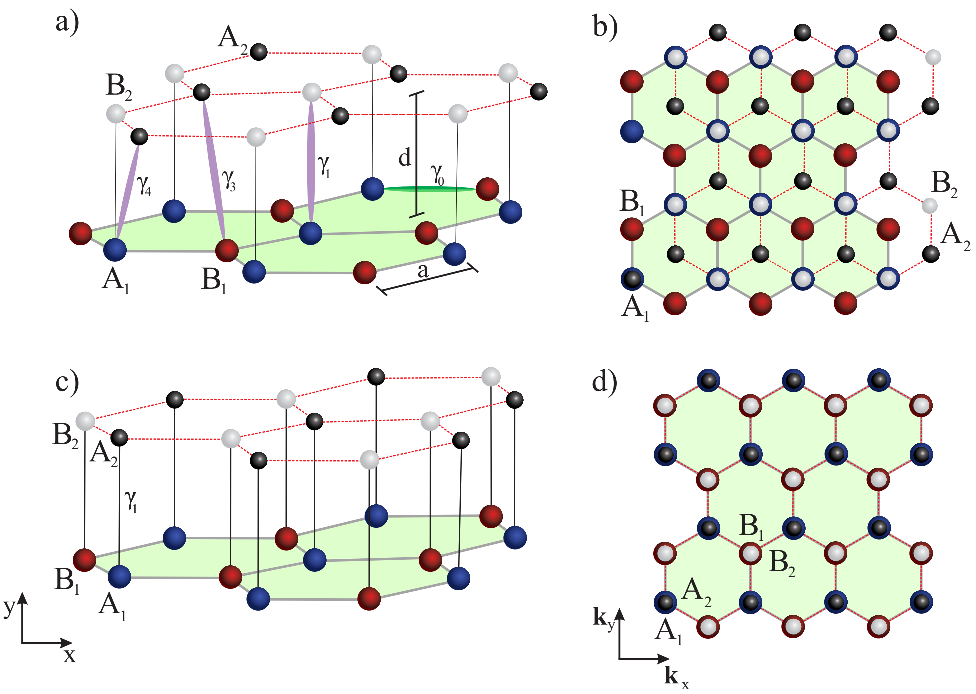

Figure 3.3: (a) Crystalline structure of a AB graphene bilayer stacking (also know as Bernal stacking) with the interlayer hopping defined by γ_1, γ_3 and γ_4. The in-plane hopping, i.e between atoms of the same lattice, are represented by γ_0. The interlayer distance is given by $d \approx 3.35$ Å, while $a = 1.42$ Å is the distance between the carbon-carbon atoms. The lower layer is represented by the solid gray lines with the triangular sublattice formed by A_1 (blue) and B_1 (red), while the upper layer is represented by the dotted red lines with sublattice defined by A_2 (black symbols) and B_2 (white symbols). (b) Top view of bernal type stacking. (c)-(d) The same as in (a)-(b), respectively, but now for an AA graphene bilayer stacking.

instead of the speed of light (c). It is exactly for this reason that electrons in graphene are considered also as massless Dirac fermions.

The Hamiltonian (3.26) can still be written, in a more compact form, as:

$$H^{\pm}_{mo} = \hbar v_f k_F \begin{pmatrix} 0 & e^{\mp i\phi} \\ e^{\pm i\phi} & 0 \end{pmatrix}, \tag{3.27}$$

with $k_F = \sqrt{(k'_x)^2 - (k'_y)^2}$ and $\phi = \text{arctg}\left(k'_y/k'_x\right)$. The way Hamiltonian (3.27) was written will be useful for the Chapters 4 and 5.

3.2 Bilayer graphene

3.2.1 Crystalline structure

A graphene bilayer (BLG) consists of stacking two graphene monolayers that can result in two types of stacking: AA or AB. This is possible due a van der Waals interlayer interaction, responsible to keep the BLG stable [184]. The value of this interlayer interaction is around 15 eV $\sim$ 20 eV, typical values of van der Waals heterostructures [192].

The AB stacking, also called Bernal stacking[1], the atoms of the sublattice A, from the upper layer (denoted by A_2), are exactly on top of the atoms of the sublattice B of the lower layer (denominated as B_1), see Fig. 3.3(a). Naturally, the atoms of the sublattice B of the upper layer (called B_2) are located above the center of the hexagon formed by the bottom layer, as can be seen from the top view in Fig. 3.3(b). In other words, the top layer is rotated by an angle of 60º relative to the bottom layer. Thus, the Bernal-type graphene bilayer has two non-equivalent atomic sites [74]. The distance between the planes is approximately $d \approx 3.35$ Å [193]. This type of graphene bilayer is the most common [184]. Figure 3.3(a) represents an illustrative model of the crystal lattice of the AB stacking, with a top view of this structure represented in Fig. 3.3(b).

The second possibility of bilayer graphene, which is however unstable, is the AA stacking [194]. In the AA pattern the atoms of sublattice A of the upper layer (A_2) are directly on top of the atoms A of the lower layer (A_1), Fig. 3.3(c). The same is true for the atoms of the sublattice B in both monolayer, as illustrated in Fig. 3.3(c). In this case, the interlayer distance is $d \approx 3.55$ Å.

Is important to note that for even numbers of graphene layers (bilayer, for example) the spatial inversion symmetry is satisfied, i.e $(x, y, z) \rightarrow (-x, -y, -z)$. On the other hand, for an odd number (three-layer, for example), the spatial inversion is not satisfied [195].

3.2.2 Tight-binding model for bilayer graphene

The tight-binding model, developed for a monolayer graphene in the previous subsection (Subsec. 3.1.2), can be easily extended to graphene layers with a finite number, but with a higher degree of complexity, since other hopping terms will emerge (γ_0, γ_1, γ_3 and γ_4). For the bilayer graphene case, the simplest situation, the Hamiltonian that describes the π band electrons for the AB-stacked graphene bilayer is defined as [184, 187, 196, 197]:

$$\begin{aligned} H_{TB} &= \sum_{i,j}\sum_{n=1}^{2}\left(E_{A_n}\hat{a}^\dagger_{i;n}\hat{a}_{i;n} + E_{B_n}\hat{b}^\dagger_{j;n}\hat{b}_{j;n}\right) - \gamma_0\sum_{i,j}\sum_{n=1}^{2}\left(\hat{a}^\dagger_{i;n}\hat{b}_{j;n} + \hat{b}^\dagger_{j;n}\hat{a}_{i;n}\right) \\ &- \gamma_1\sum_{i,j}\left(\hat{a}^\dagger_{i;1}\hat{b}_{j;2} + \hat{b}^\dagger_{j;2}\hat{a}_{i;1}\right) - \gamma_3\sum_{i,j}\left(\hat{a}^\dagger_{i;2}\hat{b}_{j;1} + \hat{b}^\dagger_{j;1}\hat{a}_{i;2}\right) \\ &- \gamma_4\sum_{i,j}\left(\hat{a}^\dagger_{i;1}\hat{a}_{j;2} + \hat{a}^\dagger_{j;2}\hat{a}_{i;2} + \hat{b}^\dagger_{i;1}\hat{b}_{j;2} + \hat{b}^\dagger_{j;2}\hat{b}_{i;2}\right). \end{aligned} \tag{3.28}$$

In Eq. (3.28), $\hat{a}_{i;n}$ ($\hat{a}^\dagger_{i;n}$) annihilates (creates) an electron at the i site of the A sublattice of the n-th layer, while $\hat{b}_{j;n}$ ($\hat{a}^\dagger_{j;n}$) annihilates (creates) an electron at site j of sublattice

---

[1] In honor of Irish scientist John Desmond Bernal for determining in 1942 a molecular structure of graphite.

B also at n-th layer. The nomenclature for the graphite hopping parameters are defined as: (i) E_{A_n} and E_{B_n} represent the energies at the sites of the sublattices A_n and B_n, respectively; (ii) $\gamma_0 = \tau \approx 2.8$ eV is the hopping energy between atoms of the same shell, that is, between $A_1(A_2)$ and B_1 (B_2) ; (iii) $\gamma_1 = t_\perp \approx 0.4$ eV is the hopping between the atoms A_1 and B_2, as illustrated in Fig. 3.3(b). For stacking type AA the hopping between the top and bottom layer atoms is 0.2 eV; (iv) $\gamma_3 \approx 0.3$ eV represents the hopping between the atoms B_1 and B_2; (v) $\gamma_4 \approx 0.04$ eV is the hopping energy between A_1 and B_2 (A_2 e B_1) [198]. All these hopping interactions are illustrated in Fig. 3.3(a) illustrates the hopping energies described in Eq. 3.28. Interactions between other neighbors are very weak, thus we neglect them [184, 187].

To obtain a simplified Hamiltonian for bilayer graphene, we approximate Eq. (3.28) considering only the hopping nearest neighbors (τ) and the interlayer hopping ($\tau_\perp$). Following the same reasoning developed for the monolayer graphene, Subsec. 3.1.2, the TB Hamiltonian, now a 4×4 matrix, for the bilayer graphene is given by:

$$H_{TB} = \begin{pmatrix} 0 & -\tau g(\boldsymbol{k}) & \tau_\perp & 0 \\ -\tau g^*(\boldsymbol{k}) & 0 & 0 & 0 \\ \tau_\perp & 0 & 0 & -\tau g^*(\boldsymbol{k}) \\ 0 & 0 & -\tau g(\boldsymbol{k}) & 0 \end{pmatrix}. \tag{3.29}$$

Note that the Hamiltonian defined in Eq. (3.29) is composed of two single-layer graphene Hamiltonian, the same defined in Eq. (3.20), on its main diagonal. On the other hand, in the secondary diagonal a 2×2 sub-matrix describe the interlayer coupling intermediate by $\tau_\perp$. Thus, diagonalizing the Hamiltonian (3.29), yields the energy spectrum for the Bernal bilayer graphene stacking (AB):

$$\varepsilon^{\pm}_{\pm k} = \pm\frac{\tau_\perp}{2} \pm \left[\tau \left|g(\boldsymbol{k})\right|^2 + \left(\frac{\tau_\perp}{2}\right)^2\right]^{1/2}, \tag{3.30}$$

composed of four eigenvalues and, consequently, four bands, as shown in the next section.

3.2.3 Continuum approximations for AB-bilayer graphene

Following the same procedure developed for monolayer graphene to obtain the Hamiltonian (3.26), that is, using the continuum model for low-energy electrons, it is possible to obtain the Hamiltonian for the AB graphene bilayer, defined as [184, 199]:

$$H_{bi} = \begin{pmatrix} 0 & \hbar v_F(\tau p_x + i p_y) & \tau_\perp & 0 \\ \hbar v_F(\tau p_x - i p_y) & 0 & 0 & 0 \\ \tau_\perp & 0 & 0 & \hbar v_F(\tau p_x - i p_y) \\ 0 & 0 & \hbar v_F(\tau p_x + i p_y) & 0 \end{pmatrix}, \tag{3.31}$$

where $p_{x,y} = \hbar k_{x,y}$ and $\tau = +1$ ($\tau = -1$) denotes the corresponding Hamiltonian for K (K'). The wave functions corresponding to Hamiltonian (3.31) are given by

$$\Psi_K = \begin{pmatrix} \varphi_A \\ \varphi_B \\ \varphi_{B'} \\ \varphi_{A'} \end{pmatrix} \quad \text{and} \quad \Psi_{K'} = \begin{pmatrix} \varphi_B \\ \varphi_A \\ \varphi_{A'} \\ \varphi_{B'} \end{pmatrix}. \tag{3.32}$$

For a free electron in a AB-stacking graphene bilayer, the dispersion relation consists of four hyperboles, defined as [200]:

$$\varepsilon_{\pm}^{\pm} = \pm\frac{\tau_\perp}{2} \pm \sqrt{\frac{1}{4}\tau_\perp^2 + k^2}. \tag{3.33}$$

Figure 3.4 illustrates the low-energy electron dispersion, in two-dimensions (only for K_x), for the (left) AB- and (right) AA-stacked bilayer graphene bilayer, respectively. As can be seen for the AB stacking, two of the four bands touch each other at $K_x = 0$. On the other hand, the two upper bands, that result from the strong coupling between the two layers, present a gap, with their energies given by $E_+^+ \geq \tau_\perp$ and $E_-^- \leq -\tau_\perp$. For the graphene bilayer[2] with AA stacking, the spectrum is similar to that of two non-degenerate graphene monolayers [201].

The Hamiltonian (3.31) also be written as a 2 × 2 matrix given by [202]:

$$H_{bi}^{\pm} = \frac{(\hbar v_f k_F)^2}{\tau_\perp} \begin{pmatrix} 0 & e^{-2i\phi} \\ e^{+2i\phi} & 0 \end{pmatrix}, \tag{3.34}$$

with $k_F = \sqrt{k_x^2 + k_y^2}$ e $\phi = \text{arctg}\,(k_y/k_x)$.

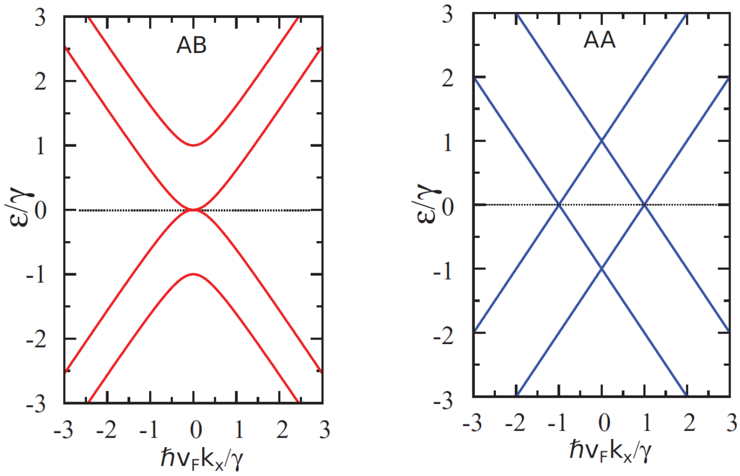

Figure 3.4: Low energy dispersion relation for bilayer graphene with AB and AA stacking, respectively, in two dimensions (only for K_x). Adapted from the Ref. [201].

---

[2] The steps to obtain the energy spectrum for the AA-stack, through the TB method, can be found in Ref. [194]

4

Effect of *Zitterbewegung* on the propagation of wave packets in ABC-stacked multilayer graphene: an analytical and computational approach

In this chapter the time evolution of a low-energy two-dimensional Gaussian wave packet in ABC-stacked n-layer graphene (ABC-NLG) is investigated. Expectation values of the position (x, y) of center-of-mass and the total probability densities of the wave packet are calculated analytically using the Green's function method. These results are confirmed using an alternative numerical method based on the split-operator technique within the Dirac approach for ABC-NLG, which additionally allows to include external fields and potentials. The main features of the *zitterbewegung* (trembling motion) of wave packets in graphene are demonstrated and are found to depend not only on the wave packet width and initial pseudospin polarization, but also on the number of layers. Moreover, the analytical and numerical methods proposed here allow to investigate wave packet dynamics in graphene systems with an arbitrary number of layers and arbitrary potential landscapes.

The study on *effect of zitterbewegung on the propagation of wave packets in ABC-stacked multilayer graphene: an analytical and computational approach* was published in Journal Physics: Condensed Matter, **33**, 095503 (2020).

4.1 Motivation

Zitterbewegung (ZBW) is a fast oscillation or trembling motion of elementary particles that obey the Dirac equation [25], which was predicted by Erwin Schrödinger in 1930 for relativistic fermions [23]. Schrödinger observed that the component of relativistic velocity for electrons in vacuum does not commute with the free-electron Hamiltonian. Consequently, the expectation value of the position of these electrons displays rapid oscillatory motion, owing to the fact that the velocity is not a constant of motion. It was also demonstrated that ZBW occurs due to the interference between the positive and negative energy states in the wave packet, and the characteristic frequency of this motion is determined by the gap between the two states.

In the last decades, Schrödinger's idea stimulated numerous theoretical studies e.g. in ultracold atoms [27, 28], semiconductors [29–34], carbon nanotubes [35], topological insulators [36], crystalline solids [37, 38] and other systems [39–42]. Although ZBW was theoretically found using a quantum simulation of the Dirac equation for trapped ions [43], Bose–Einstein condensates [44–46] and, most recently, an optical simulation [47], up to now, no direct experimental observations have been carried out. The reason is that the Dirac equation predicts ZBW with amplitude of the order of the Compton wavelength (10^{-2} Å) and a frequency of $\omega_{ZB} \approx 10^{21}$ Hz, which are not accessible with current experimental techniques.

With the discovery of graphene [8, 107], a single-layer of a honeycomb lattice of carbon atoms with unique electronic properties [9, 107, 196, 197, 203–206], the ZBW effect has been revisited recently [4, 44, 48, 207–212], since low-energy electrons in graphene behave as quasi-relativistic particles [184, 213, 214]. Maksimova *et al.* [48] investigated the wave packet evolution in monolayer graphene (MLG) analytically for different pseudo-spin polarizations using the Green's function method. Rusin and Zawadzki [208] analyzed the evolution of a Gaussian wave packet in MLG and bilayer graphene (BLG), as well as in carbon nanotubes, for one kind of initial pseudo-spin polarization, which is directly linked to the direction of propagation of the wave packet. They demonstrated that the transient character of ZBW in BLG is related to the movement in opposite directions of the sub-wave packets corresponding to the positive and negative energy contributions. A similar investigation for MLG was performed pure numerically based on the so-called split-operator technique (SOT), which will be explained more in details later on, by Chaves *et al.* [49], and, most recently, in multilayer phosphorene by Cunha *et al.*[42], that compared both SOT and Green's function results.

In this chapter, we generalize the previous studies on ZBW in MLG by proposing different techniques to study the dynamics of charged particles described by a two-dimensional (2D) Gaussian wave packet in ABC stacked $n-$layer graphene (ABC-NLG). We use an approximated 2×2 Hamiltonian valid for low-energy electrons in ABC-NLG and the Green's function formalism to obtain the time-evolved electron wave function for an arbitrary pseudospin polarization and then use this result to analytically calculate the expectation values of center-of-mass coordinates, the trajectory and spreading of the wave packet in real space, as well as their oscillations due to ZBW. We also develop a numerical method to perform the same calculation based on the SOT, but with much higher flexibility, allowing to consider ABC-NLG and any potential profile. Results from both theoretical approaches for MLG, BLG and trilayer graphene (TLG) are compared and their validity is verified. The dependence of several qualitative features of ZBW on the number of graphene layers and wave packet initial conditions is discussed in detail. The analytical and numerical methods proposed here can be straightforwardly adapted to investigate transport properties of multi-layer graphene in the presence of external fields

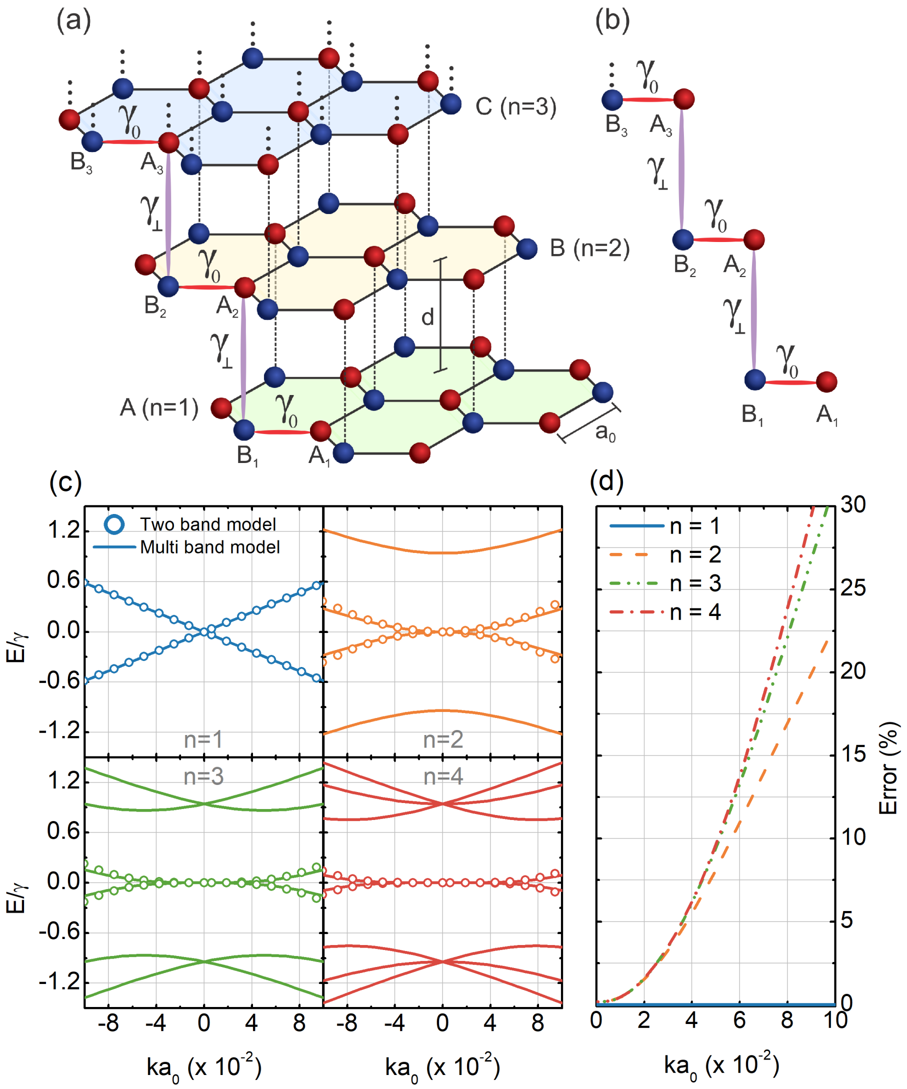

Figure 4.1: (Color online) (a) Schematic representation for NLG with rhombohedral stacking (ABC). The interlayer and intralayer distance are $d \approx 3.35$ Å and $a_0 = 1.42$ Å, respectively. The two non-equivalent carbon sublattices in each layer are indicated by red (A) and blue (B) circular symbols. (b) Representation of ABC-stacked multi-layer graphene with intralayer hopping between first nearest neighbors γ_0 and interlayer hopping energy between A_i and B_{i+1} sites of each layer given by $\gamma_\perp$. (c) Energy spectrum of multilayer graphene near one of the Dirac cones for low energies obtained by tight-binding model (solid curves) and two-band continuum m4odel (symbols). The energy is expressed in units of the interlayer hopping energy $\gamma_\perp$ and the wave vector is expressed in units of a_0^{-1}, the inverse of the nearest-neighbour interatomic distance. (d) Percentage error calculated from the lowest energy band of the two models considered in panel (c) for different number of graphene layers (n).

and arbitrary potential profiles.

4.2 The base of ZBW in N-ABC-stacked multilayer graphene

For ABC-NLG, as illustrated in Fig. 4.1(a), the effective Hamiltonian in the long wavelength approximation, near the K point on the first Brillouin zone of n graphene layers, can be written as the following approximated $2n \times 2n$ matrix [215]

$$H_n = \hbar v_F \begin{bmatrix} \boldsymbol{\sigma}\cdot\boldsymbol{k} & \tau & 0 & \cdots & 0 \\ \tau^\dagger & \boldsymbol{\sigma}\cdot\boldsymbol{k} & \tau & \cdots & 0 \\ 0 & \tau^\dagger & \boldsymbol{\sigma}\cdot\boldsymbol{k} & \ddots & 0 \\ \vdots & \vdots & \ddots & \ddots & \tau \\ 0 & 0 & 0 & \tau^\dagger & \boldsymbol{\sigma}\cdot\boldsymbol{k} \end{bmatrix}_{2n\times 2n} + \mathcal{V}\mathbb{1}, \tag{4.1}$$

by considering only nearest-neighbor interlayer transitions, τ represented the 2×2 coupling matrix given by

$$\tau = \frac{1}{\hbar v_F}\begin{bmatrix} 0 & 0 \\ \gamma_\perp & 0 \end{bmatrix}, \tag{4.2}$$

with $\gamma_\perp \approx 0.4$ eV being the interlayer hopping parameter [193], as shown in Fig. 4.1(b). $v_F = 3a_0\gamma_0/2\hbar$ is the Fermi velocity with $\gamma_0 \approx 2.7$ eV being the intralayer coupling, $\boldsymbol{\sigma} = (\sigma_x, \sigma_y, \sigma_z)$ are the Pauli matrices and $\boldsymbol{k} = (k_x, k_y)$ is the wave vector. Note that the tridiagonal matrix, Eq. (4.1), only considers the coupling between the adjacent layers, otherwise off-tridiagonal terms would be non-zero, and its main diagonal is composed by n MLG-type Hamiltonians. Within a low-energy approximation ($|\varepsilon| \ll \gamma_\perp$), it is possible to rewrite Eq. (4.1) as an effective two-band Hamiltonian [216–218]

$$H_n(k) = \frac{(\hbar v_F k)^n}{\gamma_\perp^{n-1}}\begin{bmatrix} 0 & e^{-in\phi} \\ e^{in\phi} & 0 \end{bmatrix} + \mathcal{V}\mathbb{1}, \tag{4.3}$$

where $\phi = \arctan(k_y/k_x)$ is the 2D polar angle in momentum space, and the eigenstate that was given by a $2n-$component wave function $\Psi^n = (\Psi_A^1, \Psi_B^1, \Psi_A^2, \Psi_B^2 \cdots \Psi_A^n \Psi_B^n)$ is now approximated by the two-component one $\Psi^n \to \Psi_{\text{eff}} = [\Psi_A^1 \quad \Psi_B^n]^T$. [219, 220] An arbitrary external electric potential, e.g. a perpendicular electric field, can be incorporated in the model by adding a potential energy $\mathcal{V}_i$ to the on-site energies in the main diagonal, with $i = 1, 2, \cdots n$ and n being the number of layers, as represented by the second term $\mathcal{V}\mathbb{1}$ in Eqs. (4.1) and (4.3), where $\mathbb{1}$ denotes the identity matrix with dimension $2n \times 2n$ and 2×2, respectively. The only assumption to this approach of adding an external potential in the two-band model is that the field affects equally the on-site energies of all atoms in the same layer i, and only the potential difference between the first and last layers is taken into account. For the sake of simplicity but without loss of generality, we assumed in the present study that the multilayer graphene system is free of interactions with any external sources. Low-energy bands are related to orbitals on the non-dimer sites A_1 and

B$_n$ (see Fig. 4.1(a)-4.1(b)), where $n \geq 2$, [197] although, counterintuitively, the hopping that appears in Eq. (4.3) is the strong interlayer coupling $\gamma_\perp$ of the orbitals on the dimer B_i and A_{i+1} sites. The validity of this approximation is based on the increase in energy near the dimer atomic sites. For low Fermi energy, it therefore makes sense to take into account only the orbital wave functions near the other two atoms, i.e. the non-dimer sites. [197, 221] For instance, for BLG case, the low-energy bands can be approximated as $\varepsilon \approx \pm(1/2)\gamma_\perp[\sqrt{1+4v_F^2p^2/\gamma_\perp^2}-1]$, which are composed by a linear dispersion $\boldsymbol{p} \approx v_F p$ at large momentum and a quadratic dispersion $\varepsilon \approx p^2/2m$ at small momentum values, where the mass is given by $m = \gamma_\perp/2v_F$. As discussed in Ref. [197], for low energy and momentum $p \ll \gamma_\perp/2v_F$, the dimer sites can be neglected allowing us to write a 2×2 Hamiltonian only in terms of the orbitals of the non-dimer sites, and thus, the two effective bands approach to the two lowest bands coming from the 4×4 Hamiltonian at low energies, as can be seen in Fig. 4.1(c). The eigenenergies $\varepsilon^n_{\boldsymbol{p},s}$ and the corresponding eigenstates $\Psi^n_{\boldsymbol{p},s}$ of the Hamiltonian (4.3) can be expressed as

$$\varepsilon^n_{\boldsymbol{p},s} = s\frac{p^n}{\xi}, \tag{4.4}$$

and

$$\Psi^n_{\boldsymbol{p},s} = \frac{1}{\sqrt{2}}\begin{bmatrix} 1 \\ se^{in\phi} \end{bmatrix}, \tag{4.5}$$

where $s = 1$ ($s = -1$) is the electron conduction (hole valence) band index, $p = \hbar k$, $\gamma_\perp^{n-1}/v_F^n \to \xi$ and $e^{i\phi} = (p_x + ip_y)/p$. This continuum approximation is valid in the low-energy and long-wavelength limits, and a small quantitative deviation of this approximation becomes more significant for large k values as shown in Fig. 4.1(c) by comparing the energy spectrum obtained by the two-band continuum (black solid curves) and multi-band (red dashed curves) models for mono ($n = 1$), bi ($n = 2$), tri ($n = 3$) and tetra ($n = 4$) layer graphene. Notice that for $n = 1$, both multi-band [Eq. (4.1)] and two-band [Eq. (4.3)] models give the same results, as already expected since each matrix element in the main diagonal in Eq. (4.1) represents a MLG Hamiltonian (see first left panel in Fig. 4.1(c)). In Fig. 4.1(d) we show the percentage error that arises from the discrepancy between the two lowest bands obtained within the effective two-band model [Eq. (4.3)] and the multi-band model [Eq. (4.1)]. Based on Figs. 4.1(c) and 4.1(d), one observes that the percentage error for $|ka_0| \lesssim 0.5$ is approximately the same regardless the number of graphene layers, being less than 8%, and, moreover, for a fixed momentum in the range in which $|ka_0| \gtrsim 0.5$, the percentage error between the two-band and the multi-band models increases the greater the number of graphene layers. This good agreement for the lowest two bands and near the Dirac cone, that is, for $|ka_0|$ approximately less than 0.5, as shown in Figs. 4.1(c) and 4.1(d), has been widely reported and used in multilayer graphene works in the literature (for example, see Refs. [193, 215, 218–222]). Furthermore, similar works aiming the zitterbewegung investigation in multiband Hamiltonian with arbitrary matrix elements depending only on the momentum of the quasiparticle have been reported, [223, 224] showing the applicability and versatility of this kind of multiband-type model.

4.2.1 Gaussian wave packet dynamics for ABC-NLG

Using the Green's function method, we obtained, inspired in the monolayer graphene case presented by Maksimova *et al.* [48] and Demikhvskii *et al.* [225], a generalized expression to study ZBW in ABC-NLG.

According to Eqs. (4.4) and (4.5), the time-dependent eigenfunctions of Hamiltonian (4.3) are given by

$$\Phi_{p,s}\left(\boldsymbol{r},t\right)=\frac{1}{2\sqrt{2}\pi\hbar}\exp\left(i\frac{\boldsymbol{p}\cdot\boldsymbol{r}}{\hbar}-i\frac{E^{n}_{\boldsymbol{p},s}t}{\hbar}\right)\left(\begin{array}{c}1\\ se^{in\phi}\end{array}\right). \tag{4.6}$$

In order to calculate the time evolution of an arbitrary state, we use the Green's function method defined by the non-diagonal 2×2 matrix

$$\mathbb{G}=\left(\begin{array}{cc}G_{11}&G_{12}\\ G_{21}&G_{22}\end{array}\right), \tag{4.7}$$

where the matrix elements can be written as

$$G_{\mu v}\left(\boldsymbol{r},\boldsymbol{r}',t\right)=\sum_{s=\pm1}\int\Phi_{p,s,\mu}\left(\boldsymbol{r},t\right)\Phi^{\dagger}_{p,s,v}\left(\boldsymbol{r}',0\right)d\boldsymbol{p}, \tag{4.8}$$

and $\mu,\nu=1,2$ are matrix indices, associated with the upper and lower components of $\Psi\left(\boldsymbol{r},t\right)$ that are related to the probability of finding the electron at the sublattices A (upper) and B (lower). The time-evolved electron wave function for $t>0$ can be obtained as

$$\Psi_{\mu}\left(\boldsymbol{r},t\right)=\int G_{\mu v}\left(\boldsymbol{r},\boldsymbol{r}',t\right)\psi_{v}\left(\boldsymbol{r},0\right)d\boldsymbol{r}'. \tag{4.9}$$

Combining Eqs. (4.6) and (4.8), we have that

$$G_{11}\left(\boldsymbol{r},\boldsymbol{r}',t\right)=G_{22}\left(\boldsymbol{r},\boldsymbol{r}',t\right)=\frac{1}{\left(2\pi\hbar\right)^{2}}\int\exp\left[i\frac{\boldsymbol{p}\left(\boldsymbol{r}-\boldsymbol{r}'\right)}{\hbar}\right]\cos\left(\frac{p^{n}t}{\xi\hbar}\right)d\boldsymbol{p}, \tag{4.10a}$$

$$G_{12(-)}\left(\boldsymbol{r},\boldsymbol{r}',t\right)=G_{21(+)}\left(\boldsymbol{r},\boldsymbol{r}',t\right)=\frac{-i}{\left(2\pi\hbar\right)^{2}}\int e^{\mp in\phi}\exp\left[i\frac{\boldsymbol{p}\left(\boldsymbol{r}-\boldsymbol{r}'\right)}{\hbar}\right]\sin\left(\frac{p^{n}t}{\xi\hbar}\right)d\boldsymbol{p}. \tag{4.10b}$$

Note that $G_{12}\left(\boldsymbol{r},\boldsymbol{r}',t\right)$ differs from $G_{21}\left(\boldsymbol{r},\boldsymbol{r}',t\right)$ only by a negative sign in the term $e^{\mp in\phi}=\left(p_x\mp ip_y/p\right)^{n}$, as emphasized by the subscripts in Eq. (4.10b). For more details, see App. C.1.

At $t=0$, we assume the wave function to be a circularly symmetrical 2D Gaussian wave packet with width d and non-vanishing average momentum along y-direction, i.e. $p_{0y}=\hbar k_0^y$, such that

$$\psi\left(\boldsymbol{r},0\right)=\frac{f\left(\boldsymbol{r}\right)}{\sqrt{\left|C_1\right|^{2}+\left|C_2\right|^{2}}}\begin{pmatrix}C_1\\ C_2\end{pmatrix}, \tag{4.11a}$$

with

$$f\left(\boldsymbol{r}\right)=\frac{1}{d\sqrt{\pi}}\exp\left[-\frac{r^2}{2d^2}+\frac{ip_{0y}y}{\hbar}\right]. \tag{4.11b}$$

Gaussian-like wave packets are commonly used in the ZBW analysis, since such oscillatory effect is not a stationary state but a dynamical phenomenon as well as it exhibits a minimal position-momentum uncertainty. They are essentially a combination of plane-waves, where the wave packet width represents a distribution of momenta and, consequently, of energy, and it is associated with e.g. the temperature of the system. Thus, by setting the initial state as Gaussian wave packet, this assumption covers most cases of practical interest, because any wave packet can be approximated by a superposition of a finite number of Gaussian states. Such a wave packet could be created by an ultra short laser pulse. This results in a wave packet with both positive and negative energies, since such a pulse has a very wide frequency spectrum [226, 227].

Coefficients C_1 and C_2 determine the initial pseudospin polarization of the injected wave packet and are related to the two pseudospin components in Eq. (4.5). Each component of the electron spinor wave function is then found as

$$\begin{pmatrix}\Psi_1\left(\boldsymbol{r},t\right)\\ \Psi_2\left(\boldsymbol{r},t\right)\end{pmatrix}=\frac{1}{\sqrt{\left|C_1\right|^2+\left|C_2\right|^2}}\begin{pmatrix}C_1\Phi_1\left(\boldsymbol{r},t\right)+C_2\Phi_3\left(\boldsymbol{r},t\right)\\ C_1\Phi_2\left(\boldsymbol{r},t\right)+C_2\Phi_4\left(\boldsymbol{r},t\right)\end{pmatrix}, \tag{4.12}$$

where

$$\Phi_1\left(\boldsymbol{r},t\right)=\int G_{11}\left(\boldsymbol{r},\boldsymbol{r}',t\right)f\left(\boldsymbol{r}'\right)d\boldsymbol{r}'=$$

$$\frac{de^{-\frac{\left(k_0^y d\right)^2}{2}}}{2\hbar^2\sqrt{\pi^3}}\int\exp\left(i\frac{\boldsymbol{p}\cdot\boldsymbol{r}}{\hbar}-\frac{p^2d^2}{2\hbar^2}+\frac{p_{y'}k_0^yd^2}{\hbar}\right)\cos\left(\frac{p^nt}{\xi\hbar}\right)d\boldsymbol{p}, \tag{4.13a}$$

$$\Phi_{3_-(2_+)}\left(\boldsymbol{r},t\right)=\int G_{12(21)}\left(\boldsymbol{r},\boldsymbol{r}',t\right)f\left(\boldsymbol{r}'\right)d\boldsymbol{r}'=$$

$$\frac{-ide^{-\frac{\left(k_0^y d\right)^2}{2}}}{2\hbar^2\sqrt{\pi^3}}\int e^{\mp in\phi}\exp\left(i\frac{\boldsymbol{p}\cdot\boldsymbol{r}}{\hbar}-\frac{p^2d^2}{2\hbar^2}+\frac{p_{y'}k_0^yd^2}{\hbar}\right)\sin\left(\frac{p^nt}{\xi\hbar}\right)d\boldsymbol{p}, \tag{4.13b}$$

and $\Phi_1\left(\boldsymbol{r},t\right)=\Phi_4\left(\boldsymbol{r},t\right)$ according to Eq. (4.10a). The subscript $-$ $(+)$ for Φ_3 (Φ_2) in Eq. (4.13b) refers to the sign of the argument in $e^{-in\phi}$ $(e^{+in\phi})$. To see how Eqs. (4.13a) and (4.13b) were obtained, see App. C.2.

Using cylindrical coordinates in Eqs. (4.13a) and (4.13b) and integrating over the angular variable, we obtain (see App. C.3 for more details)

$$\Phi_1\left(\boldsymbol{r},t\right)=\frac{e^{-a^2/2}}{d\sqrt{\pi}}\int_0^\infty e^{-\frac{q^2}{2}}\cos\left(q^nt'\right)J_0\left(q\sqrt{r^2-a^2-2iay}\right)qdq, \tag{4.14a}$$

$$\Phi_{3_+(2_-)}\left(\boldsymbol{r},t\right)=\frac{-ie^{-a^2/2}}{d\sqrt{\pi}}\left[\frac{ix'\pm y\mp ia}{\sqrt{r^2-a^2-2iay}}\right]^n\int_0^\infty e^{-\frac{q^2}{2}}\sin\left(q^nt'\right)J_n\left(q\sqrt{r^2-a^2-2iay}\right)qdq, \tag{4.14b}$$

where $J_0(z)$ and $J_n(z)$ are Bessel functions of the zeroth and n-th order. For the sake of simplicity, we introduced in Eqs. (4.14a) and (4.14b) the dimensionless parameter $a = k_0^y d$ and considered the time in units of d/v_F.

Once $\Psi_1(\boldsymbol{r},t)$ and $\Psi_2(\boldsymbol{r},t)$ are known, the time-dependent expectation value of the position operator can be calculated as

$$\langle \boldsymbol{r}(t)\rangle = \sum_{j=1}^{2} \int \Psi_j^*(\boldsymbol{p},t)\left[i\hbar\frac{d}{d\boldsymbol{p}}\right]\Psi_j(\boldsymbol{p},t)\,d\boldsymbol{p}, \tag{4.15}$$

with Ψ in momentum representation, that can be easily inferred from Eqs. (4.13a) and (4.13b). From Eq. (4.15) we investigate the ZBW phenomenon by an analytical calculation of the time-dependent expectation value of the position $\langle \boldsymbol{r}(t)\rangle = (\langle x(t)\rangle, \langle y(t)\rangle)$ of the center of the wave packet for different initial electron amplitudes of sublattices A and B, by taking different values for C_1 and C_2 in Eq. (4.12), as will be discussed in Sec.4.3. (See App. C.4 for more details)

In general, for the wave packet propagation results discussed further in Sec. 4.3, the momenta choices have percentage errors less then 10%, when the two-band model and the multi-band model are compared. These results for the expectation values of the Gaussian wave packet center-of-mass were obtained for the dimensionless parameters $a = k_0^y d$ assuming values $a = 1$, $a = 2$, $a = 3$, and $a = 4$ for a fixed value of wave packet width $d = 100$ Å, which corresponds to initial y-momentum: $k_0^y = 0.01$ Å^{-1}, $k_0^y = 0.02$ Å^{-1}, $k_0^y = 0.03$ Å^{-1}, and $k_0^y = 0.04$ Å^{-1}, respectively. By analyzing Fig. 4.1(d), one confirms that these used values of k_0^y's times $a_0 = 1.42$ Å lead to very low percentage errors, due to mismatch of the two models, showing approximately the same error value regardless the number of layers, as demonstrated in Fig. 4.1(d) for the whole range $|ka_0| \lesssim 0.5$. Moreover, as already reported in Refs. [48, 49] the wave-packet dynamics near the Dirac cones in graphene does not depend separately on the momentum k_y^0 or on the width d, but rather on the dimensionless quantity a. Therefore, even for large values of a, one can always choose large wave packet widths d's to keep the momentum k_0^y a small value within the validity range of the two-band model, obeying the conditions such that: k_0^y is not too far from the Dirac cone and d is not too small, so that the packet is well localized in energy space.

4.2.2 SOT for *ABC*-NLG within Dirac model

The analytical method developed here so far, despite being exact, is not flexible enough to allow the study of wave packet propagation in *ABC*-NLG in the presence of e.g. external potentials and applied electric or magnetic fields. We, thus, propose here a semi-analytical method, namely, the SOT, [49, 206, 228–235] which consists in splitting the time-evolution operator $\exp\left[-\frac{i}{\hbar}\mathcal{H}\Delta t\right]$ into different terms involving the potential $\mathcal{V}$, in real space, and the kinetic energy $\mathcal{H}_k$, in reciprocal space (see App. C.5 for more details):

$$e^{\left[-\frac{i}{\hbar}\mathcal{H}\Delta t\right]} = e^{\left[-\frac{i}{2\hbar}\mathcal{V}\Delta t\right]} e^{\left[-\frac{i}{\hbar}\mathcal{H}_k\Delta t\right]} e^{\left[-\frac{i}{2\hbar}\mathcal{V}\Delta t\right]} + O(\Delta t^3). \tag{4.16}$$

The error of order Δt^3 comes from the non-commutativity between potential and kinetic energy operators, and can be made small by assuming small time steps. Although, as we shall see below, we used the exact time-evolution operator with no approximation, we chose to refer to the method described here as SOT, first due to the similarities with the methods developed in Refs. [49, 206, 228] for spin-dependent Hamiltonians, as well as due to the fact that we are splitting the time-evolution operator.

As an example, let's consider the Dirac Hamiltonian for MLG [203] in the absence of external potentials ($V = 0$), i.e.

$$H_{MLG} = v_F \boldsymbol{\sigma} \cdot \boldsymbol{p}. \tag{4.17}$$

The time evolution operator for this case can be written as

$$\exp\left[-\frac{i}{\hbar}\mathcal{H}_{MLG}\Delta t\right] = \exp\left[-\frac{iv_F}{\hbar}(\boldsymbol{p}\cdot\boldsymbol{\sigma})\Delta t\right] = \exp[-i\boldsymbol{S}\cdot\boldsymbol{\sigma}]\,, \tag{4.18}$$

where $\boldsymbol{S} = \Delta t v_F \boldsymbol{p}/\hbar$ and its magnitude is $S = \Delta t v_F \sqrt{k_x^2 + k_y^2}$. Using the properties of the Pauli matrices, it is possible to rewrite Eq. (4.18) as a sum of two matrices, such as

$$\exp\left[-i\boldsymbol{S}\cdot\boldsymbol{\sigma}\right] = \cos\left(S\right)\mathbb{1} - i\frac{\sin\left(S\right)}{S}\left(\boldsymbol{S}\cdot\boldsymbol{\sigma}\right) = \mathbb{M}, \tag{4.19}$$

where $\mathbb{1}$ denotes the 2×2 unit matrix. This is an exact representation of the time evolution operator, including all the terms of the expansion of the exponential.

The generalized Hamiltonian H_n for ABC-NLG, Eq. (4.3), can be re-written in terms of Pauli matrices for any number of layers n, therefore, Eq. (4.19) always hold, as long as the vector $\boldsymbol{S}$ one adapts accordingly, which can be done with straightforward algebra. For instance, for BLG one can re-write $\boldsymbol{S}$ as

$$\boldsymbol{S} = \hbar v_F^2 \Delta t \gamma_\perp^{-1}\left(k_x^2 - k_y^2, 2k_x k_y, 0\right), \tag{4.20}$$

whereas for TLG, one obtains

$$\boldsymbol{S} = \hbar^2 v_F^3 \Delta t \gamma_\perp^{-2}\left(k_x^3 - 3k_y^2 k_x, 3k_x^2 k_y - k_y^3, 0\right). \tag{4.21}$$

The propagated wave function $\Psi = [\Psi_1\ \Psi_2]^T$ at a time step $t + \Delta t$ is given by

$$\Psi\left(\boldsymbol{r}, t + \Delta t\right) = e^{-iH_n\Delta t/\hbar}\Psi\left(\boldsymbol{r}, t\right) = \mathscr{F}^{-1}\{\mathbb{M}\mathscr{F}\{\Psi\left(\boldsymbol{r}, t\right)\}\}, \tag{4.22}$$

where $\mathscr{F}$ ($\mathscr{F}^{-1}$) is the (inverse) Fourier transform operator. Note that $\mathbb{M}$ depends on the wave vectors k_x and k_y, therefore, the matrix multiplication with a general initial wave packet is conveniently computed numerically in reciprocal space by performing a Fourier transform of the wave function, reason why this method is thus seen as a semi-analytical procedure. Because the solution of Eq. (4.22) is exact, it should provide the same results as the Green's function method described in Sec. 4.2.1 for free wave packets in NLG. We verified, as will be discussed latter in Sec. 4.3, that we obtain numerical *perfect* agreement between results obtained by the SOT and the Green's function formalism. A clear advantage of the SOT is that it provides a way to study the wave packet dynamics in NLG within the continuum model in the presence of arbitrary external potential profiles[49, 206, 228–235], simply by performing matrix multiplications with the potential exponential terms, as shown in Eq. (4.16). Moreover, it is worth mentioning for the general picture in the presence of external potentials ($\mathcal{V} \neq 0$), the accuracy of the results obtained by the SOT given by Eq. (4.16) is controlled by the choice of the time step Δt, being the error dropped by assuming a small time step. In contrast, for $\mathcal{V} = 0$ and spin-dependent Hamiltonians no approximation was applied and, consequently, the exact representation of the time evolution operator allows us to assume any value for the time step. The assumed time step for all obtained results here in both approaches is $\Delta t = 0.1$ fs.

4.2.3 SOT for ABC-NLG within the tight-binding model

Despite having the advantage of being semi-analytical, numerically exact, and suitable for large graphene samples, the methods developed here so far are not able to capture the microscopic features of NLG, such as rough edges and lattice defects. For that, one needs to invoke theories that deal with the 2D material on the microscopic level, such as the density functional theory and the tight-binding model. Nevertheless, for the later, the SOT has been already developed for MLG[49, 228] and BLG[230] cases. Details of this procedure and the method proposed in Ref. [230] can be easily adapted for any number of layers, but such fully numerical microscopic approach is beyond the scope of the present chapter. Although not shown in this study, the time evolution of wave packets and trajectories obtained here for all cases of wave packet pseudospinor are verified to agree well with those one based on the tight-binding SOT for low-energy wave packets in MLG[49, 206, 228, 229, 231–234] and BLG[230, 235], thus additionally validating our results.

4.3 Zitterbewegung of Gaussian wave packet for different pseudospin polarizations

4.3.1 Predictions from the Heisenberg equation

Different kinds of initial pseudospin polarization of the wave packet will be considered in this chapter. It is thus important to be able to predict beforehand the qualitative behavior of the propagating wave packet in each case. In order to do so, we introduce a method based on calculations of expectation values of wave packets by using the Heisenberg equation.

We use the subtlety of Heisenberg representation to predict which initial settings of pseudospin $(C_1\ C_2)^T$ result in non-zero averages of the electron coordinates $\langle x\left(t\right)\rangle$ and

$\langle y(t)\rangle$. The velocity vector is defined as

$$\langle \boldsymbol{v}(t)\rangle = \frac{d\boldsymbol{r}}{dt} = \frac{1}{i\hbar}[\boldsymbol{r}, H] = v_F\boldsymbol{\sigma}, \tag{4.23}$$

where $\boldsymbol{v} = (v_x, v_y)$ and $\boldsymbol{r} = (x, y)$ are the velocity and the position vectors, respectively.

Without loss of generality, as an example, let's consider the MLG Hamiltonian [Eq. (4.17)] and shall analyse a wave packet propagating in the x-direction in order to verify whether $\langle x(t)\rangle$ is a constant of motion. Therefore, from Eqs. (4.17) and (4.23), one obtains

$$\frac{d\langle x(t)\rangle}{dt} = \frac{1}{i\hbar}\langle [x, H_{MLG}]\rangle = v_F\langle \sigma_x\rangle . \tag{4.24}$$

On the other hand,

$$\frac{d\langle \sigma_x\rangle}{dt} = \frac{1}{i\hbar}\langle [\sigma_x, H_{MLG}]\rangle = \frac{2v_F p_y}{\hbar}\langle \sigma_z\rangle . \tag{4.25}$$

Thus, from Eqs. (4.24) and (4.25), we conclude that, if the initial pseudospin is oriented along the z direction, i.e., $\langle \sigma_z\rangle \neq 0$, and $p_y \neq 0$, $\langle x(t)\rangle$ is not a constant of motion and it is expected that $\langle x(t)\rangle$ will exhibit ZBW. This choice is represented by the initial pseudospinor $(C_1\ C_2)^T = (1\ 0)^T$. The same idea is straightforwardly generalized to any number of layers. Table 4.1 shows the results for MLG, BLG and TLG for other initial pseudospin configurations, which are the three cases developed in detail in the next sections.

Table 4.1: Expectation value of the position (x, y) of the injected wave packet obtained from the Heisenberg picture for different C_1 and C_2 values that determine the initial polarization of the pseudospin. The $(\neq) =$ symbols indicate expectation values that are (non-)zero.

	$\langle x(t)\rangle$			$\langle y(t)\rangle$		
$(C_1\ C_2)^T$	$(1\ 0)^T$	$(1\ 1)^T$	$(1\ i)^T$	$(1\ 0)^T$	$(1\ 1)^T$	$(1\ i)^T$
Monolayer	$\neq$	$\neq$	$=$	$=$	$=$	$\neq$
Bilayer	$\neq$	$=$	$\neq$	$=$	$\neq$	$=$
Trilayer	$\neq$	$=$	$\neq$	$=$	$\neq$	$=$

4.3.2 ZBW in MLG

Note that Eqs. (4.13a) and (4.13b) were generally obtained for NLG. Thus, one just needs to use $n = 1$ in these equations and replace them into Eq. (4.12) in order to obtain the wave function for MLG. Once the wave function is obtained, the expectation value of the position of its center of mass is calculated using Eq. (4.15). Let us first revisit the problem of ZBW in MLG as a particular case of the method developed here.

4.3.2.1 $C_1 = 1$ and $C_2 = 0$

We first consider the simple case when the lower component of the initial wave function (4.11a) is equal to zero, i.e. taking $C_1 = 1$ and $C_2 = 0$ in Eq. (4.12). It corresponds to

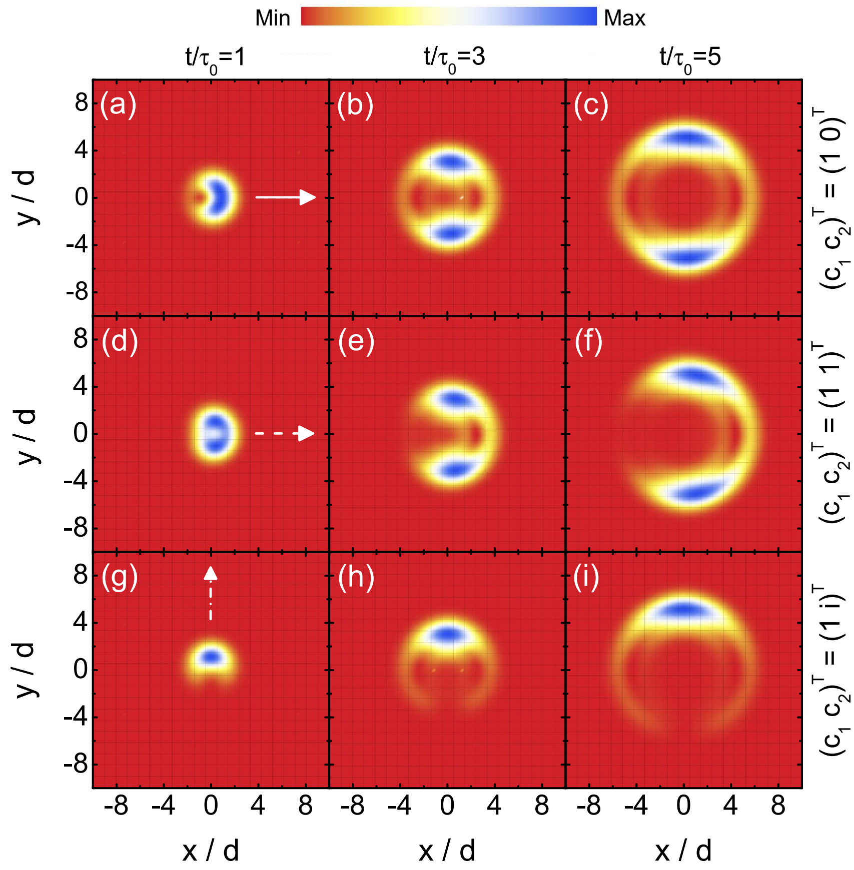

Figure 4.2: (Color online) Evolution (in units of d/v_F) of electronic probability density $\rho\left(\boldsymbol{r},t\right) = \left|\Psi_1\left(\boldsymbol{r},t\right)\right|^2 + \left|\Psi_2\left(\boldsymbol{r},t\right)\right|^2$ for MLG with (a)-(c) $\left(C_1\ C_2\right)^T = (1\ 0)^T$, (d)-(f) $\left(C_1\ C_2\right)^T = (1\ 1)^T$, (g)-(i) $\left(C_1\ C_2\right)^T = (1\ i)^T$, for $a = k_0^y d = 1.2$ ($d = 2$ nm and $k_0^y = 0.6$ nm^{-1}) and $t/\tau_0 = 1$, 3 and 5. The white arrows indicate the direction of propagation of the wave packet.

the case in which the electron probability is initially located only at sites of the sublattice A and pseudospin is polarized perpendicularly to the xy-plane, i.e., $\langle\sigma_z\rangle = 1$ and $\langle\sigma_x\rangle = \langle\sigma_y\rangle = 0$.

According to Eq. (4.12), the wave function for $t > 0$ has the form:

$$\begin{pmatrix} \Psi_1\left(\boldsymbol{r},t\right) \\ \Psi_2\left(\boldsymbol{r},t\right) \end{pmatrix} = \begin{pmatrix} \Phi_1\left(\boldsymbol{r},t\right) \\ \Phi_2\left(\boldsymbol{r},t\right) \end{pmatrix}, \tag{4.26}$$

where $\Phi_{1,2}\left(\boldsymbol{r},t\right)$ are defined by Eqs. (4.13a) and (4.13b), respectively, with $n = 1$. To illustrate the evolution of the electron probability density we show $\rho\left(\boldsymbol{r},t\right) = \left|\Psi_1\left(\boldsymbol{r},t\right)\right|^2 + \left|\Psi_2\left(\boldsymbol{r},t\right)\right|^2$ in Fig. 4.2(a)-(c) for $p_{0y} = \hbar k_0^y \neq 0$. Inset in Fig. 4.2(a) shows the projection of the 2D Gaussian wave packet centered in the xy-plane at $t = 0$. As time elapses, the wave packet splits into two parts moving along the $y-$axis with opposite speeds, Figs. 4.2(a)-4.2(c). The probability density is symmetric (asymmetric) with respect to y (x), i.e., $\rho\left(x,y,t\right) = \rho\left(x,-y,t\right)$ $\left(\rho\left(x,y,t\right) \neq \rho\left(-x,y,t\right)\right)$. Thus, the center of the wave packet oscillates (ZBW) only along the x-direction. For long enough time, the width of the wave

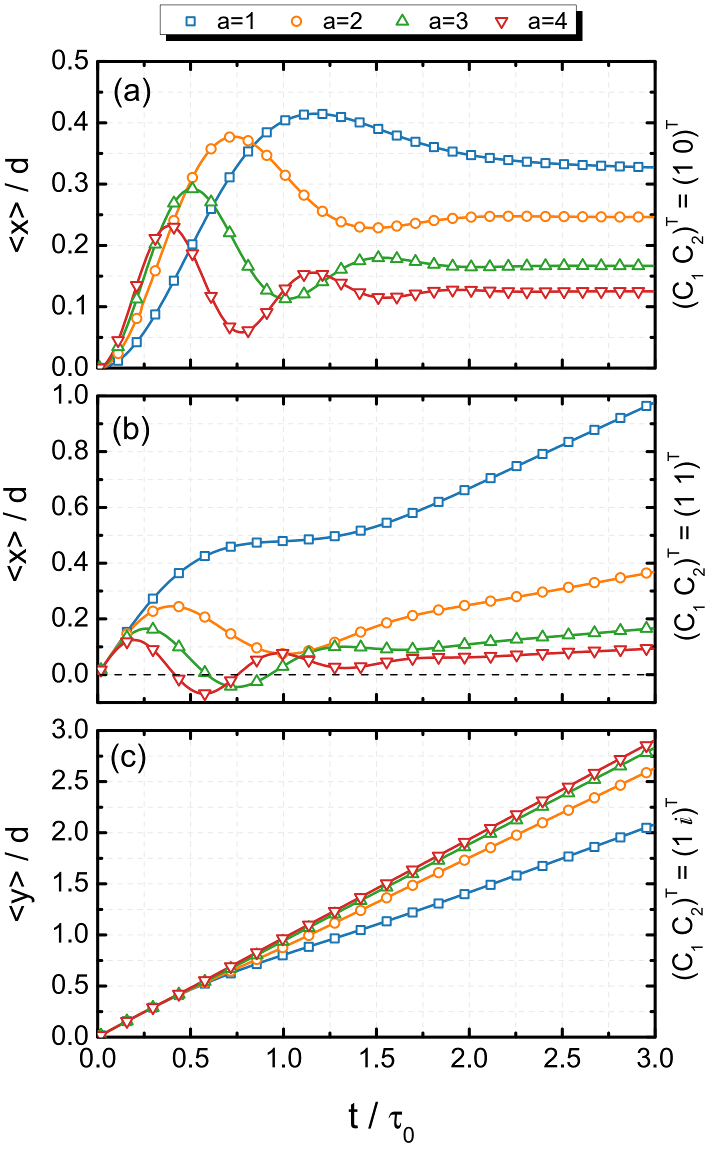

Figure 4.3: (Color online) (a) Expectation value $\langle x\,(t)\rangle$ of the Gaussian wave packet center-of-mass as a function of time ($\tau_0 = d/v_F$) for MLG with pseudospin polarization (a) $(C_1\ C_2)^T = (1\ 0)^T$, (b) $(C_1\ C_2)^T = (1\ 1)^T$ and (c) $(C_1\ C_2)^T = (1\ i)^T$, for different values of $a = k_0^y d$. The results are obtained for a fixed value of wave packet width $d = 100$ Å and different initial y-momentum: $k_0^y = 1 \cdot 10^{-2}$ Å^{-1} (blue); $k_0^y = 2 \cdot 10^{-2}$ Å^{-1} (orange); $k_0^y = 3 \cdot 10^{-2}$ Å^{-1} (green) and $k_0^y = 4 \cdot 10^{-2}$ Å^{-1} (red). The solid curves (symbols) correspond to the results obtained by the Green's function (SOT) method.

packet increases due to the effect of dispersion [1] as for the case of a free particle. This is unexpected, since the Dirac spectrum of low-energy electrons in graphene suggests a dispersionless wave function, thus the observed dispersion is a direct effect of the ZBW, as pointed out also in previous studies. [26, 38, 48]

The expectation value of the position operator were obtained by inserting Eq. (4.26)

---

[1] In fact, this is true for all other cases of pseudo-spin and number of graphene layers.

into Eq. (4.15), which leads

$$\langle x\left(t\right)\rangle = d\left[\frac{1-e^{-a^2}}{2a} - e^{-a^2}\int_0^{\infty} e^{-q^2}\cos\left(2qt'\right)I_1(2aq)\,dq\right] \tag{4.27}$$

and $\langle y\left(t\right)\rangle = 0$, where $I_1\left(z\right)$ is the modified Bessel function of the first order. These results are in accordance with Table 4.1, only obtained from the Heisenberg picture, and depends on the parameter $a = k_0^y d$. In App. C.4, as an example, is demonstrated how to obtain Eq. (4.27). The other expected values, for bilayer and trilayer, presented as follows, follow the same line of reasoning demonstrated in App. C.4 and can also be applied to the $\langle y(t)\rangle$.

The average position of the x-coordinate as a function of time, given by Eq. (4.27), is shown in Fig. 4.3(a) assuming various values of the parameter $a = k_0^y d$. For comparison, results obtained by the SOT based on the Dirac model are shown with symbols, presenting a good agreement with the analytical ones. From Fig. 4.3(a), the oscillations disappear after $t/\tau_0 \approx 2.5$ and $\langle x\left(t\right)\rangle$ converges to a specific value given by the first term of Eq. (4.27). For example, for $a = 4$, the first term in Eq. (4.27) is equal to 0.125 (in units of d), corresponding to the converged value of the red curve in Fig. 4.3. This demonstrates that the ZBW is not permanent, but a transient feature, as discussed also in Refs. [30, 236], and it is due to the time-dependence of the second term in Eq. (4.27). It can be noticed also in Fig. 4.3(a), that more oscillations occur, but with smaller amplitudes, as a increases. Consequently, the velocity $v_x = d\left\langle x\left(t\right)\right\rangle/dt$ oscillates with shorter period and smaller amplitude as a increases. Notice that $\langle \boldsymbol{r}\left(t\right)\rangle$, obtained here as a particular case of Eq. (4.12), coincide with corresponding formulas reported in Ref. [48].

4.3.2.2 $C_1 = 1$ and $C_2 = 1$

For $\left(C_1\ C_2\right)^T = \left(1\ 1\right)^T$, the initial pseudospin lies along the $x-$axis with the wave function equally distributed on sublattices A and B. From Eq. (4.12), one has

$$\begin{pmatrix}\Psi_1\left(\boldsymbol{r},t\right)\\ \Psi_2\left(\boldsymbol{r},t\right)\end{pmatrix} = \frac{1}{\sqrt{2}}\begin{pmatrix}\Phi_1\left(\boldsymbol{r},t\right)+\Phi_3\left(\boldsymbol{r},t\right)\\ \Phi_1\left(\boldsymbol{r},t\right)+\Phi_2\left(\boldsymbol{r},t\right)\end{pmatrix}, \tag{4.28}$$

with $\Phi_{1,2,3}\left(\boldsymbol{r},t\right)$ given by Eqs. (4.14a) and (4.14b), respectively. It is important to point up that an initial wave packet in which the electron probability density occupies equally all sublattices is more realistic experimentally, as an expected configuration when one creates wave packets by illuminating samples with short laser pulses and also because for an infinite system the initial wave function should describe electronic bulk states spread over all sites around the center point of the Gaussian distribution.[42, 226, 227] The time-evolved electron probability densities for $\left(1\ 1\right)^T$ case are depicted in Fig. 4.2(c)-(e). For $t > 0$, the shape of the full electron density $\rho\left(\boldsymbol{r},t\right)$ changes, see Figs. 4.2(d)-(f), splitting into two parts that move along the $y-$axis in opposite direction. As in the previous case, $\rho\left(\boldsymbol{r},t\right)$ is not mirror symmetric with respect to $x = 0$ axis and the wave packet travels asymmetrically to the positive x-direction. Consequently, the motion of the center of the Gaussian wave packet oscillates (ZBW) only along this direction. This is illustrated by two maxima of the electron density spread along the x-direction.

By substituting Eq. (4.28) into Eq. (4.15), we obtain the time-dependent expectation value of the wave packet position

$$\langle x\left(t\right)\rangle = d\left(\frac{1-e^{-a^2}}{2a^2}\right)t + \frac{de^{-a^2}}{2a}\int_0^\infty e^{-q^2}\sin\left(2qt'\right)\left[\frac{d}{dq}I_1\left(2aq\right)\right]dq, \tag{4.29}$$

$\langle y\left(t\right)\rangle = 0$.

Figure 4.3(b) presents $\langle x\left(t\right)\rangle$, given by Eq. (4.29), for different values of the parameter a and demonstrates that: (i) the higher the value of a, the smaller the amplitude of the ZBW, the period of oscillations and the velocity v_x of the center of the wave packet; and (ii) ZBW is transient. Results from SOT within the Dirac model are shown with symbols, and an excellent agreement with the analytical results (solid curves) validates our method. For small values of the wave packet initial momentum k_0^y, i.e. small values of $a = k_0^y d$, and after ZBW vanishes, one observes that $\langle x\left(t\right)\rangle$ increases linearly with time, as a consequence of the linear time-dependence on the first term of Eq. (4.29) that dominates after a while. However, as a (or equivalently k_0^y) increases, the second integral term in Eq. (4.29) becomes the dominant one.

4.3.2.3 $C_1 = 1$ and $C_2 = i$

In this last case, the initial pseudospin polarization $\left(C_1\ C_2\right)^T = \left(1\ i\right)^T$ is oriented along the same direction (y) as the plane wave momentum p_{0y} in Eq. (4.11b). From Eq. (4.12), the wave function is given by

$$\begin{pmatrix}\Psi_1\left(\boldsymbol{r},t\right)\\ \Psi_2\left(\boldsymbol{r},t\right)\end{pmatrix} = \frac{1}{\sqrt{2}}\begin{pmatrix}\Phi_1\left(\boldsymbol{r},t\right)+i\Phi_3\left(\boldsymbol{r},t\right)\\ i\Phi_1\left(\boldsymbol{r},t\right)+\Phi_2\left(\boldsymbol{r},t\right)\end{pmatrix}. \tag{4.30}$$

Figures 4.2(g)-(i) present snapshots of the propagated Gaussian wave packet for different time values. Unlike the two previous cases, discussed in Secs. 4.3.2.1 and 4.3.2.2, the wave packet now moves along the $y-$axis, i.e. the wave packet travels along the same direction as the pseudospin and average momentum p_{0y} orientation, and does not split into two parts for $t > 0$. The electron probability density obeys the following symmetry (asymmetry) for $t > 0$: $\rho\left(x,y,t\right) = \rho\left(-x,y,t\right)$ $\left(\rho\left(x,y,t\right) \neq \rho\left(x,-y,t\right)\right)$.

Inserting Eq. (4.30) into Eq. (4.15), it is easy to show that the expectation values of the x and y coordinates are, respectively: $\langle x\left(t\right)\rangle = 0$ and

$$\langle y\left(t\right)\rangle = d\left(1-\frac{1}{2a^2}+\frac{e^{-a^2}}{2a^2}\right)t + \frac{de^{-a^2}}{2a}\int_0^\infty e^{-q^2}\sin\left(2qt\right)\frac{I_1\left(2aq\right)}{q}dq. \tag{4.31}$$

Figure 4.3(c) compares the analytical results (solid curves) obtained by performing a numerical integration of Eq. (4.31), with those computed via SOT within the Dirac model (symbols). As can be seen from Fig. 4.3(c), the ZBW is almost absent and $\langle y(t)\rangle /d$ exhibits a linear time-dependence, which becomes more significant as the wave packet width a increases, without significant oscillations. That is, $\langle y(t)\rangle /d \approx t$ for large a. According to Eq. (4.31), as a increases, the second term (that causes oscillations), as well as the other two terms of the first expression which possess a parameter in their denominators, become small. Therefore, only the linear term t will dominate.

Our investigations reveal that the choice of the initial pseudospin polarization given by $(1\ i)^T$ is the best way, among the cases studied here, to avoid ZBW in MLG systems, as reported in Refs. [[49, 206, 228, 229, 231–234]]. Which is due to the fact that for this choice of pseudospin, the motion in the $y-$direction is perfectly vertical during the whole propagation (see Eq. (4.31)), being the least affected by ZBW phenomena, specially moving straight without to much dispersion as larger is the initial Gaussian wave vector.

4.3.3 ZBW in BLG

Owing to the distinct electronic and transport properties for graphene samples with different number of stacked layers, we also analyze the influence of the number of layers on the wave packet propagation with different pseudospin polarization, as well as we will verify which are the main ZBW features observed in NLG. We consider in the current section the BLG case and TLG will be investigated in next Sec. 4.3.4.

The wave function is obtained by taking $n = 2$ in Eqs. (4.13a) and (4.13b) and combining them with Eq. (4.12). Once the wave function evolves in time, its (x, y) position expectation values are calculated using Eq. (4.15).

4.3.3.1 $C_1 = 1$ and $C_2 = 0$

For $(C_1\ C_2)^T = (1\ 0)^T$, the wave packet moves in positive x-axis direction and splits in two parts moving along y axis with opposite velocities, Fig. 4.4(a). As can be seen from the Fig. 4.4(a), the total probability density $\rho(x, y, t)$ obeys the following symmetry

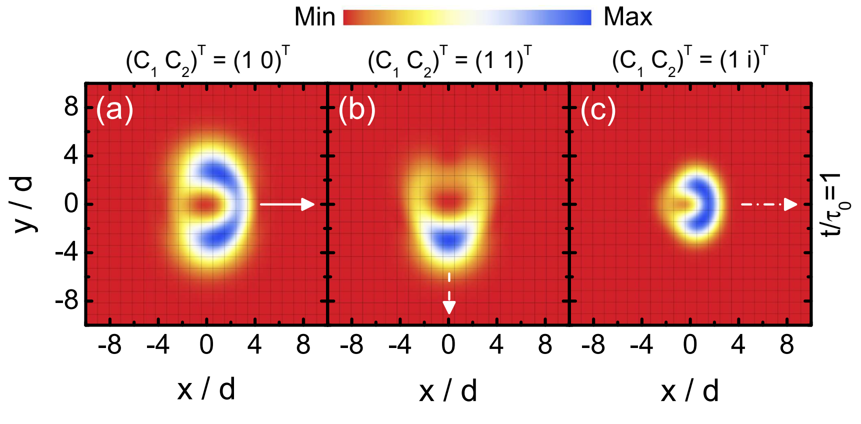

Figure 4.4: (Color online) The same as in Fig. 4.2, but now for BLG and just $t/\tau_0 = 1$.

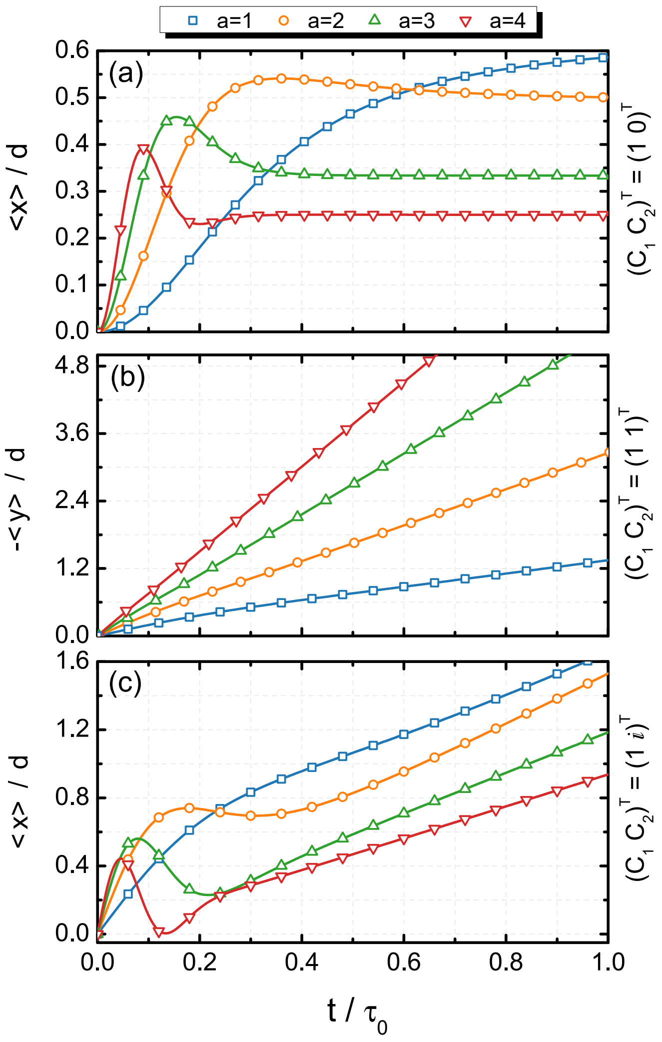

Figure 4.5: (Color online) The same as in Fig. 4.3, but now for BLG case with $\tau_0 = \gamma_\perp d^2/\hbar v_F^2$.

(asymmetry): $\rho(x,y,t) = \rho(x,-y,t)$ $(\rho(x,y,t) \neq \rho(-x,y,t))$. Therefore, the coordinate x exhibits ZBW. These results are analogous to those in the MLG case (see Sec. 4.3.2), but with a slightly different deformation shape of the propagated wave function, as illustrated in Fig. 4.4.

Equation (4.15) allows us to write the quantities $\langle x\rangle$ and $\langle y\rangle$ for BLG as

$$\langle x(t)\rangle = d\left[\frac{1-e^{-a^2}}{a} - 2e^{-a^2}\int_0^\infty e^{-q^2}\cos\left(2q^2t'\right) I_1(2aq)\, dq\right], \tag{4.32}$$

$\langle y(t)\rangle = 0$, being very similar to the MLG case with the same initial pseudo spin. The analytical (SOT) results for $\langle x(t)\rangle$ are illustrated by solid curves (symbols) in Fig. 4.5(a). As shown in Fig. 4.5(a), ZBW has a transient character that is attenuated by an exponential term e^{-q^2} in Eq. (4.32) and, after the oscillations disappear, $\langle x(t)\rangle/d$ converges to the value of the first term that is time-independent. Unlike the MLG case, Fig. 4.3(a), the ZBW frequency for BLG is less affected by increasing a.

4.3.3.2 $C_1 = 1$ and $C_2 = 1$

The total probability density for $(C_1\ C_2)^T = (1\ 1)^T$, Fig. 4.4(b), obeys the symmetry (asymmetry) relation $\rho(x, y, t) = \rho(-x, y, t)$ ($\rho(x, y, t) \neq \rho(x, -y, t)$). Consequently, the y coordinate is the one that is expected to manifest the ZBW effect. What stands out for this case, is that the wave packet moves along the negative $y-$direction, unlike the MLG case for $(1\ 1)^T$, and does not split into two parts. Its spatial distribution shape and the preferred one-directional propagation (y), Fig. 4.4(b), seems to be similar to MLG case with pseudospin $(1\ i)^T$, except by the reverse y orientation.

Expectation values of the position (x, y) were obtained in a similar manner as described before and are given by $\langle x(t)\rangle = 0$ and

$$\begin{aligned}\langle y(t)\rangle = &-ae^{-a^2}\int_0^\infty e^{-q^2}\left[q\sin\left(2q^2t'\right) {}_0F_1\left[3, a^2q^2\right]\right]dq \\ &- 4e^{-a^2}t'\int_0^\infty e^{-q^2}\left[q^2 I_1(2aq) + \frac{q}{a}I_2(2aq)\right]dq,\end{aligned} \tag{4.33}$$

where ${}_0F_1[a, z]$ in Eq. (4.33) is the confluent hypergeometric function. Solid curves (symbols) in Fig. 4.5(b) represent analytical (SOT) results for $\langle y(t)\rangle$. As for the MLG case with pseudospin $(1\ i)^T$ (see Fig. 4.3(b)), the average position y in the present BLG case exhibits a linear time-dependence with a high group velocity as larger is the a parameter without significant oscillations. It means that ZBW is absent, such that the wave packet in BLG with pseudospin $(1\ 1)^T$ shows to be the appropriated choice in order to investigate transport properties by wave packet dynamics in BLG-based systems within the low-energy approximation described by the two-band model Eq. (4.3).

4.3.3.3 $C_1 = 1$ and $C_2 = i$

Assuming $(C_1\ C_2)^T = (1\ i)^T$, for $t > 0$, the wave packet splits into two parts that moves along the y-axis in opposite directions, Fig. 4.4(c). These two propagating subpackets with the same probability densities and widths lead to a null average position $\langle y\rangle$ and null expectation value of velocity $\langle v_y\rangle$. As shown in Fig. 4.4(c), the probability density $\rho(\boldsymbol{r}, t)$ is symmetric (asymmetric) with respect to y (x) axis. Due to the lack of mirror symmetry with respect to $x = 0$ axis, the wave packet exhibits ZBW along the coordinate x, as we had already predicted in Table 4.1. It is interesting to note that, if the initial direction of pseudospin coincides with the average momentum k_0^y, for BLG, there is no motion of the wave packet in the y-direction, as would be the case for MLG, Sec. 4.3.2.3, but only in the x-direction.

By analytically calculating the average value of x and y for this polarization, it leads to

$$\begin{aligned}\langle x(t)\rangle = de^{-a^2}\int_0^\infty & e^{-q^2}\left\{\left[-2\sin\left(2q^nt'\right)\right.\right. \\ &\left.\left.\cdot\left(-2I_1(2aq) + \frac{2I_2(2aq)}{aq}\right) + \frac{8qtI_2(2aq)}{a}\right]\right\}dq\ ,\end{aligned} \tag{4.34}$$

and $\langle y(t)\rangle = 0$. The analytical Green's function based results, obtained by Eq. (4.34), are compared to those calculated via SOT within the Dirac model for different parameters a, as shown in Fig. 4.5(c). As can be seen in Fig. 4.5(c), there are very similar behaviors with those from MLG case with $(C_1\ C_2)^T = (1\ 1)^T$, Fig. 4.3(c), that is: (i) a transient character of the ZBW, (ii) the x average position is the one that oscillates, (iii) the ZBW amplitude and frequency are directly related to the wave packet width or initial wave vector, such that as higher the parameter a, smaller is the oscillation period, vanishing the oscillations faster in time and converging the group velocity v_x to a constant non-zero value.

4.3.4 ZBW in TLG

As the last example of our investigations on ZBW in NLG, we studied the dynamics of wave packet in ABC-stacked TLG, as illustrated in Fig. 4.1. Expectation values of x and y coordinates as a function of time are obtained with the same analytical and numerical methods used so far, therefore, details of these calculations for TLG will be omitted.

Assuming $(C_1\ C_2)^T = (1\ 0)^T$, one obtains

$$\langle x(t)\rangle = 3d\left(\frac{1-e^{-a^2}}{2a}\right) - 3de^{-a^2}\int_0^\infty e^{-q^2}\cos\left(2q^3t'\right)I_1\left(2aq\right)dq, \tag{4.35}$$

and $\langle y(t)\rangle = 0$. The probability density and a comparison between the analytical results, Eq. (4.35), and those from SOT within the Dirac model, are represented in Fig. 4.6(a) and Fig. 4.7(a), respectively, for different parameters a as a function of time. As a increases, Fig. 4.7(a), the ZBW becomes more evident, although still exhibiting a transient character, as in the previous MLG and BLG cases. On the other hand, for the pseudospin configuration $(C_1\ C_2)^T = (1\ 1)^T$ the results for expectation value of the position of the

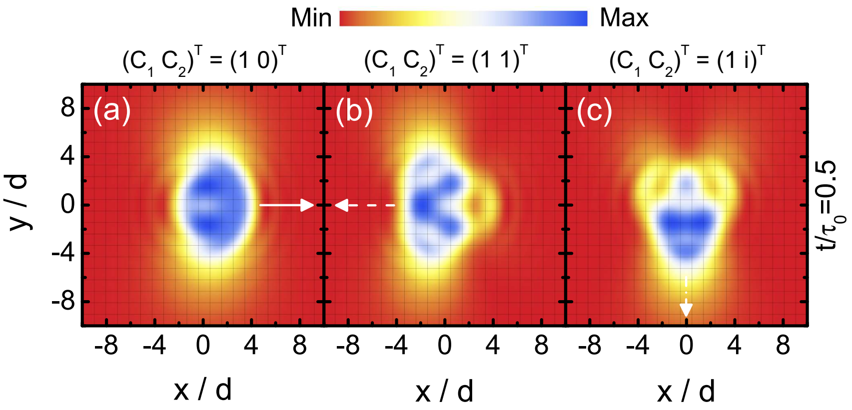

Figure 4.6: (Color online) The same as in Fig. 4.2, but now for TLG at $t/\tau_0 = 0.5$.

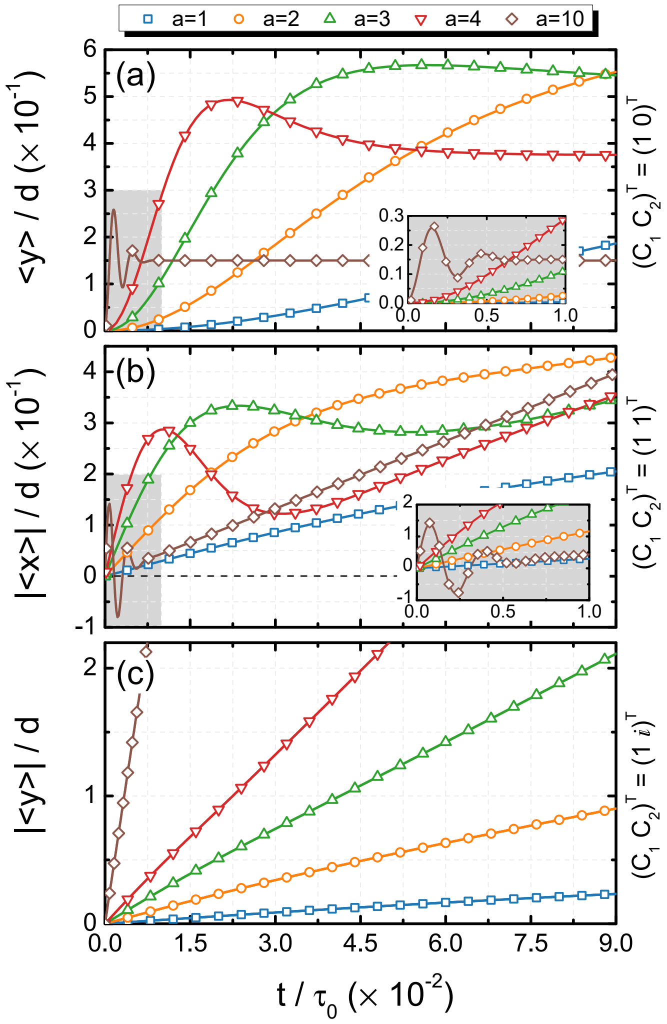

Figure 4.7: (Color online) The same as in Fig. 4.3, but now for TLG with $\tau_0 = \gamma_\perp^2 d^3/\hbar^2 v_F^3$ and including the result for $a = 10$ with $k_0^y = 0.1$ Å^{-1}. The insets in panels (a) and (b) show magnification of the gray shaded areas for better visualization at small t/τ_0 values.

wave packet are given by

$$\langle x\,(t)\rangle = -\frac{3de^{-a^2}}{2a^2}\int_0^\infty \frac{e^{-q^2}}{q^2}\left\{6aq^4 I_3(2aq)t \right.$$
$$\left. + \left[\left(2a^2q^2+6\right)I_2(2aq) - 3aqI_1(2aq)\right]\sin\left(2q^3t\right)\right\}dq \tag{4.36}$$

and $\langle y\,(t)\rangle = 0$. Figure 4.7(b) shows $\langle x\,(t)\rangle$, Eq. (4.36), and the SOT results calculated within the Dirac model. As we can be seen in Fig. 4.7(b) and its inset with an enlargement for small time steps, after the transient oscillatory behaviour, $|\langle x\rangle|$ increases linearly with time converging to a non-null constant group velocity v_x in a similar way as observed for MLG case with pseudospin $(1\ 1)^T$ (see Fig. 4.3(b)) and for BLG case with pseudospin $(1\ i)^T$ (see Fig. 4.5(c)). The probability density is illustrated in Fig. 4.6(b) and shows that the direction of propagation of the wave packet is in accordance with Eq. (4.36).

Finally, for the pseudospinor $(1\ i)^T$ the expectation values of the position operator are

$\langle x \rangle = 0$ and

$$\langle y \rangle = \frac{-3e^{-a^2}}{2a^2} \int_0^\infty \frac{e^{-q^2}}{q} \left(4q^2 t \left(a^2 q^2 + 3\right) I_2(2aq) \right. \\ \left. -6aq^3 t I_1(2aq) + 3aI_3(2aq) \sin\left(2q^3 t\right)\right) dq. \tag{4.37}$$

Figure 4.7(c) provides a comparison between the analytical results, obtained numerically from Eq. (4.37), with those obtained by the SOT within the Dirac model. This results shows to be analogous to the MLG case for $(C_1\ C_2)^T = (1\ i)^T$ and BLG case for $(C_1\ C_2)^T = (1\ 1)^T$, where (i) ZBW is absent; and (ii) as a increases, $\langle y \rangle / d$ also increases linearly with time without visible oscillations and with a non-null constant group velocity along $y-$direction. The total probability density, that is in agreement with the results presented in Tab. 4.1, is shown in Fig. 4.6(c).

4.3.5 Influence of the number of graphene layers on wave packet dynamics

As observed in Secs. 4.3.2, 4.3.3 and 4.3.4, for different pseudospin polarization $(C_1\ C_2)^T = (1\ 1)^T$ and $(C_1\ C_2)^T = (1\ i)^T$, the wave packet exhibits different propagation directions for MLG, BLG and TLG (for more details, see Appendix C.4). Figure 4.8 illustrates these three situations. In fact, such change in propagation direction is expected as n increases, since the low-energy Hamiltonian for ABC-NLG has Pauli matrices σ_x and σ_y multiplying both k_x and k_y for $n \geq 2$, unlike the MLG case. For example, for BLG, $H_{BLG} = \hbar^2 v_F^2 \gamma_\perp^{-1} \left[\left(k_x^2 - k_y^2\right) \sigma_x + 2k_x k_y \sigma_y\right]$. Consequently, the velocity components in $x-$ and $y-$directions, calculated according to the steps in Sec. 4.3.1, are expected to be proportional to $2\hbar v_F^2 \gamma_\perp^{-1} k_y \langle \sigma_y \rangle$ and $-\hbar v_F^2 \gamma_\perp^{-1} k_y \langle \sigma_x \rangle$, respectively, where we already took into account that the wave packet momentum in Eq. (4.11a) has only a component in the y-direction, i.e. $k_x \equiv 0$. As for TLG, the same procedure leads to velocity components in $x-$ and $y-$directions proportional to $-3\hbar^2 v_F^3 \gamma_\perp^{-2} k_y^2 \langle \sigma_x \rangle$ and $-\hbar^2 v_F^3 \gamma_\perp^{-2} k_y^2 \langle \sigma_y \rangle$, respectively. Thus, for a given initial pseudospin orientation, these expressions help to qualitatively predict the observed changes in propagation direction and the increasing propagation velocity as the number of layers increases, whereas the detailed behavior of the wave packet dynamics and its ZBW requires the more sophisticated approaches described in the previous Sections. Moreover, by comparing the transient duration time (t^d) in Figs. 4.3, 4.5 and 4.7, carefully taking into account the corresponding value of $\tau_0 = \gamma_\perp^{n-1} d^n / \hbar^{n-1} v_F^n$ for each case which becomes a larger value for large n, and the wave packet evolution in Figs. 4.2, 4.4 and 4.6 for MLG, BLG and TLG, respectively, one realizes that as the number of layers increases, the propagating wave function spreads slower for a certain fixed time range, that in turn leads to greater time scales for the transient behavior, i.e. $t^d_{N=3} > t^d_{N=2} > t^d_{N=1}$. Note that the group velocity increases when the number of layers also increases, but the wave packet takes longer to spread out spatially to large n.

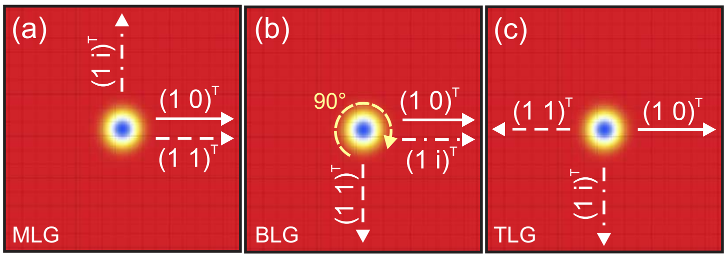

Figure 4.8: (Color online) Representation of the different directions of propagation of the Gaussian wave packet according to the choice of initial pseudospinor for (a) MLG, b) bilayer and c) trilayer graphene, obtained from Eq. (4.12). The solid, dashed and dash-dotted white curves represent the initial pseudospinor defined as $(C_1\ C_2)^T = (1\ 0)^T$, $(C_1\ C_2) = (1\ 1)^T$ and $(C_1\ C_2) = (1\ i)^T$, respectively. The long-dashed circle in (b) indicates that when one includes one more layer the direction of propagation of the wave packet motion rotates by 90° for the pseudospinor $(1\ 1)^T$ and $(1\ i)^T$.

Concerning the wave packet propagation in multi-layer graphene case and the validity of the two-band model adopted here [Eq. (4.3)], it is also important to mention that, for a fixed momentum and $|ka_0| \gtrsim 0.5$, by increasing the number of graphene layers also increases the percentage error between the 2×2 and the full model, as shown in Fig. 4.1(d). On the other hand, for a fixed momentum and $|ka_0| \lesssim 0.5$, the error remains unchanged.

4.3.6 Dirac valley selection for wave packet dynamics

The choice of the propagation direction in real space also depends on which Dirac valley the initial wave packet is taken, since the k_x^D and k_y^D directions in the Dirac model are rotated with respect to the k_x^{TB} and k_y^{TB} tight-binding directions via the standard 2D rotation matrix:

$$\begin{pmatrix} k_x^D \\ k_y^D \end{pmatrix} = \begin{pmatrix} \cos\theta & -\sin\theta \\ \sin\theta & \cos\theta \end{pmatrix} \begin{pmatrix} k_x^{TB} \\ k_y^{TB} \end{pmatrix}, \tag{4.38}$$

with $\theta = \pi/2$, $7\pi/6$, and $11\pi/6$ [$\theta = \pi/6$, $5\pi/6$, and $3\pi/2$] for K (K') Dirac valleys of the first Brillouin zone. In addition, since in our analysis the time-reversal symmetry is preserved, then $H(\boldsymbol{k}) = H(-\boldsymbol{k})^*$ and the low-energy bands are doubly degenerate. As a consequence, all results obtained along this chapter for K Dirac valley can be easily mapped into the K' valley by just rotating the reciprocal space vectors according to Eq. (4.38).

4.4 Conclusions of the chapter

A comprehensive study of the quantum dynamics of charged particles represented by a 2D Gaussian wave packet in multilayer graphene has been presented. Using the Green's function method, we obtained generalized analytical expressions for the time dependence of the wave functions in ABC-stacked NLG that allowed us to calculate the average values of position operators for an arbitrary number of graphene layers n.

A semi-analytical method, which allows one to calculate wave packet scattering by arbitrary potential profiles is proposed. The method is based on the well-known SOT, adapted here for the 2×2 Dirac approximation for the multi-layer graphene Hamiltonian. Analytical results for the expectation values of the position of the center of the wave packet show perfect agreement with those from the SOT within the Dirac approximation, for all cases of initial pseudospin orientation investigated here. This consolidates the methods proposed here, which are suitable for large graphene samples with any number of ABC-stacked layers (in contrast to tight-binding models, where the computational cost rapidly increases with the number of atoms), as very useful tools for continuum model investigations of transport properties in multilayer graphene.

As examples, the proposed methods here are applied to the study of the dynamics of wave packets in ABC-stacked MLG, BLG and TLG, with different pseudospin polarization. Our results demonstrate how ZBW depends on the number of graphene layers. Wave packets with the same pseudospin orientation in MLG, BLG and TLG are shown to propagate in different directions and with different velocities. ZBW is shown to be minimized as the pseudospin orientation is taken the same as the wave packet momentum. For the parameters considered in this chapter, when both the pseudospin and momentum are oriented along the y-direction (i.e. assuming $\langle \sigma_y \rangle \neq 0$, $(C_1 \; C_2)^T = (1 \; i)^T$, $p_{0y} \neq 0$ and $k_x \equiv 0$), the wave packet position is approximately a linear function of time, propagating along the $+y$-, $+x$- and $-y$-directions for MLG, BLG, and TLG, respectively. The ZBW phenomena in multilayer graphene displays a transient behavior, i.e. the oscillations of the physical observables decay with time and a natural damping is observed. Our results show that the transient behavior time t^d is of the order of dozens of femtoseconds and the larger the number of layers the longer the transient time, i.e. $t^d_N > t^d_{N-1}$. Therefore, multilayer graphene system could be an experimental platform to experimentally probe ZBW oscillations, since its transient duration time becomes longer the larger the n value. At the experimental point-of-view, the amplitude of the oscillations should depend very strongly on the duration of the applied pulse, whereas the duration time of the total damping is due to the light emission time scale. The latter condition is owing to the fact that the electron oscillations give rise to a time-dependent dipole moment which will be a source of electric field and it will emit or absorb radiation in the far infrared range [43, 226, 227].

5

Zitterbewegung of moiré excitons in twisted MoS_2/WSe_2 hetero-bilayers

The moiré pattern observed in stacked non-commensurate crystal lattices, such as hetero-bilayers of transition metal dichalcogenides, produces a periodic modulation of their bandgap. Excitons subjected to this potential landscape exhibit a band structure that gives rise to a quasi-particle dubbed moiré exciton. In the case of MoS_2/WSe_2 hetero-bilayers, the moiré trapping potential has honeycomb symmetry and, consequently, the moiré exciton band structure is the same as that of a Dirac-Weyl fermion, whose mass can be further tuned down to zero with a perpendicularly applied field.

In this chapter, it is shown that, analogously to other Dirac-like particles, moiré exciton exhibits a trembling motion, also known as *zitterbewegung*, whose long timescales are compatible with current experimental techniques for exciton dynamics. This promotes the study of the dynamics of moiré excitons in van der Waals heterostructures as an advantageous solid-state platform to probe *zitterbewegung*, broadly tunable by gating and inter-layer twist angle.

The study on *zitterbewegung of moiré excitons in twisted* MoS_2/WSe_2 *hetero-bilayers*, developed in this chapter, has been accepted on the Physical Review Letters and an arXiv version can be accessed through this link.

5.1 Motivation

As discussed in Chap. 4, *zitterbewegung* (ZBW) is a fast trembling motion of elementary particles that obey the Dirac equation [25], predicted by Erwin Schrödinger in 1930 for relativistic fermions [23].

Since the Dirac equation predicts ZBW with amplitude of the order of the Compton wavelength (10^{-2} Å) and a frequency of $\omega_{ZB} \approx 10^{21}$ Hz, which are not accessible with current experimental techniques [226], a direct experimental observation of this effect is challenging. Since the characteristic frequency of ZBW is determined by the energy gap between the (pseudo-)spin states [30], designing a system where the gap in the Dirac cone

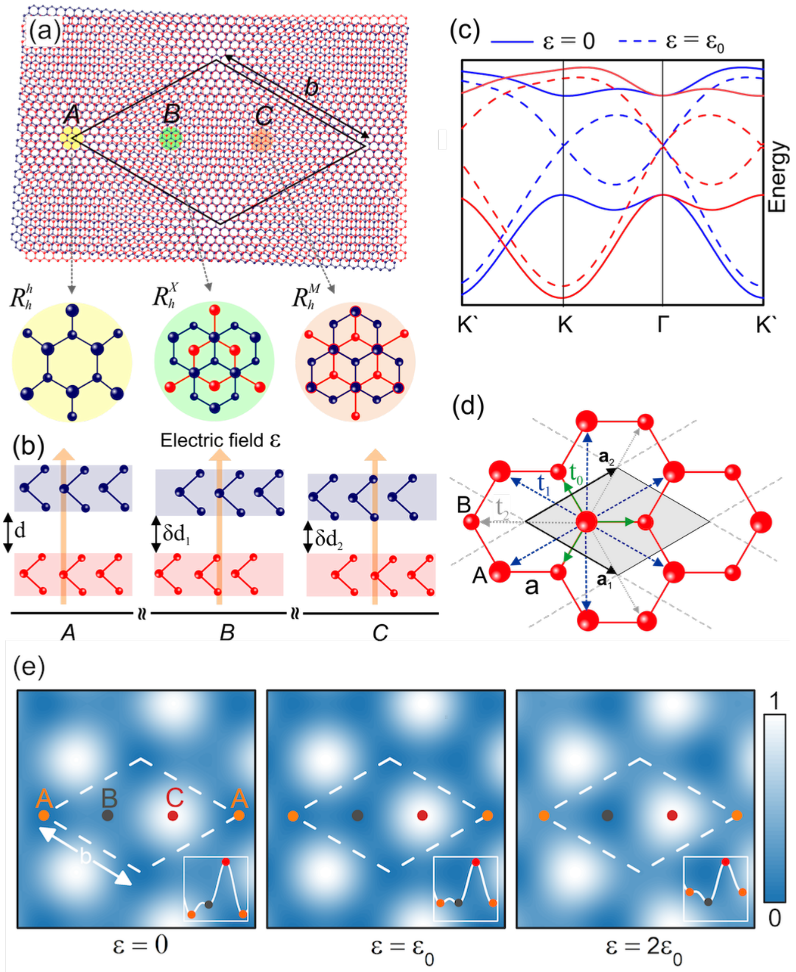

Figure 5.1: (a) Moiré pattern with period b in an MoS$_2$/WSe$_2$ hetero-bilayer, twisted by 3°. Black diamond represents the supercell. Insets magnify three characteristic locations (A, B and C), where atomic registries resemble lattice-matched bilayers of different R-type stacking. (b) Lateral view of the inter-layer distance of the regions A, B and C (for more details, see Ref. [53]). (c) Corresponding band structures, calculated with the tight-binding model, for the first moiré Brillouin zone with (dashed lines) and without (solid lines) an applied electric field $\varepsilon = \varepsilon_0 \approx 0.44$ V/nm) for the K (red) and K' (blue) valleys of the crystal. (d) Representation of a honeycomb lattice structure and unit cell (gray region) where sub-lattice sites A and B correspond to the respective stacking registries labelled in (a), and with lattice constant a. First, second and third nearest-neighbors hopping parameters are represented by t_0 (green arrows), t_1 (blue arrows) and t_2 (gray arrows), respectively. $\boldsymbol{a}_1$ and $\boldsymbol{a}_2$ are the basis vectors. (e) Colormap of the ILE potential landscape in R-type MoS$_2$/WSe$_2$, as illustrated in (a), where the excitonic potential is tuned by an applied perpendicular electric field ε. The inset in each panel shows the potential profile along the high symmetry points (A-B-C-A) of the moiré supercell. For $\varepsilon = \varepsilon_0$, the excitonic potential exhibits the same value at regions A and B, whereas for $\varepsilon = 2\varepsilon_0$ ($\varepsilon = 0$), A (B) becomes higher in energy than B (A).

can be controlled at will is fundamental for optimization of the oscillation frequency and eventual experimental detection of this phenomenon.

Most recently, advances in the isolation of monolayer semiconductors and their stacking as van der Waals heterostructures (vdWhs) opened a new field of study of artificial 2D hybrid materials [50, 51]. Combining two monolayers of semiconducting transition-metal dichalcogenides (TMDs) in a vdWhs with an inter-layer twist introduces an in-plane moiré pattern [52], as illustrated in Fig. 5.1(a). This pattern is associated with an in-plane modulation of the conduction and valence band edges, thus presenting new possibilities to engineer the electronic band structure, quasi-particle confinement, and optical properties of the system. Especially, inter-layer excitons (ILE) are profoundly affected by the moiré pattern, which creates regions in space where the ILE energy is significantly lower. For MoS_2/WSe_2 vdWhs with small twist angle (R-type stacking), lowest energy regions are those with stacking registry R_h^h and R_h^X, represented by A and B in Fig. 5.1(a). These regions form a honeycomb superlattice for excitonic confinement, thus leading to a moiré exciton band structure that resembles the one of gapped monolayer graphene. Different inter-layer distances for R_h^h and R_h^X, as illustrated in Fig. 5.1(b), lead to different ILE dipole moments in each region. Consequently, a perpendicularly applied electric field ε can be used to tune the energies of A and B ILE sub-lattices, thus making them equal at $\varepsilon = \varepsilon_0 \approx 0.44$ V/nm.[53] In this case, the moiré exciton band structure acquires a massless Dirac fermion character, as illustrated in Fig. 5.1(c). The combination of the long lifetime and bright luminescence [53] of ILE, along with their Dirac-like dispersion tunable by the twist angle and applied fields, makes twisted vdWhs a strong candidate for experimental detection of ZBW of moiré excitons.

In this chapter, we analyze the dynamics of moiré exciton wave packets as an opto-electronics-based platform to probe ZBW, as an alternative to the previous proposals, mostly based on low-energy electrons in graphene or on ultra-cold atoms (see chapter 4 for more details). To do so, we apply the time-evolution operator [228, 230] on a wave packet distribution representing a moiré exciton in twisted MoS_2/WSe_2 vdWhs. We discuss the effects of the wave packet parameters, such as its pseudospinor and width, as well as of an applied electric field and different twist angles, on the ZBW amplitude and time evolution of the exciton probability density distribution. The optimization of parameters proposed here may guide future experiments towards the experimental observation of ZBW of such neutral quasi-particles in this vdWhs, which represents an important advance in the understanding not only of this phenomenon, but also of the tunable Dirac-like character of the moiré exciton.

5.2 Tight-binding approach for excitons in a potential landscape

ILEs in a twisted hetero-bilayer experience a periodic potential of the form [53]

$$V(\boldsymbol{r}) = E_g(\boldsymbol{r}_0(\boldsymbol{r})) + e\varepsilon d(\boldsymbol{r}_0(\boldsymbol{r})) - E_b \ , \tag{5.1}$$

where d is the inter-layer distance and E_g the ILE bandgap, both modulated along the plane due to the moiré pattern (see Fig. 5.1), and ε is a perpendicularly applied electric field. Here, $\boldsymbol{r}_0$ is the in-plane displacement vector from a metal site in the hole layer to a nearest-neighbor metal site in the electron layer, depending on the location $\boldsymbol{r}$ in the moiré pattern. The binding energy E_b, on the other hand, is not expected to be significantly dependent on the local potentials [53] and is, therefore, assumed to be constant.

Excitons in such a potential landscape would be trapped at their local minima and exhibit a non-zero (complex) hopping to the neighboring minima. In a twisted MoS_2/WSe_2 bilayer, this landscape of energy minima has a honeycomb symmetry, with A (R_h^h) and B (R_h^X) sub-lattices at slightly different energies, $+\delta$ and $-\delta$, respectively. A low-energy quasi-particle - in this case, an exciton - in such a landscape would behave as a non-zero mass Dirac-Weyl fermion, whose Hamiltonian, within third-nearest neighbors approach, reads [53, 237]

$$H_{mex} = \begin{pmatrix} \delta - t_A F(\boldsymbol{k}) & t_0 Z_0(\boldsymbol{k}) + t_2 Z_2(\boldsymbol{k}) \\ t_0 Z_0^*(\boldsymbol{k}) + t_2 Z_2^*(\boldsymbol{k}) & -\delta - t_B F(\boldsymbol{k}) \end{pmatrix} , \tag{5.2}$$

where $t_{A(B)}$ is the hopping between nearest-neighbors minima of the A and B sub-lattices (see appendix D) that compose the honeycomb moiré potential, t_0 and t_2 are hopping parameters between first and third nearest-neighbors, see Fig. 5.1(d), and structure factors are given by

$$\begin{aligned} F(\boldsymbol{k}) &= 2\cos\left[\boldsymbol{k}\cdot(\boldsymbol{a_1}-\boldsymbol{a_2}) - \theta_s\right] + \\ &\qquad 2\left[\cos(\boldsymbol{k}\cdot\boldsymbol{a_1}+\theta_s) + \cos(\boldsymbol{k}\cdot\boldsymbol{a_2}-\theta_s)\right], \\ Z_0(\boldsymbol{k}) &= 1 + e^{-i(\boldsymbol{k}\cdot\boldsymbol{a_1}+\theta_s)} + e^{-i(\boldsymbol{k}\cdot\boldsymbol{a_2}-\theta_s)}, \\ Z_2(\boldsymbol{k}) &= e^{-i\boldsymbol{k}\cdot(\boldsymbol{a_1}+\boldsymbol{a_2})} + 2\cos\left[\boldsymbol{k}\cdot(\boldsymbol{a_1}-\boldsymbol{a_2}) + \theta_s\right], \end{aligned}$$

where $\theta_s = 4\pi s/3$ originates from the complex part of the hopping parameters of the moiré exciton [53] with spin sign $s = \pm 1$.

Diagonalization of H_{mex} leads to the moiré exciton band structure

$$E_{\pm} = -t_+ F(\boldsymbol{k}) \pm \sqrt{|t_0 Z_0(\boldsymbol{k}) + t_2 Z_2(\boldsymbol{k})|^2 + (t_- F(\boldsymbol{k}) - \delta)^2} \ , \tag{5.3}$$

where $t_{\pm} = (t_A \pm t_B)/2$. An example of such a band structure is shown in Fig. 5.1(c). In the absence of external field, since the energies of sub-lattices A and B are different (see left panel in Fig. 5.1(e)), $\delta \neq 0$ and the moiré exciton band structure exhibits a gap, as illustrated by solid lines in Fig. 5.1(c). However, as the applied field ε increases, the sub-lattices become similar in energy and δ approaches zero as the field reaches a critical value ε_0, which is 0.44 V/nm for the vdWhs considered here (see middle panel in Fig. 5.1(e)). In this case, the dashed lines in Fig. 5.1(c) exhibit a gapless Dirac-like band structure for the moiré exciton in the vicinity of the Γ-point of the moiré Brillouin zone, which corresponds to either the K or K' points of the crystal Brillouin zone. Different colors in Fig. 5.1(c) stand for the excitonic band structures of the two possible exciton spins, up or down for $s = +$ (red) or $s = -$ (blue), respectively. Due to the spin-valley locking, the spin-valley index s also corresponds to a moiré exciton at the **K** (**K'**) valley for $s = +$ $(-)$ in the considered case of R-type stacking registry. As we will consider only large moiré exciton wave packets centered at Γ, where the bands for the two different spins are similar, spins are not expected to play a significant role in this study.

5.3 Wave-packet dynamics

Writing the Hamiltonian as $H = \boldsymbol{\alpha} \cdot \boldsymbol{\sigma}$, where $\boldsymbol{\sigma}$ are the Pauli matrices, allows one to easily apply the time-evolution operator in an exact form as a simple matrix multiplication [42, 228, 230]. Therefore, it is convenient to re-write Eq. (5.2) as

$$H_{mex} = \boldsymbol{\alpha}(\boldsymbol{k}) \cdot \boldsymbol{\sigma} - t_+ F(\boldsymbol{k}) \mathbb{1} \ , \tag{5.4}$$

where $\mathbb{1}$ is the identity matrix and $\boldsymbol{\alpha} = (\alpha_x(\boldsymbol{k}), -\alpha_y(\boldsymbol{k}), \alpha_z(\boldsymbol{k}))$ with its components given by

$$\begin{aligned} \alpha_x(\boldsymbol{k}) = {} & [1 + \cos(\theta_s + \boldsymbol{k} \cdot \boldsymbol{a}_1) + \cos(\theta_s - \boldsymbol{k} \cdot \boldsymbol{a}_2)] t_0 \\ & + \{\cos\left[(\boldsymbol{a}_1 + \boldsymbol{a}_2) \cdot \boldsymbol{k}\right] + 2\cos\left[\theta_s + (\boldsymbol{a}_1 - \boldsymbol{a}_2) \cdot \boldsymbol{k}\right]\} \, t_2, \end{aligned} \tag{5.5a}$$

$$\alpha_y(\boldsymbol{k}) = [\sin(\theta_s + \boldsymbol{k} \cdot \boldsymbol{a_1}) - \sin(\theta_s - \boldsymbol{k} \cdot \boldsymbol{a_2})] t_0 + \sin\left[(\boldsymbol{a_1} + \boldsymbol{a_2}) \cdot \boldsymbol{k}\right] t_2 \ , \tag{5.5b}$$

and

$$\alpha_z(\boldsymbol{k}) = \delta - t_- F(\boldsymbol{k}) \ . \tag{5.5c}$$

Since H_{mex} does not explicitly depend on time and $[\boldsymbol{\alpha} \cdot \boldsymbol{\sigma}, -t_+ F(\boldsymbol{k}) \mathbb{1}] = 0$, the time-evolution operator for the Hamiltonian defined in Eq. (5.4) is given by

$$e^{-\frac{i}{\hbar} H_{mex} \Delta t} = e^{-i \boldsymbol{\beta} \cdot \boldsymbol{\sigma}} e^{-\frac{i}{\hbar} (-t_+ F(\boldsymbol{k}) \mathbb{1}) \Delta t} \ , \tag{5.6}$$

where $\boldsymbol{\beta} = \boldsymbol{\alpha} \Delta t / \hbar$.

From the well known properties of the Pauli matrices, the first exponential on the right hand-side of Eq. (5.6) yields

$$e^{-i \boldsymbol{\beta} \cdot \boldsymbol{\sigma}} = \cos(\beta) \, \mathbb{1} - \frac{i \sin(\beta)}{\beta} \begin{pmatrix} \beta_z & \beta_x - i\beta_y \\ \beta_x + i\beta_y & \beta_z \end{pmatrix} = \mathcal{M} \ , \tag{5.7}$$

where $\beta = |\boldsymbol{\beta}|$, and the second exponential of Eq. (5.6) is equivalent to

$$e^{\frac{i}{\hbar}(t_+ F(\boldsymbol{k})\mathbb{1}\Delta t)} = \mathbb{1}e^{\frac{i}{\hbar}(t_+ F(\boldsymbol{k})\Delta t)} = \mathcal{N} \ . \tag{5.8}$$

Applying the time-evolution operator defined in Eq. (5.6) on the wave function $\Psi\left(\boldsymbol{r},t\right)$, one obtains the propagated wave function after a time step Δt as

$$\Psi\left(\boldsymbol{r},t+\Delta t\right) = e^{-\frac{i}{\hbar}H_{mex}\Delta t}\Psi\left(\boldsymbol{r},t\right) = \mathcal{M}\mathcal{N}\Psi\left(\boldsymbol{r},t\right) \ . \tag{5.9}$$

Note that $\mathcal{M}$ and $\mathcal{N}$ depend on the wave vector $\boldsymbol{k}$, therefore, the matrix multiplication with a general initial wave packet is conveniently computed numerically in reciprocal space by performing a Fourier transform on the wave function, which gives this method a flavor of a semi-analytical procedure. At $t = 0$, we assume the wave function as a circularly-symmetric 2D Gaussian wave packet with width d multiplied by the pseudospinor $[C_1\ C_2]^T$, such as

$$\Psi(\boldsymbol{r},t) = N\begin{pmatrix} C_1 \\ C_2 \end{pmatrix}\exp\left[-\frac{(x-x_0)^2-(y-y_0)^2}{d^2}\right], \tag{5.10}$$

where N is the normalization factor and (x_0, y_0) are the coordinates of the center of the Gaussian wave packet in real space. As the exciton is normally excited by a low-momentum photon, we assume a moiré exciton exactly at the Γ-point of the moiré Brillouin zone, i.e. with zero energy and zero momentum.

5.4 Wave packet dynamics and *zitterbewegung*

Figure 5.2 illustrates the average position $\langle x(t)\rangle$ and $\langle y(t)\rangle$ of the wave packet as a function of time for $d = 200$ Å (blue), 300 Å (orange) and $d = 500$ Å (green). Different pseudo-spin polarizations $[C_1\ C_2]^{\mathrm{T}} = [0\ 1]^{\mathrm{T}}$ and $[1\ 1]^{\mathrm{T}}$ are considered, with and without an applied electric field ε, as indicated on top of each panel. Results for $[1\ i]^{\mathrm{T}}$ are given in the Appendix D, along with the material parameters for the vdWhs studied here. The pseudo-spinor represents the occupation of the A and B sub-lattice sites, therefore, it is expected to be controlled in an actual experiment by the polarization of the excitation light, since the R_h^h and R_h^X regions, which correspond to the A and B sub-lattices here, exhibit different selection rules for circular light polarization [53]. For instance, a circular light polarization that excites ILE only in R_h^h (R_h^X) regions would effectively produces a moiré exciton wave packet with pseudo-spinor $[C_1\ C_2]^{\mathrm{T}} = [1\ 0]^{\mathrm{T}}$ ($[0\ 1]^{\mathrm{T}}$). As for the wave packet width, it could be controlled e.g. by the focus of the short-pulse excitation light, although actual precise manipulation and engineering of excitonic wave packets may be a challenging task [238]. Laser spots as narrow as ≈ 500 Å i.e. of the same order of magnitude as the wave packets considered here, have been used for the study of exciton dynamics in 2D semiconductors in recent experiments [239–242].

In the absence of an external applied electric field ($\varepsilon = 0$), both expectation values $\langle x(t)\rangle$ and $\langle y(t)\rangle$ exhibit ZBW, but with very low amplitude and high frequency, which

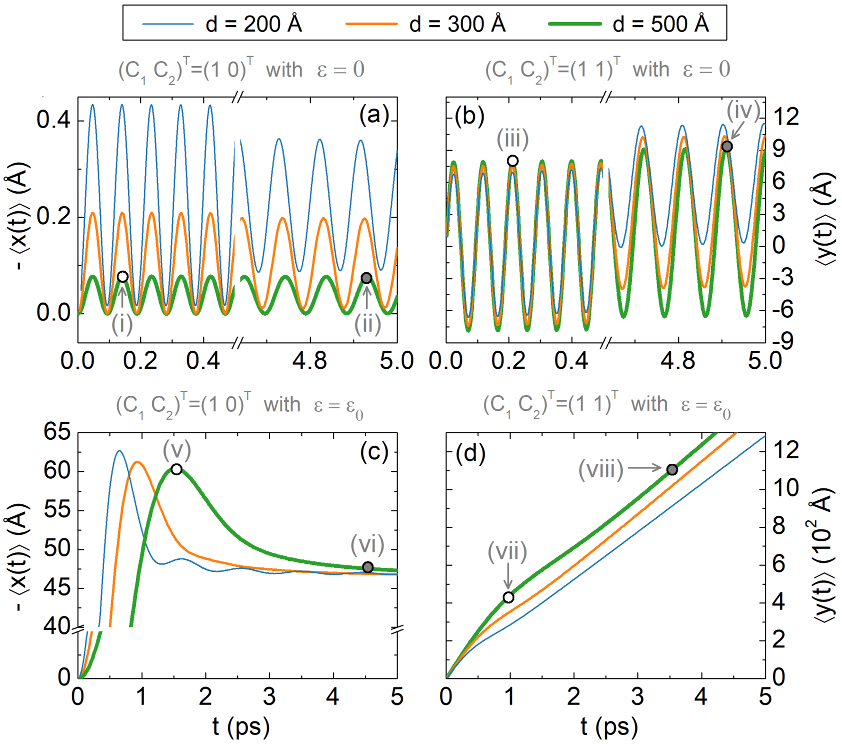

Figure 5.2: (Color online) ZBW of the expectation values of the position of a moiré exciton in a MoS_2/WSe_2 vdWhs, considering an initial Gaussian wave packet distribution with $d = 200$ Å (blue), $d = 300$ Å (orange) and $d = 500$ Å (green), and pseudo-spinors $[C_1\ C_2]^T = [1\ 0]^T$ and $[C_1\ C_2]^T = [1\ 1]^T$, under applied fields (a,b) $\varepsilon = 0$ and (c,d) $\varepsilon = \varepsilon_0$. The propagated probability densities for the time instants marked with white and gray circular dots in each panel are shown in Fig. 5.3.

hinders the actual observation of this effect. On the other hand, for $\varepsilon = \varepsilon_0$, where the gap is closed and moiré exciton effectively behaves as a massless Dirac quasi-particle, the wave packet moves only in one direction, exhibiting damped oscillations. For conciseness, Figs. 5.2 (c,d) show only the moving component of $\boldsymbol{r}$, see appendix D for the other component. In this case, the amplitude of the oscillation is much higher, of the order of tens of Å with a timescale of the order of few pico-seconds, which would make this effect clearly observable in actual experiments. Wave packets with smaller width exhibit weak oscillations, which vanish as the width increases. Nevertheless, for a $[1\ 0]^T$ spinor wave packet, a ≈ 60 Å peak, followed by a ≈ 50 Å permanent shift of the center of the wave packet, is observed for all values of wave-packet width considered here. For larger widths, the motion resembles the one of zero-energy electron wave packets in monolayer graphene [48, 243], since the wave packet becomes narrower around the Γ-point of the moiré Brillouin zone, where dispersion is approximately the same as in graphene. The dependence of the maximum displacement of the expectation value $\langle x(t) \rangle$ as a function of ϵ, as well as the time for this maximum displacement to occur, is discussed in the SM, where it is demonstrated that both the maximum wave packet displacement and its

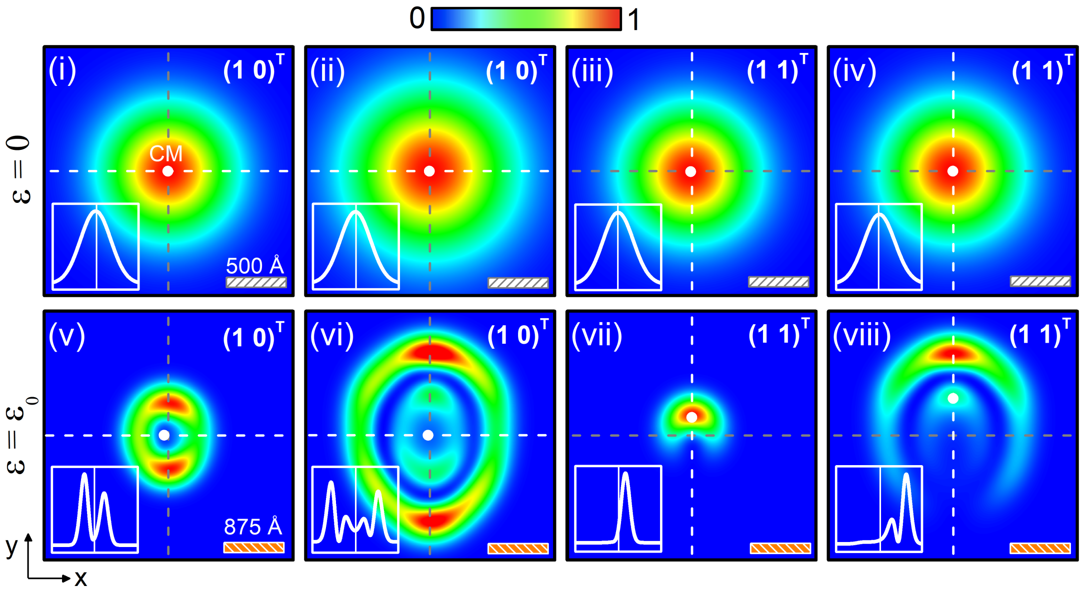

Figure 5.3: (Color online) Snapshots of the propagated probability density $|\Psi(\boldsymbol{r},t)|^2$ for an initial Gaussian wave packet with width $d = 500$ Å and pseudo-spinors $[1\ 0]^T$ and $[1\ 1]^T$. Top (bottom) row shows results for applied electric field $\varepsilon = 0$ ($\varepsilon = \varepsilon_0$). The white (orange) bar corresponds to 500 Å (875 Å) and the small white dot inside each panel represents the center-of-mass of the wave packet. The profiles of $|\Psi(\boldsymbol{r},t)|^2$ along the dashed white lines in each panel are shown as insets. The labels (i) to (viii) correspond to different time steps as marked with circular dots in Fig. 5.2.

timescale are highest at $\varepsilon = \varepsilon_0$.

As for a $[1\ 1]^T$ spinor wave packet, the center of mass is predicted to move almost linearly with time, travelling tens of Å in just a few picoseconds, before the exciton recombines.

The unique features predicted here for the moiré exciton wave packet dynamics can also be observed in the probability density distribution, as shown in Fig. 5.3. An initial Gaussian wave packet for the center-of-mass coordinate of a free exciton is expected to simply disperse across space as time elapses. Similar dispersion is observed e.g. in Refs. [239] and [241] for monolayer TMD. Notice, however, that the Gaussian packet in those experiments represented a density distribution of multiple excitons, rather than an actual single exciton wave function, so that phonon effects[244], which give rise to a halo in the exciton distribution, play an important role. In our case, in order to avoid such phonon hot-spots [244] and exciton-exciton interaction effects, one would have to employ low intensity exciting irradiation at low temperatures, so that the exciton distribution effectively matches the non-interacting excitons picture proposed here. In this case, the moiré exciton wave packet evolves as a double ring structure in the presence of an electric field with the critical value ε_0, whereas the usual dispersion is observed in the absence of field. The observation of this strikingly different wave packet dispersion in time in the presence of the applied field would thus represent a smoking gun evidence of the ZBW of moiré excitons and their Dirac-like nature.

5.5 Conclusion of the chapter

In summary, we argue that dynamics of a moiré exciton wave packet is an advantageous solid-state opto-electronic platform to probe ZBW, evasive in experiments to date. In MoS_2/WSe_2 vdWhs with small twist angles, the moiré pattern created by the interlayer lattice mismatch produces a periodic in-plane potential for the ILE center-of-mass and, consequently, a moiré exciton band structure. A moiré exciton wave packet in this system exhibits very fast and weak oscillations, hard to detect experimentally. However, in the presence of a perpendicular electric field, the gap of the moiré exciton band structure can be closed, which attributes the characteristics of a massless Dirac fermion to this quasi-particle, so ZBW becomes naturally more evident. In such a case, we reveal a shift of tens of Å in the center of the moiré exciton wave packet, along with damped oscillations with pico-second long periods. The exciton probability density profile is demonstrated to be strikingly different in the presence of gap-closing electric field, compared to the case without any field. The density profile and motion is also shown to be strongly dependent on the pseudo-spinor of the moiré exciton wave packet, which is controllable by the polarization of the incident exciting light. With relevant timescales being within reach of available experimental techniques, we expect to instigate the first experimental detection of ZBW in an exciton wave packet, which opens the gate to follow-up studies exploiting thereby proven massless Dirac fermion character of the moiré excitons in MoS_2/WSe_2 vdWhs induced by gating.

6

Graphene plasmonic

In this chapter, that supports the understanding of Chapters 7 and 8, the fundamentals tools to study graphene plasmonic are presented. First, it is introduced the basic ideas of the linear response theory (LRT), where the density-density graphene response is calculated. In a second moment, throughout the random phase approximation (RPA), the properties of graphene plasmons, also known as Dirac plasmons, are reviewed. Finally, the theory of surface plasmon-phonon polaritons in van der Waals heterostructures is briefly introduced.

This chapter is mainly based on the books *Quantum theory of the electron liquid, G. Giuliani and G. Vignale (2008)* and *An introduction to graphene plasmonics, P. A. D. Gonçalves and N. M. R. Peres (2016)*, references [16] and [17], respectively.

6.1 A brief introduction to the linear response theory

As the name suggest, within the LRT, the effects of an external perturbation are calculated to linear order. For example, all the experimental probes, such as electromagnetic fields in a typical SNOM experiment, as discussed at the introduction of this thesis, can be considered as small perturbations to the system and, consequently, these external excitation can be expressed in terms of a linear response function.

To present a general problem, the system considered here is described by a time-independent Hamiltonian $\hat{\mathcal{H}}_0$ and a time-dependent external field $F(t)$ coupled linearly to an observable $\hat{B}$ of the system. Thus, the full Hamiltonian is defined as

$$\hat{\mathcal{H}}_F(t) = \hat{\mathcal{H}}_0 + F(t)\hat{B}. \tag{6.1}$$

It is assumed that the external applied field vanishes at a time t_0, such that for $t \leq t_0$ the system is in the ground-state. As a consequence, the n-th eigenstate $|\psi_n\rangle$ of $\hat{\mathcal{H}}_0$ is populated with probability

$$P_n = \frac{e^{-\beta E_n}}{\mathcal{Z}} \ . \tag{6.2}$$

In Eq. (6.2), $\beta = (k_B T)^{-1}$, where T is the temperature and k_B is the Boltzmann's constant, while $\mathcal{Z} = \sum_n e^{-\beta E_n}$ is the canonical partition.

Now, to determine the effects of the external perturbation $F(t)$, a key assumption is that the time-dependent external field only affects the system weakly, which is needed to establish the initial thermal equilibrium. At $t = t_0$, the external field is turned on, and the time-evolution of the system, in the Schrödinger picture, is completely defined by the Schrödinger equation

$$i\hbar\frac{\partial}{\partial t}\left|\psi_n(t)\right\rangle = \hat{\mathcal{H}}_F(t)\left|\psi_n(t)\right\rangle, \tag{6.3}$$

with the initial condition at t_0 given by $|\psi_n(t_0)\rangle = |\psi_n\rangle$. The solution of this linear equation can be written as

$$\left|\psi_n(t)\right\rangle = \hat{U}(t,t_0)\left|\psi_n(t_0)\right\rangle, \tag{6.4}$$

where $\hat{U}(t,t_0)$ is the unitary time-evolution operator, which relates the state at time t to the state at time t_0. In the absence of the perturbation, the unitary time-evolution operator becomes

$$\hat{U}_0(t,t_0) = \hat{U}(t,t_0)\Big|_{F=0} = e^{-\frac{i}{\hbar}\hat{\mathcal{H}}(t-t_0)}\ . \tag{6.5}$$

From Eq. (6.4), it is clear that to find the full evolution of the wavefunction $|\psi_n(t)\rangle$, it is necessary to determine the operator $\hat{U}(t,t_0)$ that describes the time evolution of the ground state $|\psi_n(t_0)\rangle$. On the other hand, since the goal is to find a linear approximation that represents the external perturbation, we need to do this just up to first order. Thus, to perform a pertubartive expansion of $\hat{U}_0(t,t_0)$ in powers of $F(t)$ it is convenient to write

$$\hat{U}(t,t_0) = \hat{U}_0(t,t_0)\hat{U}_F(t,t_0)\ , \tag{6.6}$$

where $\hat{U}_0(t,t_0)$ is given by Eq. (6.5), while $\hat{U}_F(t,t_0)$ is due to the external field $F(t)$. Thus, from Eqs. (6.3), (6.4) and (6.6), we obtain

$$i\hbar\frac{\partial}{\partial t}\hat{U}_F(t,t_0) = F(t)\hat{B}(t-t_0)\hat{U}_F(t,t_0)\ , \tag{6.7}$$

with initial condition $\hat{U}_F(t_0,t_0) = \hat{1}$, where $\hat{1}$ is a unitary operator. In Eq. (6.7),

$$\hat{B}(t) \equiv \hat{U}_0^\dagger(t,t_0)\hat{B}\hat{U}_0(t,t_0)\ , \tag{6.8}$$

is the time evolution of the operator $\hat{B}$ in the Heisenberg picture, and coincides with the latter only at $t = 0$. Now, expanding $\hat{U}_F(t,t_0)$ to first order in $F(t)$ as

$$\hat{U}_F(t,t_0) \approx 1 + F(t)\hat{U}_{F,1}(t,t_0) + \mathcal{O}[F^2]\ , \tag{6.9}$$

and combining with Eq. (6.7), yields

$$\hat{U}_{F,1}(t,t_0) \approx -\frac{i}{\hbar}\int_{t_0}^{t}\hat{B}(t'-t_0)F(t')dt' + \mathcal{O}[F^2]. \tag{6.10}$$

Therefore, the total time-evolution operator to first order in F, obtained from Eqs. (6.10) and (6.6), is defined by

$$\hat{U}(t,t_0) \approx \hat{U}_0(t,t_0)\left[\hat{1} - \frac{i}{\hbar}\int_{t_0}^{t}\hat{B}(t'-t_0)F(t')dt'\right], \tag{6.11}$$

It is important to mention that Eq. (6.11) is one of the most important results of the linear response theory.

Now, let us consider a second observable $\hat{A}$ with a average equilibrium value for $t \leq t_0$ defined as

$$\left\langle \hat{A} \right\rangle_0 = \sum_n P_n \left\langle \psi_n(t_0) \middle| \hat{A} \middle| \psi_n(t_0) \right\rangle \ . \tag{6.12}$$

The goal here is to use the expression defined in Eq. (6.11) to calculate the expectation value of the second observable $\hat{A}$ at times later than t_0 and under the influence of a perturbation. This quantity is formally defined as [16]

$$\left\langle \hat{A} \right\rangle_F (t) = \sum_n P_n \left\langle \psi_n(t) \middle| \hat{A} \middle| \psi_n(t) \right\rangle \ . \tag{6.13}$$

Thus, starting from

$$\begin{aligned} \left\langle \psi_n(t) \middle| \hat{A} \middle| \psi_n(t) \right\rangle = & \left\langle \psi_n(t_0) \middle| \hat{U}_0^\dagger(t, t_0) \hat{A} \hat{U}_0(t, t_0) \middle| \psi_n(t_0) \right\rangle \\ & + \frac{i}{\hbar} \int_{t_0}^{t} dt' F^\dagger(t') \left\langle \psi_n(t_0) \middle| \hat{B}^\dagger(t' - t_0) \hat{A}_0(t - t_0) \middle| \psi_n(t_0) \right\rangle \\ & - \frac{i}{\hbar} \int_{t_0}^{t} dt' F(t') \left\langle \psi_n(t_0) \middle| \hat{A}(t - t_0) \hat{B}(t' - t_0) \middle| \psi_n(t_0) \right\rangle \ , \end{aligned} \tag{6.14}$$

we obtain:

$$\left\langle \hat{A} \right\rangle_F (t) - \left\langle \hat{A} \right\rangle_0 = -\frac{i}{\hbar} \int_{t_0}^{t} dt' \left\langle \left[\hat{A}(t), \hat{B}(t') \right] \right\rangle_0 F(t') \ . \tag{6.15}$$

In Eq. (6.15), both operators $\hat{A(t)}$ and $\hat{B}(t')$ are calculated via Eq. (6.8), $[\hat{A}, \hat{B}]$ is the commutator of two operators $\hat{A}$ and $\hat{B}$, and $\langle \cdots \rangle_0$ denotes the ensemble average of the thermal equilibrium defined as defined by Eq. (6.12). On the other hand, the left hand side of Eq. (6.15) represents exactly what we were looking for: a measure of the deviation from the unperturbed result due to the external perturbation. Therefore, defining for convenience $\left\langle \hat{A} \right\rangle_1 (t) \equiv \left\langle \hat{A} \right\rangle_F (t) - \left\langle \hat{A} \right\rangle_0$, Eq. (6.15) becomes

$$\left\langle \hat{A} \right\rangle_1 (t) = \int_0^\infty \chi_{AB}(\tau) F(t - \tau) d\tau \ , \tag{6.16}$$

where $\tau \equiv t - t' > 0$, and $\chi_{AB}(\tau)$ is the *retarded* linear response function given by

$$\chi_{AB}(\tau) \equiv -\frac{i}{\hbar} \Theta(\tau) \left\langle \left[\hat{A}(\tau), \hat{B} \right] \right\rangle_0 \ . \tag{6.17}$$

In Eq. (6.17), $\Theta(\tau)$ vanishes for $\tau < 0$ and equals 1 for $\tau > 0$. Also, it was assumed that the perturbing field approaches to zero as $t \to -\infty$ in order to replace the upper boundary of the integral in Eq. (6.16). In other words, for $t \to -\infty$ the system can be assumed to have been in the unperturbed equilibrium.

In summary, $\chi_{AB}(\tau)$, Eq. (6.17), describes the response an observable $\hat{A}$ at time t to an external force (impulse) that coupled to the observable $\hat{B}$ at an *earlier* time $(t - \tau)$. $\chi_{AB}(\tau)$ is called *retarded*, or *causal*, response function because it describes the *after-effect* of a perturbation.

6.1.1 Response function of a non-interacting electron liquid

As a previous step to calculate the graphene response function, the understanding of the response of the non-interacting electron liquid is essential, since provide useful expressions for the response associated with the single-particle operators. In fact, as discussed in the next chapter, the response of an interacting system can be obtained as the response of the unperturbed system to an effective self-consistent field. This is one of the most useful tools of many-body physics.

Let us start by defining two operators such that[1]

$$\hat{A} = \sum_{\alpha\beta} A_{\alpha\beta}\hat{a}^{\dagger}_{\alpha}\hat{a}_{\beta}, \tag{6.18}$$

$$\hat{B} = \sum_{\alpha\beta} B_{\gamma\beta}\hat{a}^{\dagger}_{\alpha}\hat{a}_{\beta} \ , \tag{6.19}$$

where $\hat{a}^{\dagger}_{\alpha}$ are the creation operators of one-electron states that diagonalize the independent electron Hamiltonian

$$\hat{\mathcal{H}}_0 = \sum_{\alpha} \varepsilon_{\alpha}\hat{a}^{\dagger}_{\alpha}\hat{a}_{\alpha} \ , \tag{6.20}$$

and ε_α are their energies.

Now, the problem is to calculate the time-dependence of the expectation value of $\hat{A}$ due to a perturbation that couples linearly to $\hat{B}$, i.e, for a the time-dependent Hamiltonian of the form

$$\hat{\mathcal{H}}_{0F}\left(t\right) = \hat{\mathcal{H}}_0 + F\left(t\right)\hat{B}. \tag{6.21}$$

Here, the time-dependence of the expectation value of $\hat{A}$ due to a perturbation that couples linearly to $\hat{B}$ corresponds, in fact, to the response function, represented by $\chi^{(0)}_{AB}(\tau)$, where the superscript (0) represents the fact that interactions are turned off and, therefore, it is the *non-interaction response function*. It is also important to note that, due to the form of $\hat{\mathcal{H}}_0$, the time-dependence of the operators $\hat{a}_\alpha$ and $\hat{a}^{\dagger}_{\alpha}$, under the unperturbed Hamiltonian, is equivalent to a multiplication by a phase factor, such that

$$\begin{aligned}\hat{a}_{\alpha}\left(t\right) &\equiv e^{\frac{i}{\hbar}\hat{H}_0 t}\hat{a}_{\alpha}e^{-\frac{i}{\hbar}\hat{H}_0 t} = e^{-\frac{i}{\hbar}\varepsilon_\alpha t}\hat{a}_{\alpha},\\ \hat{a}^{\dagger}_{\alpha}\left(t\right) &\equiv e^{\frac{i}{\hbar}\hat{H}_0 t}\hat{a}^{\dagger}_{\alpha}e^{-\frac{i}{\hbar}\hat{H}_0 t} = e^{\frac{i}{\hbar}\varepsilon_\alpha t}\hat{a}^{\dagger}_{\alpha}.\end{aligned} \tag{6.22}$$

Using these results, and replacing Eqs. (6.18) and (6.19) into Eq. (6.17), one finds

$$\chi^{(0)}_{AB}(\tau) = -\frac{i}{\hbar}\Theta\left(\tau\right)\sum_{\alpha\beta\gamma\delta} A_{\alpha\beta}B_{\gamma\delta}e^{-i\left(\varepsilon_\alpha-\varepsilon_\beta\right)t/\hbar}\left\langle\left[\hat{a}^{\dagger}_{\alpha}\hat{a}_{\beta},\hat{a}^{\dagger}_{\gamma}\hat{a}_{\delta}\right]\right\rangle_0. \tag{6.23}$$

Applying the Fermionic commutation relations[2] to the commutator $\left[\hat{a}^{\dagger}_{\alpha}\hat{a}_{\beta},\hat{a}^{\dagger}_{\gamma}\hat{a}_{\delta}\right]$ in Eq. (6.23), yields:

$$\left[\hat{a}^{\dagger}_{\alpha}\hat{a}_{\beta},\hat{a}^{\dagger}_{\gamma}\hat{a}_{\delta}\right]_0 = \hat{a}^{\dagger}_{\alpha}\hat{a}_{\beta}\hat{a}^{\dagger}_{\gamma}\hat{a}_{\delta} - \hat{a}^{\dagger}_{\gamma}\hat{a}_{\delta}\hat{a}^{\dagger}_{\alpha}\hat{a}_{\beta}, \tag{6.24}$$

---

[1] $\hat{A}_{\alpha\beta}$ and $\hat{B}_{\alpha\beta}$ are the matrix elements of the single particle operators $\hat{A}$ and $\hat{B}$, e.g $\langle i,\alpha|\,A\,|i,\beta\rangle$.

[2] Where $\left[\hat{a}^{\dagger}_{i},\hat{a}^{\dagger}_{j}\right]=0$, $\left[\hat{a}_i,\hat{a}_j\right]=0$ and $\left[\hat{a}_i,\hat{a}^{\dagger}_{j}\right]=\delta_{ij}$

$$\left[\hat{a}_\alpha^\dagger \hat{a}_\beta, \hat{a}_\gamma^\dagger \hat{a}_\delta\right]_0 = \delta_{\beta\gamma}\hat{a}_\alpha^\dagger \hat{a}_\delta - \delta_{\alpha\delta}\hat{a}_\gamma^\dagger \hat{a}_\beta \ . \tag{6.25}$$

Thus, replacing Eq. (6.25) in Eq. (6.23) and using the number operator $\hat{n}_\alpha = \hat{a}_\alpha \hat{a}_\alpha^\dagger$, the non-interacting response becomes

$$\chi_{AB}^{(0)}(\tau) = -\frac{i}{\hbar}\Theta(\tau)\sum_{\alpha\beta} A_{\alpha\beta}B_{\beta\alpha}e^{-i\left(\varepsilon_\alpha - \varepsilon_\beta\right)t/\hbar}\left(n_\alpha - n_\beta\right) \ . \tag{6.26}$$

Finally, taking the Fourier transform of this expression with respect to time, as

$$\chi_{AB}^{(0)}(\omega) = \lim_{\eta\to 0^+}\int_{-\infty}^{\infty} d\tau \chi_{AB}^{(0)}(\tau)e^{i(\omega+i\eta)\tau}, \tag{6.27}$$

and since the external perturbation is normally periodic in time with angular frequency ω, such as $Fe^{-i\omega t}$, for example, we have that

$$\chi_{AB}^{(0)}(\omega) = \lim_{\eta\to 0^+}\sum_{\alpha\beta}\frac{(n_\alpha - n_\beta)}{\hbar\omega + \varepsilon_\alpha - \varepsilon_\beta + i\hbar\eta}A_{\alpha\beta}B_{\beta\alpha} \ . \tag{6.28}$$

6.1.2 Graphene Density-density response function

Following the same line of reasoning developed in the previous subsection, the graphene density-density response is now calculated. To do so, the field operator $\hat{c}_{\lambda\boldsymbol{k}}^\dagger$ ($\hat{c}_{\lambda\boldsymbol{k}}$) is introduced as the creation (annihilation) operators in state α, and the non-interacting Hamiltonian (6.20) is rewritten as [245]

$$\hat{\mathcal{H}}_0 = \sum_{\lambda\boldsymbol{k}}\varepsilon_{\lambda\boldsymbol{k}}\hat{c}_{\lambda\boldsymbol{k}}^\dagger \hat{c}_{\lambda\boldsymbol{k}} \ , \tag{6.29}$$

where $\varepsilon_{\lambda\boldsymbol{k}}$ is the graphene energy dispersion defined in Eq. (3.21). The Hamiltonian that describes the electron-electron interaction is given by [245]

$$\hat{\mathcal{H}}_{\text{e−e}} = \frac{1}{2}\sum_{\boldsymbol{q}} v_{\boldsymbol{q}}\hat{n}_{\boldsymbol{q}}\hat{n}_{-\boldsymbol{q}} \ , \tag{6.30}$$

where the density operator is defined as [245]

$$\hat{n}_{\boldsymbol{q}} = \sum_{\boldsymbol{k},\lambda,\lambda'} = \mathcal{D}_{\lambda\lambda'}(\boldsymbol{k}-\boldsymbol{q}/2, \boldsymbol{k}+\boldsymbol{q}/2, \lambda)\hat{c}_{\boldsymbol{k}-\boldsymbol{q}/2}^\dagger \hat{c}_{\boldsymbol{k}-\boldsymbol{q}/2,\lambda'}. \tag{6.31}$$

In Eq. (6.31), $v_{\boldsymbol{q}}$ is the 2D Fourier transform of the Coulomb interaction and $\mathcal{D}_{\lambda\lambda'}$, known as *density vertex* [245], comes from the evaluation of the density operator in the single-particle states, defined by [246–248]

$$\mathcal{D}_{\lambda\lambda'}(\boldsymbol{k},\boldsymbol{k}') = \langle\Psi_{\lambda,\boldsymbol{k}}|\Psi_{\lambda'\boldsymbol{k}'}\rangle = \frac{1+\lambda\lambda' e^{i(\phi_{\boldsymbol{k}'}-\phi_{\boldsymbol{k}})}}{2}. \tag{6.32}$$

Note that Eq. (6.32) is exactly the projection of the non-interacting eigenstates $\langle\Psi_{\lambda,\boldsymbol{k}}|\Psi_{\lambda'\boldsymbol{k}'}\rangle$ and, at the low energy limit around the Dirac points, $\phi_{\boldsymbol{k}}$ reduces to the angle between the vector $\boldsymbol{k}$ and the x-axis [245, 246].

Now, the density-density response function of graphene can be calculated as [245, 246]

$$\chi^{(0)}_{nn}(\boldsymbol{q},\omega) = \frac{1}{L^2}\chi^{(0)}_{n_q n_{-q}}(\omega) = \frac{1}{L^2}\sum_{\lambda\boldsymbol{k},\lambda'\boldsymbol{k}'}\frac{n_{\lambda\boldsymbol{k}} - n_{\lambda'\boldsymbol{k}'}}{\hbar\omega + \varepsilon_{\lambda\boldsymbol{k}} - \varepsilon_{\lambda'\boldsymbol{k}+\boldsymbol{q}} + i\hbar\eta}\left|(n_{\boldsymbol{q}})_{\lambda\boldsymbol{k},\lambda'\boldsymbol{k}'}\right|^2 , \tag{6.33}$$

$$\chi^{(0)}_{nn}(\boldsymbol{q},\omega) = \frac{1}{L^2}\sum_{\lambda\lambda'\boldsymbol{k}}|\mathcal{D}_{\lambda\lambda'}(\boldsymbol{k},\boldsymbol{k}+\boldsymbol{q})|^2\frac{n_{\lambda\boldsymbol{k}} - n_{\lambda'\boldsymbol{k}'}}{\hbar\omega + \varepsilon_{\lambda\boldsymbol{k}} - \varepsilon_{\lambda'\boldsymbol{k}+\boldsymbol{q}} + i\hbar\eta} . \tag{6.34}$$

Since electrons and holes are need to be included, the occupation probability $n_{\lambda\boldsymbol{k}}$ is given by the Fermi Dirac distribution function [246]

$$n_{\lambda\boldsymbol{k}} \equiv f_D(\varepsilon_{\lambda\boldsymbol{k}},\nu,T) = \frac{1}{1+\exp\left(\frac{\varepsilon_{\lambda\boldsymbol{k}}-\mu}{k_BT}\right)} , \tag{6.35}$$

with μ being the chemical potential. In addition, due to the chirality[3], yields [246]

$$|\mathcal{D}_{\lambda\lambda'}(\boldsymbol{k},\boldsymbol{k}+\boldsymbol{q})|^2 = \frac{1+\lambda\lambda'\cos(\phi_{\boldsymbol{k}}-\phi_{\boldsymbol{k}+\boldsymbol{q}})}{2} . \tag{6.36}$$

Finally, to write a general expression to the Density-density response function of graphene, the spin and valley degeneracy factor, up to this point ignored, need to be included. To do so, the variables $g_s = 2$ and $g_v = 2$, that represent the spin and valley degeneracy factors, respectively, are introduced in Eq. (6.34) resulting in [17, 246, 250, 251]:

$$\chi^{(0)}_{nn}(\boldsymbol{q},\omega) = \frac{g_sg_v}{L^2}\sum_{\lambda\lambda'\boldsymbol{k}}|\mathcal{D}_{\lambda\lambda'}(\boldsymbol{k},\boldsymbol{k}+\boldsymbol{q})|^2\frac{n_{\lambda\boldsymbol{k}} - n_{\lambda'\boldsymbol{k}'}}{\hbar\omega + \varepsilon_{\lambda\boldsymbol{k}} - \varepsilon_{\lambda'\boldsymbol{k}+\boldsymbol{q}} + i\hbar\eta} . \tag{6.37}$$

For graphene $g_s,\ g_v = 4$ [250, 251]. Note that, if the energy $\varepsilon_{\lambda\boldsymbol{k}}$ is given by the linear approximation described by Eq. (3.21), Eq. (6.37), correspond to the Density-density response function of graphene in the continuum limit.

6.1.2.1 Density response function of doped graphene at zero Kelvin

For completeness, the density-density response function of a doped[4] graphene at zero Kevin ($T = 0$) is presented here. A complete description, step-by-step, of how this expression can be obtained is carefully presented in Refs. [17, 246, 250, 251].

The key point to take $T = 0$ is to consider that in this case, Fermi distributions, Eq. (6.35), reduce to step functions $n_{\lambda\boldsymbol{k}} = \Theta(E_F - \lambda\hbar v_F k)$. Here E_F is the Fermi energy level and $\Theta(\cdots)$ is the Heaviside step function. Thus, taking $\sum_k \to \int d^2\boldsymbol{k}$, Eq. (6.37) yields[5] [246, 251]:

$$\chi^{(0)}_{nn}(\boldsymbol{q},\omega) = \chi^{+}(\boldsymbol{q},\omega) + \chi^{-}(\boldsymbol{q},\omega) - \chi^{-}_{\Lambda}(\boldsymbol{q},\omega) , \tag{6.38}$$

---

[3] The direction along which an electron propagates and the amplitude of its wave function are not independent. Therefore, the electrons are said to possess the property of chirality [249].

[4] See Ref. [251] for more details.

[5] For simplicity, the subscript nn and the superscript (0) were omitted on the right side of Eq. (6.38).

where

$$\chi_\xi^{\pm}(\boldsymbol{q},\omega) = \frac{g_s g_v}{(2\pi)^2}\int_{k\leq\xi} d^2\boldsymbol{k}\sum_{\alpha=\pm 1}\frac{\alpha\left|\mathcal{D}_{\lambda\lambda'}(\boldsymbol{k},\boldsymbol{k}+\boldsymbol{q})\right|^2}{\hbar\omega+\alpha(\varepsilon_{\boldsymbol{k}}\mp\varepsilon_{\boldsymbol{k}+\boldsymbol{q}}+i\hbar\eta)}\ . \tag{6.39}$$

The superscript sign $+(-)$ in Eq. (6.38) correspond to the intra(inter)-band transitions, discussed detailed as a following, ξ is a general upper limit and the energy is defined as $\varepsilon_{\boldsymbol{k}} \equiv \varepsilon_{+\boldsymbol{k}}$.

By introducing the dimensionless quantities $\bar{\boldsymbol{k}} = \boldsymbol{k}/k_F$, $\bar{\boldsymbol{q}} = \boldsymbol{q}/k_F$ and $\bar{\omega} = \hbar\omega/E_F$, where the Fermi wave vector is now given by $k_F = E_F/\hbar v_f$, Eq. (6.39) becomes [17, 250, 251]

$$\chi_\xi^{\pm}(\boldsymbol{q},\omega) = \frac{D(E_F)}{2\pi}\int_{k\leq\xi} d^2\bar{\boldsymbol{k}}\sum_{\alpha=\pm 1}\frac{\alpha\left|\mathcal{D}_{\lambda\lambda'}(\bar{\boldsymbol{k}},\bar{\boldsymbol{k}}+\boldsymbol{q})\right|^2}{\hbar\omega+\alpha\left(\bar{k}\mp\left|\bar{\mathbf{k}}+\bar{\mathbf{q}}\right|\right)+i\bar{\eta}}\ . \tag{6.40}$$

where $D(E_F)$ is the graphene DOS at Fermi energy.

After some lengthy algebra[6] to calculate Eq. (6.40) for all terms of Eq. (6.38), the full solution of $\chi_{nn}^{(0)}(\boldsymbol{q},\omega) = \mathrm{Re}[\chi_{nn}^{(0)}(\boldsymbol{q},\omega)] + \mathrm{Im}[\chi_{nn}^{(0)}(\boldsymbol{q},\omega)]$ is obtained as [246, 250, 251]:

$$\mathrm{Re}[\chi_{nn}^{(0)}(\boldsymbol{q},\omega)] = -D(E_F) + f(q,\omega)\begin{cases} \pi & \text{, in region 1A} \\ -G_>(\frac{2-\bar{\omega}}{\bar{q}}) + G_>(\frac{2+\bar{\omega}}{\bar{q}}) & \text{, in region 1B} \\ -G_<(\frac{\bar{\omega}-2}{\bar{q}}) & \text{, in region 2A} \\ G_>(\frac{2+\bar{\omega}}{\bar{q}}) & \text{, in region 2B} \end{cases}\ , \tag{6.41}$$

and

$$\mathrm{Im}[\chi_{nn}^{(0)}(\boldsymbol{q},\omega)] = -D(E_F) + f(q,\omega)\begin{cases} G_>(\frac{2-\bar{\omega}}{\bar{q}}) - G_>(\frac{2+\bar{\omega}}{\bar{q}}) & \text{, in region 1A} \\ \pi & \text{, in region 1B} \\ -G_>(\frac{2+\bar{\omega}}{\bar{q}}) & \text{, in region 2A} \\ -G_<(\frac{2+\bar{\omega}}{\bar{q}}) & \text{, in region 2B} \end{cases}\ , \tag{6.42}$$

where

$$f(q,\omega) = \frac{D(E_F)}{8}\frac{\bar{q}^2}{\sqrt{|\bar{\omega}^2-\bar{q}^2|}}\ , \tag{6.43}$$

$$G_>(x) = x\sqrt{x^2-1} - \mathrm{arcosh}(x)\ , \tag{6.44}$$

$$G_>(x) = x\sqrt{1-x^2} - \mathrm{arcos}(x)\ , \tag{6.45}$$

for $x > 1$ and $|x| < 1$ in Eqs.(6.44) and (6.45), respectively.

The domains of Eqs. (6.41) and (6.42) are depicted in Fig. 6.1, while their respective color map plots are presented in Fig. 6.2. Regions 1A, 2A and 2B are the Landau damping, sometimes also denominated as electron-hole continuum. Long-lived plasmons only reside in region 1B, due to the fact that outside this region the $\mathrm{Im}[\chi_{nn}^{(0)}(\boldsymbol{q},\omega)] \neq 0$, see Fig. 6.2(a), which yields absorption. To be more precise, when the electrons in the graphene are moving slower than the electromagnetic wave (as explained in the next section, this specific wave is defined as a graphene plasmon), they remove energy from the

---

[6] See Refs. [246, 250, 251] for a step-by-step solution.

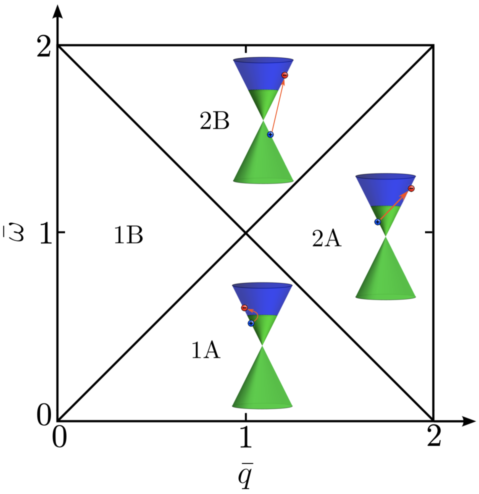

Figure 6.1: Regions in the (q, ω) plane of the non-interacting Density-density response function of graphene $\chi^{(0)}_{nn}(\boldsymbol{q}, \omega)$ defined by Eqs. (6.41) and (6.42). Regions 1A, 2A and 2B are the Landau damping, pictorially illustrated by the inset, while in 1B the $Im[\chi^{(0)}_{nn}(\boldsymbol{q}, \omega)] = 0$, see Fig 6.2, allowing long-lived graphene plasmon. The figure is adapted from Ref. [17]

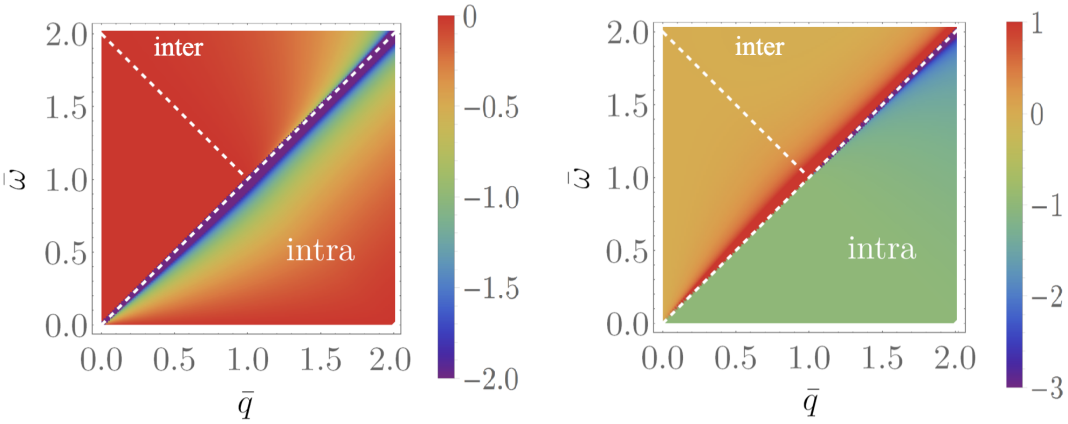

Figure 6.2: (Left) Imaginary and (right) real parts of the non-interacting density-density response function of graphene $\chi^{(0)}_{nn}(\boldsymbol{q}, \omega)$ in the (q, ω) plane. The scale in panel left (right) are in units of $\mathrm{Im}[\chi^{(0)}_{nn}(\boldsymbol{q}, \omega)/D(E_F)]$ $(\mathrm{Re}[\chi^{(0)}_{nn}(\boldsymbol{q}, \omega)/D(E_F)])$. The inter- and intra-band regions are defined in both panels delimitated by a white dashed lines. Note that the $\mathrm{Im}[\chi^{(0)}_{nn}]$, left panel, is always negative, since is a retarded function. Adapted from Ref. [246]

wave. Mathematically, the condition for this is $v_p = \hbar\omega/q \leq v_F$, where v_p is the phase velocity. Since the regions 1A and 2A are on the right of the line $\hbar\omega = \hbar q v_F$, these regions are where the Landau damping can take place. On the other hand, in region 2B, this electromagnetic wave in graphene can lose energy by creating electron-hole pairs, due to its large momenta when compared to those from the free radiation, and, then, participate in indirect interband electron-hole transitions [17].

6.2 Graphene plasmonic

In general, plasmons are collective electron excitation [16, 18]. Although the focus of the next two chapters are plasmons in graphene, plasmons were first studied in metallic surfaces, where the collective oscillations of the free electron liquid oscillate in resonance with an external electromagnetic field. From a classical point of view, for a 2D system, the plasmons response can be qualitatively described by a time-dependent density profile [16, 246]:

$$n(\boldsymbol{r},t) = n_0 + n_1(\boldsymbol{r},t) \ , \tag{6.46}$$

where n_0 is uniform and time-independent, representing the unperturbed electron concentration, while $n_1(\boldsymbol{r},t)$ is the density disturbance. Similar to other physical restoring forces, after excited by an electromagnetic wave, the forces that acting on the electron liquid will try to restore the equilibrium, due to an attempt to screen the external perturbation. Thus, the subsequent restoring of the electric field, induced by the density distribution before vanished completely, corresponds to a quantum of plasma oscillation.

Considering that the electron oscillations are sufficiently slow for the system to remain in thermodynamic equilibrium for any time t, i.e for $n_1(\boldsymbol{r},t) \ll n$, we can use the long-wavelength limit $q \ll k_F$ to obtain the plasmon dispersion on the grounds of hydrodynamics. Within this theory, the electron liquid is described by the density disturbance $n_1(\boldsymbol{r},t)$ and the associated induced current $j_1(\boldsymbol{r},t)$. If the relation between $n_1(\boldsymbol{r},t)$ and n_0 is satisfied as $n_1(\boldsymbol{r},t)/n_0 \ll 1$, these relations can be linearised and are related to each other through the continuity equation [246]

$$\frac{\partial}{\partial t}\left[n_1\left(\boldsymbol{r},t\right)\right] + \nabla \cdot \boldsymbol{j}_1(\boldsymbol{r},t) = 0 \ , \tag{6.47}$$

and the Euler equation of motion

$$\frac{\partial}{\partial t}\left[\boldsymbol{j}_1\left(\boldsymbol{r},t\right)\right] = -\frac{\mathcal{D}}{\pi e^2}\nabla\left(\int d\boldsymbol{r}'\frac{e^2}{\epsilon\left|\boldsymbol{r}-\boldsymbol{r}'\right|}n_1\left(\boldsymbol{r}',t\right)\right) \ , \tag{6.48}$$

Here, ϵ is the dielectric response of the environment, $\mathcal{D}$ is the Drude weight, which determines the relation between the induced current density and the restoring force, and $-e$ is the electron charge.

After some algebra, namelly taking the divergence, using the continuity equation, and Fourier transforming both sides of Eq. (6.48) with respect to $\boldsymbol{r}$ and t, we obtain [16]

$$\left(\omega^2 - \frac{\mathcal{D}}{\pi e^2}q^2 v_q\right) n_1\left(\boldsymbol{q},\omega\right) = 0, \tag{6.49}$$

where $v_{\boldsymbol{q}} = \pi e^2/(\epsilon q)$ is the 2D Fourier transform of the Coulomb interaction. Therefore, as a consequence of Eq. (6.49), we can conclude that is possible to excite a density wave with frequency (or dispersion) given by:

$$\omega_{pl}\left(q\right) = \sqrt{\frac{2\mathcal{D}}{\epsilon}q} \ . \tag{6.50}$$

As expected, since graphene is a 2D material, the graphene plasmon (also known as Dirac plasmon) frequency presents a $\omega_{pl} \propto \sqrt{q}$ scaling, similar to other 2D electron systems [16]. Also, from Eq. (6.50), we notice that the plasmons vanish when $q \to 0$, and this regime is called long-wavelength.

6.2.1 The random phase approximation

As final step to present the basic tools to study plasmons in graphene, all we need now is to include the electron-electron interactions. To do so, we will use the *random phase approximation* (RPA), originally introduced by Gell-Mann and Brückner [252] and by Bohm and Pines [253], both in 1957.

For an interacting electron liquid under n external potential perturbation $V_{\text{ext}}(\boldsymbol{r}, \omega)$, the screened potential, due to the electron redistribution, is then given by [16, 246]

$$V_{sc}\left(\boldsymbol{r}, \omega\right) = V_{ext}\left(\boldsymbol{r}, \omega\right) + V_{ind}\left(\boldsymbol{r}, \omega\right) \ , \tag{6.51}$$

where the electrostatic field $V_{ind}\left(\boldsymbol{r}, \omega\right)$, defined as

$$V_{ind}\left(\boldsymbol{r}, \omega\right) = \int d\boldsymbol{r}' \frac{e^2}{\epsilon \left|\boldsymbol{r} - \boldsymbol{r}'\right|} n_1\left(\boldsymbol{r}', \omega\right) \ , \tag{6.52}$$

is created by the induced density $n_1(\boldsymbol{r}, t)$. This potential is exactly the same that appeared on the right side of Eq. (6.48). According to the RPA, the electron liquid responds to the screened potential as if it was a non-interacting liquid, that is [246]

$$n_1\left(\boldsymbol{r}, \omega\right) = \int \chi^{(0)}_{nn}(\boldsymbol{r}, \boldsymbol{r}', \omega) V_{sc}\left(\boldsymbol{r}, \omega\right) \ , \tag{6.53}$$

But, on the other hand, the density perturbation, that created the induced potential initially, responds to the external potential as

$$n_1\left(\boldsymbol{r}, \omega\right) = \int \chi^{RPA}_{nn}(\boldsymbol{r}, \boldsymbol{r}', \omega) V_{ext}\left(\boldsymbol{r}, \omega\right) \ . \tag{6.54}$$

Taking a Fourier transform of Eqs. (6.53) and (6.54), we can relate the response functions, for a homogeneous electron liquid case, as

$$\chi^{(0)}_{nn}(q, \omega) \left[1 + v_{\mathbf{q}} \chi^{RPA}_{nn}(\mathbf{q}, \omega)\right] = \chi^{RPA}_{nn}(\mathbf{q}, \omega). \tag{6.55}$$

That immediately results in the *RPA Density-density response function*

$$\chi^{RPA}_{nn}(\mathbf{q}, \omega) = \frac{\chi^{(0)}_{nn}}{\epsilon^{RPA}(q, \omega)} = \frac{\chi^{(0)}_{nn}(q, \omega)}{1 - v_{\mathbf{q}} \chi^{(0)}_{nn}(q, \omega)} \ , \tag{6.56}$$

where

$$\epsilon^{RPA}(q, \omega) = 1 - v_{\mathbf{q}} \chi^{(0)}_{nn}(q, \omega) \tag{6.57}$$

is the dynamical RPA dielectric function. Note that both Eqs. (6.56) and (6.57) can be obtained through the non-interacting response function $\chi^{(0)}_{nn}(\mathbf{q}, \omega)$. From Eq. (6.57), we can see that the Dirac plasmons can be obtained by solving this equation, which corresponds to the zeroes of the total system's dielectric function $\epsilon^{RPA}(q,\omega)$ [16–18, 250, 251, 254, 255]. Reference [246] demonstrate how the 2D Fourier transform of the Coulomb interaction $v_{\boldsymbol{q}}$, present in Eq. (6.57), can be calculated for a monolayer graphene encapsulated by two different dielectric medium.

6.2.1.1 Non-retarded regime

It is possible to calculate the plasmons dispersion analytically through the non-retarded regime (or long-wavelength limit) defined for $\hbar v_f q < \hbar\omega \ll E_F$ [16–18, 246, 250, 251, 254, 255]. This region of interest, i.e for $q \to 0$, is located in the region 1B of Fig. 6.1. Thus, using the 1B expressions for the response function $\chi^{(0)}_{nn}(\boldsymbol{q},\omega)$, defined in Eq. (6.38), and expanding up to first order (see Ref. [246] for more details), we obtain the plasmon dispersion in the non-retarded regime as [17, 246, 250, 251]:

$$\hbar\omega_{pl} \approx \sqrt{\frac{\hbar g_s g_v \alpha_{ee} v_F E_F}{2} q} = \sqrt{\frac{2e^2 E_F}{\epsilon_{env}} q} \ , \tag{6.58}$$

with a typical $\omega^{(0)}_{pl} \propto \sqrt{q}$ scaling. This same dependence is present in Eq. (6.50). In terms of the Fermi energy, Eq. (6.50) is also proportional to $\sqrt{E_F}$. Since $E_F = \hbar v_F \sqrt{4\pi n_c/N_F}$, then the graphene plasmon frequency, in the non-retarded regime, depends on the electronic density as $\hbar\omega_{pl} \propto n_c^{1/4}$. It is important to mention that while plasmon dispersion $\omega_{pl} \propto \sqrt{q}$ is intrinsically inherent to all 2D systems, the dependence of the frequency as $\omega^{(0)}_{pl} \propto n_c^{1/4}$ is exclusive of graphene as a consequence of the quantum relativistic nature of graphene monolayer [17, 246, 251]. In Eq. (6.58), $\alpha_{ee} = e^2/(\epsilon_{env}\hbar v_F)$ is the graphene fine-structure constant, while ϵ_{env} is the effective dynamical background dielectric function.

7

Probing the structure and composition of vdWhs using the nonlocality of Dirac plasmons in the terahertz regime

Dirac plasmons in graphene are very sensitive to the dielectric properties of the environment making it possible to be used to probe the structure and composition of van der Waals heterostructures (vdWh) put underneath a single graphene layer. In order to do so, we investigated vdWh composed of hexagonal boron nitride and different types of transition metal dichalcogenides (TMDs).

Thus, in this chapter, by performing realistic simulations that account for the contribution of each layer of the vdWh separately and including the importance of the substrate phonons, it is shown that one can achieve single-layer resolution by investigating the nonlocal nature of the Dirac plasmon-polaritons. The composition of the vdWh stack can be inferred from the plasmon-phonon coupling once it is composed by more than two TMD layers. Furthermore, it is shown that the bulk character of TMD stacks for plasmonic screening properties in the terahertz regime is reached only beyond 100 layers.

The study *Probing the structure and composition of vdWhs using the nonlocality of Dirac plasmons in the terahertz regime*, developed in this chapter, was published in 2D Materials, **8** 015014 (2020).

7.1 Motivation

Graphene [8] and other two-dimensional (2D) materials, such as the transition metal dichalcogenides [107, 147] (TMDs), have been intensively investigated due to their unique opto-electronic properties [20, 145, 146, 158–165], as discussed in sections 2.4 and 2.6. The optical response of each material is different due to, e.g., the presence or absence of band gaps [152, 154], the specific type of the electronic structure, and is also influenced by the intrinsic mobility of the electrons themselves [203]. The latter is especially important for graphene because it is responsible for the manifestation of so-called plasmons, collective excitations of the 2D electron liquid [16, 18]. It has been shown that graphene

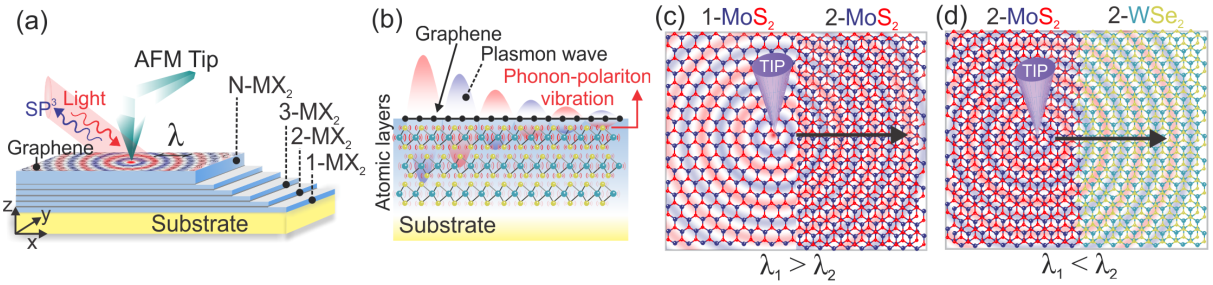

Figure 7.1: (Color online) (a) Schematic illustration of the Dirac plasmon wave in van der Waals heterostructures (vdWh) composed by a monolayer graphene (G) on N-MX$_2$ (M=W,Mo and X=S,Se) and a substrate (SiO$_2$). The graphene surface plasmon-phonon polariton wavelength is λ. Note that the monolayer graphene covers the entire sample. (b) Illustration of the phonon-polariton vibration in a vdWh composed of G/3-MX$_2$/SiO$_2$. Its hybridization with Dirac plasmon originates from the hybridized surface plasmons (SP^3). (c) and (d) illustrate the method presented in here. λ changes when (c) the number of layers in the same material changes, or (d) due to change of materials. λ is larger (smaller) when the screening is stronger (weaker). The situation shown in panel (d) occurs for a specific Fermi level and frequency if the phonon frequencies in both materials are different.

plasmons, also called Dirac plasmons, referring to the single-particle energy spectrum of graphene [256], can be supported at mid infra-red [83, 159, 257] to terahertz (THz) frequencies [159, 163, 258, 259] and show strong electromagnetic field confinement [17, 256]. TMDs, on the other hand, due to their large band gap [152, 153], behave as dielectrics at low frequencies, thus not supporting plasmons if not extrinsically doped [260].

These 2D materials can be combined in so-called van der Waals heterostructures (vdWh) [146]. Such structures can be made by stacking different layers on top of each other [145–147, 158, 162, 165, 175] or even next to each other forming so-called lateral heterostructures [147, 172–177]. A large corpus of literature has been devoted to the investigation of fabrication techniques to create these nanostructures [107, 145–147, 157, 158, 171–177]. It has been shown that different opto-electronic properties of the components making up the heterostructure are merged and that by carefully selecting the different constituents, one could achieve materials that are tailor-made to bolster specific behaviour [157, 171]. Conversely, this means that one could also investigate the opto-electronic response of certain vdWhs to assess their composition and atomic structure. In this study, are investigate Dirac plasmon states for specific types of vdWh stacks consisting of layers of hexagonal boron nitride (hBN) and different MX$_2$ types of TMDs, composed by a metal (M = Mo or W) layer surrounded by two layers of a chalcogen (X = S$_2$ or Se$_2$), topped by a single graphene layer, as illustrated in Fig. 7.1(a). Specifically, is investigate the way in which Dirac plasmons in the graphene layer are affected by the constituents of the remainder of the heterostructure and propose a method to infer its local layer number and composition based on local plasmonic properties. Notice that by investigating the effect on Dirac plasmons, the spectral region of investigation is narrow down to the THz to the far-infrared regime. Consequently, other kinds of collective effects, such as excitons, trions or biexcitons, for which traditionally TMDs are well-studied and that have excitation energies of more than 1 eV [261], will not be affecting the spectral range discussed in this study. Also, is considered doping only in the graphene layer. This means that there are no free electrons in the hBN and TMD layers and, therefore, the plasmonic response can only come from graphene's Dirac plasmons. Consequently, properties such as carrier mobility of the TMD layers are not affecting the obtained results.

Dirac plasmons in graphene arise as collective excitations of the electronic liquid in the 2D material because of electron-electron Coulomb interaction acting as a restoring force for deformations in the otherwise homogeneous electron density [16–18, 159, 160, 256]. While the electrons themselves are confined to the 2D material, the electromagnetic field lines associated with the Coulomb force, propagate through the surroundings, and as such are very sensitive to its composition, i.e dielectric properties. Indeed, as shown in Fig. 7.1(b), the electromagnetic field is screened due to a polarization of the dielectric environment which effectively slows down plasmon propagation. This combined excitation, i.e. a Dirac plasmon with the surrounding polarization cloud, is often called a surface plasmon-polariton (SP^2) [262]. However, if the plasmon frequency and wavevector match those of intrinsic phonons in the dielectric environment, both modes can hybridize, yielding a combined surface plasmon-phonon-polariton mode (SP^3) [256, 263–265].

The Dirac plasmon modes, coupled to the underlying heterostructure, can be measured by making use of the well-known scatter-type scanning near-field optical microscope (s-SNOM) [259, 266, 267] as shown schematically in Fig. 7.1(a). This allows to measure the plasmonic wavelength, with a typical resolution of the order of 20 nm [20, 21, 265–270], using interference fringes formed with the plasmon modes scattering of the edge of the heterostructure or at lateral defects in the system. Upon investigation of the dependency of the plasmon wavelength on the tunable graphene carrier concentration, this technique allows to use plasmonic excitations as near-field probes of the material's properties underneath the graphene sheet. In Figs. 7.1(c) and (d), is illustrated how this can be used to measure locally the layer structure and composition of the heterostructure.

In this chapter, is applied the above-mentioned method to study the dependency of SP^2 and SP^3 modes on the number and type of layers underneath the graphene sheet. We consider on the one hand hexagonal boron nitride (hBN) and on the other hand four types of TMDs (WS_2, WSe_2, MoS_2 and $MoSe_2$). By using realistic simulations that combine the random phase approximation (RPA) and density functional theory (DFT) calculations, in combination with the quantum electrostatic heterostructure model (QEH) [271], it is able possible to investigate the way in which plasmon properties depend on the number of heterostructure layers and the chemical composition of these heterostructures. Furthermore, the use of QEH also allows to properly account for substrate induced effects such as surface phonons that can interfere with the plasmons as well [272]. We provide a realistic evaluation of the way in which different numbers of layers of the heterostructure screens the electromagnetic field of the plasmon modes and, as such, decreases its wavelength. Also, the QEH allows to assess SP^3 modes, which are characteristic of the chemical composition of the TMDs. In this way, one can achieve a layer sensitivity of a single layer and differentiate between different TMDs for heterostructures thicker than 2 layers.

7.2 Theory of the dielectric response of heterostructures

Dirac plasmons are resonances of the free electron liquid in graphene (for more details, see section 6.2). These modes can be obtained by solving the plasmon equation which corresponds to the zeroes of the total system's dielectric function $\epsilon(q,\omega)$ [16, 18, 250, 251, 254, 255]

$$\epsilon(q,\omega) = 1 - v\,(q,\omega)\,\tilde{\chi}_{\rm nn}(q,\omega) = 0\ . \tag{7.1}$$

In Eq. (7.1), $\tilde{\chi}_{\rm nn}(q,\omega)$ is the proper density-density response function [16] and $v\,(q,\omega)$ is the Fourier transform of the Coulomb interaction between the Dirac electrons. In general, both factors depend on the properties of the system as a whole. However, in this is study, we approximate the former by the non-interacting density-density response function $\chi^0(q,\omega)$ is considered, which corresponds to the RPA[1]. This only depends on the properties of graphene. The latter, however, describes electromagnetic field lines that mainly propagate through the surrounding of the graphene sheet, and are, therefore, strongly affected by them. In general, the 2D Fourier transform of the Coulomb interaction is given by

$$v\,(q,\omega) = \frac{2\pi e^2}{q\bar{\epsilon}\,(\omega)}\ . \tag{7.2}$$

Equation (7.2) makes the role of the heterostructure very clear. Indeed, it is the screening of the Coulomb interaction introduced by the dynamical background dielectric function $\bar{\epsilon}(\omega)$ that encodes the presence of the environment. In order to exemplify how the background dielectrics are affecting the Dirac plasmons, one can calculate the dispersion in the long-wavelength limit and obtain [17, 250, 251]

$$\lambda(\omega;\bar{\epsilon},E_{\rm F}) = \frac{2\pi}{q(\omega;\bar{\epsilon},E_{\rm F})} = \frac{\pi\alpha_{\rm ee}N_f v_{\rm F}}{\hbar\omega^2}\frac{E_{\rm F}}{\bar{\epsilon}(\omega)}\ . \tag{7.3}$$

In Eq. (7.3), $\alpha_{\rm ee} = 2.2$, $N_f = 4$ and $v_{\rm F} = 10^6$ m/s are parameters related to the graphene sheet corresponding to the graphene fine structure constant, the number of fermion flavours and the Fermi velocity, respectively [203]. $E_{\rm F}$ is the Fermi level of graphene. Eq. (7.3) exemplifies how an increase in the average dielectric constant of the environment decreases the overall plasmon wavelength. As such, since hBN and TMDs

---

[1] The subscript nn, as in Eq. (6.57), was omitted.

all have a larger dielectric screening constant than vacuum, adding more layers to the system should, in general, decrease the wavelength of the collective excitation yielding a screened SP^2. However, the environmental dielectric function $\bar{\epsilon}(\omega)$ can have a non-trivial dynamical dependency on ω. This strongly affects the plasmonic wavelength when ω is close to the frequency of collective lattice vibrations of the environment, such as phonons, which gives rise to the hybrid collective modes SP^3.

In this study, we consider set-ups as schematically depicted in Figs. 7.1(a) and (b), i.e. a system consisting of a substrate, N layers of dielectric such as hBN or MX_2, and topped with a layer of graphene. We shall denote them as G/N-dielectric/sub. Considering the substrate, we choose to always compare SiO_2. One may also consider other substrates, such as SiC [273], HfO_2 and $\mathrm{Al}_2\mathrm{O}_3$ [274]. Our choice for SiO_2 as a substrate is motivated as follows: (i) it is widely used in graphene-based plasmon experiments [20, 21, 145, 158, 160, 162, 163, 259, 263, 265, 268–270, 275]; (ii) considering a different substrate, will affect the observed results only in a quantitative way. We do, however, take into account substrate specific effects such as substrate phonons, which will naturally be different for other substrates, but the qualitative result and accuracy of the method will not be affected by this. Both the substrate, as well as the N-layer dielectric, can induce non-trivialities in the environmental dielectric function. In the following, we lay down how to account for both of them.

7.2.1 Coupling to substrate phonons

An important non-trivial inclusion of substrate effects are surface phonons (see Ref. [17] for more details). In order to account for them, the most straightforward manner is by considering a frequency-dependent dielectric function of the form [17, 263]

$$\epsilon_{\mathrm{sub}}(\omega) = \epsilon_{\parallel}^{\infty} + \sum_{n=1}^{M} \frac{f_n \omega_{\mathrm{TO},n}^2}{\omega_{\mathrm{TO},n}^2 - \omega^2 - i\omega\gamma_{\mathrm{TO},n}} . \tag{7.4}$$

In Eq. (7.4), $\epsilon_{\parallel}^{\infty}$ is the in-plane high-frequency dielectric constant, M represent the number of surface transverse optical (TO) phonon modes, and $\omega_{\mathrm{TO},n}$ and $\gamma_{\mathrm{TO},n}$ are respectively the frequency and damping of the n-th TO surface phonon mode, weighted by f_n. To find the exact plasmon-phonon dispersion, and subsequent the wavelength defined in Eq. (7.3), it suffices to solve the plasmon equation shown in Eq. (7.1), where in the absence of a dielectric in-between the substrate and the graphene, $\bar{\epsilon}(\omega) = (\epsilon_0 + \epsilon_{\mathrm{sub}}(\omega))/2$. Note that plasmon, phonon and their hybrid modes also correspond to the maxima of the loss function $L(q, \omega)$, which is defined as

$$L(q, \omega) = -\mathrm{Im}\left[\frac{1}{\epsilon(q, \omega)}\right] . \tag{7.5}$$

In the following section, we will include the role of the intermediate dielectric through the use of the QEH model. As it accounts for each layer separately, the output of this model is a loss function. Finally, notice that the $\gamma_{\mathrm{TO},n}$ coefficients are determined by extrinsic factors, such as impurities [276] and defects [277] in-between the substrate and the heterostructure. They will result in a spectral broadening of the surface phonons. Since their magnitude depends on the specific set-up [263], in this study we will not include them[272].

7.2.2 Quantum electrostatic heterostructure model

The quantum electrostatic heterostructure (QEH) [271] model is used to calculate the non-local dynamical response of the considered vdWh. The model is especially suited for the current investigation because it calculates the dielectric properties of stacks of layers through a bottom-up approach in which the impact of each layer is treated separately.

More recently, the QEH model received an implementation for doped graphene layers in the low energy regime [272, 278]. This regime requires a much more dense grid of k-points to correctly describe its properties, which is achieved by the use of an analytical solution for the density response function. The combination of analytical solutions for the response function and DFT[2] calculated induced densities enables more accurate and fast calculations with graphene layers.

The QEH uses the density-density response function of the i-th layer $\chi_i\left(z, z', \mathbf{q}_\parallel, \omega\right)$ individually, that was previously obtained through ab-initio calculations. Notice that in this case the vertical spatial dimension z is retained. Subsequently, the total response function of the heterostructure is built by coupling each single layer together by the long-range Coulomb interaction by solving a Dyson-like equation. Omitting the $\mathbf{q}_\parallel$ and ω variables for simplicity, the Dyson equation of the total density-density response function of the complete vdWh reads [271]

$$\chi_{i\alpha,j\beta} = \chi_{i\alpha}\delta_{i\alpha,j\beta} + \chi_{i\alpha}\sum_{k\neq i,\gamma} V_{i\alpha,k\gamma}\chi_{k\gamma,j\beta} \ , \tag{7.6}$$

where the Coulomb matrices are defined as

$$V_{i\alpha,k\gamma}\left(\mathbf{q}_\parallel\right) = \int \rho_{i\alpha}\left(z, \mathbf{q}_\parallel\right)\Phi_{k\gamma}\left(z, \mathbf{q}_\parallel\right) dz \ , \tag{7.7}$$

and $\Phi_{k\gamma}\left(z, \mathbf{q}_\parallel\right)$ is the potential created by the density profile, $\rho_{k\gamma}\left(z, \mathbf{q}_\parallel\right)$. In Eq. (7.6), $\alpha = 0, 1$ represents the monopole and dipole components, respectively.

Through this formalism, one obtains the inverse dielectric function of the vdWh as

$$\epsilon^{-1}_{i\alpha,j\beta}\left(\mathbf{q}_\parallel, \omega\right) = \delta_{i\alpha,j\beta} + \sum_{k\gamma} V_{i\alpha,j\beta}\left(\mathbf{q}_\parallel\right)\chi_{k\gamma,j\beta}\left(\mathbf{q}_\parallel, \omega\right) \ . \tag{7.8}$$

Notice that in contrast to the dielectric function presented in Eq. (7.1), here we obtain a tensorial form. Consequently, the loss function can be found through

$$L\left(\mathbf{q}_\parallel, \omega\right) = -\mathrm{Im}\left[\mathrm{Tr}\left(\epsilon^{-1}\left(\mathbf{q}_\parallel, \omega\right)\right)\right] \ . \tag{7.9}$$

---

[2] More precisely, the QEH uses the DFT-PBE (Perdew–Burke-Ernzerhof) method [272].

Collective modes can now be found as the maxima of this loss function.

Finally, notice that the QEH model also allows to account for intrinsic phonons in the constituent layers. It manages to do so by adding the phonon contribution to the dielectric response function of the individual layers through the calculation of the lattice polarizability, $\alpha_{ij}^{\text{lat}}(\omega)$, in the optical limit [272]. This calculation can be considered parameter free, because it is mainly derived from the Born effective charges of the isolated layers [279, 280]. The Born effective charges are defined as tensors that give the proportionality between the variation of the polarization density due to an atomic displacement and are obtained by the discretized derivative of the 2D polarization density, that follows the Berry phase formalism, in the finite difference method [272, 279, 280]. Thus, considering the contributions of electrons and phonons, the total monopole and dipole component of i-th layer are defined as

$$\chi_{i0}^{\text{total}}\left(\mathbf{q}_{\parallel},\omega\right) = \chi_{i0}^{\text{el}}\left(\mathbf{q}_{\parallel},\omega\right) - \mathbf{q}_{\parallel}^{2}\alpha_{\parallel}^{\text{lat}}(\omega) \tag{7.10a}$$

$$\chi_{i1}^{\text{total}}\left(\mathbf{q}_{\parallel},\omega\right) = \chi_{i1}^{\text{el}}\left(\mathbf{q}_{\parallel},\omega\right) - \alpha_{zz}^{\text{lat}}(\omega) \ , \tag{7.10b}$$

where $\alpha_{\parallel}^{\text{lat}}$ denotes the 2×2 in-plane submatrix of α^{lat}. The total response functions are then used in Eq. (7.6), from which the consecutive loss function is obtained. (More details of the QEH model and the way it includes phonons is described in Ref. [272]).

The major advantage of the use of the QEH model is the availability of a vast database containing the dielectric building blocks of 2D materials[3], allowing us to reuse previously obtained DFT results. This enables the careful analysis of different vdWh systems on a layer-by-layer basis, without the need to treat the dielectric environment as slabs of bulk material.

Table 7.1: Phonon parameters of the substrate. Three optical transverse (TO) phonons were considered for SiO_2. The values of TO frequencies ($\omega_{TO,n}$) and their respective oscillator strength contribution (f_n) were extracted from Ref. [263]].

	$n = 1$	$n = 2$	$n = 3$
$\omega_{TO,n}$ (meV)	55.58	98.22	139.95
f_n	0.7514	0.1503	0.60111

---

[3] The dielectric building blocks and QEH software can be downloaded at https://cmr.fysik.dtu.dk/vdwh/vdwh.html

7.3 Substrate effects and calibration

Before we discuss the impact of the number of layers and composition of the vdWhs on the plasmon properties, we first investigate the role of the substrate on which the total system of vdW coupled layers rest. We assume this substrate to be SiO_2, which is frequently used for this purpose [263, 268, 275, 281]. Furthermore, we use the well-studied hBN-graphene heterostructure as a means to calibrate the QEH code against two sets of experimental results [21, 265].

7.3.1 The importance of substrate surface phonons

In order to elucidate the effect of the SiO_2 substrate and to calibrate the QEH implementation of substrate effects, we consider the environmental dielectric function $\epsilon_{\text{sub}}(\omega)$ as discussed in Sec. 7.2.1 both in the RPA treatment and with the QEH model. Table 7.1 contains the values of the frequency $\omega_{\text{TO},n}$ and oscillator strength f_n of the three TO surface phonons present in SiO_2 [263]. The high-frequency limit of the SiO_2 in-plane dielectric constant is $\epsilon_{\parallel}^{\infty} = 2.4$.

In Fig. 7.2(a) we show that RPA and QEH are in excellent agreement by comparing

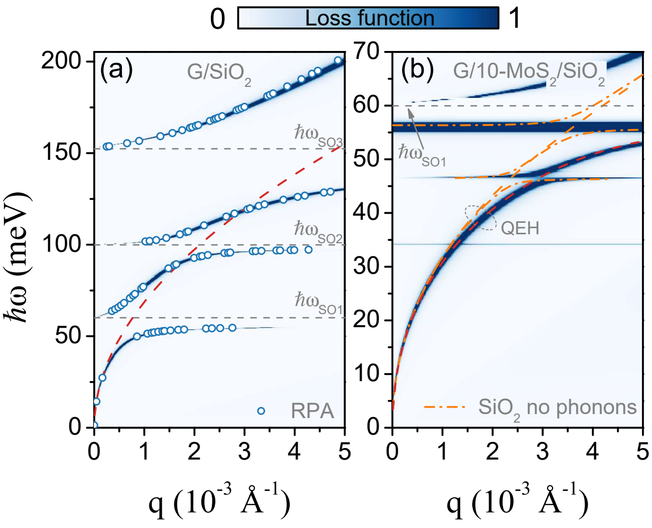

Figure 7.2: (Color online) (a) Comparison between the QEH (loss function) and RPA (symbols) for the SP^3 dispersion in graphene with $E_F = 0.4$ eV on SiO_2 as a substrate. Hybridization with the substrate phonons ($\hbar\omega_{SOi=1,2,3}$, horizontal gray dashed lines) is clearly visible. (b) Results at $E_F = 0.1$ eV for G/10-MoS_2 on SiO_2 with phonons (loss function) and without phonons (dash-dotted orange lines), as calculated the QEH. The unhybridized phonon modes, horizontal blue branches in the loss function, have been omitted for G/10-MoS_2 on SiO_2 without phonons (dash-dotted orange lines). For reference, in (a) and (b), the SP^2 dispersion without phonons is presented as dashed lines (red and orange, respectively).

the loss function of QEH with the exact zeroes of the RPA dielectric function. Here, we assumed a graphene $E_F = 0.37$ eV on SiO_2 with three phonons as indicated by the horizontal lines. There are three regions where the SP^2 hybridizes into SP^3 modes due to the coupling with the surface phonons of the SiO_2 substrate. For reference, we represent in Fig. 7.2(a) the SP^2 dispersion for G/SiO_2 (dashed red curve) with a static dielectric constant $\epsilon_0 = 3.9$ [282].

The inclusion of substrate phonons is important in studying plasmon properties of vdWhs. This is shown in Fig. 7.2(b), where we used the QEH model for a vdWh with ten layers of MoS_2 with and without substrate phonons. This reflects directly on the SP^3 dispersion, where in addition to coupling with two of the MoS_2 phonons, the plasmons will also couple with the SiO_2 surface phonons. Notice that the influence on the SP^3 mode is not only manifested at the first phonon frequency $\hbar\omega_{\mathrm{SO1}}$, but results in an up to 27% decrease in plasmon wavelength at $\hbar\omega = 50$ meV, i.e. increase in plasmon wave vector q even at much lower frequencies.

7.3.2 Calibration of the QEH model for G/N-hBN vdWhs

Using the QEH, we shown in Fig. 7.3(a) the dispersion of SP^2 modes for different values of the Fermi energy E_F. In the non-retarded regime, these parabolic curves are described by the simple equation [17, 250, 251] $\omega \sim \sqrt{E_{\mathrm{F}} q/\epsilon}$. In Fig. 7.3(b), we show the QEH loss function in the absence of a doped graphene sheet for a system containing 100 hBN layers, i.e. a slab of about 33.3 nm thick [283]. We see the presence of so-called hyperbolic phonon polaritons (HP^2) that appear in two given energy bands due to the anisotropy of the hBN dielectric tensor [145, 270]. The two hyperbolic regions, denominated as Reststrahlen (RS) bands, are defined as energy regions where one of the coefficients of the dielectric tensor becomes negative. Due to the fact that these modes are trapped inside the hBN slab, discretization of energy appears.

Upon the addition of a doped graphene sheet, the SP^2 modes can hybridize with the HP^2 modes of the hBN material, giving rise to new mixed SP^3 and hyperbolic plasmon-polariton (HP^3) modes as presented in Fig. 7.3(c) for G/10-hBN and G/50-hBN with $E_{\mathrm{F}} = 400$ meV. We point out that due to the hyperbolicity of the HP^2 modes, the wavelength dependence on the number of hBN layers is opposite for the upper branch of the SP^3 modes with respect to the lower branch. This comes as a surprise, since one would expect that screening for a thicker hBN slab should be more important than for a thinner one. However, this observation underlines the difference of HP^2 modes with respect to normal phonon polariton modes as presented in the MX_2 examples in the next section. Also, notice that upon comparison of the hBN results with the MoS_2 results presented in Fig. 7.2(b), one can see that in the absence of hyperbolicity, no confined modes appear.

A comparison of the results obtained from the QEH and those obtained experimentally for the SP^3 and HP^3(II) modes (the experimental data were extracted from Refs. [21] and [265], respectively) is illustrated in Figs. 7.3(d)-(e) and shows very good agreement. Fig-

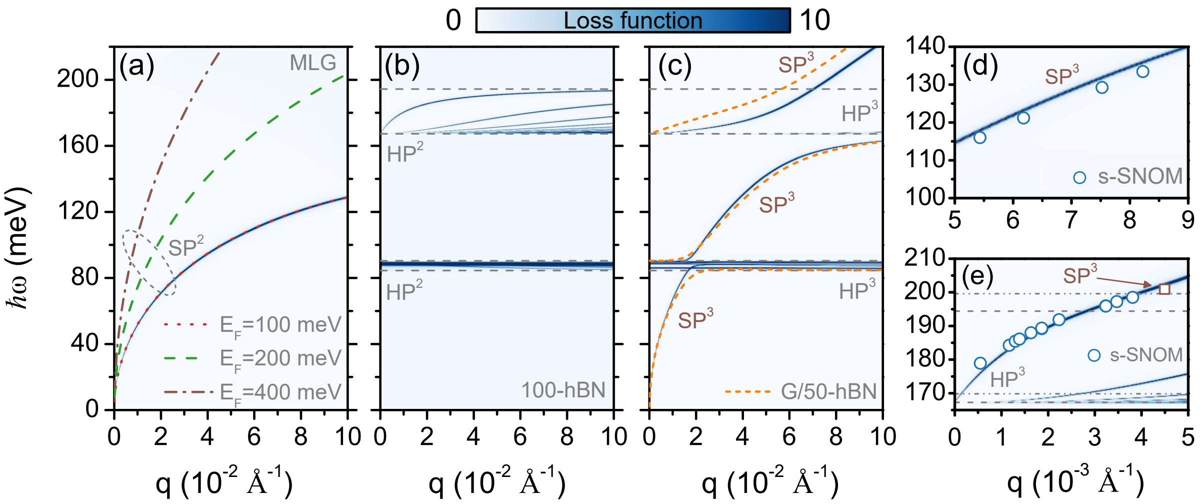

Figure 7.3: (Color online) (a) Plasmon dispersion of the SP^2 in free-standing MLG with Fermi energies of $E_F = 100$ meV, 200 meV and 400 meV. (b) Calculated dispersion of the HP^2 in 100 h-BN layers. The hyperbolic regions type I and II correspond to the regions between the two upper and lower grey dashed lines, respectively. (c) Plasmon-phonon dispersion for MLG with $E_F = 400$ meV on 10, represented by the loss function, and 50 h-BN layers with SiO$_2$ (without phonons) as substrate (G/N-hBN/SiO$_2$), represented by the orange dashed lines. (d) and (e) are a comparison between the QEH model and experimental results (symbols) [21, 265] for 21-hBN/G/138-hBN and G/75-hBN, respectively. In panel (e), the RS band II, obtained from the QEH, is delimited by the dashed gray lines (for comparison, the horizontal gray dashed dotted-dotted lines obtained from Ref [[284]] using solely first principles calculations is used as reference in (e)). The experimental data used in (d) and (e) were extracted from Refs. [21] and [265]. A false color map represents the loss function in arbitrary units.

ure 7.3(d) shows the SP^3 dispersion for graphene encapsulated by hBN (21-hBN/G/138-hBN) and Fig. 7.3(e) presents the results for G/75-hBN. Notice that upon comparison to the literature, it becomes clear that the exact spectral position of the RS bands is not yet uniquely determined. In the Appendix, we compare the QEH model to different definitions and show our obtained results for the frequencies that define the two RS in hBN, as well as the phonon frequencies for a free-standing monolayer of all TMDs considered in this chapter.

7.4 Probing layer structure and composition

Now, we are in a position to show how one can use SP^2 and SP^3 modes to probe the layer structure and the composition of the vdWhs. To do so, we assess the plasmon-phonon dispersion of four types of TMDs, namely MoS$_2$, MoSe$_2$, WS$_2$ and WSe$_2$. These materials are often used in the construction of vdWhs [146, 157, 158, 162, 165, 171, 270,

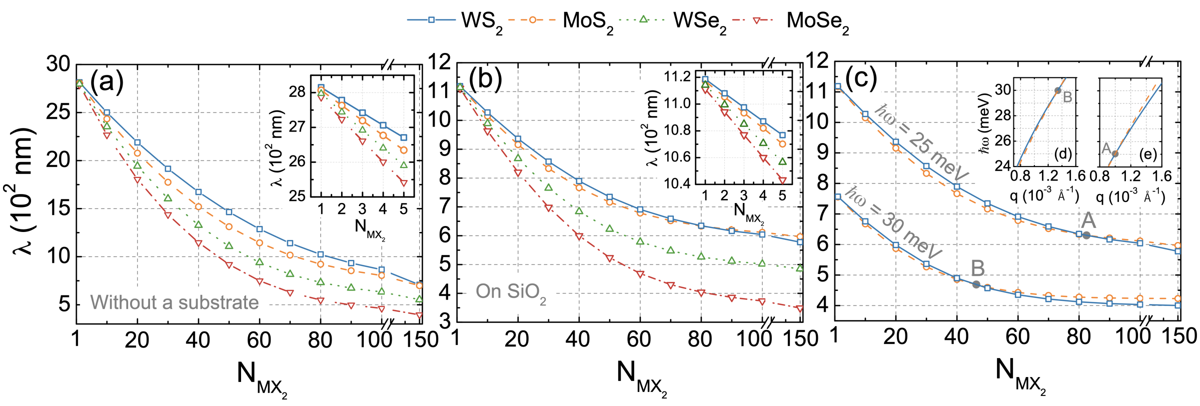

Figure 7.4: (Color online) Graphene surface plasmon-polariton wavelength as a function of the number of layers of $MoSe_2$ (red), WSe_2 (green), MoS_2 (orange) and WS_2 (blue) for $\hbar\omega = 25$ meV (≈6 THz) at $E_F = 100$ meV, (a) without a substrate and (b) with SiO_2 as a substrate. The insets in (a) and (b) show a magnification of the the results for 1 to 5 layers of MX_2 without and with a substrate, respectively. (c) Comparison between the SP^3 wavelength for G/N-MoS_2/SiO_2 and G/N-WS_2/SiO_2 at frequencies 25 and 30 meV, respectively. The crossing between the plasmon wavelengths at frequency 30 meV (25 meV) is represented by a grey circle labeled B (A). Inset (d) shows a comparison between the plasmon dispersions for G/44-MoS_2/SiO_2 and G/44-WS_2/SiO_2. Inset (e) is the same as (d) but now considering 82 layers of WS_2 and MoS_2.

285]. Moreover, their chemical similarity makes them interesting candidates to show the sensitivity of the proposed approach. Finally, because of their shared crystallographic structure, namely they all have a MX_2 form, the number of phonon modes in the 2D materials is all the same, but their respective phonon frequencies differ. For reference, the phonon frequencies of freestanding monolayer for each TMDs used in this study, i.e for MoS_2, WS_2, $MoSe_2$ and WSe_2, obtained from the QEH, are provided in Table E.2.

7.4.1 Probing the number of layers

In Fig. 7.4 we show how the addition of individual MX_2 layers affects the Dirac plasmon wavelength λ for each structure. We fixed the graphene doping at $E_F = 100$ meV and excitation frequency $\hbar\omega = 25$ meV. The latter is chosen to be below all phonon frequencies in both the substrate and the different MX_2 layers. In this way, we mainly excite SP^2 modes and the effect should be mainly attributed to an increase in dielectric screening due to the permittivity of the MX_2 layers.

Panel (a) in Fig. 7.4 shows how the plasmon wavelength decreases with the number of MX_2 layers added when no substrate is considered. Also, we show the 'bulk' limit, which is achieved only at about 150 layers. Results for $N > 150$ are verified to be the same (within numerical accuracy) up to 350 MX_2 layers, thus confirming this bulk limit. This is a surprisingly large number of layers. It was previously established that

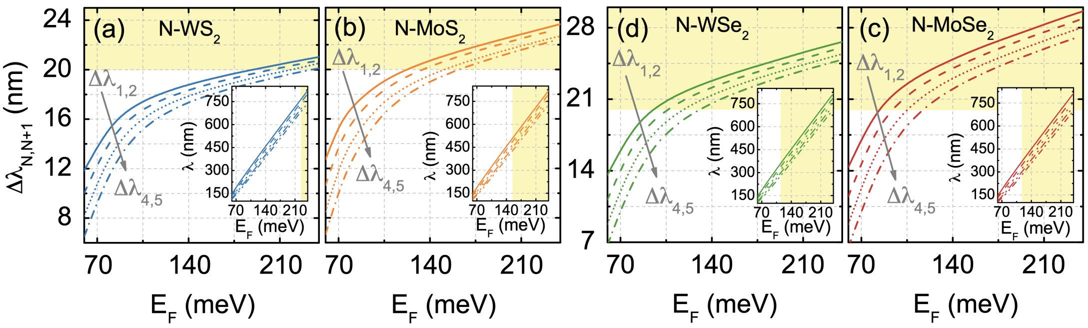

Figure 7.5: (Color online) Difference in the wavelength ($\Delta\lambda_{N,N+1}$) at $\hbar\omega = 65$ meV ($\approx$15.7 THz) between numbers of layers N and N+1, from $N = 1$ to 5, for (a) G/N-WS$_2$/SiO$_2$, (b) G/N-MoS$_2$/SiO$_2$, (c) G/N-MoSe$_2$/SiO$_2$ and (d) G/N-WSe$_2$/SiO$_2$. Inset is the wavelength as a function of Fermi level E_F at the same frequency. Yellow regions corresponds to $\Delta\lambda_{N,N+1} \geq 20$ nm.

multilayered structures, such as graphite [193], achieve their bulk electronic properties at about 10 layers. However, here we show that this does not work for the plasmonic properties, where at least hundreds of layers are needed for bulk behaviour to occur. This observation underlines the necessity for a realistic modeling of plasmon properties, as performed with the QEH model. In Fig. 7.4(b), we show how a SiO$_2$ substrate affects the layer dependency. As expected, the substrate results in an overall screening and the wavelength is reduced. Also here, bulk TMD behaviour is reached for about 150 layers.

Notice that, interestingly, the order of the wavelength values of WS$_2$ and MoS$_2$ is switched when increasing the number of layers. Indeed, while for a few layers, the wavelength in the WS$_2$ system is the largest, in the bulk case, it is the MoS$_2$ system that has the largest wavelength. To describe this peculiar effect, in Fig. 7.4(c), we show both results for two different frequencies. As one can see, for a frequency closer to the first phonon frequency of MoS$_2$ (see Tab. E.2), for example $\hbar\omega = 30$ meV, the crossing occurs for a smaller number of layers than for $\hbar\omega = 25$ meV. This is a direct consequence of the presence of phonons in MoS$_2$. The lowest of them has a frequency given by 34 meV. In WS$_2$, the phonons at 36 meV are not significantly hybridized into SP^3 modes, causing this crossing between the plasmon wavelength of these two TMDs. A comparison between the plasmon dispersions for 44 and 82 layers of WS$_2$ and MoS$_2$ is depicted in Figs. 7.4(d) and 7.4(e), respectively, where one can see the crossings at 30 meV (d) and 25 meV (e).

Finally, in Fig. 7.5 we show the sensitivity of the proposed method with respect to the number of MX$_2$ layers. As a function of the induced Fermi level in the graphene layer, we show the difference in plasmon wavelength between structures that differ only by one layer. Assuming a lower threshold of 20 nm for the wavelength resolution, we see that for Fermi levels of more than 140 meV, we can achieve single-layer resolution for every considered TMD-based vdWh.

7.4.2 Probing vdWh composition

In order to assess the difference between several MX_2 structures, in Fig. 8.4 we show the full loss function for the four considered vdWHs, accounting for substrate and TMD phonons. The number of layers remains constant $N_{\mathrm{MX}_2} = 1$ (loss function) and 50 (orange lines), and we consider free-standing structures and those on a SiO_2 substrate.

The loss function presented in the (q, ω)-plane shows more insight in the behaviour of the different SP^3 modes than only through calculating the experimentally relevant wavelength. Indeed, in the different panels of Fig. 8.4 one can not only distinguish the way in which an increase in the number of vdWhs layers increases the wavevector q (hence decreasing the wavelength λ), but also verify that each TMD structure bears its own spectrum of phonons. These phonons are the ones that hybridize with the Dirac plasmons and form the SP^3 modes and, by investigating the specific type of hybridization, one can infer the chemical properties of the vdWh under consideration. In general, the MX_2 type TMDs considered in this chapter have, in their monolayer form, three acoustic and six optical phonon modes [285–290]. However, because of the long-wavelength character of the discussed modes, we only excite optical ones at the frequencies considered here. Furthermore, due to symmetry considerations, two pairs of modes are degenerate in the $q \to 0$ limit. More details about the phonon structure of these materials are laid down in appendix E.2.

First, we scrutinize the top row of Fig. 8.4, in which there is no substrate. Although such TMDs have four distinct optical phonon frequencies, as presented in Tab. E.2 of the Appendix appendix E.2, not all modes are strongly coupled to plasmons. Typically, the highest energy mode, i.e. the A_2'' mode, is strongly active in the loss function. However, it is clear that the Dirac plasmon mode also interferes with the other three phonon modes. Furthermore, this interference becomes much more pronounced as the thickness of the TMD stack is increased. This is shown in the insets of panels (a) and (b), where small hybridization with the E'' modes is shown.

In Fig. 8.4(b) we show the results for a WS_2 heterostructure. While the A_2'' mode is more pronounced, the plasmon-phonon hybridization of the other three modes is significantly smaller. Notice that the spectral width of the top mode is also broader than in the case of the MoS_2 stack. In Figs. 8.4(c) and 8.4(d), the chemical composition of the TMD stacks is changed with a replacement of the sulfur atoms by selenium. Again, a typical phonon spectrum is present, yielding specific types of SP^3 modes.

The bottom row of Fig. 8.4 shows the loss function when a SiO_2 substrate is added. A gray dashed horizontal line indicates the presence of the substrate surface phonons as discussed in the previous section. These substrate phonons also hybridize with the Dirac plasmons and render the high-frequency response of the different vdWhs almost identical. For lower frequencies, the additional SiO_2 environment significantly reduces the plasmon wavelength. But furthermore, the most significant effect of the presence of the substrate is the broadening of the A_2'' phonon spectrum. A more in-depth analysis of

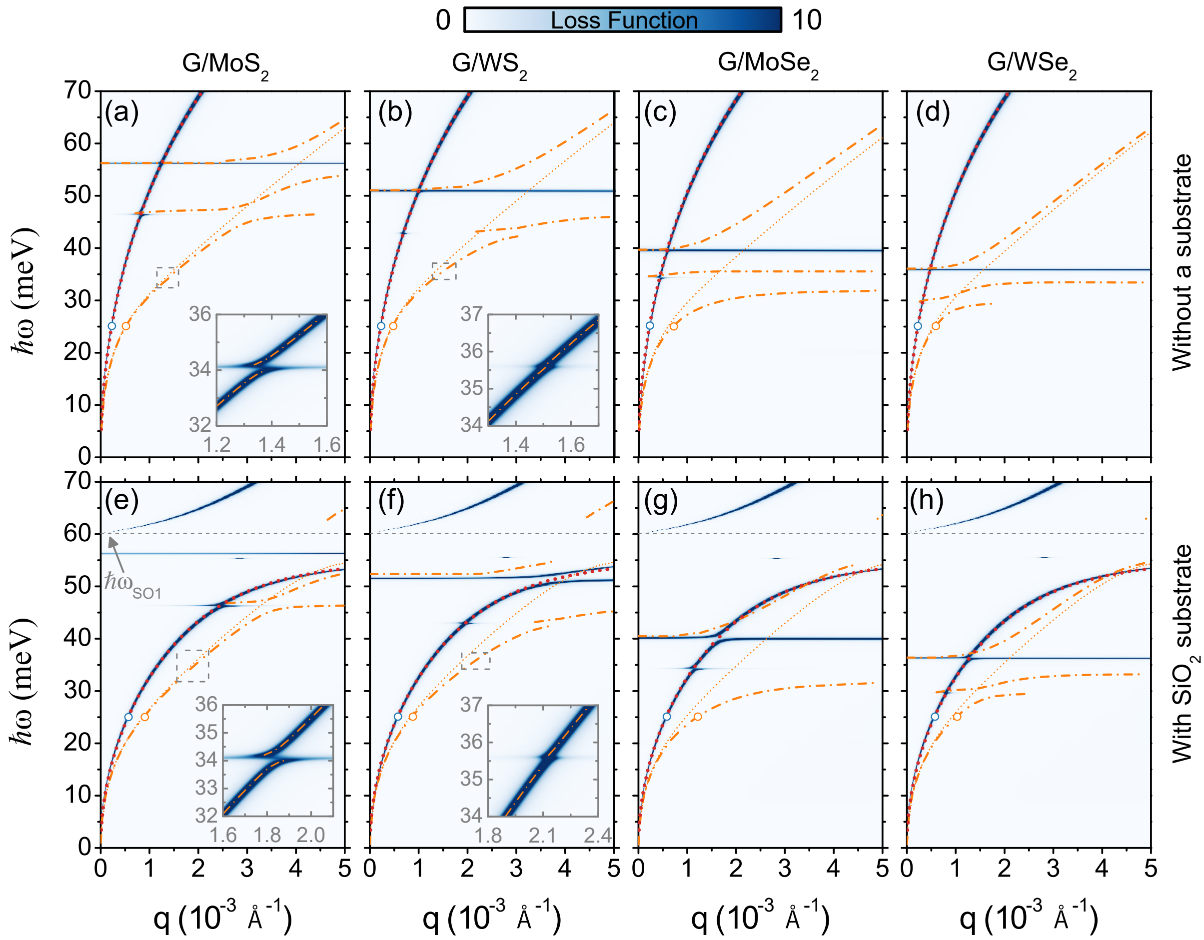

Figure 7.6: (Color online) Overview of the frequency and wave vector dependence of the plasmon SP^3, at $E_F = 100$ meV, for vdWhs with 1 and 50 TMD layers. The background shading is the loss function for $N = 1$ TMD layers. The orange curves correspond to $N = 50$. The different TMDs under consideration are indicated on the top of each column. The top row are for vdWhs without a substrate, while for the bottom row they are positioned on top of a SiO$_2$ substrate. The inset in (a), (b), (e) and (f) show magnifications around the anti-crossing. The red and orange dotted curves denote the SP^2 modes, for reference.

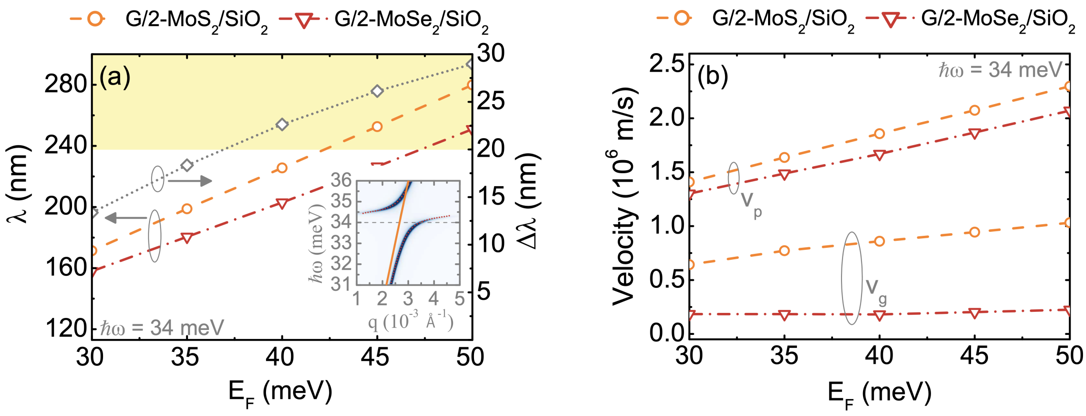

Figure 7.7: (Color online) (a) Graphene surface plasmon-polariton wavelength as a function of the Fermi energy E_F for G/2-MoS$_2$/SiO$_2$ (orange dashed line) and G/2-MoSe$_2$/SiO$_2$ (red dash-dotted line) and their respective differences $\Delta\lambda$ (gray dotted lines), at $\hbar\omega = 34$ meV ($\approx$8.2 THz). The yellow region represents $\Delta\lambda \geq 20$ nm (see right scale). The inset shows the plasmon-phonon dispersion at $E_F = 45$ meV near the hybridization region. The grey dashed line in the inset is at $\hbar\omega = 34$ meV and the orange solid line (dotted red lines) is the result for G/2-MoS$_2$/SiO$_2$ (G/2-MoSe$_2$/SiO$_2$). (b) Group velocity (V_g) and phase velocity (V_p) for the same vdWh as in (a).

the relation between the substrate phonons in SiO$_2$ and the TMD phonons is referred to future research.

Finally, we are now in a position to propose a method to discriminate between different vdWhs based on the Dirac plasmon wavelength. To do so, in Fig. 7.7, we have calculated the wavelength of two types of heterostructures that differ only in one type of atom, MoS$_2$ and MoSe$_2$, at a given plasmon energy $\hbar\omega = 34$ meV ($\approx$8.2 THz). In Fig. 7.7(a), the left axis gives the total value of the wavelength for given vdWhs, while the right axis refers to the difference $\Delta\lambda$ between both modes' wavelengths. The result indicates that once the Fermi level E_F is large enough, in the present case larger than 35 meV, $\Delta\lambda$ is large enough to be distinguished by current techniques [20, 21, 265–270]. Notice that the difference between both heterostructures wavelengths depends also sensitively on the number of TMD layers in the vdWh. In the presented result, we assumed at least two TMD layers. For an increasing number of layers, the effect will be even stronger, rendering $N = 2$ as the lower threshold for distinguishing between chemical components, which is a remarkably sensitive result. Fig. 7.7(b) shows the group (V_g) and phase velocity (V_p) of the corresponding modes. Notice that, in this case, the group velocity of the MoSe$_2$ heterostructure Dirac plasmon is almost constant as a function of the Fermi level. This is in stark contrast with the doping dependency of the MoS$_2$-based system.

7.5 Conclusions of the chapter

We have demonstrated the possibility of using graphene plasmons to probe the non-local dynamical response of vdWHs composed by monolayer graphene on top of TMD multi-layers. In order to do so, we have calculated the loss function of graphene on top of different TMDs and demonstrated how its plasmon dispersion changes by the presence of the different materials and different numbers of layers underneath it. We have shown that the QEH model for this system provides excellent results when compared not only to available experimental data, but also to results obtained within the random phase approximation, rendering the QEH a good alternative for the theoretical understanding of experimental results involving plasmons in graphene-based vdWHs, as well as for the theoretical predictions shown here. Plasmons in graphene can be experimentally observed using, for example, scattering-type scanning near-field optical microscope (s-SNOM) in photocurrent mode, which has spatial resolution of at least 20 nm. Within this resolution, our results for the four TMD used here, namely MoS_2, $MoSe_2$, WS_2 and WSe_2, show that it is possible to use surface plasmon-polaritons in the graphene monolayer to probe the number of layers in the TMD stack underneath it, by analyzing the difference in the plasmon wavelength as the number of layers change. Moreover, since different TMDs exhibit distinct phonon frequencies, the hybrid surface plasmon-phonon-polariton states can be used to identify which species of TMD is underneath the graphene layer. The latter, however, require strong coupling between plasmons and phonons to allow one to distinguish between the characteristic wavelengths of different TMDs. Nevertheless, our results show that for a number of layers as low as $N = 2$, the plasmon-phonon coupling is still strong enough to produce distinguishable wavelengths for different materials, thus suggesting the method proposed here as a remarkably sensitive tool.

8

Tunable coupling of terahertz Dirac plasmons and phonons in transition metal dicalchogenide-based van der Waals heterostructures

Dirac plasmons in graphene hybridize with phonons of transition metal dichalcogenides (TMDs) when the materials are combined in so-called van der Waals heterostructures (vdWh), thus forming surface plasmon-phonon polaritons (SPPPs). The extend to which these modes are coupled depends on the TMD composition and structure, but also on the plasmons' properties.

In this chapter, the QEH is used again to study how the strength of plasmon-phonon coupling depends on the number and composition of TMD layers, on the graphene Fermi energy and the specific phonon mode. From this, we present a semiclassical theory that is capable of capturing all relevant characteristics of the SPPPs. We find that it is possible to realize both strong and ultra-strong coupling regimes by tuning graphene's Fermi energy and changing TMD layer number.

The study on *tunable coupling of terahertz Dirac plasmons and phonons in transition metal dicalchogenide-based van der Waals heterostructures*, developed in this chapter, was already submitted and an arXiv version can be accessed through this link.

8.1 Introduction

In the past few years, after the advent of graphene [8], a two-dimensional (2D) monolayer of carbon atoms arranged in a honeycomb lattice, the interest of the scientific community in isolating and studying new 2D materials has been significantly increasing due to the unique features of these materials [146, 164, 291], as discussed in sections 2.4 and 2.6. For example, 2D transition metal dichalcogenides (TMDs) [107, 147], such as MoS_2, $MoSe_2$, WS_2 and WSe_2, have attracted considerable attention due to their remarkable opto-electronic properties [20, 145, 146, 158–165] that arises, for example, due to their electronic band gaps [152, 154], the specific type of the electronic structure, and the intrinsic mobility of the electrons [203]. These 2D materials can be combined in so-called van der Waals heterostructures (vdWh) [146, 156, 157] by stacking different layers on top of each other [145–147, 158, 162, 165, 175], or even next to each other forming so-called lateral heterostructures [147, 172–177], resulting in the creation of many different multilayered artificial materials, each with specific behaviour [157, 171]. Recently, significant advances have been made to obtain and manufacture such heterostructures [107, 145–147, 157, 158, 171–177].

Graphene plasmons, collective excitations of the 2D electron liquid in graphene [16, 18], also known as Dirac plasmons [256], are heavily studied due to their low loss [281, 292], a dispersion relation that is tunable by the Fermi energy [20, 163, 268, 275] and their possible applications in photonics [117, 256, 293]. Besides, graphene can support plasmons at mid infrared (IR) [83, 159, 257] to terahertz (THz) frequencies [159, 163, 258, 259] and show strong electromagnetic field confinement [17, 256]. On the other hand, in TMDs (such as MoS_2 or WS_2, for example), active modes reside in the mid-IR range [285] and, due to their large electronic band gap [152, 153], these materials behave as dielectrics at low frequencies, thus not supporting plasmons if not extrinsically doped [260].

As illustrated in Fig. 8.1(a), when a monolayer graphene (MLG) is combined with layers of TMDs, forming graphene-based vdWhs, a hybrid excitation arises that is known as surface plasmon-phonon polaritons (SPPPs). These quasiparticles are formed when phonons in the TMDs are coupled to the electron oscillations in graphene [17]. One can excite and measure them using scatter-type scanning near-field optical microscopy (s-SNOM) [259, 266, 267]. This allows one to measure the SPPPs wavelength, with a resolution of up to 20 nm [20, 21, 265–270], using interference fringes formed by the scattering of SPPPs modes at the edge of the heterostructure or at lateral defects in the system. Although monolayer TMDs have four phonon modes in the IR spectrum, only two of them, the in-plane E'' and out-of-plane A_2'', illustrated in Fig. 8.1(b), are IR-active and can couple to Dirac plasmons [294, 295].

In analogy to two coupled harmonic oscillators [296], Fig. 8.1(c), when graphene plasmons and TMDs phonons are coupled, the eigenfrequencies of the system are modified, presenting a characteristic anti-crossing [294, 297], as shown in Fig. 8.1(d). By investigating the specific way in which the anti-crossing is manifested, one can infer the way in which hybridization occurs, quantified by the coupling strength, Ω, between Dirac plasmons and environmental phonons.

Whether hybridization is significant or not depends on the strength of the plasmon-phonon coupling when compared to other relevant energy scales, for example, the phonon energy and linewidth [297]. The latter is schematically presented in Fig. 8.1(d) as an orange shade along the hybrid modes. In this context, the splitting becomes only significant when the coupling Ω exceeds the linewidths of the two coupled systems, which also enables the experimental observation of these two modes. Thus, if Ω is very small compared to other important energy scales, for example, the phonon energy, the coupling is negligible and is not strong enough to change the original (uncoupled) frequencies. This defines

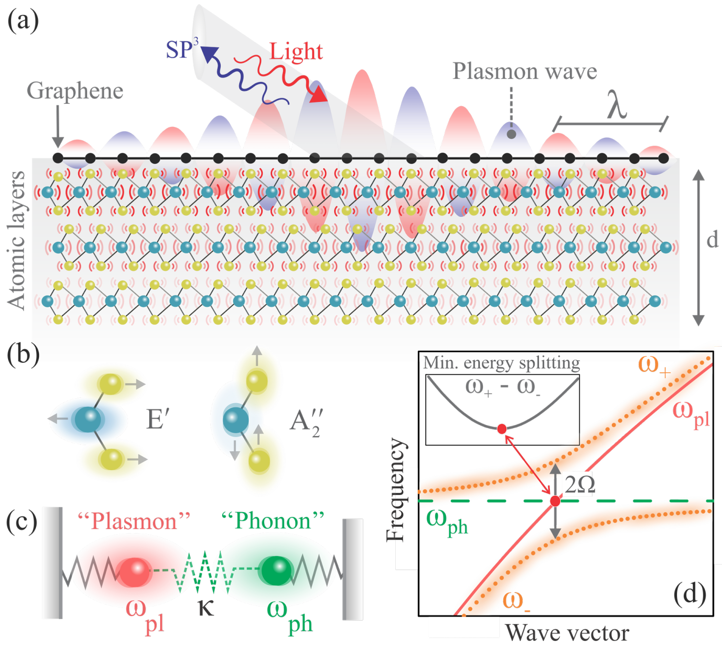

Figure 8.1: (Color online) (a) Schematic illustration of the Dirac plasmon wave and the phonon-polariton vibration in van der Waals heterostructures (vdWh) composed by a monolayer graphene (G) on 3-MX_2 (M=W,Mo and X=S,Se). The graphene surface plasmon-phonon polariton wavelength is λ. Note that the monolayer graphene covers the entire sample. The hybridization of the phonon-polariton vibration in a vdWh with the Dirac plasmon originates from the hybridized surface plasmons (SP_3). (b) Representation of the in-plane ($E_{//}$) and out-of-plane (A''_2) phonon vibration. (c) Plasmon and phonon coupling pictorially depicted as two coupled classical mechanical oscillators. The strength of the coupling is determined by κ and gives rise to a splitting in the two eigenfrequencies ω_{ph} and ω_{pl}. (d) Qualitative representation of the eigenfrequencies ω_{ph} (horizontal green dashed line) and ω_{pl} (solid red line) of the uncoupled ($\kappa = 0$) plasmon-phonon system. The modes of the coupled system is represented by the upper (ω_+) and lower (ω_-) eigenfrequencies (orange dotted lines), its difference is called minimal energy splitting (see inset). Ω quantifies the strength of the plasmon-phonon coupling.

different coupling regimes: the first one, where Ω is small, is classified as "weak coupling" (WC) [297, 298]. On the other hand, if Ω is large when compared to the phonon energy, the coupling modifies the original energy spectrum, creating hybrid plasmon-phonon modes. In this case, the coupling regime is classified as "strong" (SC) or "ultrastrong" coupling[1] (USC) [297, 298]. The latter enables more efficient plasmon-phonon interactions, resulting in electro-optical devices with high efficiency when compared to those based on SC [300]. For the purposes of this article, we define the WC, SC and USC regimes in a pragmatic way: after obtaining Ω, we normalize the coupling strength in relation to the phonon

---

[1] Although in this study we only address WC, SC and USC regimes, the deep-strong coupling (DSC), experimentally achieved in 2017 [299], is stronger then those threes.

frequency that originates the hybridization as $\eta = \Omega/\omega_{ph}$; then, we classify the system as WC, SC and USC when $\eta < 0.01$, $0.01 \leq \eta < 0.1$ and $\eta \geq 0.1$, respectively [300].

In this chapter an investigation on the coupling between Dirac plasmon and IR-active TMDs phonons is presented. Through realistic simulations at the level of density functional theory (DFT), many-body perturbation theory and the random phase approximation (RPA) [301, 302], in combination with the quantum electrostatic heterostructure model (QEH) [271], we are able to investigate the way in which the plasmon-phonon coupling depends on the number of heterostructure layers, define the coupling regime and, more significantly, identify how the Fermi energy contributes to maximize the coupling strength. Furthermore, the use of QEH also allows us to analyse how the properties of the environment are affected even when a single monolayer is added to the vdWhs. We show that a semiclassical theory within the RPA is capable of capturing all relevant characteristics of the SPPPs coupling taking into account the TMDs thickness up to several layers. Therefore, we provide a realistic evaluation of the way in which the phonon modes of the TMDs layers couple to the electromagnetic field of the plasmon modes and describe the dependence of the coupling strength up to the bulk limit. Finally, we show how controlling the graphene Fermi energy can maximize the coupling, towards SC and USC regimes in TMDs-based vdWhs. Although the study presented here considers only hexagonal MoS_2 and WS_2, it can easily be extended to all other TMDs.

8.2 Plasmon-phonon-polaritons and hybrid modes

Dirac plasmons, density oscillations of Dirac fermions in graphene, can be obtained from the total system's dielectric function $\epsilon(q,\omega)$ within the random phase approximation (RPA) [16, 254]. To do so, we find the solution of the plasmon equation which corresponds to the zeroes of $\epsilon(q,\omega)$ taking [16, 18, 250, 251, 254, 255]

$$\epsilon(q,\omega) = 1 - v(q,\omega)\tilde{\chi}_{\rm nn}(q,\omega) = 0 \ , \tag{8.1}$$

where $v\,(q,\omega)$ is the Fourier transform of the Coulomb interaction between the Dirac electrons and $\tilde{\chi}_{\rm nn}(q,\omega)$ is the proper density-density response function [16]. In general, both functions depend on the properties of the system as a whole. Nevertheless, within the RPA, we can approximate $\tilde{\chi}_{\rm nn}(q,\omega)$ by the non-interacting density-density response function[2] of a 2D massless Dirac fermion $\chi^0(q,\omega)$, which depends only on the properties of graphene [250, 251, 255]. On the other hand, $v\,(q,\omega)$ describes the electromagnetic field lines that mainly propagate through the surrounding of the graphene sheet, and are, therefore, strongly affected by them. In general, the 2D Fourier transform of the electron-electron Coulomb interaction is defined as

$$v(q,\omega) = \frac{2\pi e^2}{q\epsilon_{\rm env}(q,d)} \ . \tag{8.2}$$

---

[2] For simplicity, the subscript nn was omitted.

As one can see from Eq. (8.2), it is the screening of the Coulomb interaction introduced by the effective dynamical background dielectric function $\epsilon_{\text{env}}(q)$ that encodes the presence of the environment. To include the contribution of the TMDs thickness d (see Fig. 8.1(a)) to the screening, we define the background dielectric function as [303]

$$\epsilon_{\text{env}}(q,d) = \left(\frac{2}{\epsilon_a + \epsilon_b} \frac{\sqrt{\epsilon_x(d)\epsilon_z(d)} + \epsilon_b\, \xi(d)}{\sqrt{\epsilon_x(d)\epsilon_z(d)} + \tilde{\epsilon}\, \xi(d)} \right)^{-1} . \tag{8.3}$$

In Eq. (8.3), we have $\xi(d) = \tanh(qd\sqrt{\epsilon_x(d)/\epsilon_z(d)}$ and $\tilde{\varepsilon} = (\epsilon_x(d)\epsilon_z(d) + \epsilon_a\epsilon_b)/\,(\epsilon_a + \epsilon_b)$. $\epsilon_{a,b} = 1$ is the dielectric constant of the vacuum above and below the 2D materials slab. $\epsilon_x(d)$ and $\epsilon_z(d)$ are, respectively, the static in-plane and out-of-plane dielectric constants of the TMDs, where we have modified the notation to explicitly indicate its dependence on the TMDs thickness [304, 305]. In order to facilitate the understanding of how plasmons couple with phonons, giving rise to hybrid modes, we assume that the plasmon dispersion attains its long-wavelength form, [17, 250, 251]

$$\hbar\omega_{pl} = \sqrt{\frac{\alpha_{ee} N_F \hbar v_F}{2} \frac{E_F q}{\epsilon_{\text{env}}(q,d)}} . \tag{8.4}$$

In Eq. (8.4), $\alpha_{\text{ee}} = 2.2$, $N_F = 4$ and $v_{\text{F}} = 10^6$ m/s are parameters related to the graphene sheet corresponding to the graphene fine structure constant, the number of Fermion flavours and the Fermi velocity, respectively [203]. E_{F} is the Fermi level of graphene.

8.2.1 Coupling Dirac plasmon to phonons polaritons

To introduce the concept of plasmon-phonon coupling, the simple classical analogy with two coupled harmonic oscillators, pictorially represented in Fig. 8.1(c) with “plasmon" and “phonon" representing the masses a and b, respectively, is commonly used [294, 297]. When $\kappa \neq 0$ the two oscillators interact with each other, forming a unique system, with hybridized eigenfrequencies [296]. Due to this hybridization, an anticrossing of dispersion curves is formed, resulting in a coupling strength[296]:

$$2\Omega = \frac{\kappa}{\sqrt{m_a \omega_a m_b \omega_b}} . \tag{8.5}$$

In the context of SPPPs, the coupling is similar to this classical point of view: when Dirac plasmons couple to the TMDs IR-active phonons, a hybridization occurs at $\omega_{\text{pl}} = \omega_{\text{ph}}$, giving rise to an anticrossing in the SPPPs dispersion for frequencies close to the phonon frequency, as presented in Fig. 8.1(d). For frequencies further away from the phonon frequency, the original energy remains practically unchanged from the uncoupled case. In other words, the uncoupled phonon (ω_{ph}) and graphene plasmon (ω_{pl}) frequencies, represented in Fig. 8.1(d) as a horizontal green dashed and a solid red ($\propto \sqrt{q}$) lines, respectively, presents hybrid modes (ω_+ and ω_-) close to the phonon frequency when coupled.

To quantify the SPPPs coupling (Ω), we start from its Hamiltonian, defined as [306]

$$H = H_{\mathrm{pl}} + H_{\mathrm{ph}} + H_{\mathrm{pl-ph}} \ . \tag{8.6}$$

Here, H_{pl} is the Hamiltonian for the plasmons in the absence of the coupling to the phonons H_{ph}, while $H_{\mathrm{pl-ph}}$ describes the coupling between them. In second quantization notation, this yields [306]

$$H = \hbar[\omega_{\mathrm{pl}}\hat{a}^{\dagger}_{\mathbf{q}}\hat{a}_{\mathbf{q}} + \omega_{\mathrm{ph}}\hat{b}^{\dagger}_{\mathbf{q}}\hat{b}_{\mathbf{q}} + \Omega_{\mathbf{q}}(\hat{a}^{\dagger}_{\mathbf{q}} + \hat{a}_{-\mathbf{q}})(\hat{b}^{\dagger}_{-\mathbf{q}} + \hat{b}_{\mathbf{q}})] \ , \tag{8.7}$$

where $\hat{a}^{\dagger}_{\mathbf{q}}$ and $\hat{a}_{\mathbf{q}}$ are creation and annihilation operators, respectively, for a Dirac plasmon (SP^2) with frequency $\hbar\omega_{\mathrm{pl}}$ given by Eq. (8.4), and wave vector $\mathbf{q}$. $\hat{b}^{\dagger}_{\mathbf{q}}$ and $\hat{b}_{\mathbf{q}}$ are those for the collective vibration modes with energy $\hbar\omega_{\mathrm{ph}}$ (taken as a constant, as presented in Tab. E.2). In Eq. (8.7), $\Omega_{\mathbf{q}}$ plays the role of the coupling energy associated with the interaction between phonons and the Dirac plasmon. Consequently, the eigenfrequencies are obtained taking $\det[H] = 0$, resulting in [306]

$$\omega^2_{\pm} = \frac{1}{2}\left[\omega^2_{\mathrm{ph}} + \omega^2_{\mathrm{pl}} \pm \sqrt{(\omega^2_{\mathrm{ph}} - \omega^2_{\mathrm{pl}})^2 + 16\Omega^2\omega_{\mathrm{ph}}\omega_{\mathrm{pl}}}\ \right] . \tag{8.8}$$

For simplicity, the subscript $\boldsymbol{q}$ in the variable Ω was omitted. Equation (8.8) is similar to those obtained from a classical system formed by two coupled oscillators [296], where the coupling Ω arises due to the hybridization between two (quasi)-particles, as shown in Fig. 8.1(d).

The goal of the current study is to identify the coupling strength Ω from realistic calculations of the anticrossing between plasmon and phonon branches. From Eq. (8.8), one finds that Ω can be calculated in two ways: on the one hand, one can find the minimum of the energy difference between the two branches, i.e. $\Omega_{\mathrm{min}} = \min_q(\omega_+(q) - \omega_-(q))$ (see Fig. 8.1(d)). On the other hand, it can also be calculated at the crossing point of the phonon frequency with the unperturbed plasmon. Here, the coupling strength corresponds to the energy difference between the two branches evaluated at the wave vector $q_{\mathrm{pl}}(\omega_{\mathrm{ph}})$, i.e. $\Omega_{\mathrm{cp}} = \omega_+(q_{\mathrm{pl}}) - \omega_-(q_{\mathrm{pl}})$. Note that in the case of a system consisting of a single plasmon and phonon, both methods are equivalent, because in that case Eq. (8.7) corresponds to the full system. However, once multiple phonons start to interfere with the plasmon, the model is only approximately correct and both methods will not yield the same result. In order to quantify the plasmon-phonon interaction also in the presence of multiple phonons, we always evaluate Ω using both methods. If the difference between both methods is large with respect to the nominal value of the coupling, i.e. if $\Delta\Omega = |\Omega_{\mathrm{cp}} - \Omega_{min}| \sim \Omega_i$, a hierarchy is necessary. For example, in the case where there are two relevant phonon modes, as discussed in the succeeding examples of this work, we find that it is necessary to calculate Ω_{min} for the smallest value, while Ω_{cp} is needed for the strongest coupling. This is because, in that case, the plasmon-phonon coupling becomes of the order of the frequency difference between the two involved phonon modes.

Table 8.1: Phonon frequencies for the free-standing monolayer of MoS_2 and WS_2 considered in the QEH calculations. Their vibrational phonon modes are represented by E'' (R), E' (IR and R), A_1' (R) and A_2'' (IR), where IR (R) means that the mode is active for infrared (Raman) excitations [285–290].

	Phonon frequencies (meV)			
	1 (E'')	2 (E')	3 (A_1')	4 (A_2'')
MoS_2	34.19	46.35	47.59	56.80
WS_2	35.56	42.85	50.12	52.98

8.2.2 Quantum electrostatic heterostructure

To obtain realistic results for the plasmon-phonon coupling, we used again the quantum-electrostatic heterostructure (QEH) model, a DFT-based method [271]. This model has been demonstrated to be a very useful tool for the study of plasmons in different heterostructures [179, 272, 278, 307, 308]. In the QEH model, the dielectric constant of the monolayer that composes the vdWhs is calculated individually within the DFT. Then, using Coulomb interaction, the contributions of each freestanding atomic layer are coupled, and the total responses of the vdWhs is obtained [271]. The SPPPs coupling Ω is obtained from the loss function, which is defined as

$$L(q,\omega) = -\mathrm{Im}\left[\frac{1}{\epsilon(q,\omega)}\right] . \tag{8.9}$$

8.3 Strength of plasmon-phonon coupling in van der Waals heterostructures

TMDs are slightly polar materials i.e its crystalline structure contains atoms with different electronegativities, consequently, certain IR-active phonon modes at the Γ-point give rise to a macroscopic electric field [262, 287]. Both MoS_2 and WS_2, the TMDs considered in this here, present four phonon modes labelled, in ascending order of energy (see Tab. E.2), as: E'' (R), E' (IR and R), A_1' (R) and A_2'' (IR), where IR (R) means that the phonon mode is active for infrared (Raman) excitations [285].

In Fig. 8.2(a), we present the plasmon dispersion of SP^2 modes, i.e Dirac plasmons with the surrounding polarization cloud [17, 262], but disregarding the TMDs phonon vibrations, at the Fermi energy given by $E_F = 100$ meV, for a G/N-MoS_2 vdWhs, with $N = 1$, 10 and 20 TMD layers. The loss functions obtained by the QEH calculation, shown as a color map for $N = 10$, are in accordance with Eq. (8.4), whose results are represented by white dashed curves in Fig. 8.2(a). As the number of layers increases, q increases for a fixed frequency in the plasmon dispersion, since the total dielectric function of the environment $\epsilon_{\mathrm{env}}(q, d)$ also increases, since the screening is proportional to the

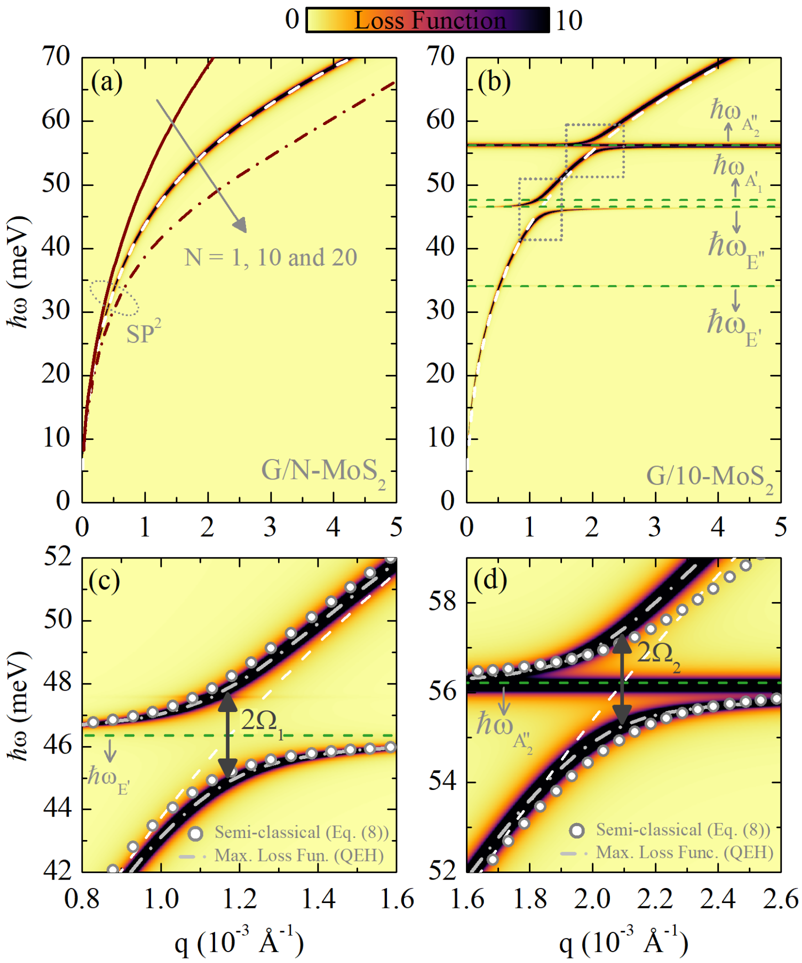

Figure 8.2: (Color online) (a) Plasmon dispersion of the SP^2 for G/N-MoS$_2$ with N=1 (solid), 10 (white dashed) and 20 (dashed-dotted) at E_F = 100 meV obtained from the QEH without plasmon-phonon coupling ($\Omega = 0$). The loss function is shown as a color map for N = 10. (b) SPPPs dispersion for G/10-MoS$_2$ with E_F = 100 meV. The two regions with IR-active phonons modes, namely E$''$ and A$''_2$, that hybridize with the Dirac plasmons giving rise to anti-crossings in the eigenfrequencies when $\omega_{pl} = \omega_{ph}$, are highlighted by two rectangles. Horizontal green dashed lines represents the phonon frequencies (see Tab. E.2). (c) and (d) are magnifications of the results in (b) around the anticrossings, close to the E'' and A$''_2$ phonon modes, with frequencies $\hbar\omega_{E'}$ and $\hbar\omega_{A''_2}$, respectively. In panel (c) and (d) $\Omega_{1(2)}$ represents the coupling strength between Dirac plasmon and IR-active in-plane (out-of-plane) vibrational phonon mode. Symbols are the eigenfrequencies obtained from the semi-classical model, Eq. (8.8). Dashed-doted gray lines are the maxima in the loss function, while the dashed white line is the SP^2 dispersion for reference.

number of layers. This is verified by the solid and dashed-dotted lines in Fig. 8.2(a), which represent the maxima of the loss function for $N = 1$ and 20, respectively. When phonon contributions are taken into account, as shown in Fig. 8.2(b), anticrossings in the SP^2 dispersion arise close to the regions where $\omega_{\text{pl}} = \omega_{\text{ph}}$. Although MoS$_2$ has four phonon modes, only two of them are IR-active, as mentioned earlier, giving rise to significant hybrid modes. These hybrid SPPPs modes are presented in Figs. 8.2(c)-(d) as a magnification of the two square boxes highlighted in Fig. 8.2(b). The coupling strength between the Dirac plasmons and the in-plane E$'$ (out-of-plane A$_2''$) phonon mode is defined as Ω_1 (Ω_2). In panels (c) and (d), the symbols refer to the hybrid eigenfrequencies obtained from Eq. (8.8).

8.3.1 The influence of the number of TMDs layers

Using the QEH, we show in Fig. 8.3(a)-(d) the evolution of the SPPPs coupling strength ($\Omega_{1(2)}$) as a function of the number of layers for a vdWhs composed by MLG on top of N-MoS$_2$ (blue symbols and lines) and N-WS$_2$ (orange symbols and lines). As the number of layers increase, the SPPPs coupling ($\Omega_{1(2)}$) also increases, since more oscillators are involved, i.e more phonons are available to couple with the Dirac plasmons [309, 310]. For a few TMD layers ($N < 10$), there are two important and peculiar aspects to be considered in here: (i) the $\sqrt{N}$ behavior of Ω_1, that is the coupling between plasmon and in-plane phonon modes, Fig. 8.3(b), and (ii) the linear dependence of the out-of-plane phonon coupling Ω_2, Fig. 8.3(d). To explain this behaviour, we analyse the effective dielectric function [309, 311]

$$\epsilon_i^{\text{eff}} \approx \epsilon_{\text{env}} \left(1 - \frac{\omega_{pl}^2}{\omega^2} - \frac{M_i \delta_i^2}{\omega^2 - \omega_{\text{ph},i}^2 + \delta_i^2} \right) . \tag{8.10}$$

Equation (8.10) describes an effective coupling between a plasmon and the i-th phonon mode. Notice that in the current case, the E' phonon and the A_2'' phonons exhibit different geometric properties. The former is an in-plane mode of which degeneracy M_i increases linearly with the number of layers N. Conversely, the latter is an out-of-plane mode with degeneracy scaling with N^2. In Eq. (8.10), δ_i is the coupling between a single TMD layer and the Dirac plasmon. Notice that this approximation only holds as long as the penetration depth of the plasmon mode is larger than the TMD thickness. In this case, the zeroes of Eq. (8.10) yield the relation between the hybrid modes as [309]

$$\omega_i \approx \omega_{\text{ph},i} \pm \frac{1}{2} \sqrt{M_i} \delta_i \; . \tag{8.11}$$

Therefore, Eq. (8.11) reveals that, within this model, the SPPPs coupling $\Omega_{1(2)}$ is indeed expected to depend on the number of layers N as $\Omega_{1(2)} = \sqrt{M_{1(2)}} \delta_{1(2)}$, where $M_{1(2)} = N^{1(2)}$.

8.3.2 SPPPs interaction: weak, strong and ultra-strong coupling regime

We now define the normalized parameter $\eta = \Omega_{1(2)}/\omega_{E''(A_2'')}$ as a way to quantify the coupling strength [300]. Figure 8.3(e) shows the normalized SPPPs coupling η as

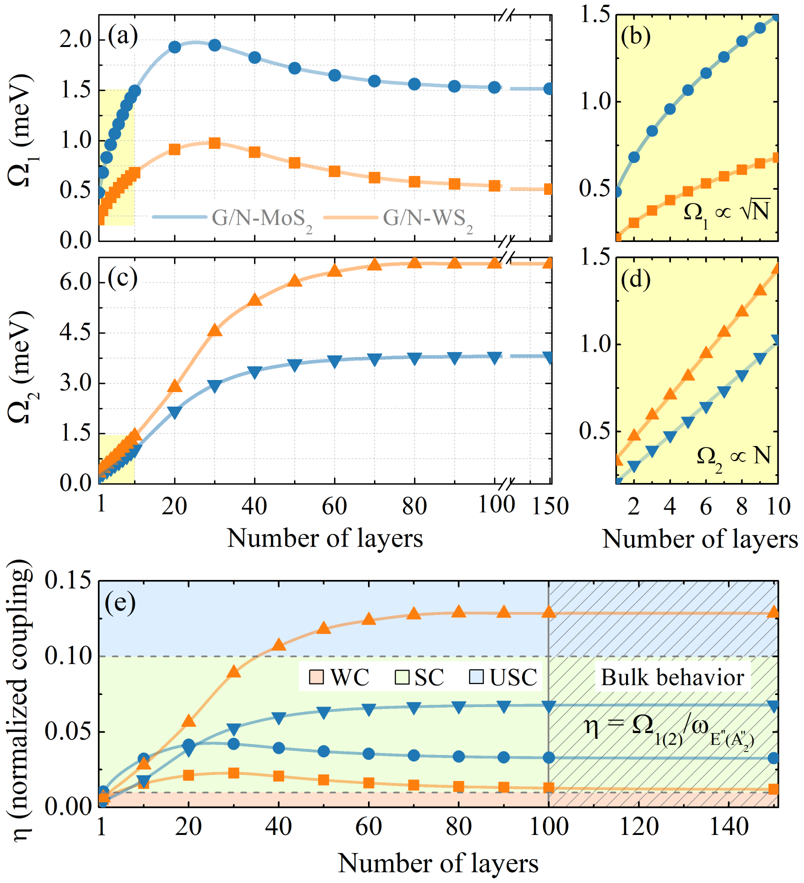

Figure 8.3: (Color online) SPPPs coupling strength ($\Omega_{1(2)}$) as a function of the number of TMDs layers for graphene at $E_F = 100$ meV on top of N-MoS$_2$ (blue lines and symbols) and N-WS$_2$ (orange lines and symbols). (a) Coupling energy between Dirac plasmon and the IR-active in-plane E' phonon mode and (b) a magnification of the results in (a) from 1 to 10 layers (yellow region), emphasizing that $\Omega_1 \propto \sqrt{N}$. (c) The same as in (a), but now for the coupling strength Ω_2, i.e considering the IR-active out-of-plane A$''_2$ phonon mode. (d) Magnification in panel (c) from 1 to 10 layers (yellow region), emphasizing that $\Omega_2 \propto N$. (e) SPPPs coupling strength normalized in relation to their respective phonon frequencies defined as $\eta = \Omega_{1(2)}/\omega_{E''(A''_2)}$. Three different regions, blue, green and pink, represent the WC ($\eta < 0.01$), SC ($0.01 \leq \eta < 0.1$) and USC ($\eta \geq 0.1$), respectively [300]. The hatched area represents the bulk limit of the SPPPs coupling, reached for approximately 100 TMDs layers.

a function of the number of N-MoS$_2$ and N-WS$_2$ layers. Three different regions, blue, green and pink, represent the WC ($\eta < 0.01$), SC ($0.01 \leq \eta < 0.1$) and USC ($\eta \geq 0.1$) regimes, respectively [300]. A remarkable result is obtained for the coupling between Dirac plasmons and the IR-active out-of-plane WS$_2$ phonon mode, where we observe that they reach the USC regime, as illustrated in Fig. 8.3(e) by orange triangles. Furthermore, for $N > 100$ all results remain unchanged, showing that the bulk behavior was reached for 100 TMD layers or more (see hatched area in Fig. 8.3(e)).

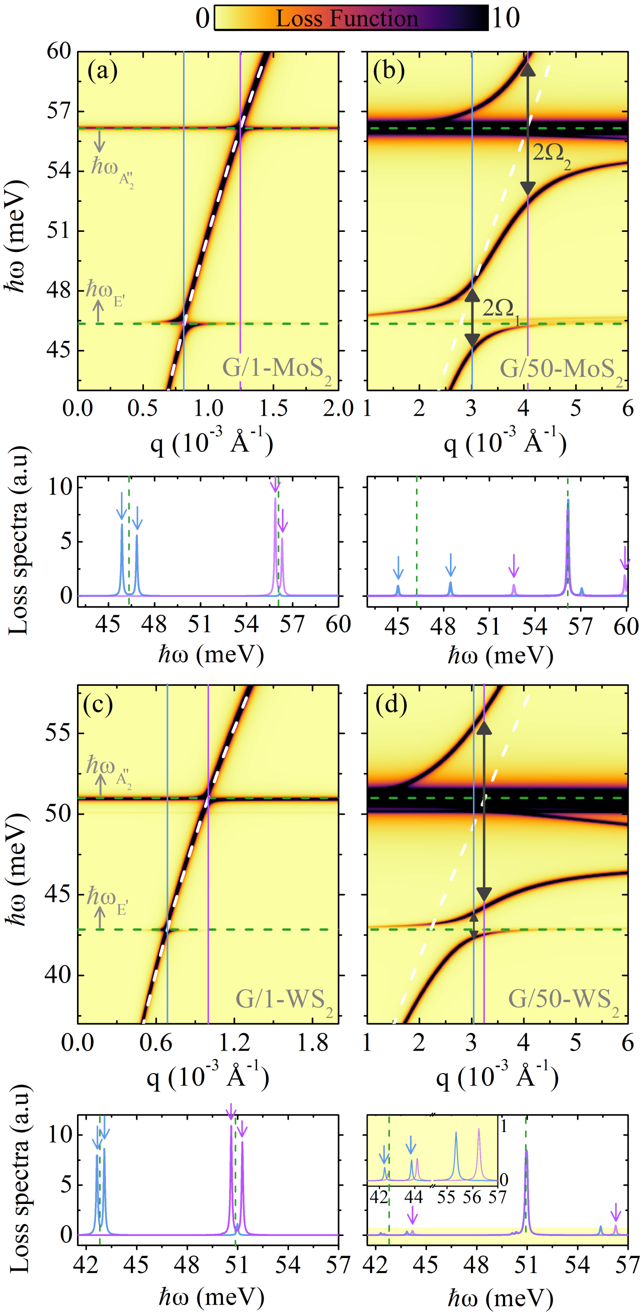

Figure 8.4: (Color online) Overview of SPPPs dispersion in the (q,ω)-plane through the loss function for a MLG, at $E_F = 100$ meV, on top of (a) 1 and (b) 50 MoS$_2$, and on top of (c) 1 and (d) 50 WS$_2$. Ω_1 (Ω_2) corresponds to the coupling strength between Dirac plasmons and the IR-active in-plane E$'$ (out-of-plane A$''_2$) phonon mode. The horizontal green curves correspond to the uncoupled phonon modes calculated for a monolayer of each correspondent TMD (see Tab. E.2 for the corespondent phonon frequencies $\hbar\omega_{E'}$ and $\hbar\omega_{A''_2}$). The uncoupled SP^2 plasmons are represented by white dashed lines, for reference. The results in each bottom panel are the loss spectra for a fixed q at the point were the SPPPs coupling strengths $\Omega_{1(2)}$ were calculated. In the bottom panel (d), a magnification of the loss spectra is shown as inset.

To illustrate the WC, SC and USC regime in a TMDs-based vdWhs, we shown in Fig. 8.4 an overview of SPPPs dispersion in the (q,ω)-plane through the color maps of the loss function, defined by Eq. (8.9), and the loss spectra for a fixed q at the point were the SPPPs coupling $\Omega_{1(2)}$ were calculated. As expected, for a MLG on top of 1-MoS$_2$ or 1-WS$_2$, Figs. 8.4(a) and 8.4(c), respectively, the SPPPs coupling are in the WC regime. In this case, the modes that compose the anticrossing, arising due their hybridization, are practically indistinguishable, as compared to the line width of the non-coupled modes. The loss spectra below each panel emphasizes how weak this couplings is, since the peaks, represented by blue (purple) arrows for Ω_1 (Ω_2), are very close to each other, presenting a normalized coupling η less than 0.01. In Fig. 8.4(b), both Ω_1 and Ω_2 are in the SC, presenting a well defined anticrossing and a loss spectra with well separated peaks, where η is given by 0.047 and 0.063, respectively. Finally, although Ω_1 in Fig. 8.4(d) presents a SC, with $\eta = 0.18$, Ω_2 is in the USC coupling regime with $\eta = 0.12$ in this case.

8.3.3 Tuning the SPPPs coupling strength through the Fermi energy

Figure 8.5 shows how the Fermi energy can be used to tune the SPPPs coupling, as to maximize the plasmon-phonon interaction. In Fig. 8.5(a), we present the SPPPs dispersion for a vdWhs made by G/25-MoS$_2$ for three different values of the Fermi energy (in units of the phonon frequency $\hbar\omega_{E'}$, see Tab. E.2): $E_F^A = 1\hbar\omega_{E'}$, $E_F^B = 2.3\hbar\omega_{E'}$ and $E_F^C = 3.8\hbar\omega_{E'}$, represented by the black dotted, red dashed and brown dash-dotted lines, respectively. The horizontal green line is the phonon frequency and the other solid lines are the SP$_2$ dispersion for reference. Fig. 8.5(a) shows that there is a Fermi energy value that maximizes the SPPPs coupling strength. To explain this, we show in Figs. 8.5(b)-(e) the SPPPs coupling parameters Ω_1 and Ω_2 as a function of the Fermi energy. In all situations, Ω_1 and Ω_2 increase until they reach a maximum value, and then they decrease with E_F, exhibiting $\propto 1/\sqrt{E_F}$ dependence.

To explain this behaviour, we identify two different coupling mechanisms that depend on the Fermi energy E_F. If the E_F is large, due to Pauli blocking, single-particle inter-band processes are suppressed. In that case, the Dirac liquid effectively behaves as a liquid of Fermions with a mass equal to the cyclotron mass $m_\mathrm{c} = 2E_\mathrm{F}/v_\mathrm{F}^2$ [203]. Eq. (8.5) shows that in this case the plasmon-phonon coupling Ω is expected to decrease as $1/\sqrt{E_F}$. However, when the Fermi energy is small, Pauli blocking is lifted and inter-band single-particle processes are allowed [17, 159]. This strongly inhibits plasmon lifetime and, therefore, suppresses plasmon-phonon coupling.

Note that, for the vdWhs considered in Figs. 8.5(b)-(e), both SPPPs coupling Ω_1 and Ω_2 are in the SC regime. However, controlling the Fermi energy and increasing the number of layers it is possible to go from the SC to even the USC regime. The latter can be reached for Ω_2 in a MLG on top of 50 (or more) WS$_2$ layers, for example.

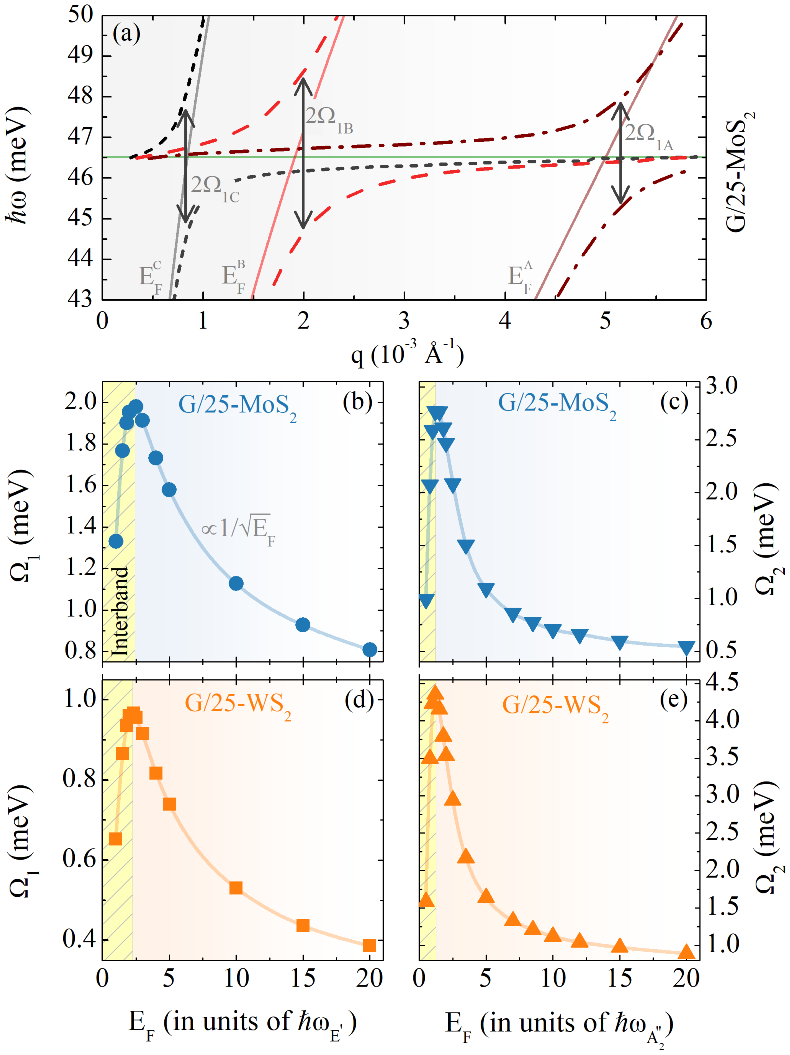

Figure 8.5: (Color online) Tuning the plasmon-phonon coupling strength $\Omega_{1(2)}$ by changing the Fermi energy (in units of the corresponding phonon frequency). (a) Plasmonic dispersion of G/25-MoS$_2$ for different values of the Fermi energy (in units of $\hbar\omega_{E'}$) given by $E_F^A = 1\hbar\omega_{E'}$, $E_F^B = 2.3\hbar\omega_{E'}$ and $E_F^C = 3.8\hbar\omega_{E'}$. The uncoupled phonon state corresponds to the horizontal solid green line and the SP$_2$ plasmons are represented by the square root ($\propto \sqrt{q}$) solid lines, for reference. The SPPPs couplings (b)-(c) Ω_1 and (d)-(e) Ω_2 are shown as a function of the Fermi energy for G/25-MoS$_2$. The yellow region in (b)-(e) represents the interband regime, where the plasmon dispersion is damped. After that, $\Omega_{1(2)} \propto 1/\sqrt{E_F}$, i.e the Fermi energy is large enough to keep the plasmon-phonon dispersion in the long-wavelength limit, keeping the plasmonic dispersion below the interband region.

8.4 Conclusions of the chapter

We have demonstrated how graphene (Dirac) plasmons couple to IR-active in-plane E' and out-of-plane A_2'' phonon modes in transition metal dichalcogenide-based van der Waals heterostructures, from few layers until the bulk limit. In order to do so, we have presented a semi-classical theory, obtained from the random phase approximation, to calculate the surface plasmon-phonon polaritons dispersion in the q-ω plane. Comparing this semi-classical theory to the results obtained through a DFT-based method, known as the quantum-electrostatic heterostructure, we have shown that the semi-classical approach provides an excellent match for many TMDs layers, capturing all relevant characteristics of the surface plasmon-phonon polaritons.

Furthermore, using the quantum-electrostatic heterostructure model, we have calculated the loss function of vdWHs composed by monolayer graphene on top of TMDs multi-layers. Our results prove that, although we have weak and strong coupling regimes in this TMDs-based vdWhs, it is also possible to achieve the ultra strong coupling regime for the coupling between Dirac plasmons and A_2'' for 40 or more WS_2 layers. In addition, we explain the nature of the graphene plasmons coupling to IR-active E' and A_2'' phonon modes, from a few TMDs layers to the bulk behavior. Not less important, we have demonstrated the possibility of tuning the SPPPs coupling strength through the graphene Fermi energy, explaining its $1/\sqrt{E_F}$ dependence. It is important to highlight that plasmons in graphene can be experimentally observed using, for example, scattering-type scanning near-field optical microscope (s-SNOM) in photocurrent mode. Therefore, using current experimental techniques, our results suggest the possibility of creating/exciting SPPPs and to study the coupling regimes discussed here for vdWhs composed by graphene and MoS_2 or WS_2.

9

Concluding remarks and perspectives

In this thesis, the trembling motion known as *zitterbewegung*, that arises in Dirac-like quasi-particles, were theoretically investigated in multilayer graphene and as well as for Moiré exciton. Through the analysis, the questions that were posed in the first chapter can be answered as follows:

How is the *zitterbewegung* affected by changing the number of graphene layers?

In chapter 4 it is demonstrated, analytically (*Green's functions*) and computationally (*split-operator technique*), that the dynamics of wave packets in ABC-stacked multilayer graphene, with different pseudospin polarization, presented different behaviors as the number of layers increases. Moreover, the time t^d of the transient behavior of the ZBW is of the order of dozens of femtoseconds and the larger the number of layers the longer the transient time, i.e. $t^d_N > t^d_{N-1}$. Also, as the number of layers increases, for the pseudospin polarization given by $(1\ 1)^T$ and $(1\ i)^T$, the wave packet propagated in different directions and were rotated by 90° from those initially seen for the monolayer case, as N increases. For all the cases analysed, i.e. from monolayer graphene to three layer graphene, the ZBW phenomena was transient, i.e. the oscillations of the physical observables decay with time and a natural damping is observed. Also, using the Heisenberg equation of motion we were capable of predicting all directions of propagation considered previously.

Is it possible to use moiré excitons in van der Waals heterostructures as an advantageous solid-state platform to directly probe the *zitterbewegung* phenomena and its Dirac-like nature?

In chapter 5 it is shown that, in the presence of a perpendicular electric field in MoS_2/WSe_2 vdWhs with small twist angles, the gap of the moiré exciton band structure can be closed, which attributes the characteristics of a massless Dirac fermion to moiré exciton quasi-particles. Applying the *split-operator technique* to this system, it was possible to see that *zitterbewegung* phenomena became evident presenting a shift of tens of Å in the center of the moiré exciton wave packet, along with damped oscillations with pico-second long periods. Furthermore, it was demonstrated that the exciton probability density profile is strikingly different in the presence of gap-closing electric field, compared to the case without any applied field. In this system, as in the case of ABC-stacked multilayer graphene, the density profile and direction of the motion were also shown to be strongly dependent on the pseudo-spinor of the moiré exciton wave packet. In such platform, the pseudo-spinor can be controlled by the polarization of the incident exciting light. Once in this system the timescales is considerably large, being within reach of available experimental techniques, we expect to instigate the first experimental detection of ZBW in an exciton wave packet, which opens the gate to follow-up studies exploiting thereby proven massless Dirac fermion character of the moiré excitons in $\mathrm{MoS_2/WSe_2}$ vdWhs induced by gating.

In the second part of this thesis, the plasmonic properties of graphene in van der Waals heterostructure vdWh, composed by graphene and different types of transition metal dichalcogenide, were theoretically explored from terahertz to mid-infrared regime. Within the *random phase approximation* and through the *quantum electrostatic heterostructure* (QEH), a computational model, the the nonlocality of Dirac plasmons modes were calculated for different vdWh. Through the analysis, the questions that were posed in the first chapter can be answered as follows:

> **Can Dirac plasmons, excited from terahertz to mid-infrared regime, be used to probe the structure and composition of van der Waals heterostructure?**

In chapter 7 it is shown that, due to the high sensitivity of Dirac plasmons in graphene to the dielectric properties of the surrounding environment, it is possible to use graphene plasmons to probe the non-local dynamical response of vdWHs composed by monolayer graphene on top of transition metal dichalcogenide multi-layers. Once plasmons in graphene can be experimentally observed using, for example, scattering-type scanning near-field optical microscope (s-SNOM) in photocurrent mode, with spatial resolution of at least 20 nm, the results presented in chapter 6 for a vdWhs composed by $\mathrm{MoS_2}$, $\mathrm{MoSe_2}$, $\mathrm{WS_2}$ and $\mathrm{WSe_2}$ can be measured experimentally by analyzing the difference in the plasmon wavelength as the number of layers change the plasmon dispersion in the (q, ω)-plane. Nevertheless, our results show that for a number of layers as low as $N = 2$, the plasmon-phonon coupling is still strong enough to produce distinguishable wavelengths for different materials, thus suggesting the method proposed in chapter 6 as a remarkably sensitive tool.

> **How strong is the coupling of terahertz Dirac plasmons to phonons in transition metal dicalchogenide-based van der Waals heterostructures, and how the tuning of the Fermi energy can be used to increase the coupling strength?**

In chapter 8 it is shown that graphene (Dirac) plasmons couple to IR-active in-plane E' and out-of-plane A_2'' phonon modes in TMDs-based vdWhs and, although we have weak and strong coupling regimes in this TMDs-based vdWhs, it is also possible to achieve the ultra strong coupling regime for the coupling between Dirac plasmons and A_2'' for 40 or more WS_2 layers. In addition, was explained the nature of the graphene plasmons coupling to IR-active E' and A_2'' phonon modes, from a few TMDs layers to the bulk behavior. Not less important, it was demonstrated the possibility of tuning the SPPPs coupling strength through the graphene Fermi energy, explaining its $1/\sqrt{E_F}$ dependence and allowing to use this property to maximize the coupling strength. In the same way that the results presented in chapter 7 can be measured by s-SNOM, it is also possible to use the same technique to create/excite SPPPs and to study the coupling regimes discussed here for vdWhs composed by graphene and MoS_2 or WS_2. The results presented in chapter 8 can also be extended to other TMDs.

As explained in the first part of this thesis, the study of the dynamics of charge particles, represented by a Gaussian wave packet, in 2D systems is still a important field of research on the condensed matter physics. As demonstrated in Chapters 4 and 5, the use of the split-operator technique, although simple, is still a very power full tool to study electronic transport in 2D materials, once this method can be easily adapted to other different 2D systems, as was the case of graphene in Chapter 4, and of moiré excitons in twisted hetero-bilayers presented in Chapter 5, for example. In fact, the SOT, used in the first part of this thesis to study the ZBW phenomena, can also be used to investigate other relevant phenomena such as valley filtering in bilayer graphene [230], valley filter in graphene nanoribbons using snake states [232] and in strained graphene [49], for example.

Therefore, as a perspective of the study presented in Chapter 4, we believe that both theoretical methods proposed in that chapter will be useful for future simulations of wave packet propagation and scattering in multilayer graphene, and that the discussions about the results found in this chapter will contribute to a better understanding of ZBW in these systems. In the context of the study of propagation of Gaussian wave packets, an investigation on the scattering of a Gaussian wave packet in a interface between mono and bilayer graphene and how the graphene edges affect this phenomena are important open questions and should be investigated in the near future.

Regarding on the study developed in Chapter 5, since the direct experimental detection of ZBW has been not yet done in 2D systems, as explained Chap. 5, we expect to instigate the first experimental detection of ZBW in an exciton wave packet. With this, new studies exploiting thereby proven massless Dirac fermion character of the moiré excitons in MoS_2/WSe_2vdWhs induced by gating will arise, contributing to a better understanding of the Dirac-like nature of moiré excitons in this system. Furthermore, as previously said, the tools presented in both chapters 4 and 5 can be extend to new other 2D systems, allowing us to describe important physics phenomena in theses systems.

In the context of plasmonics research in graphene in vdWhs-based systems, as explained in the second part of this thesis, this field still progresses at a tremendous pace and is still a *hot topic* on the condensed matter physics. In this context, many questions related to the use of graphene and other materials related to 2D, such as TMDs, as platforms for plasmonic applications or for important new physical properties in these systems, have not yet been answered. Therefore, from the study presented in the second part of this thesis, there is a lot o potential to extend the presented plasmonic study, as mentioned as a following.

The first important point we need to mention is that all the results presented in the chapters 7 and 8 can be measured experimentally using current techniques, such as scattering-type scanning near-field optical microscope (s-SNOM) in photocurrent mode, for example, which presents spatial resolution of at least 20 nm.

As an extension of the work that is done in the second part of this thesis, it is interesting to investigating, for example, plasmons in vdWhs composed by a bilayer graphene with TMDs in-between. In this case, unlike plasmons in monolayer graphene which only has an optical mode, the plasmon dispersion will present also an acoustic mode. Thus, to understand and answer some questions, such as *how is the coupling between the acoustic plasmons mode that arises in bilayer graphene, and TMDs' phonons and how it depends on the number o TMDs layers in between both monolayers graphene?*, we started an study considering this kind of vdWhs-based system.

A

Publications related to this thesis

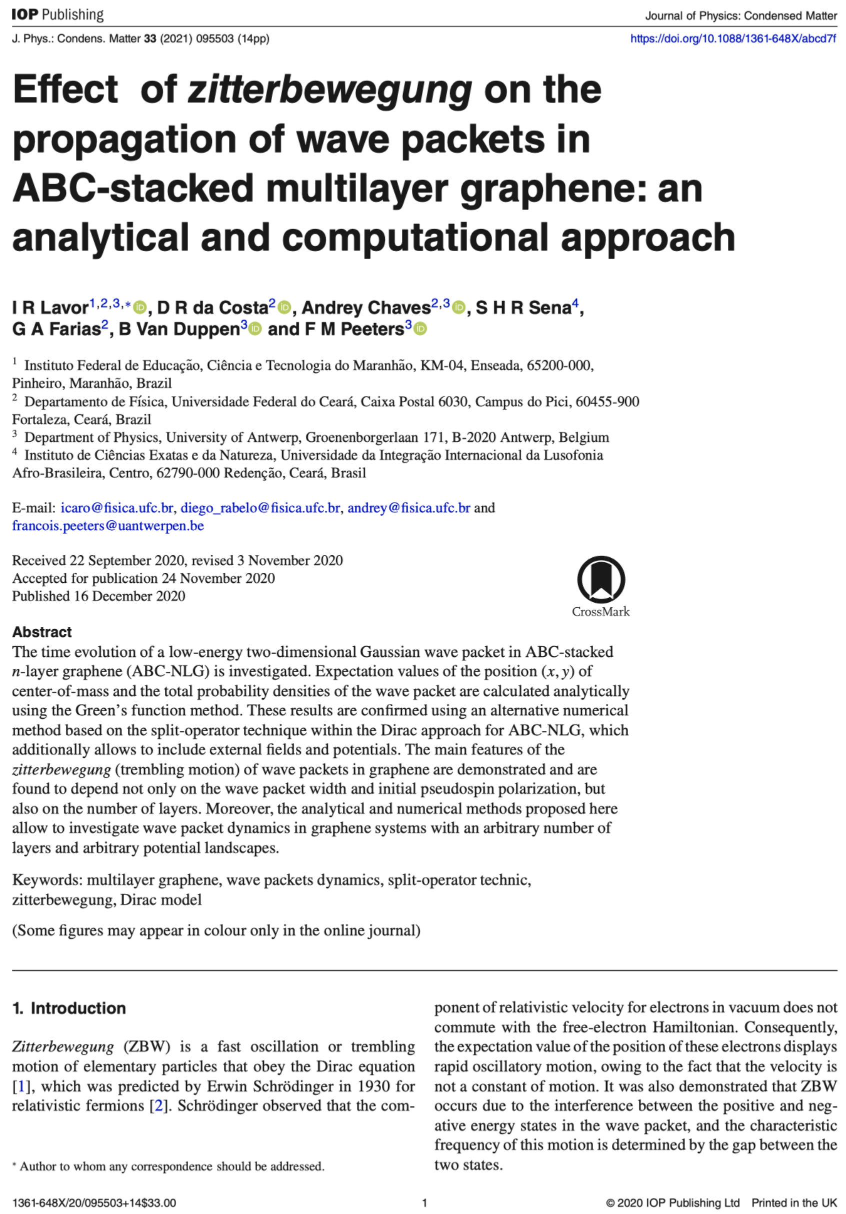

IOP Publishing
Journal of Physics: Condensed Matter
J. Phys.: Condens. Matter **33** (2021) 095503 (14pp)
https://doi.org/10.1088/1361-648X/abcd7f

Effect of *zitterbewegung* on the propagation of wave packets in ABC-stacked multilayer graphene: an analytical and computational approach

I R Lavor[1,2,3,*], D R da Costa[2], Andrey Chaves[2,3], S H R Sena[4], G A Farias[2], B Van Duppen[3] and F M Peeters[3]

[1] Instituto Federal de Educação, Ciência e Tecnologia do Maranhão, KM-04, Enseada, 65200-000, Pinheiro, Maranhão, Brazil
[2] Departamento de Física, Universidade Federal do Ceará, Caixa Postal 6030, Campus do Pici, 60455-900 Fortaleza, Ceará, Brazil
[3] Department of Physics, University of Antwerp, Groenenborgerlaan 171, B-2020 Antwerp, Belgium
[4] Instituto de Ciências Exatas e da Natureza, Universidade da Integração Internacional da Lusofonia Afro-Brasileira, Centro, 62790-000 Redenção, Ceará, Brasil

E-mail: icaro@fisica.ufc.br, diego_rabelo@fisica.ufc.br, andrey@fisica.ufc.br and francois.peeters@uantwerpen.be

Received 22 September 2020, revised 3 November 2020
Accepted for publication 24 November 2020
Published 16 December 2020

Abstract

The time evolution of a low-energy two-dimensional Gaussian wave packet in ABC-stacked n-layer graphene (ABC-NLG) is investigated. Expectation values of the position (x, y) of center-of-mass and the total probability densities of the wave packet are calculated analytically using the Green's function method. These results are confirmed using an alternative numerical method based on the split-operator technique within the Dirac approach for ABC-NLG, which additionally allows to include external fields and potentials. The main features of the *zitterbewegung* (trembling motion) of wave packets in graphene are demonstrated and are found to depend not only on the wave packet width and initial pseudospin polarization, but also on the number of layers. Moreover, the analytical and numerical methods proposed here allow to investigate wave packet dynamics in graphene systems with an arbitrary number of layers and arbitrary potential landscapes.

Keywords: multilayer graphene, wave packets dynamics, split-operator technic, zitterbewegung, Dirac model

(Some figures may appear in colour only in the online journal)

1. Introduction

Zitterbewegung (ZBW) is a fast oscillation or trembling motion of elementary particles that obey the Dirac equation [1], which was predicted by Erwin Schrödinger in 1930 for relativistic fermions [2]. Schrödinger observed that the component of relativistic velocity for electrons in vacuum does not commute with the free-electron Hamiltonian. Consequently, the expectation value of the position of these electrons displays rapid oscillatory motion, owing to the fact that the velocity is not a constant of motion. It was also demonstrated that ZBW occurs due to the interference between the positive and negative energy states in the wave packet, and the characteristic frequency of this motion is determined by the gap between the two states.

---

[*] Author to whom any correspondence should be addressed.

IOP Publishing 2D Mater. 8 (2021) 015014 https://doi.org/10.1088/2053-1583/abbecc

2D Materials

CrossMark

RECEIVED
3 August 2020

REVISED
24 September 2020

ACCEPTED FOR PUBLICATION
6 October 2020

PUBLISHED
30 October 2020

PAPER

Probing the structure and composition of van der Waals heterostructures using the nonlocality of Dirac plasmons in the terahertz regime

I R Lavor[1,2,3], **L S R Cavalcante**[4], **Andrey Chaves**[2], **F M Peeters**[3] **and B Van Duppen**[3]

[1] Instituto Federal de Educação, Ciência e Tecnologia do Maranhão, KM-04, Enseada, 65200-000, Pinheiro, Maranhão, Brazil
[2] Departamento de Física, Universidade Federal do Ceará, Campus do Pici, Fortaleza, Ceará 60455-900, Brazil
[3] Department of Physics, University of Antwerp, Groenenborgerlaan 171, B-2020 Antwerp, Belgium
[4] Department of Chemical Engineering, University of California—Davis, Davis, CA, United States of America

E-mail: icaro@fisica.ufc.br **and** ben.vanduppen@uantwerpen.be

Keywords: graphene, dirac plasmons, transition metal dichalcogenide, van der waals heterostructures, phonons, plasmon-phonon hybridization

Abstract

Dirac plasmons in graphene are very sensitive to the dielectric properties of the environment. We show that this can be used to probe the structure and composition of van der Waals heterostructures (vdWh) put underneath a single graphene layer. In order to do so, we assess vdWh composed of hexagonal boron nitride and different types of transition metal dichalcogenides (TMDs). By performing realistic simulations that account for the contribution of each layer of the vdWh separately and including the importance of the substrate phonons, we show that one can achieve single-layer resolution by investigating the nonlocal nature of the Dirac plasmon-polaritons. The composition of the vdWh stack can be inferred from the plasmon-phonon coupling once it is composed by more than two TMD layers. Furthermore, we show that the bulk character of TMD stacks for plasmonic screening properties in the terahertz regime is reached only beyond 100 layers.

1. Introduction

Graphene [1] and other two-dimensional (2D) materials, such as the transition metal dichalcogenides [2, 3] (TMDs), have been intensively investigated due to their unique opto-electronic properties [4–14]. The optical response of each material is different due to, e.g. the presence or absence of band gaps [15, 16], the specific type of the electronic structure, and is also influenced by the intrinsic mobility of the electrons themselves [17]. The latter is especially important for graphene because it is responsible for the manifestation of so-called plasmons, collective excitations of the 2D electron liquid [18, 19]. It has been shown that graphene plasmons, also called Dirac plasmons, referring to the single-particle energy spectrum of graphene [20], can be supported at mid infra-red [6, 21, 22] to terahertz (THz) frequencies [6, 11, 23, 24] and show strong electromagnetic field confinement [20, 25]. TMDs, on the other hand, due to their large band gap [16, 26], behave as dielectrics at low frequencies, thus not supporting plasmons if not extrinsically doped [27].

These 2D materials can be combined in so-called van der Waals heterostructures (vdWh) [4]. Such structures can be made by stacking different layers on top of each other [2, 4, 5, 9, 10, 14, 28] or even next to each other forming so-called lateral heterostructures [2, 28–33]. A large corpus of literature has been devoted to the investigation of fabrication techniques to create these nanostructures [2–5, 10, 28–35]. It has been shown that different opto-electronic properties of the components making up the heterostructure are merged and that by carefully selecting the different constituents, one could achieve materials that are tailor-made to bolster specific behaviour [34, 35]. Conversely, this means that one could also investigate the opto-electronic response of certain vdWhs to assess their composition and atomic structure. In this paper, we investigate Dirac plasmon states for specific types of vdWh stacks consisting of layers of hexagonal boron nitride (hBN) and different MX_2 types of TMDs, composed by a metal ($M = Mo$

B

Publications non-related to the thesis

IOP Publishing Journal of Physics: Condensed Matter

J. Phys.: Condens. Matter **32** (2020) 155501 (11pp) https://doi.org/10.1088/1361-648X/ab6463

Magnetic field induced vortices in graphene quantum dots

I R Lavor[1], D R da Costa[1], A Chaves[1], G A Farias[1], R Macêdo[2] and F M Peeters[1,3]

[1] Departamento de Física, Universidade Federal do Ceará, Caixa Postal 6030, Campus do Pici,
60455-900 Fortaleza, Ceará, Brazil
[2] James Watt School of Engineering, Electronics and Nanoscale Engineering Division,
University of Glasgow, Glasgow G12 8QQ, United Kingdom
[3] Department of Physics, University of Antwerp, Groenenborgerlaan 171, B-2020 Antwerp, Belgium

E-mail: icaro@fisica.ufc.br, diego_rabelo@fisica.ufc.br, andrey@fisica.ufc.br
and francois.peeters@ua.ac.be

Received 30 August 2019, revised 2 December 2019
Accepted for publication 20 December 2019
Published 14 January 2020

Abstract

The energy spectrum and local current patterns in graphene quantum dots (QD) are investigated for different geometries in the presence of an external perpendicular magnetic field. Our results demonstrate that, for specific geometries and edge configurations, the QD exhibits vortex and anti-vortex patterns in the local current density, in close analogy to the vortex patterns observed in the probability density current of semiconductor QD, as well as in the order parameter of mesoscopic superconductors.

Keywords: graphene quantum dots, vortex patterns, probability density current

(Some figures may appear in colour only in the online journal)

1. Introduction

In superconducting materials under an applied magnetic field, supercurrents of Cooper pairs circulate in order to expel the field, which is known as the Meissner effect [1]. However, especially in superconducting alloys, if the field is greater than a certain critical value, it is able to penetrate the superconducting sample, forming localised quantized magnetic flux lines, around which a vortex is formed in the supercurrent. As the field increases, more vortices enter the sample with quantized magnetic flux, and are eventually stabilized in a triangular Abrikosov lattice [2–11].

In 2003, Chibotaru and co-authors [12] studied superconducting mesoscopic samples with various geometries and found that the pattern of vortices formed in these structures follows not only the formation of the Abrikosov lattice, but also the sample symmetry: if the system is a mesoscopic square, for example, vortex patterns are arranged in such squared symmetry [4, 5, 12]. Experimentally, vortices were observed in materials ranging from: electron plasmas [13] to mesoscopic superconductors with triangular [14], square [15, 16] and circular [17] geometries. More recently, vortex patterns were also studied in artificial photonic graphene [18] and thin films [19, 20] using optical induction method, scanning SQUID (superconducting quantum interference devices) microscopy and scanning Hall probe respectively. However, vortices have not been observed in graphene yet. One possibility to find vortices in graphene is indirectly, using scanning tunneling microscopy in order to obtain the level density of states. Other imaging techniques, like magnetic force microscopy and scanning Hall probe are also promising for visualization the magnetic fields generated by these circular currents.

Inspired by such vortex lattice formation, Slachmuylders *et al* investigated a similar effect in semiconductor quantum dots (QD) [21]. In fact, for electrons confined in a semiconductor planar circular dot under an external magnetic field perpendicular to the system, the energy levels exhibit a series of crossings as a function of field [21–24]. As the angular momentum operator in this case commutes with the Hamiltonian, the energy eigenstates are also eigenstates of angular momentum, therefore, crossing points in the energy spectrum as a function of magnetic field, in fact, represent different degenerate states of the angular momentum operator. However, if the circular symmetry is broken, e.g. by a triangular or square confinement

1361-648X/20/155501+11$33.00

One of the figures of the my publication *Magnetic field induced vortices in graphene quantum dots* was selected to be at the cover of the JPCM.

Journal of Physics Condensed Matter

Vol 32, No 15 153001–159501

10 April 2020

ISSN 0953-8984

Journal of Physics

Condensed Matter

Volume 32 Number 15 10 April 2020

Topical Reviews

Revealing the initial steps in homogeneous photocatalysis by time-resolved spectroscopy
Ayla Päpcke, Aleksej Friedrich and Stefan Lochbrunner

Thermal transport of carbon nanomaterials
Xue-Kun Chen and Ke-Qiu Chen

Deterministically fabricated solid-state quantum-light sources
Sven Rodt, Stephan Reitzenstein and Tobias Heindel

Fig.: Magnetic field induced vortices in graphene quantum dots
I R Lavor, D R da Costa, A Chaves, G A Farias, R Macêdo and F M Peeters

iopscience.org/jpcm

IOP Publishing

C

Support information for the ZBW in ABC-NLG

C.1 Wavefunction written using Green's functions

Here is presented the details of how to calculate the Green's functions coefficients, Eq. (4.8) in the main text, Subsec. 4.2.1, defined as

$$G_{\mu v}\left(\boldsymbol{r},\boldsymbol{r}',t\right)=\sum_{s=\pm1}\int\Phi_{p,s,\mu}\left(\boldsymbol{r},t\right)\Phi^{\dagger}_{p,s,v}\left(\boldsymbol{r}',0\right)d\boldsymbol{p}\ . \tag{C.1}$$

In Eq. (C.1), $\mu,\nu=1,2$ are matrix indices, associated with the upper and lower components of $\Psi\left(\boldsymbol{r},t\right)$ that are related to the probability of finding the electron at the sublattices A (upper) and B (lower). Once these coefficients are known, we can write the wave function $\Psi_{\mu}\left(\boldsymbol{r},t\right)$, Eq. (4.9) of the main text, in terms of Green's functions.

To do so, we need to calculate $G_{11}\left(\boldsymbol{r},\boldsymbol{r}',t\right)$, $G_{12}\left(\boldsymbol{r},\boldsymbol{r}',t\right)$, $G_{21}\left(\boldsymbol{r},\boldsymbol{r}',t\right)$ and $G_{22}\left(\boldsymbol{r},\boldsymbol{r}',t\right)$ using Eq. (C.1).

Replacing Eq. (4.6) of the main text, defined as

$$\Phi_{p,s}\left(\boldsymbol{r},t\right)=\frac{1}{2\sqrt{2}\pi\hbar}\exp\left(i\frac{\boldsymbol{p}\cdot\boldsymbol{r}}{\hbar}-i\frac{E^{n}_{\boldsymbol{p},s}t}{\hbar}\right)\begin{pmatrix}1\\ se^{in\phi}\end{pmatrix}\ , \tag{C.2}$$

into Eq. (C.1), yields:

$$G_{11}\left(\boldsymbol{r},\boldsymbol{r}',t\right)=\frac{1}{2\sqrt{2}\pi\hbar}\cdot\frac{1}{2\sqrt{2}\pi\hbar}\sum_{s=\pm1}\int\left[\exp\left(i\frac{\boldsymbol{p}\cdot\boldsymbol{r}}{\hbar}-i\frac{E^{n}_{p,s}t}{\hbar}\right)\right]\cdot\left[\exp\left(-i\frac{\boldsymbol{p}\cdot\boldsymbol{r}'}{\hbar}\right)\right]d\boldsymbol{p}\ , \tag{C.3}$$

$$G_{11}\left(\boldsymbol{r},\boldsymbol{r}',t\right)=\frac{1}{\left(2\pi\hbar\right)^{2}}\cdot\frac{1}{2}\int\left[\exp\left(i\frac{\boldsymbol{p}\left(\boldsymbol{r}-\boldsymbol{r}'\right)}{\hbar}\right)\right]\left[\sum_{s=\pm1}\exp\left(-i\frac{E^{n}_{p,s}t}{\hbar}\right)\right]d\boldsymbol{p}\ . \tag{C.4}$$

But $E^{n}_{p,s}=sp^{n}/\gamma$, thus Eq. (C.4) becomes

$$G_{11}\left(\boldsymbol{r},\boldsymbol{r}',t\right)=\frac{1}{\left(2\pi\hbar\right)^{2}}\cdot\frac{1}{2}\int\left[\exp\left(i\frac{\boldsymbol{p}\left(\boldsymbol{r}-\boldsymbol{r}'\right)}{\hbar}\right)\right]\left[\sum_{s=\pm1}\exp\left(-i\frac{sp^{n}t}{\xi\hbar}\right)\right]d\boldsymbol{p}\ . \tag{C.5}$$

On the other hand, the summation in Eq. (C.5) can be written as:

$$\sum_{s=\pm 1} \exp\left(-i\frac{sp^n t}{\xi\hbar}\right) = \exp\left(-i\frac{p^n t}{\xi\hbar}\right) + \exp\left(i\frac{p^n t}{\xi\hbar}\right), \tag{C.6}$$

or, using $e^{i\theta} = \cos\theta + i\mathrm{sen}\theta$, as,

$$\sum_{s=\pm 1} \exp\left(-i\frac{sp^n t}{\xi\hbar}\right) = \cos\left(\frac{p^n t}{\xi\hbar}\right) - i\mathrm{sen}\left(\frac{p^n t}{\xi\hbar}\right) + \cos\left(\frac{p^n t}{\xi\hbar}\right) + i\mathrm{sen}\left(\frac{p^n t}{\xi\hbar}\right) \tag{C.7}$$

$$\sum_{s=\pm 1} \exp\left(-i\frac{sp^n t}{\xi\hbar}\right) = 2\cos\left(\frac{p^n t}{\xi\hbar}\right). \tag{C.8}$$

Thus, replacing Eq. (C.8) into Eq. (C.5), we have:

$$G_{11}\left(\boldsymbol{r}, \boldsymbol{r}', t\right) = \frac{1}{(2\pi\hbar)^2} \cdot \frac{1}{2} \int \left[\exp\left(i\frac{\boldsymbol{p}\left(\boldsymbol{r}-\boldsymbol{r}'\right)}{\hbar}\right)\right] \left[2\cos\left(\frac{p^n t}{\xi\hbar}\right)\right] d\boldsymbol{p}, \tag{C.9}$$

$$G_{11}\left(\boldsymbol{r}, \boldsymbol{r}', t\right) = \frac{1}{(2\pi\hbar)^2} \int \exp\left[i\frac{\boldsymbol{p}\left(\boldsymbol{r}-\boldsymbol{r}'\right)}{\hbar}\right] \cos\left(\frac{p^n t}{\xi\hbar}\right) d\boldsymbol{p}. \tag{C.10}$$

Analogously, we can get $G_{22}\left(\boldsymbol{r}, \boldsymbol{r}', t\right)$, such that:

$$G_{22}\left(\boldsymbol{r}, \boldsymbol{r}', t\right) = G_{11}\left(\boldsymbol{r}, \boldsymbol{r}', t\right). \tag{C.11}$$

On the other hand, to $G_{12}\left(\boldsymbol{r}, \boldsymbol{r}', t\right)$, we have:

$$\begin{aligned} G_{12}\left(\boldsymbol{r}, \boldsymbol{r}', t\right) = \frac{1}{2\sqrt{2}\pi\hbar} \cdot \frac{1}{2\sqrt{2}\pi\hbar} \sum_{s=\pm 1} \int \left[\exp\left(i\frac{\boldsymbol{p}\cdot\boldsymbol{r}}{\hbar} - i\frac{E^n_{p,s} t}{\hbar}\right)\right] \\ \cdot \left[\exp\left(-i\frac{\boldsymbol{p}\cdot\boldsymbol{r}'}{\hbar}\right)\right] \cdot \left(se^{-in\phi}\right) d\boldsymbol{p} \end{aligned} \tag{C.12}$$

$$\begin{aligned} G_{12}\left(\boldsymbol{r}, \boldsymbol{r}', t\right) = \frac{1}{(2\pi\hbar)^2} \cdot \frac{1}{2} \int \left[\exp\left(i\frac{\boldsymbol{p}\left(\boldsymbol{r}-\boldsymbol{r}'\right)}{\hbar}\right)\right] \\ \cdot \left[\sum_{s=\pm 1} s \cdot \exp\left(-i\frac{E^n_{p,s} t}{\hbar}\right)\right] \cdot e^{-in\phi} d\boldsymbol{p}\,. \end{aligned} \tag{C.13}$$

Using $E^n_{p,s} = sp^n/\gamma$, one can obtain

$$\begin{aligned} G_{12}\left(\boldsymbol{r}, \boldsymbol{r}', t\right) = -\frac{1}{(2\pi\hbar)^2} \cdot \frac{1}{2} \int \left[\exp\left(i\frac{\boldsymbol{p}\left(\boldsymbol{r}-\boldsymbol{r}'\right)}{\hbar}\right)\right] \\ \cdot \left[\sum_{s=\pm 1} s \cdot \exp\left(-i\frac{sp^n t}{\xi\hbar}\right)\right] \cdot e^{-in\phi} d\boldsymbol{p}, \end{aligned} \tag{C.14}$$

Using $e^{i\theta} = \cos\theta + i\mathrm{sen}\theta$, the summation in Eq. (C.14) can be rewritten as:

$$\sum_{s=\pm 1} s \cdot \exp\left(-i\frac{sp^n t}{\xi\hbar}\right) = \exp\left(-i\frac{p^n t}{\xi\hbar}\right) - \exp\left(i\frac{p^n t}{\xi\hbar}\right), \tag{C.15}$$

$$\sum_{s=\pm1}\exp\left(-i\frac{sp^{n}t}{\xi\hbar}\right)=\cos\left(\frac{p^{n}t}{\xi\hbar}\right)-i\text{sen}\left(\frac{p^{n}t}{\xi\hbar}\right)-\cos\left(\frac{p^{n}t}{\xi\hbar}\right)-i\text{sen}\left(\frac{p^{n}t}{\xi\hbar}\right)\quad,\tag{C.16}$$

$$\sum_{s=\pm1}\exp\left(-i\frac{sp^{n}t}{\xi\hbar}\right)=-2i\text{sen}\left(\frac{p^{n}t}{\xi\hbar}\right).\tag{C.17}$$

From Eqs. (C.17) and Eq. (C.14), we have that:

$$G_{12}\left(\boldsymbol{r},\boldsymbol{r}',t\right)=\frac{1}{\left(2\pi\hbar\right)^{2}}\cdot\frac{1}{2}\int\left[\exp\left(i\frac{\boldsymbol{p}\left(\boldsymbol{r}-\boldsymbol{r}'\right)}{\hbar}\right)\right]\left[-2i\text{sen}\left(\frac{p^{n}t}{\xi\hbar}\right)\right]\left(\frac{p_{x}-ip_{y}}{p}\right)^{n}d\boldsymbol{p}.\tag{C.18}$$

$$G_{12}\left(\boldsymbol{r},\boldsymbol{r}',t\right)=\frac{-i}{\left(2\pi\hbar\right)^{2}}\int\exp\left[i\frac{\boldsymbol{p}\left(\boldsymbol{r}-\boldsymbol{r}'\right)}{\hbar}\right]\text{sen}\left(\frac{p^{n}t}{\xi\hbar}\right)\cdot\left(\frac{p_{x}-ip_{y}}{p}\right)^{n}d\boldsymbol{p}.\tag{C.19}$$

The same procedure described here can be done for $G_{21}\left(\boldsymbol{r},\boldsymbol{r}',t\right)$, such that we obtain

$$G_{21}\left(\boldsymbol{r},\boldsymbol{r}',t\right)=\frac{-i}{\left(2\pi\hbar\right)^{2}}\int\exp\left[i\frac{\boldsymbol{p}\left(\boldsymbol{r}-\boldsymbol{r}'\right)}{\hbar}\right]\text{sen}\left(\frac{p^{n}t}{\xi\hbar}\right)\cdot\left(\frac{p_{x}+ip_{y}}{p}\right)^{n}d\boldsymbol{p}.\tag{C.20}$$

Note that $G_{12}\left(\boldsymbol{r},\boldsymbol{r}',t\right)$ differs from $G_{21}\left(\boldsymbol{r},\boldsymbol{r}',t\right)$ only by a negative sign in the term $\left(p_{x}\mp ip_{y}/p\right)^{n}$.

C.2 Details to obtain the auxiliary functions $\Phi_i(\boldsymbol{r},t)$

Here is provide the details to obtain $\Phi_{1,2,3,4}\left(\boldsymbol{r},t\right)$ defined as

$$\Phi_{1}\left(\boldsymbol{r},t\right)=\int G_{11}\left(\boldsymbol{r},\boldsymbol{r}',t\right)f\left(\boldsymbol{r}',0\right)d\boldsymbol{r}',\tag{C.21}$$

$$\Phi_{2}\left(\boldsymbol{r},t\right)=\int G_{12}\left(\boldsymbol{r},\boldsymbol{r}',t\right)f\left(\boldsymbol{r}',0\right)d\boldsymbol{r}'\tag{C.22}$$

$$\Phi_{3}\left(\boldsymbol{r},t\right)=\int G_{21}\left(\boldsymbol{r},\boldsymbol{r}',t\right)f\left(\boldsymbol{r}',0\right)d\boldsymbol{r}'\tag{C.23}$$

and

$$\Phi_{4}\left(\boldsymbol{r},t\right)=\int G_{22}\left(\boldsymbol{r},\boldsymbol{r}',t\right)f\left(\boldsymbol{r}',0\right)d\boldsymbol{r}'.\tag{C.24}$$

used to obtain the spinor wave functions

$$\Psi_{1}\left(\boldsymbol{r},t\right)=\frac{1}{\sqrt{\left|C_{1}\right|^{2}+\left|C_{2}\right|^{2}}}\left[C_{1}\Phi_{1}\left(\boldsymbol{r},t\right)+C_{2}\Phi_{3}\left(\boldsymbol{r},t\right)\right]\tag{C.25}$$

and

$$\Psi_{2}\left(\boldsymbol{r},t\right)=\frac{1}{\sqrt{\left|C_{1}\right|^{2}+\left|C_{2}\right|^{2}}}\left[C_{2}\Phi_{2}\left(\boldsymbol{r},t\right)+C_{1}\Phi_{4}\left(\boldsymbol{r},t\right)\right].\tag{C.26}$$

Since $G_{11}\left(\boldsymbol{r},\boldsymbol{r}',t\right)=G_{22}\left(\boldsymbol{r},\boldsymbol{r}',t\right)$, thus $\Phi_{1}\left(\boldsymbol{r},t\right)=\Phi_{4}\left(\boldsymbol{r},t\right)$. Therefore, is necessary calculate just $\Phi_{1}\left(\boldsymbol{r},t\right)$, $\Phi_{2}\left(\boldsymbol{r},t\right)$ e $\Phi_{3}\left(\boldsymbol{r},t\right)$. In Eq. (C.21), $f(\boldsymbol{r}',0)$ is given by Eq. (4.11b) in the main text and it is defined as:

$$f\left(\boldsymbol{r}\right)=\frac{1}{d\sqrt{\pi}}\exp\left[-\frac{r^{2}}{2d^{2}}+\frac{ip_{0y}y}{\hbar}\right].\tag{C.27}$$

By substituting Eqs. (C.27) and (C.10) into Eq. (C.21), we have that:

$$\Phi_1(\boldsymbol{r},t) = \frac{1}{(2\pi\hbar)^2}\cdot\frac{1}{d\sqrt{\pi}}\int\int \exp\left[i\frac{\boldsymbol{p}(\boldsymbol{r}-\boldsymbol{r}')}{\hbar}\right]\cos\left(\frac{p^n t}{\xi\hbar}\right) \cdot \exp\left[-\frac{r'^2}{2d^2}+ik_0 y'\right] d\boldsymbol{p}d\boldsymbol{r}', \quad \text{(C.28)}$$

$$\Phi_1(\boldsymbol{r},t) = \frac{1}{(2\pi\hbar)^2}\cdot\frac{1}{d\sqrt{\pi}}\int\int \exp\left[i\frac{\boldsymbol{p}\cdot\boldsymbol{r}}{\hbar}\right]\cos\left(\frac{p^n t}{\xi\hbar}\right) \cdot \exp\left[-i\frac{\boldsymbol{p}\cdot\boldsymbol{r}'}{\hbar}-\frac{r'^2}{2d^2}+ik_0 y'\right] d\boldsymbol{p}d\boldsymbol{r}'. \quad \text{(C.29)}$$

The integral in $\boldsymbol{r}'$, defied as $I_{\boldsymbol{r}'}$, is defined as:

$$I_{\boldsymbol{r}'} = \int \exp\left[-i\frac{\boldsymbol{p}\cdot\boldsymbol{r}'}{\hbar}-\frac{r'^2}{2d^2}+ik_0 y'\right] d\boldsymbol{r}', \quad \text{(C.30)}$$

$$I_{\boldsymbol{r}'} = \int \exp\left[-i\frac{(p_{x'}x'+p_{y'}y')}{\hbar}-\frac{(x'^2+y'^2)}{2d}+ik_0\right] dx'dy' \quad \text{(C.31)}$$

$$I_{\boldsymbol{r}'} = \left\{\int \exp\left[-\frac{x'^2}{2d^2}-i\frac{p_{x'}x'}{\hbar}\right]dx'\right\}\left\{\int \exp\left[-\frac{y'^2}{2d^2}+\frac{i}{\hbar}(-p_{y'}+k_0\hbar)\,y'\right]dy'\right\}. \quad \text{(C.32)}$$

From the table of integrals present in Ref. [312], we have that

$$\int_{-\infty}^{+\infty} \exp\left[-p^2a^2 \pm qa\right] da = \exp\left(\frac{q^2}{4p^2}\right)\frac{\sqrt{\pi}}{p}, \quad \text{(C.33)}$$

for $[\mathrm{Re}\,(p^2) > 0]$. Thus, we obtain:

$$I_{x'} = \int \exp\left[-\frac{x'^2}{2d^2}-i\frac{p_{x'}x'}{\hbar}\right] dx' \,. \quad \text{(C.34)}$$

Taking $p^2 = 1/2d^2$ and $q = ip_{x'}/\hbar$, yields

$$I_{x'} = \exp\left[\frac{(ip_{x'}/\hbar)^2}{4\,(1/2d^2)}\right]\frac{\sqrt{\pi}}{\sqrt{1/2d^2}}, \quad \text{(C.35)}$$

$$I_{x'} = \exp\left(\frac{-p_{x'}^2 d^2}{2\hbar^2}\right) d\sqrt{2\pi}. \quad \text{(C.36)}$$

Analogously, for $I_{y'}$ we have that:

$$I_{y'} = \int \exp\left[-\frac{y'^2}{2d^2}+\frac{i}{\hbar}(-p_{y'}+k_0\hbar)\,y'\right] dx' \,. \quad \text{(C.37)}$$

Taking $p^2 = 1/2d^2$ and $q = i\,(-p_{y'}+k_0\hbar)\,/\hbar$, yields

$$I_{y'} = \exp\left[\frac{-\left(-p_{y'}+k_0\hbar\right)^2/\hbar^2}{4\,(1/2d^2)}\right]\frac{\sqrt{\pi}}{(1/d\sqrt{2})}, \quad \text{(C.38)}$$

$$I_{y'} = \exp\left[\frac{-\left(-p_{y'} + k_0\hbar\right)^2 d^2}{2\hbar^2}\right] d\sqrt{2\pi}. \tag{C.39}$$

Inserting Eqs. (C.36) and (C.39) in Eq. (C.32), we obtain:

$$I_{\boldsymbol{r}'} = \left[\exp\left(\frac{-p_{x'}^2 d^2}{2\hbar^2}\right) d\sqrt{2\pi}\right]\left\{\exp\left[\frac{-\left(-p_{y'} + k_0\hbar\right)^2 d^2}{2\hbar^2}\right] d\sqrt{2\pi}\right\}, \tag{C.40}$$

$$I_{\boldsymbol{r}'} = \exp\left(\frac{-p_{x'}^2 d^2}{2\hbar^2}\right)\exp\left[\frac{-\left(-p_{y'} + k_0 y'\right)^2 d^2}{2\hbar^2}\right] 2\pi d^2, \tag{C.41}$$

$$I_{\boldsymbol{r}'} = \exp\left(\frac{-p_{x'}^2 d^2}{2\hbar^2}\right)\exp\left[\frac{-\left(p_{y'}^2 - 2p_{y'}k_0\hbar + k_0^2\hbar^2\right) d^2}{2\hbar^2}\right] 2\pi d^2, \tag{C.42}$$

$$I_{\boldsymbol{r}'} = \exp\left(\frac{-p_{x'}^2 d^2}{2\hbar^2}\right)\exp\left(-\frac{p_{y'}^2 d^2}{2\hbar^2} + \frac{p_{y'}k_0 d^2}{\hbar} - \frac{k_0^2 d^2}{2}\right) 2\pi d^2, \tag{C.43}$$

$$I_{\boldsymbol{r}'} = \exp\left[-\frac{\left(p_{x'}^2 + p_{y'}^2\right) d^2}{2\hbar^2} + \frac{p_{y'}k_0 d^2}{\hbar} - \frac{k_0^2 d^2}{2}\right] 2\pi d^2, \tag{C.44}$$

$$I_{\boldsymbol{r}'} = \exp\left(-\frac{p^2 d^2}{2\hbar^2} + \frac{p_{y'}k_0 d^2}{\hbar} - \frac{k_0^2 d^2}{2}\right) 2\pi d^2. \tag{C.45}$$

Substituting Eq. (C.45) into Eq. (C.29), yeilds:

$$\begin{aligned}\Phi_1\left(\boldsymbol{r}, t\right) = \frac{1}{\left(2\pi\hbar\right)^2}\cdot\frac{1}{d\sqrt{\pi}}\int \exp\left(i\frac{\boldsymbol{p}\cdot\boldsymbol{r}}{\hbar}\right)\cos\left(\frac{p^n t}{\xi\hbar}\right)& \\ \cdot\exp\left(-\frac{p^2 d^2}{2\hbar^2} + \frac{p_{y'}k_0 d^2}{\hbar} - \frac{k_0^2 d^2}{2}\right) 2\pi d^2 d\boldsymbol{p}\ .&\end{aligned} \tag{C.46}$$

Since

$$\frac{1}{\left(2\pi\hbar\right)^2}\cdot\frac{1}{d\sqrt{\pi}}\cdot 2\pi d^2 = \frac{d}{2\hbar^2\sqrt{\pi^3}} \tag{C.47}$$

and $\exp\left(-k_0^2 d^2/2\right)$ is a constant, finally we obtain:

$$\Phi_1\left(\boldsymbol{r}, t\right) = \frac{de^{-\frac{(k_0^y d)^2}{2}}}{2\hbar^2\sqrt{\pi^3}}\int \exp\left(i\frac{\boldsymbol{p}\cdot\boldsymbol{r}}{\hbar} - \frac{p^2 d^2}{2\hbar^2} + \frac{p_{y'}k_0 d^2}{\hbar}\right)\cos\left(\frac{p^n t}{\xi\hbar}\right) d\boldsymbol{p}. \tag{C.48}$$

Following the same steps for $\Phi_2\left(\boldsymbol{r}, t\right)$, we obtain

$$\begin{aligned}\Phi_2\left(\boldsymbol{r}, t\right) = \frac{-i}{\left(2\pi\hbar\right)^2}\cdot\frac{1}{d\sqrt{\pi}}\int\int\left(\frac{p_x - ip_y}{p}\right)^n \exp\left[i\frac{\boldsymbol{p}\cdot\left(\boldsymbol{r} - \boldsymbol{r}'\right)}{\hbar}\right]& \\ \cdot\operatorname{sen}\left(\frac{p^n t}{\xi\hbar}\right)\exp\left[-\frac{r'^2}{2d^2} + ik_0 y'\right] d\boldsymbol{p}d\boldsymbol{r}'.&\end{aligned} \tag{C.49}$$

$$\begin{aligned}\Phi_2\left(\boldsymbol{r}, t\right) = \frac{-i}{\left(2\pi\hbar\right)^2}\cdot\frac{1}{d\sqrt{\pi}}\int\int\left(\frac{p_x - ip_y}{p}\right)^n \exp\left(i\frac{\boldsymbol{p}\cdot\boldsymbol{r}}{\hbar}\right)\operatorname{sen}\left(\frac{p^n t}{\xi\hbar}\right)& \\ \cdot\exp\left[i\frac{\boldsymbol{p}\cdot\boldsymbol{r}'}{\hbar} - \frac{r'^2}{2d^2} + ik_0 y'\right] d\boldsymbol{r}'d\boldsymbol{p}.&\end{aligned} \tag{C.50}$$

Since we already obtained the integral in $\boldsymbol{r}'$, Eq. (C.45), thus:

$$\Phi_2\left(\boldsymbol{r},t\right) = \frac{-i}{\left(2\pi\hbar\right)^2}\cdot\frac{1}{d\sqrt{\pi}}\int\left(\frac{p_x - ip_y}{p}\right)^n \exp\left(i\frac{\boldsymbol{p}\cdot\boldsymbol{r}}{\hbar}\right)\operatorname{sen}\left(\frac{p^n t}{\xi\hbar}\right) \cdot \exp\left(-\frac{p^2d^2}{2\hbar^2}+\frac{p_{y'}k_0d^2}{\hbar}-\frac{k_0^2d^2}{2}\right)2\pi d^2 d\boldsymbol{p}, \tag{C.51}$$

$$\Phi_2\left(\boldsymbol{r},t\right) = \frac{-ide^{-\frac{(k_0^y d)^2}{2}}}{2\hbar^2\sqrt{\pi^3}}\int\left(\frac{p_x - ip_y}{p}\right)^n \exp\left(i\frac{\boldsymbol{p}\cdot\boldsymbol{r}}{\hbar}-\frac{p^2d^2}{2\hbar^2}+\frac{p_{y'}k_0d^2}{\hbar}\right)\operatorname{sen}\left(\frac{p^n t}{\xi\hbar}\right)d\boldsymbol{p}. \tag{C.52}$$

For $\Phi_3\left(\boldsymbol{r},t\right)$, we have that

$$\Phi_3\left(\boldsymbol{r},t\right) = \frac{-ide^{-\frac{(k_0^y d)^2}{2}}}{2\hbar^2\sqrt{\pi^3}}\int\left(\frac{p_x + ip_y}{p}\right)^n \exp\left(i\frac{\boldsymbol{p}\cdot\boldsymbol{r}}{\hbar}-\frac{p^2d^2}{2\hbar^2}+\frac{p_{y'}k_0d^2}{\hbar}\right)\operatorname{sen}\left(\frac{p^n t}{\xi\hbar}\right)d\boldsymbol{p}\,. \tag{C.53}$$

C.3 Wave functions in terms of the Bessel function

Here, is presented the details of how to use cylindrical coordinates (see Fig. C.1), to rewrite Eqs. (C.48) and (C.53) (note that $\Phi_3\left(\boldsymbol{r},t\right)$ differs from $\Phi_3\left(\boldsymbol{r},t\right)$ by a + in the term $((p_x+ip_y)/p)^n$) in terms of the Bessel's functions. To do so, we defined the following transformations:

$$a = k_0 d, \tag{C.54}$$

$$q^2 = \frac{p^2d^2}{\hbar^2} \;\rightarrow\; qdq = \frac{pd^2}{\hbar^2}dp \tag{C.55}$$

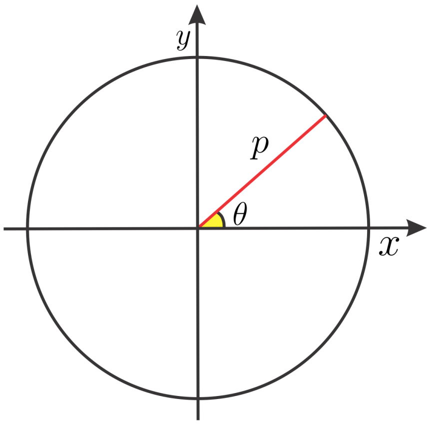

Figure C.1: Cylindrical coordinates. The radius of the circle is given by p and the angle it forms with the axis-x is given by θ.

and

$$\boldsymbol{p} = (p\text{cos}\theta, p\text{sen}\theta)\,. \tag{C.56}$$

For the sake of simplicity, but without loss of generality, the following dimensionless variables were considered:

$$t \;\rightarrow\; t' = \frac{\hbar^{n-1}t}{\xi d^n}, \tag{C.57}$$

$$x \;\rightarrow\; x' = \frac{x}{d}, \tag{C.58}$$

$$y \;\rightarrow\; y' = \frac{y}{d}, \tag{C.59}$$

and

$$r \;\rightarrow\; r' = \frac{r}{d}. \tag{C.60}$$

In Eq. (C.57) n is the number of layers.

Thus, replacing Eqs. (C.54) and (C.56) into $p_{y'}k_0d^2/\hbar$, yeilds:

$$\frac{p_{y'}k_0d^2}{\hbar} = \frac{(p\text{sen}\theta)\,(a)\,d}{\hbar}\;. \tag{C.61}$$

Once $q = pd/\hbar$, Eq. (C.55), we have:

$$\frac{p_{y'}k_0d^2}{\hbar} = qa\text{sen}\theta. \tag{C.62}$$

Now, inserting $q = pd/\hbar$, obtained from Eq. (C.55), into q^nt', results in:

$$q^nt' = \left(\frac{pd}{\hbar}\right)^n t'\;. \tag{C.63}$$

From Eqs. (C.57) and (C.63), we obtain

$$q^nt' = \left(\frac{pd}{\hbar}\right)^n \frac{\hbar^{n-1}t}{\xi d^n}, \tag{C.64}$$

$$q^nt' = \frac{p^nt}{\xi\hbar}. \tag{C.65}$$

Thus, we have that

$$\exp\left(-\frac{k_0^2d^2}{2}\right) = \exp\left(-\frac{a^2}{2}\right), \tag{C.66}$$

and

$$\exp\left(i\frac{\boldsymbol{p}\cdot\boldsymbol{r}}{\hbar} - \frac{p^2d^2}{2\hbar^2} + \frac{p_{y'}k_0d^2}{\hbar}\right) = \exp\left(i\frac{(p_xx + p_yy)}{\hbar} - \frac{q^2}{2} + qa\text{sen}\theta\right)\;. \tag{C.67}$$

On the other hand, we can rewrite $p_xx + p_yy$ as:

$$p_xx + p_yy = p\text{cos}\theta x'd + p\text{sen}\theta y'd \tag{C.68}$$

$$p_xx + p_yy = pd\,(x'\text{cos}\theta + y'\text{sen}\theta)\,, \tag{C.69}$$

$$p_x x + p_y y = q\hbar \left(x'\mathrm{cos}\theta + y'\mathrm{sen}\theta\right). \tag{C.70}$$

Substitution Eq. (C.70) int Eq. (C.67) yields:

$$\exp\left(i\frac{\boldsymbol{p}\cdot\boldsymbol{r}}{\hbar} - \frac{p^2 d^2}{2\hbar^2} - \frac{p_{y'} k_0 d^2}{\hbar}\right) = \exp\left(iq\left(x'\mathrm{cos}\theta + y'\mathrm{sen}\theta\right) - \frac{q^2}{2} + qa\mathrm{sen}\theta\right). \tag{C.71}$$

Equation (C.71) is exactly the exponential that appear in the integral of $\Phi_1(\boldsymbol{r},t)$. Therefore, replacing Eqs. (C.63), (C.66) and (C.71) into Eq. (C.48), and using the fact that$d\boldsymbol{p} = \left(\hbar^2/d^2\right) qdqd\theta$, we obtain

$$\begin{aligned}\phi_1(\boldsymbol{r},t) = \frac{1}{2d\sqrt{\pi^3}}\exp\left(-\frac{a^2}{2}\right)\int\int \exp\left[iq\left(x'\mathrm{cos}\theta + y'\mathrm{sen}\theta\right)\right.\\ \left.\cdot -\frac{q^2}{2} + qa\mathrm{sen}\theta\right]\cos\left(q^n t'\right) qdqd\theta,\end{aligned} \tag{C.72}$$

where

$$\int_{-\infty}^{+\infty} d\boldsymbol{p} \;\rightarrow\; \int_0^{\infty} qdq \int_{-\pi}^{+\pi} d\theta. \tag{C.73}$$

Finally, we have that:

$$\begin{aligned}\phi_1(\boldsymbol{r},t) = \frac{e^{-a^2/2}}{2d\sqrt{\pi^3}}\int_0^{\infty}\exp\left(-\frac{q^2}{2}\right)\cos\left(q^n t'\right)\\ \cdot\int_{-\pi}^{+\pi}\exp\left[iq\left(x'\mathrm{cos}\theta + y'\mathrm{sen}\theta\right) + qa\mathrm{sen}\theta\right] d\theta qdq.\end{aligned} \tag{C.74}$$

By the same line of reasoning, Eq. (C.53) can be written as:

$$\begin{aligned}\phi_2(\boldsymbol{r},t) = \frac{-i}{2d\sqrt{\pi^3}}\exp\left(-\frac{a^2}{2}\right)\int\int\left(i\frac{p_x + ip_y}{p}\right)^n\\ \cdot\exp\left[iq\left(x'\mathrm{cos}\theta + y'\mathrm{sen}\theta\right) - \frac{q^2}{2} + qa\mathrm{sen}\theta\right]\mathrm{sen}\left(q^n t'\right) qdqd\theta,\end{aligned} \tag{C.75}$$

$$\begin{aligned}\phi_2(\boldsymbol{r},t) = \frac{-i}{2d\sqrt{\pi^3}}\exp\left(-\frac{a^2}{2}\right)\int_0^{\infty}\exp\left(-\frac{q^2}{2}\right)\mathrm{sen}\left(q^n t'\right)\\ \int_{-\pi}^{+\pi} e^{in\theta}\cdot\exp\left[iq\left(x'\mathrm{cos}\theta + y'\mathrm{sen}\theta\right) + qa\mathrm{sen}\theta\right] d\theta qdq.\end{aligned} \tag{C.76}$$

Let us first solve the integral in $d\theta$ defined as:

$$\int_{-\pi}^{+\pi}\exp\left[iq\left[x'\mathrm{cos}\theta + \left(y' - ia\right)\mathrm{sen}\theta\right]\right] d\theta. \tag{C.77}$$

Considering $z = \left(x', \left(y' - ia\right)\right)$, we have that

$$z = x' + i\left[\left(y' - ia\right)\right] \tag{C.78}$$

$$z = x' + iy' + a, \tag{C.79}$$

where z is the absolut value of z and is defined as

$$|z| = \sqrt{r^2 - a^2 - 2iay'}. \tag{C.80}$$

It is necessary another transformation, defined by

$$x'\cos\theta + (y' - ia)\,\mathrm{sen}\theta = |z|\,\mathrm{sen}\alpha, \tag{C.81}$$

with

$$x' = |z|\cos\beta \;\;\mathrm{e}\;\; (y' - ia) = |z|\,\mathrm{sen}\beta, \tag{C.82}$$

such that

$$\cos\beta\cos\theta + \mathrm{sen}\beta\mathrm{sen}\theta = \cos\left[(\pi/2) - \alpha\right]. \tag{C.83}$$

From the fact that $\cos(\beta - \theta) = \cos\beta\cos\theta + \mathrm{sen}\beta\mathrm{sen}\theta$ and $\mathrm{sen}\alpha = \cos(\pi/2 - \alpha)$, we obtain

$$\cos(\beta - \theta) = \cos\left(\frac{\pi}{2} - \alpha\right), \tag{C.84}$$

which implies that

$$\beta - \theta = \frac{\pi}{2} - \alpha, \tag{C.85}$$

$$\alpha = \frac{\pi}{2} + \theta - \beta, \tag{C.86}$$

and

$$d\alpha = d\theta. \tag{C.87}$$

Multiplying Eq. (C.81) by qi, the integrand of Eq. (C.77) is obtained and since $d\theta = d\alpha$, we obtain

$$\int_{-\pi}^{+\pi} \exp\left[iq\left[x'\cos\theta + (y' - ia)\,\mathrm{sen}\theta\right]\right] d\theta = \int_{-\frac{\pi}{2}-\beta}^{\frac{3\pi}{2}-\beta} \exp\left[iq\,|z|\,\mathrm{sen}\alpha\right] d\alpha. \tag{C.88}$$

From Ref.[312], we have that

$$J_n(z) = \frac{1}{2\pi}\int_{-\pi}^{+\pi} e^{-ni\theta + iz\mathrm{sen}\theta} d\theta \tag{C.89}$$

$$J_n(z) = \frac{1}{\pi}\int_0^{\pi} \cos(n\theta - z\mathrm{sen}\theta)\, d\theta, \;\text{ with } n = 0, 1, 2, ... \tag{C.90}$$

Here, $J_n(z)$ is the Bessel function with index n. From Eqs. (C.88) and (C.90) we can conclude that

$$\int_{-\frac{\pi}{2}-\beta}^{\frac{3\pi}{2}-\beta} \exp\left(i\,|z|\,\mathrm{sen}\alpha\right) d\alpha = 2\pi J_0(|z|) = 2\pi J_0\left(q\sqrt{r^2 - a^2 - 2iay'}\right). \tag{C.91}$$

Once Eq. (C.91) is equivalent to Eq. (C.77), we can replace it into Eq. (C.74) and rewrite $\phi_1(\boldsymbol{r}, t)$ as:

$$\phi_1(\boldsymbol{r},t) = \frac{1}{2d\sqrt{\pi^3}}\exp\left(-\frac{a^2}{2}\right)\int_0^{\infty}\exp\left(-\frac{q^2}{2}\right)\cos\left(q^n t'\right) \cdot 2\pi J_0\left(q\sqrt{r^2-a^2-2iay'}\right)qdq, \quad (C.92)$$

$$\phi_1(\boldsymbol{r},t) = \frac{e^{-a^2/2}}{d\sqrt{\pi}}\int_0^{\infty}\exp\left(-\frac{q^2}{2}\right)\cos\left(q^n t'\right)J_0\left(q\sqrt{r^2-a^2-2iay'}\right)qdq. \quad (C.93)$$

Now, we need to solve the integral for θ in Eq. (C.76) given by

$$\int_{-\pi}^{+\pi} e^{in\theta}\exp\left\{iq\left[x'\cos\theta+(y'-ia)\,\mathrm{sen}\theta\right]\right\}d\theta = \int_{-\frac{\pi}{2}-\beta}^{\frac{3\pi}{2}-\beta} e^{in\theta}\exp\left(i\left|z\right|\mathrm{sen}\alpha\right)d\alpha. \quad (C.94)$$

Rewriting $e^{in\theta}$, in order to let it in terms ofα, we have that:

$$e^{in\theta} = e^{in(\alpha-\pi/2+\beta)} = e^{in\alpha}\cdot e^{-in\pi/2}\cdot e^{in\beta} \quad (C.95)$$

On the other hand,

$$e^{-in\pi/2} = \cos\left(\frac{n\pi}{2}\right) - i\,\mathrm{sen}\left(\frac{n\pi}{2}\right) = (-i)^n \quad (C.96)$$

and

$$e^{in\beta} = \left(e^{i\beta}\right)^n = \left(\cos\beta + i\,\mathrm{sen}\beta\right)^n \ . \quad (C.97)$$

Using x' e y' from Eq. (C.82), one can gets

$$e^{in\beta} = \left[\frac{x'}{|z|} + i\frac{(y'-ia)}{|z|}\right], \quad (C.98)$$

$$e^{in\beta} = \left[\frac{x'+a+iy'}{\sqrt{r^2-a^2-2iay'}}\right]^n. \quad (C.99)$$

From Eqs. (C.95), (C.96) and (C.99), the integral defined by Eq. (C.94) becomes:

$$\int_{-\pi}^{+\pi} e^{in\theta}\cdot\exp\left(i\left|z\right|\mathrm{sen}\alpha\right)d\alpha = (-i)^n\left[\frac{x'+a+iy'}{\sqrt{r^2-a^2-2iay'}}\right]^n \cdot \int_{-\pi}^{+\pi}\exp\left(in\alpha + i\left|z\right|\mathrm{sen}\alpha\right)d\alpha. \quad (C.100)$$

Using Eq. (C.90) again, yields

$$\int_{-\pi}^{+\pi}\exp\left(in\alpha + i\left|z\right|\mathrm{sen}\alpha\right)d\alpha = 2\pi J_{-n}\left(|z|\right). \quad (C.101)$$

Substituting Eq. (C.101) into Eq. (C.100) and the relation of the Bessel function defined as $J_{-n}(x) = (-1)^n J_n(x)$, we conclude that

$$\int_{-\frac{\pi}{2}-\beta}^{\frac{3\pi}{2}-\beta} e^{in\theta}\cdot\exp\left(i\left|z\right|\mathrm{sen}\alpha\right)d\alpha = 2\pi\,(i)^n\left[\frac{x'+a+iy'}{\sqrt{r^2-a^2-2iay'}}\right]^n \cdot J_n\left(q\sqrt{r^2-a^2+2iay'}\right). \quad (C.102)$$

Thus, replacing Eq. (C.102) into Eq. (C.76) we finally obtain:

$$\phi_2(\boldsymbol{r},t) = \frac{-i}{d\sqrt{\pi^3}}\left[\frac{ix'-y'+ia}{\sqrt{r^2-a^2+2iay'}}\right]^n \exp\left(-\frac{a^2}{2}\right) \cdot \int_0^\infty \exp\left(-\frac{q^2}{2}\right)\operatorname{sen}\left(q^n t'\right) 2\pi J_n\left(q\sqrt{r^2-a^2-2iay'}\right) q dq, \quad \text{(C.103)}$$

$$\phi_2(\boldsymbol{r},t) = \frac{-ie^{-a^2/2}}{d\sqrt{\pi}}\left[\frac{ix'-y'+ia}{\sqrt{r^2-a^2-2iay'}}\right]^n \cdot \int_0^\infty \exp\left(-\frac{q^2}{2}\right)\operatorname{sen}\left(q^n t'\right) J_n\left(q\sqrt{r^2-a^2-2iay'}\right) q dq. \quad \text{(C.104)}$$

C.4 Expected value $\langle x\rangle$ for monolayer graphene with $C_1 = 1$ e $C_2 = 0$

As an example of how to calculate the expected value $\langle \boldsymbol{r}(t)\rangle$ in the context of the Chap. 4, we demonstrate here, step-by-step, how to $\langle x\rangle$ for monolayer graphene with pseudospin polarization defined by $C_1 = 1$ e $C_2 = 0$

From Eqs. (C.25) e (C.26), we have that:

$$\psi_1(\boldsymbol{r},t) = \frac{C_1}{\sqrt{|C_1|^2+|C_2|^2}}\int G_{11}(\boldsymbol{r},\boldsymbol{r}',t) f(\boldsymbol{r}') d\boldsymbol{r}' + \frac{C_2}{\sqrt{|C_1|^2+|C_2|^2}}\int G_{12}(\boldsymbol{r},\boldsymbol{r}',t) f(\boldsymbol{r}') d\boldsymbol{r}', \quad \text{(C.105)}$$

$$\psi_2(\boldsymbol{r},t) = \frac{C_1}{\sqrt{|C_1|^2+|C_2|^2}}\int G_{21}(\boldsymbol{r},\boldsymbol{r}',t) f(\boldsymbol{r}') d\boldsymbol{r}' + \frac{C_2}{\sqrt{|C_1|^2+|C_2|^2}}\int G_{22}(\boldsymbol{r},\boldsymbol{r}',t) f(\boldsymbol{r}') d\boldsymbol{r}'\,. \quad \text{(C.106)}$$

For C_1=1 and $C_2 = 0$, Eqs. (C.105) and (C.106) reduces to:

$$\psi_1(\boldsymbol{r},t) = \int G_{11}(\boldsymbol{r},\boldsymbol{r}',t) f(\boldsymbol{r}') d\boldsymbol{r} \quad \text{(C.107)}$$

and

$$\psi_2(\boldsymbol{r},t) = \int G_{21}(\boldsymbol{r},\boldsymbol{r}',t) f(\boldsymbol{r}') d\boldsymbol{r}. \quad \text{(C.108)}$$

Using Eqs. (C.48) e (C.53), yields:

$$\psi_1(\boldsymbol{r},t)=\frac{d}{2\hbar^2\sqrt{\pi^3}}\exp\left(-\frac{k_0^2d^2}{2}\right)\cdot\int\exp\left(i\frac{\boldsymbol{p}\cdot\boldsymbol{r}}{\hbar}-\frac{p^2d^2}{2\hbar^2}+\frac{p_{y'}k_0d^2}{\hbar}\right)\cos\left(\frac{p^nt}{\xi\hbar}\right)d\boldsymbol{p}\quad\text{(C.109)}$$

and

$$\psi_2(\boldsymbol{r},t)=\frac{-id}{2\hbar^2\sqrt{\pi^3}}\exp\left(-\frac{k_0^2d^2}{2}\right)\int\left(\frac{p_x+ip_y}{p}\right)^n\cdot\exp\left(i\frac{\boldsymbol{p}\cdot\boldsymbol{r}}{\hbar}-\frac{p^2d^2}{2\hbar^2}+\frac{p_{y'}k_0d^2}{\hbar}\right)\operatorname{sen}\left(\frac{p^nt}{\xi\hbar}\right)d\boldsymbol{p}.\quad\text{(C.110)}$$

Since the objective is to obtain the expected value of $\boldsymbol{r}(t)$, i.e $\langle\boldsymbol{r}(t)\rangle$ using the momentum representation, it is necessary to calculate the $\langle\boldsymbol{r}(t)\rangle$ through

$$\langle\boldsymbol{r}(t)\rangle=\sum_{j=1}^{2}\int\overline{\psi_j}^{\dagger}(\boldsymbol{p},t)\left[i\hbar\nabla_p\right]\overline{\psi_j}(\boldsymbol{p},t)\,d\boldsymbol{p},\quad\text{(C.111)}$$

where

$$\overline{\psi_j}(\boldsymbol{p},t)=\frac{1}{2\pi\hbar}\int\exp\left[-i\frac{\boldsymbol{p}\cdot\boldsymbol{r}}{\hbar}\right]\psi_j(\boldsymbol{r},t)\,d\boldsymbol{r}\quad\text{(C.112)}$$

is the Fourier transform of $\psi_j(\boldsymbol{r},t)$. Thus,

$$\overline{\psi}_1(\boldsymbol{p},t)=\frac{d}{2\hbar^2\sqrt{\pi^3}}\left(\frac{1}{2\pi\hbar}\right)\exp\left(-\frac{k_0^2d^2}{2}\right)\cdot\int\exp\left[-i\frac{\boldsymbol{p}\cdot\boldsymbol{r}}{\hbar}\right]d\boldsymbol{r}\cdot\int\exp\left(i\frac{\boldsymbol{p}'\cdot\boldsymbol{r}}{\hbar}-\frac{p'^2d^2}{2\hbar^2}+\frac{p_{y'}k_0d^2}{\hbar}\right)\cos\left(\frac{p'^nt}{\xi\hbar}\right)d\boldsymbol{p}'\quad\text{(C.113)}$$

$$\overline{\psi}_1(\boldsymbol{p},t)=\frac{d}{4\hbar^3\pi\sqrt{\pi^3}}\exp\left(-\frac{k_0^2d^2}{2}\right)\cdot\left\{\int\exp\left[-i\frac{(\boldsymbol{p}-\boldsymbol{p}')\cdot\boldsymbol{r}}{\hbar}\right]d\boldsymbol{r}\right\}\cdot\int\exp\left(-\frac{p'^2d^2}{2\hbar^2}+\frac{p_{y'}k_0d^2}{\hbar}\right)\cos\left(\frac{p'^nt}{\xi\hbar}\right)d\boldsymbol{p}'\ .\quad\text{(C.114)}$$

From the fact that the term between brackets ($[\cdots]$) in Eq. (C.114) is exactly a Dirac delta, defined as $(2\pi\hbar)^2\,\delta(\boldsymbol{p}-\boldsymbol{p}')$, thus we have:

$$\overline{\psi}_1(\boldsymbol{p},t)=\frac{d}{\hbar\sqrt{\pi}}\exp\left(-\frac{k_0^2d^2}{2}\right)\exp\left(-\frac{p^2d^2}{2\hbar^2}+\frac{p_yk_0d^2}{\hbar}\right)\cos\left(\frac{p^nt}{\xi\hbar}\right).\quad\text{(C.115)}$$

From Eq. (C.110), we conclude that:

$$\overline{\psi}_2(\boldsymbol{p},t)=\frac{1}{2\pi\hbar}\left[\frac{-id}{2\hbar^2\sqrt{\pi^3}}\cdot\exp\left(-\frac{k_0^2d^2}{2}\right)\right]\int\exp\left[-i\frac{\boldsymbol{p}\cdot\boldsymbol{r}}{\hbar}\right]d\boldsymbol{r}\cdot\int\left(\frac{p'_x+ip'_y}{p'}\right)^n\cdot\exp\left(i\frac{\boldsymbol{p}'\cdot\boldsymbol{r}}{\hbar}-\frac{p'^2d^2}{2\hbar^2}+\frac{p'_{y'}k_0d^2}{\hbar}\right)\operatorname{sen}\left(\frac{p'^nt}{\xi\hbar}\right)d\boldsymbol{p},\quad\text{(C.116)}$$

$$\begin{aligned}\overline{\psi}_2(\boldsymbol{p},t) = \frac{-id}{4\hbar^3\pi\sqrt{\pi^3}} \cdot \exp\left(-\frac{k_0^2d^2}{2}\right)&\left\{\int \exp\left[-i\frac{(\boldsymbol{p}-\boldsymbol{p}')\cdot\boldsymbol{r}}{\hbar}\right]d\boldsymbol{r}\right\}\\ &\cdot \int\left(\frac{p'_x+ip'_y}{p'}\right)^n \cdot \exp\left(-\frac{p'^2d^2}{2\hbar^2}+\frac{p'_{y'}k_0d^2}{\hbar}\right)\text{sen}\left(\frac{p'^n t}{\xi\hbar}\right)d\boldsymbol{p}\,.\end{aligned}\tag{C.117}$$

Again, the term between brackets ($[\cdots]$) a Dirac delta, then:

$$\overline{\psi}_2(\boldsymbol{p},t) = \frac{-id}{\hbar\sqrt{\pi}} \cdot \exp\left(-\frac{k_0^2d^2}{2}\right)\left(\frac{p_x+ip_y}{p}\right)^n \cdot \exp\left(-\frac{p^2d^2}{2\hbar^2}+\frac{p_yk_0d^2}{\hbar}\right)\text{sen}\left(\frac{p^n t}{\xi\hbar}\right).\tag{C.118}$$

In Cartesian coordinates, the moment operator is given by

$$\nabla_p = \hat{x}\frac{\partial}{\partial p_x}+\hat{y}\frac{\partial}{\partial p_y}.\tag{C.119}$$

For $\partial\overline{\psi}_1/p_x$ and considering $p^n=\left(p_x^2+p_y^2\right)^{n/2}$, we have that:

$$\frac{\partial\overline{\psi}_1}{\partial p_x} = \frac{d}{\hbar\sqrt{\pi}}\exp\left(-\frac{k_0^2d^2}{2}\right)\frac{\partial}{\partial p_x}\left[\exp\left(-\frac{p^2d^2}{2\hbar^2}+\frac{p_yk_0d^2}{\hbar}\right)\cos\left(\frac{p^n t}{\xi\hbar}\right)\right],\tag{C.120}$$

$$\begin{aligned}\frac{\partial\overline{\psi}_1}{\partial p_x} = \frac{d}{\hbar\sqrt{\pi}}&\exp\left(-\frac{k_0^2d^2}{2}\right)\exp\left(-\frac{p^2d^2}{2\hbar^2}+\frac{p_yk_0d^2}{\hbar}\right)\\ &\cdot\left[-\frac{2p_xd^2}{2\hbar^2}\cos\left(\frac{p^n t}{\xi\hbar}\right)-\text{sen}\left(\frac{p^n t}{\xi\hbar}\right)\frac{t}{\xi\hbar}\frac{n}{2}\left(p_x^2+p_y^2\right)^{\frac{n}{2}-1}\cdot(2p_x)\right],\end{aligned}\tag{C.121}$$

that can be rewritten as

$$\begin{aligned}\frac{\partial\overline{\psi}_1}{\partial p_x} = \frac{d}{\hbar\sqrt{\pi}}&\exp\left(-\frac{k_0^2d^2}{2}\right)\exp\left(-\frac{p^2d^2}{2\hbar^2}+\frac{p_yk_0d^2}{\hbar}\right)\\ &\cdot\left[-\frac{p_xd^2}{\hbar^2}\cos\left(\frac{p^n t}{\xi\hbar}\right)-\text{sen}\left(\frac{p^n t}{\xi\hbar}\right)\frac{nt}{\xi\hbar}p_xp^{n-2}\right].\end{aligned}\tag{C.122}$$

Using the dimensionless variables defined by Eqs. (C.55), (C.56), (C.62) and (C.63), we can rewrite to Eq.(C.122) as

$$\begin{aligned}\frac{\partial\overline{\psi}_1}{\partial p_x} = \frac{d^2}{\hbar^2\sqrt{\pi}}&\exp\left(-\frac{a^2}{2}\right)\exp\left(-\frac{q}{2}+aq\text{sen}\theta\right)\\ &\cdot\left[-q\cos\theta\cos\left(q^nt'\right)-nq^{n-1}t'\cos\theta\text{sen}\left(q^nt'\right)\right].\end{aligned}\tag{C.123}$$

Analogously, $\partial\overline{\psi}_1/\partial p_y$ can be expressed as

$$\frac{\partial\overline{\psi}_1}{\partial p_y} = \frac{d}{\hbar\sqrt{\pi}}\exp\left(-\frac{k_0^2d^2}{2}\right)\frac{\partial}{\partial p_y}\left[\exp\left(-\frac{p^2d^2}{2\hbar^2}+\frac{p_yk_0d^2}{\hbar}\right)\cos\left(\frac{p^n t}{\xi\hbar}\right)\right],\tag{C.124}$$

$$\begin{aligned}\frac{\partial\overline{\psi}_1}{\partial p_y} = \frac{d}{\hbar\sqrt{\pi}}&\exp\left(-\frac{k_0^2d^2}{2}\right)\exp\left(-\frac{p^2d^2}{2\hbar^2}+\frac{p_yk_0d^2}{\hbar}\right)\\ &\cdot\left[\left(-\frac{2p_yd^2}{2\hbar^2}+\frac{k_0d^2}{\hbar}\right)\cos\left(\frac{p^n t}{\xi\hbar}\right)-\text{sen}\left(\frac{p^n t}{\xi\hbar}\right)\frac{t}{\xi\hbar}\frac{n}{2}\left(p_x^2+p_y^2\right)^{\frac{n}{2}-1}\cdot(2p_y)\right],\end{aligned}\tag{C.125}$$

$$\begin{aligned}\frac{\partial\overline{\psi}_1}{\partial p_y} &= \frac{d}{\hbar\sqrt{\pi}}\exp\left(-\frac{k_0^2d^2}{2}\right)\exp\left(-\frac{p^2d^2}{2\hbar^2}+\frac{p_yk_0d^2}{\hbar}\right)\\ &\cdot\left[\left(-\frac{p_yd^2}{\hbar^2}+\frac{k_0d^2}{\hbar}\right)\cos\left(\frac{p^nt}{\xi\hbar}\right)-\text{sen}\left(\frac{p^nt}{\xi\hbar}\right)\frac{nt}{\xi\hbar}p_yp^{n-2}\right].\end{aligned}\tag{C.126}$$

Introducing the dimensionless variables, yields:

$$\begin{aligned}\frac{\partial\overline{\psi}_1}{\partial p_y} &= \frac{d}{\hbar\sqrt{\pi}}\exp\left(-\frac{a^2}{2}\right)\exp\left(-\frac{q^2}{2}+aq\text{sen}\theta\right)\\ &\cdot\left[\left(-\frac{dq\text{sen}\theta}{\hbar}+\frac{ad}{\hbar}\right)\cos\left(q^nt'\right)-nq^{n-1}t'\text{sen}\theta\text{sen}\left(q^nt'\right)\right],\end{aligned}\tag{C.127}$$

$$\begin{aligned}\frac{\partial\overline{\psi}_1}{\partial p_y} &= \frac{d^2}{\hbar^2\sqrt{\pi}}\exp\left(-\frac{a^2}{2}\right)\exp\left(-\frac{q^2}{2}+aq\text{sen}\theta\right)\\ &\cdot\left[\left(-q\text{sen}\theta+a\right)\cos\left(q^nt'\right)-nq^{n-1}t'\text{sen}\theta\text{sen}\left(q^nt'\right)\right].\end{aligned}\tag{C.128}$$

Once

$$\overline{\psi}_1^\dagger\nabla_p\overline{\psi}_1=\left[\overline{\psi}_1^\dagger\left(\frac{\partial\overline{\psi}_1}{\partial p_x}\right)\hat{x}+\overline{\psi}_1^\dagger\left(\frac{\partial\overline{\psi}_1}{\partial p_y}\right)\hat{y}\right],\tag{C.129}$$

then

$$\begin{aligned}\overline{\psi}_1^\dagger\nabla_p\overline{\psi}_1 &= \left\{\left[\frac{d}{\hbar\sqrt{\pi}}\exp\left(-\frac{a^2}{2}\right)\exp\left(-\frac{q^2}{2}+aq\text{sen}\theta\right)\cos\left(q^nt'\right)\right]\right\}\\ &\cdot\left\{\frac{d^2}{\hbar^2\sqrt{\pi}}\exp\left(-\frac{a^2}{2}\right)\exp\left(-\frac{q^2}{2}+aq\text{sen}\theta\right)\cdot\left[-q\text{cos}\theta\text{cos}\left(q^nt'\right)-nq^{n-1}t'\text{cos}\theta\text{sen}\left(q^nt'\right)\right]\right\}\hat{x}\\ &+\left\{\left[\frac{d}{\hbar\sqrt{\pi}}\exp\left(-\frac{a^2}{2}\right)\exp\left(-\frac{q^2}{2}+aq\text{sen}\theta\right)\cos\left(q^nt'\right)\right]\right\}\\ &\cdot\left\{\frac{d^2}{\hbar^2\sqrt{\pi}}\exp\left(-\frac{a^2}{2}\right)\exp\left(-\frac{q^2}{2}+aq\text{sen}\theta\right)\right.\\ &\left.\cdot\left[\left(-q\text{sen}\theta+a\right)\cos\left(q^nt'\right)-nq^{n-1}t'\text{sen}\theta\text{sen}\left(q^nt'\right)\right]\right\}\hat{y}\end{aligned}\tag{C.130}$$

$$\begin{aligned}\overline{\psi}_1^\dagger\nabla_p\overline{\psi}_1 &= \frac{d^3}{\hbar^3\pi}\exp\left(-a^2\right)\exp\left(-q^2+2aq\text{sen}\theta\right)\\ &\cdot\left\{\left[-q\text{cos}\theta\text{cos}^2\left(q^nt'\right)-nq^{n-1}t'\text{cos}\theta\text{sen}\left(q^nt'\right)\cos\left(q^nt'\right)\right]\hat{x}\right.\\ &\left.+\left[\left(-q\text{sen}\theta+a\right)\cos^2\left(q^nt'\right)-nq^{n-1}t'\text{sen}\theta\text{sen}\left(q^nt'\right)\cos\left(q^nt'\right)\right]\hat{y}\right\}.\end{aligned}\tag{C.131}$$

On the other hand, $\text{sen}\left(a\right)\cos\left(a\right)=\text{sen}(2a)/2$, thus

$$\begin{aligned}\overline{\psi}_1^\dagger\nabla_p\overline{\psi}_1 &= \frac{d^3}{\hbar^3\pi}\exp\left(-a^2\right)\exp\left(-q^2+2aq\text{sen}\theta\right)\\ &\cdot\left\{\left[-q\text{cos}\theta\text{cos}^2\left(q^nt'\right)-\frac{n}{2}q^{n-1}t'\text{cos}\theta\text{sen}\left(2q^nt'\right)\right]\hat{x}\right.\\ &\left.+\left[\left(-q\text{sen}\theta+a\right)\cos^2\left(q^nt'\right)-\frac{n}{2}q^{n-1}t'\text{sen}\theta\text{sen}\left(2q^nt'\right)\right]\hat{y}\right\}.\end{aligned}\tag{C.132}$$

Now, repeating the same procedure for $\overline{\psi}_2$, we obtain

$$\frac{\partial\overline{\psi}_2}{\partial p_x} = \frac{-id}{\hbar\sqrt{\pi}} \cdot \exp\left(-\frac{a^2}{2}\right) \frac{\partial}{\partial p_x}\left\{\left(\frac{p_x+ip_y}{p}\right)^n \exp\left(-\frac{p^2d^2}{2\hbar^2}+\frac{p_y ad}{\hbar}\right) \operatorname{sen}\left(\frac{p^n t}{\xi\hbar}\right)\right\} \quad , \tag{C.133}$$

$$\begin{aligned}\frac{\partial\overline{\psi}_2}{\partial p_x} = \frac{-id}{\hbar\sqrt{\pi}} \cdot \exp\left(-\frac{a^2}{2}\right) \cdot \exp\left(-\frac{p^2d^2}{2\hbar^2}+\frac{p_y ad}{\hbar}\right) &\left\{ n\left[\frac{p_x+ip_y}{p}\right]^{n-1}\right. \\ \cdot \frac{\partial}{\partial p_x}\left[p_x\left(p_x^2+p_y^2\right)^{-1/2} + ip_y\left(p_x^2+p_y^2\right)^{-1/2}\right] \operatorname{sen}\left(\frac{p^n t}{\xi\hbar}\right) \\ -\frac{p_x d^2}{\hbar^2}\left(\frac{p_x+ip_y}{p}\right)^n \operatorname{sen}\left(\frac{p^n t}{\xi\hbar}\right) + \left(\frac{p_x+ip_y}{p}\right)^n \cos\left(\frac{p^n t}{\xi\hbar}\right)\frac{nt}{\xi\hbar}p_x p^{n-2} &\left.\right\},\end{aligned} \tag{C.134}$$

$$\begin{aligned}\frac{\partial\overline{\psi}_2}{\partial p_x} = \frac{-id}{\hbar\sqrt{\pi}} \cdot \exp\left(-\frac{a^2}{2}\right) \cdot \exp\left(-\frac{p^2d^2}{2\hbar^2}+\frac{p_y ad}{\hbar}\right) \\ \cdot \left\{ n\left[\frac{p_x+ip_y}{p}\right]^{n-1}\left[\frac{1}{p}-\frac{p_x\left(p_x+ip_y\right)}{p^3}\right] \operatorname{sen}\left(\frac{p^n t}{\xi\hbar}\right)\right. \\ \left. -\frac{p_x d^2}{\hbar^2}\left(\frac{p_x+ip_y}{p}\right)^n \operatorname{sen}\left(\frac{p^n t}{\xi\hbar}\right) + \left(\frac{p_x+ip_y}{p}\right)^n \cos\left(\frac{p^n t}{\xi\hbar}\right)\frac{nt}{\xi\hbar}p_x p^{n-2}\right\} .\end{aligned} \tag{C.135}$$

Since $e^{i\theta} = \left(p_x+ip_y\right)/p$, we have that

$$\begin{aligned}\frac{\partial\overline{\psi}_2}{\partial p_x} = \frac{-id}{\hbar\sqrt{\pi}} \cdot \exp\left(-\frac{a^2}{2}\right) \cdot \exp\left(-\frac{p^2d^2}{2\hbar^2}+\frac{p_y ad}{\hbar}\right) \\ \cdot \left\{ ne^{i(n-1)\theta}\left[\frac{1}{p}-\frac{(p\cos\theta)}{p^2}e^{i\theta}\right] \operatorname{sen}\left(\frac{p^n t}{\xi\hbar}\right)\right. \\ \left. -\frac{p\cos\theta d^2}{\hbar^2}e^{in\theta}\operatorname{sen}\left(\frac{p^n t}{\xi\hbar}\right) + e^{in\theta}\cos\left(\frac{p^n t}{\xi\hbar}\right)\frac{nt}{\xi\hbar}p\cos\theta p^{n-2}\right\} .\end{aligned} \tag{C.136}$$

Introducing the dimensionless variables, yields:

$$\begin{aligned}\frac{\partial\overline{\psi}_2}{\partial p_x} = \frac{-id^2}{\hbar^2\sqrt{\pi}} \cdot \exp\left(-\frac{a^2}{2}\right) \cdot \exp\left(-\frac{q^2}{2}+aq\operatorname{sen}\theta\right) \cdot \left\{ne^{i(n-1)\theta}\left[\frac{1}{q}-\frac{\cos\theta}{q}e^{i\theta}\right]\right. \\ \left. \cdot\operatorname{sen}\left(q^n t'\right) - q\cos\theta e^{in\theta}\operatorname{sen}\left(q^n t'\right) + nq^{n-1}t'\cos\theta e^{in\theta}\cos\left(q^n t'\right)\right\} ,\end{aligned} \tag{C.137}$$

$$\begin{aligned}\frac{\partial\overline{\psi}_2}{\partial p_x} = \frac{-id^2}{\hbar^2\sqrt{\pi}} \cdot \exp\left(-\frac{a^2}{2}\right) \cdot \exp\left(-\frac{q^2}{2}+aq\operatorname{sen}\theta\right) \\ \cdot \left\{ e^{in\theta}\operatorname{sen}\left(q^n t'\right)\left[n\left(\frac{e^{-i\theta}}{q}-\frac{\cos\theta}{q}\right) - q\cos\theta\right] + nt'q^{n-1}\cos\theta e^{in\theta}\cos\left(q^n t'\right)\right\} .\end{aligned} \tag{C.138}$$

Repeating the same procedure for $\partial\overline{\psi}_2/\partial p_y$, we obtain

$$\frac{\partial\overline{\psi}_2}{\partial p_y} = \frac{-id}{\hbar\sqrt{\pi}} \cdot \exp\left(-\frac{a^2}{2}\right)\frac{\partial}{\partial p_y}\left\{\left(\frac{p_x+ip_y}{p}\right)^n \cdot \exp\left(-\frac{p^2d^2}{2\hbar^2}+\frac{p_yad}{\hbar}\right)\mathrm{sen}\left(\frac{p^nt}{\xi\hbar}\right)\right\} \tag{C.139}$$

$$\begin{aligned}\frac{\partial\overline{\psi}_2}{\partial p_y} = \frac{-id}{\hbar\sqrt{\pi}} \cdot \exp\left(-\frac{a^2}{2}\right)\exp\left(-\frac{p^2d^2}{2\hbar^2}+\frac{p_yad}{\hbar}\right)\\ \cdot\left\{n\left(\frac{p_x+ip_y}{p}\right)^{n-1}\frac{\partial}{\partial p_y}\left[(p_x+ip_y)\left(p_x+ip_y\right)^{-1/2}\right]\mathrm{sen}\left(\frac{p^nt}{\xi\hbar}\right)\right.\\ +\left(\frac{p_x+ip_y}{p}\right)^n\left(-\frac{p_yd^2}{\hbar^2}+\frac{ad}{\hbar}\right)\mathrm{sen}\left(\frac{p^nt}{\xi\hbar}\right)\\ \left.+\left(\frac{p_x+ip_y}{p}\right)^n\cos\left(\frac{p^nt}{\xi\hbar}\right)\frac{\partial}{\partial p_y}\left(\frac{p^nt}{\xi\hbar}\right)\right\},\end{aligned} \tag{C.140}$$

$$\begin{aligned}\frac{\partial\overline{\psi}_2}{\partial p_y} = \frac{-id}{\hbar\sqrt{\pi}} \cdot \exp\left(-\frac{a^2}{2}\right)\exp\left(-\frac{p^2d^2}{2\hbar^2}+\frac{p_yad}{\hbar}\right)\\ \cdot\left\{n\left(\frac{p_x+ip_y}{p}\right)^{n-1}\left[\frac{i}{p}-\frac{p_y\left(p_x+ip_y\right)}{p^3}\right]\mathrm{sen}\left(\frac{p^nt}{\xi\hbar}\right)\right.\\ +\left(-\frac{p_yd^2}{\hbar^2}+\frac{ad}{\hbar}\right)\left(\frac{p_x+ip_y}{p}\right)^n\mathrm{sen}\left(\frac{p^nt}{\xi\hbar}\right)\\ \left.+\frac{np_yp^{n-2}t}{\xi\hbar}\left(\frac{p_x+ip_y}{p}\right)^n\cos\left(\frac{p^nt}{\xi\hbar}\right)\right\}.\end{aligned} \tag{C.141}$$

Since $e^{i\theta}=\left(p_x+ip_y\right)/p$, and making the variable changes, yields

$$\begin{aligned}\frac{\partial\overline{\psi}_2}{\partial p_y} = \frac{-id^2}{\hbar^2\sqrt{\pi}} \cdot \exp\left(-\frac{a^2}{2}\right)\exp\left(-\frac{q^2}{2}+qa\mathrm{sen}\theta\right)\\ \cdot\left\{ne^{i(n-1)\theta}\left[\frac{i}{q}-\frac{\mathrm{sen}\theta e^{i\theta}}{q}\right]\mathrm{sen}\left(q^nt'\right)\right.\\ +\left(-q\mathrm{sen}\theta+a\right)e^{in\theta}\mathrm{sen}\left(q^nt'\right)\\ \left.+nq^{n-1}t'\mathrm{sen}\theta e^{in\theta}\cos\left(q^nt'\right)\right\},\end{aligned} \tag{C.142}$$

$$\begin{aligned}\frac{\partial\overline{\psi}_2}{\partial p_y} = \frac{-id^2}{\hbar^2\sqrt{\pi}} \cdot \exp\left(-\frac{a^2}{2}\right)\exp\left(-\frac{q^2}{2}+qa\mathrm{sen}\theta\right)\\ \cdot\left\{e^{in\theta}\mathrm{sen}\left(q^nt'\right)\left[n\left(\frac{e^{-i\theta}}{q}-\frac{\mathrm{sen}\theta}{q}\right)-q\mathrm{sen}\theta+a\right]\right.\\ \left.+nq^{n-1}t'\mathrm{sen}\theta e^{in\theta}\cos\left(q^nt'\right)\right\}.\end{aligned} \tag{C.143}$$

Once

$$\overline{\psi}_2^\dagger\nabla_p\overline{\psi}_2 = \left[\overline{\psi}_2^\dagger\left(\frac{\partial\overline{\psi}_2}{\partial p_x}\right)\hat{x}+\overline{\psi}_2^\dagger\left(\frac{\partial\overline{\psi}_2}{\partial p_y}\right)\hat{y}\right], \tag{C.144}$$

thus

$$\begin{aligned}
\overline{\psi}_2^{\dagger}\nabla_p\overline{\psi}_2 = {} & \left\{\frac{id}{\hbar\sqrt{\pi}}\cdot\exp\left(-\frac{a^2}{2}\right)e^{-in\theta}\cdot\exp\left(-\frac{q^2}{2}+aq\text{sen}\theta\right)\text{sen}\left(q^nt'\right)\right\} \\
& \left\{\frac{-id^2}{\hbar^2\sqrt{\pi}}\cdot\exp\left(-\frac{a^2}{2}\right)\cdot\exp\left(-\frac{q^2}{2}+aq\text{sen}\theta\right)e^{in\theta}\text{sen}\left(q^nt'\right)\left[n\left(\frac{e^{-i\theta}}{q}-\frac{\cos\theta}{q}\right)-q\cos\theta\right]\right. \\
& \left. +nt'q^{n-1}\cos\theta e^{in\theta}\cos\left(q^nt'\right)\right\}\hat{x} \\
& +\left\{\frac{id}{\hbar\sqrt{\pi}}\cdot\exp\left(-\frac{a^2}{2}\right)e^{-in\theta}\cdot\exp\left(-\frac{q^2}{2}+aq\text{sen}\theta\right)\text{sen}\left(q^nt'\right)\right\} \\
& \cdot\left\{\frac{-id^2}{\hbar^2\sqrt{\pi}}\cdot\exp\left(-\frac{a^2}{2}\right)\exp\left(-\frac{q^2}{2}+qa\text{sen}\theta\right)e^{in\theta}\text{sen}\left(q^nt'\right)\right. \\
& \left.\cdot\left[n\left(\frac{e^{-i\theta}}{q}-\frac{\text{sen}\theta}{q}\right)-q\text{sen}\theta+a\right]+nt'q^{n-1}\text{sen}\theta e^{in\theta}\cos\left(q^nt'\right)\right\}\hat{y},
\end{aligned} \tag{C.145}$$

$$\begin{aligned}
\overline{\psi}_2^{\dagger}\nabla_p\overline{\psi}_2 = {} & \frac{d^3}{\hbar^3\pi}\cdot\exp\left(-a^2\right)\exp\left(-q^2+2aq\text{sen}\theta\right) \\
& \cdot\left\{\left[\text{sen}^2\left(q^nt'\right)\left[n\left(\frac{e^{-i\theta}}{q}-\frac{\cos\theta}{q}\right)-q\cos\theta\right]+\frac{n}{2}t'q^{n-1}\cos\theta\text{sen}\left(2q^nt'\right)\right]\hat{x}\right. \\
& \left.\cdot\left[\text{sen}^2\left(q^nt'\right)\left[n\left(\frac{e^{-i\theta}}{q}-\frac{\text{sen}\theta}{q}\right)-q\text{sen}\theta+a\right]+\frac{n}{2}t'q^{n-1}\text{sen}\theta\text{sen}\left(2q^nt'\right)\right]\hat{y}\right\}.
\end{aligned} \tag{C.146}$$

Adding Eqs. (C.132) and (C.146), results in

$$\begin{aligned}
\sum_{j=1}^{2}\overline{\psi}_j^{\dagger}\nabla_p\overline{\psi}_j = {} & \frac{d^3}{\hbar^3\pi}\cdot\exp\left(-a^2\right)\exp\left(-q^2+2aq\text{sen}\theta\right) \\
& \cdot\left\{\left[-q\cos\theta\cos^2\left(q^nt'\right)-\frac{n}{2}q^{n-1}t'\cos\theta\text{sen}\left(2q^nt'\right)\right]\hat{x}\right. \\
& +\left[\text{sen}^2\left(q^nt'\right)\left[n\left(\frac{e^{-i\theta}}{q}-\frac{\cos\theta}{q}\right)-q\cos\theta\right]+\frac{n}{2}t'q^{n-1}\cos\theta\text{sen}\left(2q^nt'\right)\right]\hat{x} \\
& +\left[\left(-q\text{sen}\theta+a\right)\cos^2\left(q^nt'\right)-\frac{n}{2}q^{n-1}t'\text{sen}\theta\text{sen}\left(2q^nt'\right)\right]\hat{y} \\
& \left.+\left[\text{sen}^2\left(q^nt'\right)\left[n\left(\frac{e^{-i\theta}}{q}-\frac{\text{sen}\theta}{q}\right)-q\text{sen}\theta+a\right]+\frac{n}{2}t'q^{n-1}\text{sen}\theta\text{sen}\left(2q^nt'\right)\right]\hat{y}\right\},
\end{aligned} \tag{C.147}$$

$$\begin{aligned}
\sum_{j=1}^{2}\overline{\psi}_j^{\dagger}\nabla_p\overline{\psi}_j = {} & \frac{d^3}{\hbar^3\pi}\cdot\exp\left(-a^2\right)\exp\left(-q^2+2aq\text{sen}\theta\right) \\
& \cdot\left\{\left[-q\cos\theta\left[\cos^2\left(q^nt'\right)+\text{sen}^2\left(q^nt'\right)\right]+n\left(\frac{e^{-i\theta}}{q}-\frac{\cos\theta}{q}\right)\text{sen}^2\left(q^nt'\right)\right]\hat{x}\right. \\
& \left.+\left[\left(-q\text{sen}\theta+a\right)\left[\cos^2\left(q^nt'\right)+\text{sen}^2\left(q^nt'\right)\right]+n\left(\frac{e^{-i\theta}}{q}-\frac{\text{sen}\theta}{q}\right)\text{sen}^2\left(q^nt'\right)\right]\hat{y}\right\},
\end{aligned} \tag{C.148}$$

$$\sum_{j=1}^{2}\overline{\psi}_j^{\dagger}\nabla_p\overline{\psi}_j=\frac{d^3}{\hbar^3\pi}\cdot\exp\left(-a^2\right)\exp\left(-q^2+2aq\text{sen}\theta\right)$$
$$\cdot\left\{\left[-q\text{cos}\theta+n\left(\frac{e^{-i\theta}}{q}-\frac{\text{cos}\theta}{q}\right)\text{sen}^2\left(q^nt'\right)\right]\hat{x}\right.$$
$$\left.+\left[\left(-q\text{sen}\theta+a\right)+n\left(\frac{e^{-i\theta}}{q}-\frac{\text{sen}\theta}{q}\right)\text{sen}^2\left(q^nt'\right)\right]\hat{y}\right\}. \quad (C.149)$$

Replacing Eq.(C.149) into Eq.(C.111) and using Eq.(C.73)[1], one can gets:

$$\langle x\left(t\right)\rangle=\left(i\hbar\frac{\hbar^2}{d^2}\right)\left(\frac{d^3e^{-a^2}}{\hbar^3\pi}\right)\int_0^{\infty}\int_{-\pi}^{\pi}\left\{\exp\left(-q^2+2aq\text{sen}\theta\right)\right.$$
$$\left.\left[-q^2\text{cos}\theta+n\left(e^{-i\theta}-\text{cos}\theta\right)\text{sen}^2\left(q^nt'\right)\right]\right\}dqd\theta\ . \quad (C.150)$$

Using $e^{i\theta}-\text{cos}\theta=-i\text{sen}\theta$, then

$$\langle x\left(t\right)\rangle=\left(\frac{ide^{-a^2}}{\pi}\right)\int_0^{\infty}e^{-q^2}dq\left\{\int_{-\pi}^{\pi}\exp\left(2aq\text{sen}\theta\right)\left[-in\text{sen}\theta\text{sen}^2\left(q^nt'\right)-q^2\text{cos}\theta\right]d\theta\right\}. \quad (C.151)$$

Now it is necessary to solve the integral in the variable θ, such that:

$$-in\text{sen}^2\left(q^nt'\right)\int_{-\pi}^{\pi}\exp\left(2aq\text{sen}\theta\right)\text{sen}\theta d\theta-q^2\int_{-\pi}^{\pi}\exp\left(2aq\text{sen}\theta\right)\text{cos}\theta d\theta\ . \quad (C.152)$$

But $\text{sen}\theta=\left(e^{i\theta}-e^{-i\theta}\right)/2i$ and $\text{cos}\theta=\left(e^{i\theta}+e^{-i\theta}\right)/2$, then

$$-\frac{n}{2}\text{sen}^2\left(q^nt'\right)\int_{-\pi}^{\pi}\exp\left(2aq\text{sen}\theta+i\theta\right)d\theta+\frac{n}{2}\text{sen}^2\left(q^nt'\right)\int_{-\pi}^{\pi}\exp\left(2aq\text{sen}\theta-i\theta\right)d\theta$$
$$-\frac{q^2}{2}\int_{-\pi}^{\pi}\exp\left(2aq\text{sen}\theta+i\theta\right)d\theta-\frac{q^2}{2}\int_{-\pi}^{\pi}\exp\left(2aq\text{sen}\theta-i\theta\right)d\theta. \quad (C.153)$$

$$-\frac{n}{2}\text{sen}^2\left(q^nt'\right)\left[2\pi iI_1\left(2aq\right)\right]+\frac{n}{2}\text{sen}^2\left(q^nt'\right)\left[-2\pi iI_1\left(2aq\right)\right]$$
$$-\frac{q^2}{2}\left[2\pi iI_1\left(2aq\right)\right]-\frac{q^2}{2}\left[-2\pi iI_1\left(2aq\right)\right]. \quad (C.154)$$

$$-n\pi i\text{sen}^2\left(q^nt'\right)I_1\left(2aq\right)-n\pi i\text{sen}^2\left(q^nt'\right)I_1\left(2aq\right)-\pi iq^2I_1\left(2aq\right)+\pi iq^2I_1\left(2aq\right), \quad (C.155)$$

$$-2n\pi i\text{sen}^2\left(q^nt'\right)I_1\left(2aq\right). \quad (C.156)$$

Substituting Eq.(C.156) into Eq.(C.151), yields:

$$\langle x\left(t\right)\rangle=\left(\frac{ide^{-a^2}}{\pi}\right)\int_0^{\infty}e^{-q^2}\left[-2n\pi i\text{sen}^2\left(q^nt'\right)I_1\left(2aq\right)\right]dq, \quad (C.157)$$

---

[1] Equation (C.73) correspond to: $\int_{-\infty}^{\infty}d\boldsymbol{p}\rightarrow\int_0^{\infty}pdp\int_{-\pi}^{\pi}d\theta=\left(\hbar^2/d^2\right)\int_0^{\infty}qdq\int_{-\pi}^{\pi}d\theta$

$$\langle x\left(t\right)\rangle=\left(2nde^{-a^{2}}\right)\int_{0}^{\infty}e^{-q^{2}}\mathrm{sen}^{2}\left(q^{n}t'\right)I_{1}\left(2aq\right)dq. \tag{C.158}$$

On the other hand, $\mathrm{sen}^{2}\left(q^{n}t'\right)=\left[1-\cos\left(2q^{n}t'\right)\right]/2$, thus:

$$\langle x\left(t\right)\rangle=\left(2nde^{-a^{2}}\right)\int_{0}^{\infty}e^{-q^{2}}\left(\frac{1-\cos\left(2q^{n}t'\right)}{2}\right)I_{1}\left(2aq\right)dq, \tag{C.159}$$

$$\langle x\left(t\right)\rangle=\left(nde^{-a^{2}}\right)\int_{0}^{\infty}e^{-q^{2}}I_{1}\left(2aq\right)dq-\left(nde^{-a^{2}}\right)\int_{0}^{\infty}e^{-q^{2}}\cos\left(2q^{n}t'\right)I_{1}\left(2aq\right)dq. \tag{C.160}$$

From the table of integrals available in Ref. [312], we have that:

$$\int_{0}^{\infty}e^{-\alpha x^{2}}I_{\nu}\left(\beta x\right)dx=\frac{\sqrt{\pi}}{2\sqrt{\alpha}}\exp\left(\frac{\beta^{2}}{8\alpha}\right)I_{\nu/2}\left(\frac{\beta^{2}}{8\alpha}\right), \tag{C.161}$$

then

$$\int_{0}^{\infty}e^{-q^{2}}I_{1}\left(2aq\right)dq=\frac{\sqrt{\pi}}{2}\exp\left(\frac{a^{2}}{2}\right)I_{1/2}\left(\frac{a^{2}}{2}\right). \tag{C.162}$$

Replacing Eq.(C.162) into Eq.(C.160), yields

$$\langle x\left(t\right)\rangle=\frac{nd\sqrt{\pi}}{2}e^{-a^{2}/2}I_{1/2}\left(\frac{a^{2}}{2}\right)-\left(nde^{-a^{2}}\right)\int_{0}^{\infty}e^{-q^{2}}\cos\left(2q^{n}t'\right)I_{1}\left(2aq\right)dq. \tag{C.163}$$

It is still also possible to simplify Eq.(C.163), since the first order modified Bessel function can be written as [313]:

$$I_{\nu}\left(x\right)=\frac{1}{\left(\sqrt{\pi}\right)\Gamma\left(n+1/2\right)}\left(\frac{x}{2}\right)^{\nu}\int_{-1}^{1}e^{-xt}\left(1-t^{2}\right)^{\nu-1/2}dt. \tag{C.164}$$

Taking $\nu=1/2$ in Eq.(C.164), yields:

$$I_{1/2}\left(x\right)=\frac{1}{\left(\sqrt{\pi}\right)\Gamma\left(1\right)}\left(\frac{x}{2}\right)^{1/2}\int_{-1}^{1}e^{-xt}dt, \tag{C.165}$$

$$I_{1/2}\left(x\right)=\frac{1}{\sqrt{\pi}}\left(\frac{x}{2}\right)^{1/2}\left[-\frac{e^{-xt}}{x}\right]_{-1}^{1}, \tag{C.166}$$

$$I_{1/2}\left(x\right)=\frac{1}{\sqrt{\pi}}\left(\frac{x}{2}\right)^{1/2}\left(\frac{e^{x}-e^{-x}}{x}\right). \tag{C.167}$$

Now, taking $x=a^{2}/2$ we obtain:

$$I_{1/2}\left(\frac{a^{2}}{2}\right)=\frac{1}{\sqrt{\pi}}\left(\frac{a^{2}}{4}\right)^{1/2}\left(\frac{2}{a^{2}}\right)\left(e^{a^{2}/2}-e^{-a^{2}/2}\right), \tag{C.168}$$

$$I_{1/2}\left(\frac{a^{2}}{2}\right)=\left(\frac{e^{a^{2}/2}-e^{-a^{2}/2}}{a\sqrt{\pi}}\right), \tag{C.169}$$

Organizing the first term of Eq.(C.164), yields:

$$\frac{nd\sqrt{\pi}}{2}e^{-a^{2}/2}I_{1/2}\left(\frac{a^{2}}{2}\right)=\left(\frac{nd\sqrt{\pi}}{2}e^{-a^{2}/2}\right)\left(\frac{e^{a^{2}/2}-e^{-a^{2}/2}}{a\sqrt{\pi}}\right), \tag{C.170}$$

$$\frac{nd\sqrt{\pi}}{2}e^{-a^2/2}I_{1/2}\left(\frac{a^2}{2}\right)=\frac{1-e^{-a^2}}{2a}nd. \tag{C.171}$$

Finally, replacing Eq.(C.171) into Eq. (C.163), we obtain

$$\langle x\,(t)\rangle = nd\frac{1-e^{-a^2}}{2a} - nde^{-a^2}\int_0^\infty e^{-q^2}\cos\left(2q^n t'\right)I_1\left(2aq\right)dq. \tag{C.172}$$

Therefore, for $n = 1$ we obtain

$$\langle x\,(t)\rangle = d\left[\frac{1-e^{-a^2}}{2a} - e^{-a^2}\int_0^\infty e^{-q^2}\cos\left(2qt'\right)I_1(2aq)\,dq\right] \tag{C.173}$$

that is the same Eq. (4.27) of the main text.

The procedure described here can be applied for the other pseudospin polarization and it can be extended to the component y of the center mass of the Gaussian wave packet in order to calculate $\langle y\,(t)\rangle$. In order not to be repetitive, this procedure has been omitted here.

C.5 Split-operator: a computational method

In this appendix, the numerical method *split-operator* is discussed in more detail.

Using the Schrödinger representation, we can describe the dynamics of a particle using the time evolution operator $\hat{U}(t,t_0)$. Assuming that the initial state is represented by $\psi(\boldsymbol{r},t_0)$, we can get the state for a later time $(t>0)$ from

$$\psi(\boldsymbol{r},t)=\hat{U}(t,t_0)\psi(\boldsymbol{r},t_0). \tag{C.174}$$

When the Hamiltonian does not explicitly depend on time t, the time evolution operator can be written as [185]:

$$\hat{U}(t,t_0)=\exp\left[-\frac{i}{\hbar}H(t-t_0)\right]. \tag{C.175}$$

In the TB model, we can consider atomic sites to be a lattice of potential wells, such that each site that can confine an electron, which has a non-zero probability of tunneling from one well to another first neighbor.

First, let us consider the case where we have a periodic row of atoms. This system can be represented by a one-dimensional lattice of quantum wells, as represented in Fig. C.2. Considering that the barriers between the wells have infinite height, such that the electron would have zero probability of tunneling, and defining the Hamiltonian of this system as H_∞, we have that: $H_\infty\left|\psi_i\right\rangle = E_0\left|\psi_i\right\rangle$. That is, an electron trapped in the i-th well is a eigenstate of the system, with ground state energy of the well E_0, for any value of i. On the other hand, if the barrier between the wells is finite (Fig.C.2), there will be a non-zero probability of the tunneling, such that it is not possible to guarantee that $\left|\psi_i\right\rangle$ is a system eigenstate.

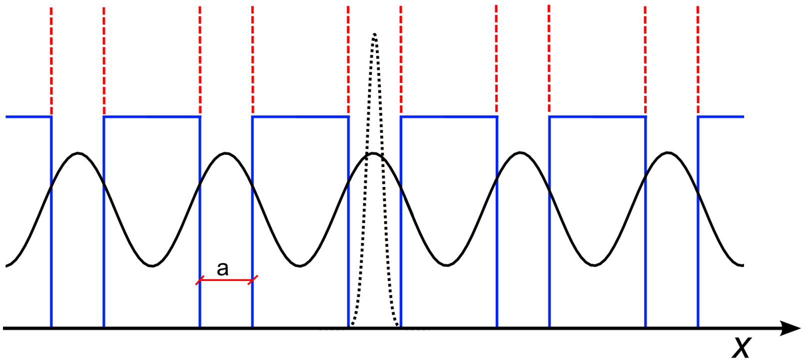

Figure C.2: Illustration of periodic potential wells with width a representing a row of atoms. When the potential is infinite (red), the probability of the tunneling is zero. As a consequence, the wavefunction is completely confined inside the well. On the other hand, if the potential well is finite (blue color) the electron will have a non-zero probability of tunneling from one well to another.

However, we can estimate that by applying H over $|\psi_i\rangle$, where H is the Hamiltonian of the system with finite well, we have that:

$$H\,|\psi_i\rangle = ... + \tau_{i-1}\,|\psi_{i-1}\rangle + E_0\,|\psi_i\rangle + \tau_{i+1}\,|\psi_{i+1}\rangle + ... \tag{C.176}$$

where τ_i represents the energy hopping of an electron between the wells $i-1$ and $i+1$. Note that the states $|\psi_i\rangle$, with $i = 1, 2, 3, ...$, where $|\psi_i\rangle$ represents an electron confined in each well, are orthogonal, because in the case where we had infinite wells, an electron could not occupy two sites simultaneously. Therefore, these states form an orthonormal basis and is possible to write any state of the system, with finite potential, as $|\Psi\rangle = \sum_i a_i\,|\psi_i\rangle$. The eigenenergy and the coefficients a_i of its eigenstates can be determined by writing H on this basis and diagonalizing it. But diagonalize the Hamiltonian defined in Eq. (C.176), which has infinite terms, is not the best way to do this. To contour this problem, we can consider the hopping only between the nearest-neighbors, such that Eq. (C.176) reduces to

$$H\,|\psi_i\rangle \approx \tau_{i-1}\,|\psi_{i-1}\rangle + E_0\,|\psi_i\rangle + \tau_{i+1}\,|\psi_{i+1}\rangle\,. \tag{C.177}$$

Therefore, considering the base given by $|\Psi\rangle = \sum_i a_i\,|\psi_i\rangle$, the Hamiltonian H can be

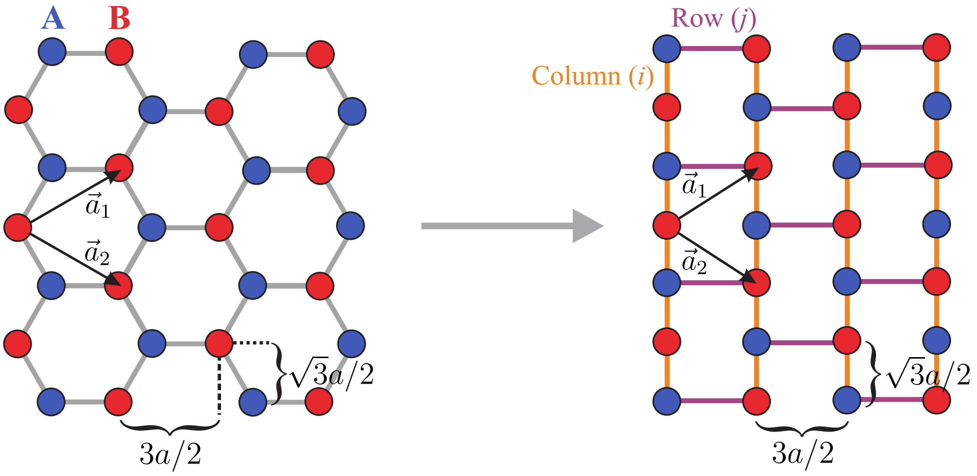

Figure C.3: Mapping the hexagonal lattice to a rectangular lattice. Topological equivalence: each site has three other nearest neighbors, the lattice area is equal to $3\sqrt{3}a^2/2$ and the unit vectors that generate the sublattices are equivalent in both representations. In the structure on the right we also have the representation of the columns (rows) by the letter i (j).

written as a sparse tridiagonal matrix[2] defined as:

$$H \approx H_{TB} = \begin{pmatrix} \ddots & \ddots & 0 & 0 & 0 & 0 \\ \ddots & E_0 & t_{i-1} & 0 & 0 & 0 \\ 0 & t_{i-1} & E_0 & t_i & 0 & 0 \\ 0 & 0 & t_i & E_0 & t_{i+1} & \ddots \\ 0 & 0 & 0 & t_{i+1} & E_0 & \ddots \\ 0 & 0 & 0 & 0 & \ddots & \ddots \end{pmatrix} \tag{C.178}$$

Since our problem is bi-dimensional, we thus need to rewrite the Hamiltonian H_{TB}, Eq. (C.177). To do so, is necessary take into account two different index i e j, instead only one i, as in the 1D case, in order to define the atomic position. As can be seen in Fig. C.3, that illustrates the mapping of the honeycomb (representing the graphene lattice) lattice into a rectangular lattice, i represents the row and j the line. Thus, to consider the atomic positions in two-dimensions, Eq. (C.177) becomes:

$$\begin{aligned} H\left|\psi_{i,,j}\right\rangle \approx +E_0\left|\psi_{i,j}\right\rangle + \tau_{(i-1),j}\left|\psi_{(i-1),j}\right\rangle + \tau_{(i+1),j}\left|\psi_{(i+1),j}\right\rangle \\ + \tau_{i,(j-1)}\left|\psi_{i,(j-1)}\right\rangle + \tau_{i,(j+1)j}\left|\psi_{i,(j+1)j}\right\rangle . \end{aligned} \tag{C.179}$$

This new matrix, unlike the one-dimensional matrix given by Eq. (C.177), has five non-zero diagonals and can be classified as a sparse pentadiagonal matrix, which we can

---

[2] Sparse matrices are matrices in which most positions are equal to zero. In this type of structure, only the significant values are stored, in order to obtain a better performance in the execution of the numerical calculation.

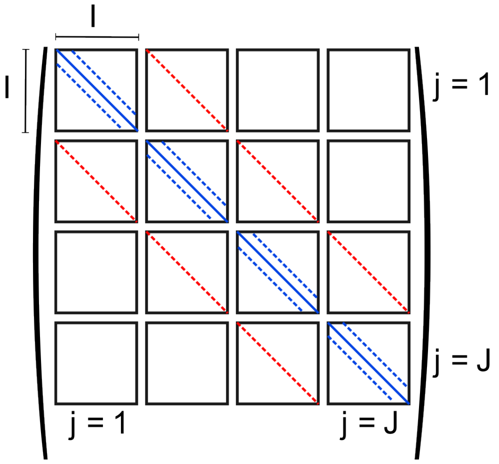

Figure C.4: Illustration of the structure of the pentadiagonal matrix corresponding to the *tight-binding* model for a two-dimensional lattice. The main diagonal (solid blue line) and the blue dotted sub-diagonal have all non-zero terms, while the red dotted sub-diagonal have interspersed non-null and null terms. All other elements outside these five diagonals are null. Each block represents a square matrix of order I, the number of rows of the lattice. The number of columns of the lattice sites defines the number of blocks (J). Therefore, the total number of elements in the H_{TB} array in two dimensions will be: $I \times I \times J \times J$.

separate into blocks, as illustrated in Fig. C.4. Note that each term of the secondary diagonals of the matrix in Fig. C.4 represents the hopping between an atom and its upper and lower neighbors (with different $i's$), represented by the blue dotted lines, and between an atom and the right and left nearest neighbors (with different $j's$), represented by the red dotted lines. As the atomic interaction at the right and left to the nearest neighbors occur alternately (see Fig. C.3), the red subdiagonals presents null and non-null values also alternately[3].

Thus, in two dimensions Eq. (C.179) becomes

$$H|\psi_{i,j}\rangle = H_i|\psi_{i,j}\rangle + H_j|\psi_{i,j}\rangle, \tag{C.180}$$

where H_i and H_j are given by

$$H_i|\psi_{i,j}\rangle = \left(\frac{E_0 + V_{i,j}}{2}\right)|\psi_{i,j}\rangle + \tau_{i,j-1}|\psi_{i,j-1}\rangle + \tau_{i,j+1}|\psi_{i,j+1}\rangle \tag{C.181}$$

and

$$H_j|\psi_{i,j}\rangle = \left(\frac{E_0 + V_{i,j}}{2}\right)|\psi_{i,j}\rangle + \tau_{i-1,j}|\psi_{i-1,j}\rangle + \tau_{i+1,j}|\psi_{i+1,j}\rangle. \tag{C.182}$$

From Ref.[55], the time evolution operator can be defined as:

$$\exp\left[-\frac{i}{\hbar}H\Delta t\right] = \exp\left[-\frac{i}{2\hbar}H_j\Delta t\right]\exp\left[-\frac{i}{\hbar}H_i\Delta t\right]\exp\left[-\frac{i}{2\hbar}H_j\Delta t\right] + \mathcal{O}(\Delta t^3), \tag{C.183}$$

---

[3] To facilitate the use of computational methods for Graphene, Wakabayashi, etc. al [314], he suggested mapping the hexagonal lattice through a rectangular lattice, as shown in Fig. C.3.

where the error comes from the non-commutativity between the operators H_i and H_j [315].

Thus, the wave function for an infinitesimally later time will be given by

$$|\psi_{i,j}\rangle_{t+\Delta t} \cong \exp\left[-\frac{i}{2\hbar}H_j\Delta t\right]\exp\left[-\frac{i}{\hbar}H_i\Delta t\right]\exp\left[-\frac{i}{2\hbar}H_j\Delta t\right]|\psi_{i,j}\rangle_t. \tag{C.184}$$

Equation (C.184) can be divided in three parts:

$$\eta_{i,j} = \exp\left[-\frac{i}{2\hbar}H_j\Delta t\right]|\psi_{i,j}\rangle_t, \tag{C.185}$$

$$|\psi_{i,j}\rangle_{t+\Delta t} = \exp\left[-\frac{i}{2\hbar}H_j\Delta t\right]\xi_{i,j} \tag{C.186}$$

and

$$\eta_{i,j} = \exp\left[-\frac{i}{2\hbar}H_j\Delta t\right]|\psi_{i,j}\rangle_t. \tag{C.187}$$

Using the Cayley[4] relation for exponential, is possible to rewrite Eqs. (C.185), (C.186) and (C.187) as

$$\left(1+\frac{i}{4\hbar}H_j\Delta t\right)\eta_i,j = \left(1-\frac{i}{4\hbar}H_j\Delta t\right)|\psi_{i,j}\rangle_t, \tag{C.188}$$

$$\left(1+\frac{i}{4\hbar}H_i\Delta t\right)\xi_i,j = \left(1-\frac{i}{4\hbar}H_i\Delta t\right)\eta_i,j, \tag{C.189}$$

and

$$\left(1+\frac{i}{4\hbar}H_j\Delta t\right)|\psi_{i,j}\rangle_{t+\Delta t} = \left(1-\frac{i}{4\hbar}H_j\Delta t\right)\xi_i,j. \tag{C.190}$$

Thus, the 2D problem, which should initially be represented by a pentadiagonal matrix, can now be reduced to three equations that only contain tridiagonal matrices.

Orientation of the coordinate systems of momentum in the Dirac model (red arrows) and *tight-binding* (black arrows) in the vicinity of the non-equivalent Dirac points K and K' . For the point labeled as 4, with coordinates given by $\mathbf{K} = \left(0, -4\pi/3\sqrt{3}a_0\right)$, the Dirac Hamiltonian is obtained by rotating the axes by an angle of 90º, which means that the coordinates will be transformed as follows:

As a last point to be mentioned here, as the objective was to compare the numerical method (split-operator) with the analytical one (Dirac) it is also important to note that, for example, for the point $\mathbf{K} = \left(0, -4\pi/3\sqrt{3}a_0\right)$, the Hamiltonian of Dirac is obtained by rotating the axes by an angle of 270º, Fig. **??**. This means that the coordinates will be transformed by: $x \longrightarrow -\mathbf{y}$ and $y \longrightarrow \mathbf{x}$. As this is just a redefinition, we just need to assume that the coordinates x and y will be the same for the numerical and analytical model, such that we can obtain concise results in these two models.

---

[4] $\exp\left[\epsilon\hat{A}\right] = \left[1-\frac{\epsilon\hat{A}}{2}\right]^{-1}\left[1+\frac{\epsilon\hat{A}}{2}\right] + \mathcal{O}(\epsilon^4)$

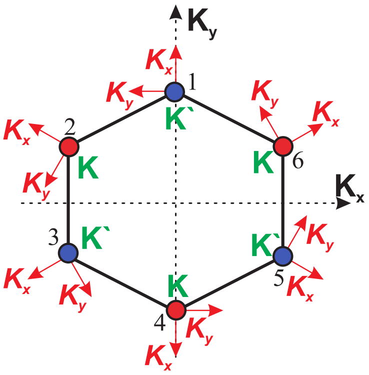

Figure C.5: Orientation of the coordinate systems of momentum in the Dirac model (red arrows) and tight-binding (black arrows) in the vicinity of the non-equivalent Dirac points K and K' . For the point labeled as 4, with coordinates given by $\mathbf{K} = \left(0, -4\pi/3\sqrt{3}a_0\right)$, the Dirac Hamiltonian is obtained by rotating the axes by an angle of 90º, which means that the coordinates will be transformed as follows: $x \longrightarrow -\mathbf{y}$ e $y \longrightarrow \mathbf{x}$.

C.6 Direction of the wave packet as a function of layers number

Analytically, a general expression for $\langle x\left(t\right)\rangle$ and $\langle y\left(t\right)\rangle$, in cylindrical coordinate, as a function of N-ABC layers, can be obtained from Eq. (4.15). Since for $(C_1\ C_2)^T = (1\ 0)^T$ the wave packet always moves in the positive direction of the x-axis, as shown in Fig. 4.8, we analysed here only the other two initial pseudospinor configuration, i.e $(1\ 1)^T$ and $(1\ i)^T$. Thus, for these cases, $\langle x\left(t\right)\rangle$ is defined, respectively, as

$$\langle x\left(t\right)\rangle = \alpha(2q^n t\cos(\phi)\cos(n\phi) + \sin(2q^n t)\sin(n\phi)\sin(\phi)) \tag{C.191a}$$

$$\langle x\left(t\right)\rangle = \alpha(2q^n t\cos(\phi)\sin(n\phi) - \sin(2q^n t)\cos(n\phi)\sin\left(\phi\right)), \tag{C.191b}$$

where $\alpha = \left(nde^{-a^2}/2\pi\right)\int e^{-q^2}dq\int e^{2aq\sin(\phi)}d\phi$. Solving the integral in ϕ of Eq. (C.191a) (Eq. (C.191b)), we concluded that for n even (odd), $\langle x\left(t\right)\rangle$ is null. On the other hand, the opposite occurs for $\langle y\left(t\right)\rangle$ (this can be verified in a similar way). This alternation of the nullity of $\langle x\left(t\right)\rangle$ and $\langle y\left(t\right)\rangle$, for up to 3 layers, for different initial pseudospinor, is illustrated in Fig. 4.8. Once the analytical expressions of $\langle x\left(t\right)\rangle$ and $\langle y\left(t\right)\rangle$ were obtained, we used the default method of Mathematica® Software (Gauss - Kronrod quadrature method) to perform numerically the integrals present in such expressions.

D

Support information for ZBW of moiré excitons in twisted MoS_2/WSe_2 hetero-bilayers

In this support information section, we present (i) the parameters of the moiré exciton used in the main text; (ii) the expression for the hopping energy dependence on the moiré trapping potential and other system parameters; and (iii) the expectation values of the position $\langle \boldsymbol{r}(t) \rangle$ of a moiré exciton in a MoS2/WSe2 van der Waals heterostructure (vdWhs) for an initial Gaussian wave packet with different pseudo-spinors, in addition to those discussed in the main text.

D.1 Material parameters of R-type MoS_2/WSe_2: inter-layer exciton bandgap and moiré exciton band structure

An important consequence of the moiré pattern in a twisted MoS_2/WSe_2 hetero-bilayer is the fact that the inter-layer excitons bandgap, $E_g(\boldsymbol{r}_0)$, is a function of the in-plane

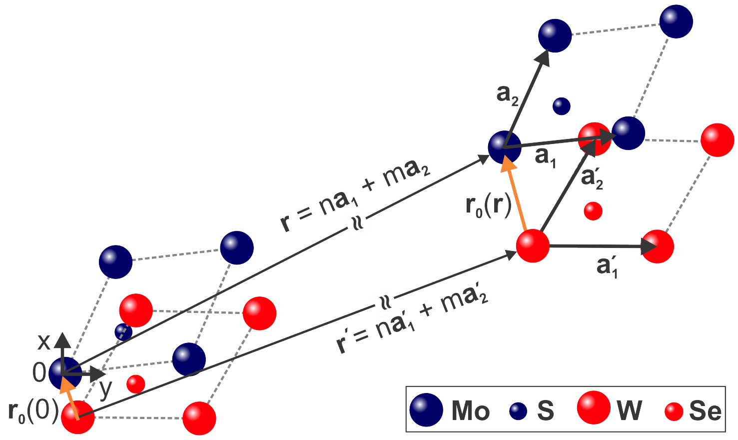

Figure D.1: Dependence of interlayer translation vector $\boldsymbol{r}_0(\boldsymbol{r})$ on the interplane position vector $\boldsymbol{r}$ in a MoS_2/WSe_2 hetero-bilayer (adapted from Ref. [53]).

displacement vector from a metal site in the hole layer to a nearest-neighbor metal site in the electron layer. In turn, $\boldsymbol{r}_0(\boldsymbol{r})$ depends on the location $\boldsymbol{r}$ in the moiré pattern. A complete description of the approximation to obtain the equation for $E_g(\boldsymbol{r}_0)$ can be found in Ref. [316] and also in the Supplementary Material of Ref. [53]. Therefore, we will limit ourselves here to just reproducing such equation, for the sake of completeness, which is defined as:

$$E_g(\boldsymbol{r}_0) = E_{g,0} + \Delta E_{g,1}|f_0(\boldsymbol{r_0})|^2 + \Delta E_{g,2}|f_+(\boldsymbol{r_0})|^2 \ , \tag{D.1}$$

with the mapping from the moiré supercell to the monolayer unit cell defined by the function

$$\boldsymbol{r}_0(\boldsymbol{r}) = \boldsymbol{r}_0(0) + \boldsymbol{R} - \boldsymbol{R}' = \boldsymbol{r}_0(0) + n(\boldsymbol{a}_1 - \boldsymbol{a}_1') + m(\boldsymbol{a}_2 - \boldsymbol{a}_2') \ , \tag{D.2}$$

where $\boldsymbol{r} \equiv n\boldsymbol{a}_1 + m\boldsymbol{a}_2$ and $\boldsymbol{r}' \equiv n\boldsymbol{a}_1' + m\boldsymbol{a}_2' = (1+\delta)\hat{C}_{-\delta\theta}\boldsymbol{r}$. The primitive lattice vectors of WSe_2 (MoS_2) are given by $\boldsymbol{a}_{1,2}'$ ($\boldsymbol{a}_{1,2} = \frac{1}{1+\delta}\hat{C}_{\delta\theta}\boldsymbol{a}_{1,2}'$), see Fig. D.1. n and m are integers and $\hat{C}_{-\delta\theta}$ represents the rotation of $\boldsymbol{r}$ by an angle $-\delta\theta$. In Eq. (D.1), as discussed in Ref. [316], $\boldsymbol{f}_0(\boldsymbol{r}_0)$ and $\boldsymbol{f}_\pm(\boldsymbol{r}_0)$ are defined, respectively, as:

$$f_0(\boldsymbol{r}_0) = \frac{e^{-i\boldsymbol{K}\cdot\boldsymbol{r}_0} + e^{-i\hat{C}_3\boldsymbol{K}\cdot\boldsymbol{r}_0} + e^{-i\hat{C}_3^2\boldsymbol{K}\cdot\boldsymbol{r}_0}}{3} \ , \tag{D.3}$$

and

$$f_\pm(\boldsymbol{r}_0) = \frac{e^{-i\boldsymbol{K}\cdot\boldsymbol{r}_0} + e^{-i(\hat{C}_3\boldsymbol{K}\cdot\boldsymbol{r}_0 \pm \frac{2\pi}{3})} + e^{-i(\hat{C}_3^2\boldsymbol{K}\cdot\boldsymbol{r}_0 \pm \frac{4\pi}{3})}}{3} \ . \tag{D.4}$$

The coupling between two bands in different layers at the $\boldsymbol{K}$-point, considering only the leading Fourier components, are defined by $\boldsymbol{f}_\pm(\boldsymbol{r}_0)$, as discussed in Refs. [53, 316].

On the other hand, the interlayer separation can also be defined as [53]

$$d(\boldsymbol{r}_0) = \boldsymbol{d}_0 + \Delta d_1|f_0(\boldsymbol{r_0})|^2 + \Delta d_2|f_+(\boldsymbol{r_0})|^2 \ , \tag{D.5}$$

obtained from an experimental data fitting in Ref. [53] (for more details, see Ref. [53], Sec. II).

Table D.1: The parameters to obtain the colormap and moiré exciton band structure of R-type MoS_2/WSe_2 hetero-bilayer obtained from Refs. [53, 316].

Variable	Value
b	10 nm
δ	3 meV
$\Delta E_{g,1}$	-116 meV
$\Delta E_{g,2}$	-94 meV
d_0	6.387 Å
Δd_1	0.544 Å
Δd_2	0.042 Å

All parameters used to obtain the moiré exciton band structure and the colormap of the inter-layer exciton in Figs. 1(c) and 1(e) in the main text, respectively, are summarized in Tab. D.1.

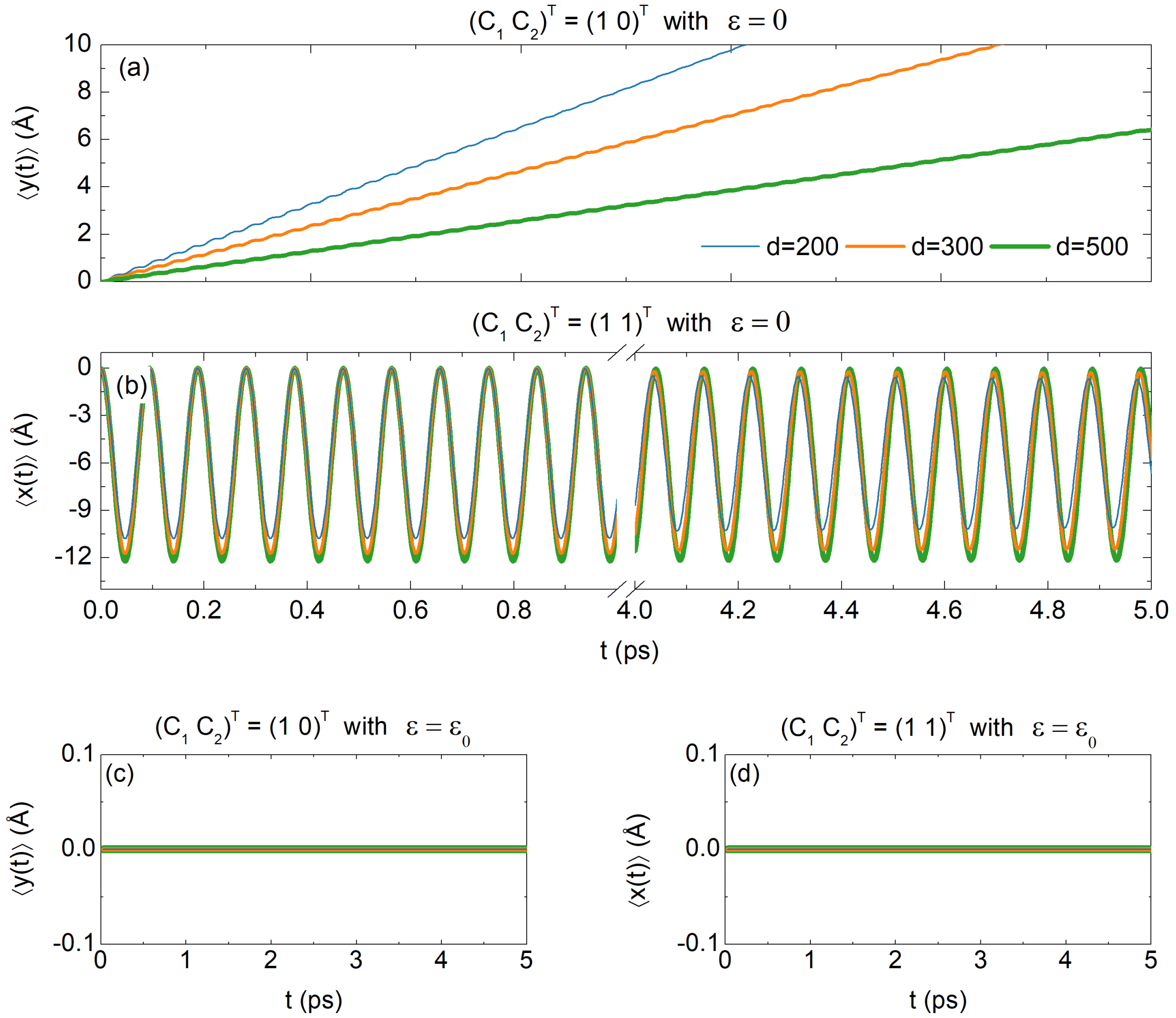

Figure D.2: (a)-(d) *Zitterbewegung* of a moiré exciton in a MoS$_2$/WSe$_2$ hetero-bilayer for an initial Gaussian wave packet distribution with $d = 200$ Å (blue), 300 Å (orange) and 500 Å (green) and pseudo-spinors $[C_1\ C_2]^{\mathrm{T}} = [1\ 0]^{\mathrm{T}}$ and $[C_1\ C_2]^T = [1\ 1]^T$, under applied fields (a,b) $\varepsilon = 0$ and (c,d) $\varepsilon = \varepsilon_0$.

D.2 Hopping strength of the exciton bands in a superlattice potential

The hopping magnitude t_ν ($\nu = A, B$) between nearest-neighbors minima of the A and B sub-lattices, used in Eq. (2) in the main text, can be approximated as [53, 237]

$$t_\nu \approx 0.78 E_R (V_\nu(\varepsilon)/E_R)^{1.85} \exp\left[-3.404\sqrt{V_\nu(\varepsilon)/E_R}\right] \,, \tag{D.6}$$

where $E_R = \dfrac{\hbar^2}{2M_0}\left(\frac{4\pi}{3b}\right)^2$ is the recoil energy with $M_0 = 0.8m$ [317] being the exciton mass written in units of the free-electron mass m, and $V_\nu(\varepsilon)$ is the confining barrier height of A and B minima, as defined in Fig. 1 in the main text.

D.2.1 Wave packet dynamics and zitterbewegung: complementary results

In this section, we present complementary results of the average positions $\langle x(t)\rangle$ and $\langle y(t)\rangle$ of the Gaussian wave packet, not shown in Fig. 2 of the main manuscript, for the pseudo-spinors $[1\ 1]^T$ and $[1\ 0]^T$, respectively, as well as results for the $[1\ i]^T$ pseudo-spinor.

Figure D.2 presents results of the ZBW on the expectation values of the position of a moiré exciton in a MoS$_2$/WSe$_2$ vdWhs, considering an initial Gaussian wave packet

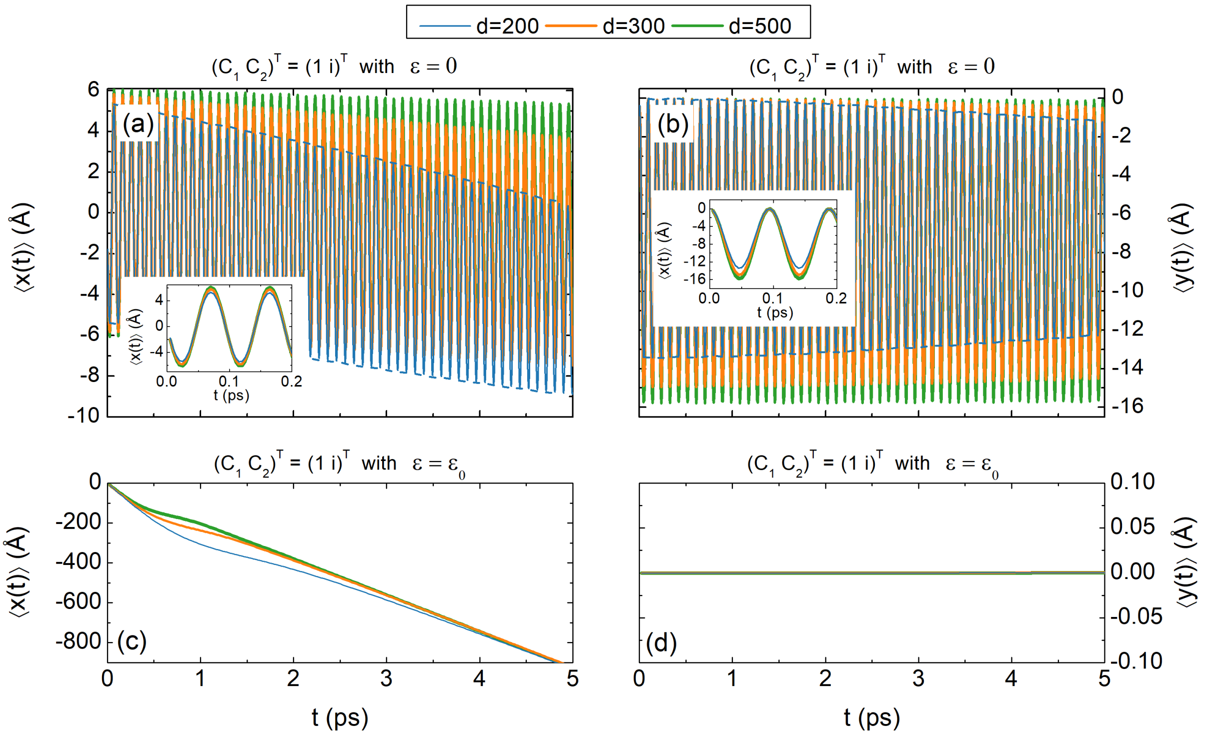

Figure D.3: The same as in Fig. D.2, but now for a pseudo-spinor defined as $[\mathrm{C}_1\ \mathrm{C}_2]^{\mathrm{T}} = [1\ i]^{\mathrm{T}}$.

distribution with width given by $d = 200$ Å (blue), $d = 300$ Å (orange) and $d = 500$ Å (green), and pseudo-spinors $[\mathrm{C}_1\ \mathrm{C}_2]^\mathrm{T} = [1\ 0]^\mathrm{T}$ and $[\mathrm{C}_1\ \mathrm{C}_2]^T = [1\ 1]^T$, under applied fields (a,b) $\varepsilon = 0$ and (c,d) $\varepsilon = \varepsilon_0$. For both pseudo-spin configurations, when $\varepsilon = \varepsilon_0$, Figs. D.2(c,d) show that the ZBW is suppressed for $\langle y(t)\rangle$ and $\langle x(t)\rangle$ with $[1\ 0]^\mathrm{T}$ and $[1\ 1]^T$, respectively. On the other hand, as shown in Fig. 2(c,d) in the main manuscript, $\langle x(t)\rangle$ and $\langle y(t)\rangle$ oscillate. Consequently, applying a perpendicular electric field (ϵ) to the hetero-bilayer structure and considering the pseudo-spinor given by $[1\ 0]^\mathrm{T}$ or $[1\ 1]^T$, means to restrict the wave packet propagation to only one direction in the $xy-$plane. If the electric field is zero, both coordinates of the center mass will exhibit ZBW, as one verifies in Fig. D.2(a,b) here and Fig. 2(a,b) in the main manuscript.

As another example, we analyze a very commonly investigated initial pseudo-spinor polarization, $[\mathrm{C}_1\ \mathrm{C}_2]^\mathrm{T} = [1\ i]^\mathrm{T}$. The ZBW for both coordinates of the center-of-mass of the Gaussian wave packet with ($\epsilon \neq 0$) and without ($\epsilon = 0$) an applied electric field ϵ are presented in Fig. D.3 for different values of the packet width d. Similarly to the $[1\ 0]^T$ and $[1\ 1]^T$ pseudo-spinor configurations, when $\epsilon \neq 0$, Fig. D.3(c,d), only one of the components features ZBW, i.e $\langle x(t)\rangle \neq 0$ and $\langle y(t)\rangle = 0$. On the other hand, for $\epsilon = 0$, Fig. D.3(a,b), both coordinates oscillate, exhibiting ZBW with the same frequency for different width d and a small difference in their amplitudes as time increases.

Finally, in order to reinforce the importance of the proper choice of the external electric field for the observation of the phenomena discussed in the main manuscript, the dependence of the absolute value of the maximum displacement (MD) for the expectation

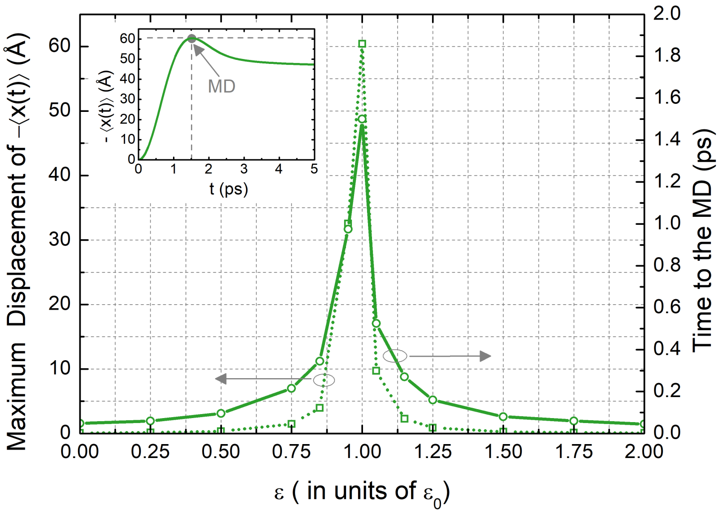

Figure D.4: Dependence of the absolute value of the maximum displacement (MD) for the expectation value $\langle x(t)\rangle$ (left vertical axis), as well as the time to the MD, (right vertical axis), for an initial wave packet with $d = 500$Å and pseudo-spinor $[\mathrm{C}_1\ \mathrm{C}_2]^\mathrm{T} = [1\ 0]^\mathrm{T}$. For $\epsilon = \epsilon_0$, where $\epsilon_0 \approx 0.44$V/nm, both results are maximized. The inset shows $\langle x(t)\rangle$ as a function of time at the critical field, see Fig. 2(c) in the main manuscript. The arrow indicates the time and magnitude of the MD.

value $\langle x(t) \rangle$ of the wave packet as a function of the applied field is illustrated in Fig. D.4. Results are shown for a wave packet with $d = 500$Å width and pseudo-spinor $[\mathrm{C}_1\ \mathrm{C}_2]^{\mathrm{T}} = [1\ 0]^{\mathrm{T}}$. When the applied electric field is $\epsilon = \epsilon_0$, where $\epsilon_0 \approx 0.44$V/nm, both the MD and the time the wave packet takes to reach the MD (see right axis) are maximized. The inset in Fig. D.4 shows the time dependence of $\langle x(t) \rangle$ at the critical field ϵ_0, where the arrow identifies the time and magnitude of the MD.

E

Phononic structure of considered vdWh stacks

Here is provided some important data for hBN and the four TMDs, i.e MoS_2, WS_2, $MoSe_2$ and WSe_2, used in chapter 7.

E.1 hBN reststrahlen bands

It is important to mention that the upper and lower RS bands, shown in Fig. 7.3(b), obtained from the QEH, presents a small shift with respect to those obtained purely from first principles [284] and used as a reference in the two considered experiments [21, 265]. These values are provided in Tab. E.1. There are, however, no qualitative differences, as shown in Fig. 7.3(e).

The difference for the hyperbolic region II is highlighted by the horizontal gray dashed dotted-dotted lines (first principles [284]) and the dashed gray lines (QEH) in Fig. 7.3(e). However, the observed SP^3 and HP^3 modes, obtained from the QEH and the experimental methods, are in good agreement with each other, as compared in Figs. 7.3(d)-(e).

Table E.1 gives the phonon energies that define the two RS bands in hBN obtained from the QEH and those from first principles[284]. As can be seen, these two methods differ in the order of 12% ($1 \sim 2\%$) in the RS(I) (RS(II)).

Table E.1: Frequencies that define the two Reststrahlen (RS) bands in hBN obtained from first principles calculations [284] and from the QEH model.

	RS (I)		RS (II)	
	$\hbar\omega_{TO}$ (meV)	$\hbar\omega_{LO}$ (meV)	$\hbar\omega_{TO}$ (meV)	$\hbar\omega_{LO}$ (meV)
First Prin. [284]	96.70	102.90	169.85	199.61
QEH	84.52	90.43	167.27	194.42
Diferrence (%)	12.59	12.53	1.17	2.60

E.2 Phonon frequencies of the TMDs

All phonons frequencies for the transition metal dichalcogenide MX_2 (MoS_2, WS_2, $MoSe_2$ and WSe_2) included in the QEH calculations for $q \rightarrow 0$, are provided in Tab. E.2. The optical modes of vibration are represented by E'', E', A_1' and A_2'' (for more details see Refs. [285–290]).

Table E.2: Phonon frequencies for free-standing monolayer of MoS_2, WS_2, $MoSe_2$ and WSe_2 included in the QEH calculations. The relevant vibration modes are represent by E'', E', A_1' and A_2''. [285–290]

	Phonon frequencies (meV)			
	1 (E'')	2 (E')	3 (A_1')	4 (A_2'')
MoS_2	34.19	46.35	47.59	56.80
WS_2	35.56	42.85	50.12	52.98
$MoSe_2$	20.18	28.10	34.37	42.53
WSe_2	20.71	29.67	30.19	37.21

Bibliography

[1] R. P. Feynman, “There’s plenty of room at the bottom”, Journal of Microelectromechanical Systems **1**, 60–66 (1992) (cit. on p. 37).

[2] H. W. Kroto, J. R. Heath, S. C. O’Brien, R. F. Curl, and R. E. Smalley, “C_{60}: buckminsterfullerene”, Nature **318**, 162–163 (1985) (cit. on p. 37).

[3] S. Iijima, “Helical microtubules of graphitic carbon”, Nature **354**, 56–58 (1991) (cit. on p. 37).

[4] K. S. Novoselov and A. Geim, “The rise of graphene”, Nat. Mater **6**, 183–191 (2007) (cit. on pp. 38, 84).

[5] R. Peierls, “Quelques propriétés typiques des corps solides”, Annales de l’institut Henri Poincaré **5**, 177–222 (1935) (cit. on p. 38).

[6] “On the theory of sound dispersion”, in *Collected papers of l.d. landau* (Elsevier, 1965), pp. 147–153 (cit. on p. 38).

[7] M. V. Berry and A. K. Geim, “Of flying frogs and levitrons”, European Journal of Physics **18**, 307–313 (1997) (cit. on p. 38).

[8] K. S. Novoselov, A. K. Geim, S. V. Morozov, D. Jiang, Y. Zhang, S. V. Dubonos, I. V. Grigorieva, and A. A. Firsov, “Electric field effect in atomically thin carbon films”, Science **306**, 666–669 (2004) (cit. on pp. 38, 53, 55, 56, 60, 84, 126, 142).

[9] P. R. Wallace, “The band theory of graphite”, Physical Review **71**, 622–634 (1947) (cit. on pp. 38, 84).

[10] *British museum highlights: the lycurgus cup*, `https://www.britishmuseum.org/collection/object/H_1958-1202-1`, 2021 (accessed March 10, 2021) (cit. on p. 39).

[11] *Plasmonic color engineering*, `https://nanocomposix.com/pages/color-engineering`, 2021 (accessed March 10, 2021) (cit. on p. 39).

[12]S. Dean, G. Mansoori, and T. F. Soelaiman, "Nanotechnology — an introduction for the standards community", Journal of ASTM International **2**, 13110 (2005) (cit. on p. 39).

[13]D. J. Barber and I. C. Freestone, "An investigation of the origin of the coulour of the lycurgus cup by analytical transmission electron microscopy", Archaeometry **32**, 33–45 (1990) (cit. on p. 40).

[14]F. E. Wagner, S. Haslbeck, L. Stievano, S. Calogero, Q. A. Pankhurst, and K. .-P. Martinek, "Before striking gold in gold-ruby glass", Nature **407**, 691–692 (2000) (cit. on p. 40).

[15]M. Loos, *Carbon nanotube reinforced composites* (Elsevier Science Techn., Sept. 2014), 304 pp. (cit. on p. 40).

[16]G. Giuliani and G. Vignale, *Quantum theory of the electron liquid* (Cambridge University Press, Mar. 2008), 800 pp. (cit. on pp. 40, 115, 117, 123–126, 128, 129, 143, 145).

[17]P. A. D. Gonçalves and N. M. R. Peres, *An introduction to graphene plasmonics* (World Scienctific, Dec. 2015) (cit. on pp. 40, 115, 120–122, 125, 127–130, 134, 143, 146, 148, 153).

[18]S. A. Maier, *Plasmonics: fundamentals and applications* (Springer-Verlag GmbH, May 16, 2007) (cit. on pp. 40, 123, 125, 126, 128, 129, 143, 145).

[19]K. A. Willets and R. P. V. Duyne, "Localized surface plasmon resonance spectroscopy and sensing", Annual Review of Physical Chemistry **58**, 267–297 (2007) (cit. on pp. 40, 41).

[20]J. Chen et al., "Optical nano-imaging of gate-tunable graphene plasmons", Nature **487**, 77–81 (2012) (cit. on pp. 40, 41, 68, 71, 126, 128, 130, 140, 142, 143).

[21]A. Woessner et al., "Highly confined low-loss plasmons in graphene–boron nitride heterostructures", Nat. Mater. **14**, 421–425 (2014) (cit. on pp. 41, 128, 130, 133–135, 140, 143, 195).

[22]W. Greiner et al., *Relativistic quantum mechanics*, Vol. 2 (Springer, 2000) (cit. on p. 42).

[23]E. Schrödinger, *Über die kräftefreie bewegung in der relativistischen quantenmechanik* (Akademie der wissenschaften in kommission bei W. de Gruyter u. Company, 1930) (cit. on pp. 42, 83, 106).

[24]E. Schrödinger, "An undulatory theory of the mechanics of atoms and molecules", Physical Review **28**, 1049–1070 (1926) (cit. on p. 42).

[25]"The quantum theory of the electron", Proceedings of the Royal Society of London. Series A, Containing Papers of a Mathematical and Physical Character **117**, 610–624 (1928) (cit. on pp. 42, 83, 106).

[26] W. Zawadzki and T. M. Rusin, "Zitterbewegung (trembling motion) of electrons in semiconductors: a review", Journal of Physics: Condensed Matter **23**, 143201 (2011) (cit. on pp. 42, 95).

[27] J. Vaishnav and C. W. Clark, "Observing zitterbewegung with ultracold atoms", Physical review letters **100**, 153002 (2008) (cit. on pp. 42, 84).

[28] M. Merkl, F. E. Zimmer, G. Juzeliūnas, and P. Öhberg, "Atomic zitterbewegung", EPL (Europhysics Letters) **83**, 54002 (2008) (cit. on pp. 42, 84).

[29] J. Schliemann, D. Loss, and R. M. Westervelt, "Zitterbewegungof electronic wave packets in III-v zinc-blende semiconductor quantum wells", Physical Review Letters **94**, 206801 (2005) (cit. on pp. 42, 84).

[30] W. Zawadzki, "Zitterbewegung and its effects on electrons in semiconductors", Phys. Rev. B **72**, 085217 (2005) (cit. on pp. 42, 84, 96, 106).

[31] J. Schliemann, D. Loss, and R. M. Westervelt, "Zitterbewegung of electrons and holes in III–v semiconductor quantum wells", Phys. Rev. B **73**, 085323 (2006) (cit. on pp. 42, 84).

[32] T. M. Rusin and W. Zawadzki, "Zitterbewegung of nearly-free and tightly-bound electrons in semiconductors", J. Phys.: Condens. Matter **19**, 136219 (2007) (cit. on pp. 42, 84).

[33] J. Schliemann, "Cyclotron motion and magnetic focusing in semiconductor quantum wells with spin-orbit coupling", Phys. Rev. B **77**, 125303 (2008) (cit. on pp. 42, 84).

[34] T. Biswas and T. K. Ghosh, "Wave packet dynamics and zitterbewegung of heavy holes in a quantizing magnetic field", J. Appl. Phys. **115**, 213701 (2014) (cit. on pp. 42, 84).

[35] W. Zawadzki, "One-dimensional semirelativity for electrons in carbon nanotubes", Phys. Rev. B **74**, 205439 (2006) (cit. on pp. 42, 84).

[36] L. K. Shi, S. C. Zhang, and K. Chang, "Anomalous electron trajectory in topological insulators", Phys. Rev. B **87**, 161115 (2013) (cit. on pp. 42, 84).

[37] L. Ferrari and G. Russo, "Nonrelativistic zitterbewegung in two-band systems", Phys. Rev. B **42**, 7454–7461 (1990) (cit. on pp. 42, 84).

[38] W. Zawadzki and T. M. Rusin, "Nature of electron zitterbewegung in crystalline solids", Phys. Lett. A **374**, 3533–3537 (2010) (cit. on pp. 42, 84, 95).

[39] F. Cannata and L. Ferrari, "Effects of the nonrelativisticZitterbewegungon the electron-phonon interaction in two-band systems", Phys. Rev. B **44**, 8599–8604 (1991) (cit. on pp. 42, 84).

[40] S. V. Vonsovskii, M. S. Svirskii, and L. M. Svirskaya, "Electron zitterbewegung in a linear crystal with alternating parity", Theor. Math. Phys. **94**, 243–249 (1993) (cit. on pp. 42, 84).

[41]L. Lamata, J. León, T. Schätz, and E. Solano, “Dirac equation and quantum relativistic effects in a single trapped ion”, Phys. Rev. Lett. **98**, 253005 (2007) (cit. on pp. 42, 84).

[42]S. M. Cunha, D. R. da Costa, G. O. de Sousa, A. Chaves, J. M. Pereira, and G. A. Farias, “Wave-packet dynamics in multilayer phosphorene”, Phys. Rev. B **99**, 235424 (2019) (cit. on pp. 42, 84, 96, 110).

[43]R. Gerritsma, G. Kirchmair, F. Zähringer, E. Solano, R. Blatt, and C. F. Roos, “Quantum simulation of the Dirac equation”, Nature **463**, 68–71 (2010) (cit. on pp. 42, 84, 105).

[44]Y.-X. Wang, Z. Yang, and S.-J. Xiong, “Study of Zitterbewegungin graphene bilayer with perpendicular magnetic field”, EPL **89**, 17007 (2010) (cit. on pp. 42, 84).

[45]L. J. LeBlanc, M. C. Beeler, K. Jiménez-Garcıa, A. R. Perry, S. Sugawa, R. A. Williams, and I. B. Spielman, “Direct observation of zitterbewegung in a Bose–Einstein condensate”, New J. Phys. **15**, 073011 (2013) (cit. on pp. 42, 84).

[46]C. Qu, C. Hamner, M. Gong, C. Zhang, and P. Engels, “Observation of zitterbewegung in a spin-orbit-coupled Bose-Einstein condensate”, Phys. Rev. A **88**, 021604 (2013) (cit. on pp. 42, 84).

[47]T. L. Silva, E. R. F. Taillebois, R. M. Gomes, S. P. Walborn, and A. T. Avelar, “Optical simulation of the free Dirac equation”, Phys. Rev. A **99**, 022332 (2019) (cit. on pp. 42, 84).

[48]G. M. Maksimova, V. Y. Demikhovskii, and E. V. Frolova, “Wave packet dynamics in a monolayer graphene”, Phys. Rev. B **78**, 235321 (2008) (cit. on pp. 43, 84, 88, 90, 95, 96, 112).

[49]A. Chaves, L. Covaci, K. Y. Rakhimov, G. A. Farias, and F. M. Peeters, “Wave-packet dynamics and valley filter in strained graphene”, Phys. Rev. B **82**, 205430 (2010) (cit. on pp. 43, 84, 90–92, 98, 158).

[50]M.-Y. Li, C.-H. Chen, Y. Shi, and L.-J. Li, “Heterostructures based on two-dimensional layered materials and their potential applications”, Materials Today **19**, 322–335 (2016) (cit. on pp. 43, 108).

[51]Y. Liu, N. O. Weiss, X. Duan, H.-C. Cheng, Y. Huang, and X. Duan, “Van der Waals heterostructures and devices”, Nature Reviews Materials **1**, 1–17 (2016) (cit. on pp. 43, 69, 71, 72, 108).

[52]C. Zhang, C.-P. Chuu, X. Ren, M.-Y. Li, L.-J. Li, C. Jin, M.-Y. Chou, and C.-K. Shih, “Interlayer couplings, moiré patterns, and 2D electronic superlattices in MoS_2/WSe_2 hetero-bilayers”, Science Advances **3**, e1601459 (2017) (cit. on pp. 43, 108).

[53]H. Yu, G.-B. Liu, J. Tang, X. Xu, and W. Yao, “Moiré excitons: from programmable quantum emitter arrays to spin-orbit–coupled artificial lattices”, Science Advances **3**, e1701696 (2017) (cit. on pp. 43, 107–109, 111, 189, 190, 192).

[54] *Moiré excitons in a 2D semiconductor heterobilayer*, `https://devicematerialscommunity.nature.com/posts/44519-moire-excitons-in-a-2d-semiconductor-heterobilayer`, 2021 (accessed March 10, 2021) (cit. on p. 43).

[55] D. R. da Costa, “Transport and confinement in monolayer and bilayer graphene nanostructures with different edges, interfaces and potentials”, PhD thesis (Universidade Federal do Ceará, 2014) (cit. on pp. 47, 50, 51, 59, 186).

[56] J. Kotz, P. Treichel, and J. Townsend, *Chemistry and chemical reactivity* (Cengage Learning, 2012) (cit. on p. 47).

[57] H. O. Pierson, *Handbook of carbon, graphite, diamond, and fullerenes: properties, processing, and applications* (Noyes Publications, Park Ridge, N.J., U.S.A, 1993) (cit. on p. 47).

[58] J. McMurry, *Organic chemistry*, Ninth edition, OCLC: ocn907259297 (Cengage Learning, Boston, MA, USA, 2016) (cit. on p. 48).

[59] P. Bruice, *Essential organic chemistry: pearson new international edition*, Always learning (Pearson Education Limited, 2013) (cit. on p. 48).

[60] R. Feltre, *Quimica orgânica* (Editora Moderna, 2004) (cit. on p. 48).

[61] Z.-S. Wu, G. Zhou, L.-C. Yin, W. Ren, F. Li, and H.-M. Cheng, “Graphene/metal oxide composite electrode materials for energy storage”, Nano Energy **1**, 107–131 (2012) (cit. on pp. 50, 51).

[62] E. H. Falcao and F. Wudl, “Carbon allotropes: beyond graphite and diamond”, Journal of Chemical Technology & Biotechnology **82**, 524–531 (2007) (cit. on p. 50).

[63] R. W. G. Wyckoff and R. W. G. Wyckoff., *Crystal structures* (Interscience, 1948) (cit. on p. 51).

[64] R. E. Smalley, “Discovering the fullerenes (nobel lecture)”, Angewandte Chemie International Edition in English **36**, 1594–1601 (1997) (cit. on p. 52).

[65] E. R. Micelotta, A. P. Jones, J. Cami, E. Peeters, J. Bernard-Salas, and G. Fanchini, “The formation of cosmic fullerenes from arophatic clusters”, The Astrophysical Journal **761**, 35 (2012) (cit. on p. 52).

[66] R. B. Fuller, *Inventions*, 1st ed (St. Martin’s Press, New York, 1983) (cit. on p. 52).

[67] L. Dai and A. W. H. Mau, “Controlled synthesis and modification of carbon nanotubes and C60: carbon nanostructures for advanced polymeric composite materials”, Advanced Materials **13**, 899–913 (2001) (cit. on p. 52).

[68] M. H. Herbst, M. I. F. Macêdo, and A. M. Rocco, “Tecnologia dos nanotubos de carbono: tendências e perspectivas de uma área multidisciplinar”, Qumica Nova **27**, 986–992 (2004) (cit. on p. 52).

[69] E. G. Gamaly, A. V. Rode, and B. Luther-Davies, "Ultrafast ablation with high-pulse-rate lasers. Part I: theoretical considerations", Journal of Applied Physics **85**, 4213–4221 (1999) (cit. on p. 53).

[70] A. V. Rode, B. Luther-Davies, and E. G. Gamaly, "Ultrafast ablation with high-pulse-rate lasers. Part II: experiments on laser deposition of amorphous carbon films", Journal of Applied Physics **85**, 4222–4230 (1999) (cit. on p. 53).

[71] A. Rode, S. Hyde, E. Gamaly, R. Elliman, D. McKenzie, and S. Bulcock, "Structural analysis of a carbon foam formed by high pulse-rate laser ablation", Applied Physics A: Materials Science & Processing **69**, S755–S758 (1999) (cit. on pp. 53, 54).

[72] C. Chen, E. B. Kennel, A. H. Stiller, P. G. Stansberry, and J. W. Zondlo, "Carbon foam derived from various precursors", Carbon **44**, 1535–1543 (2006) (cit. on p. 53).

[73] M. Inagaki, J. Qiu, and Q. Guo, "Carbon foam: preparation and application", Carbon **87**, 128–152 (2015) (cit. on p. 53).

[74] K. S. Novoselov, "Nobel lecture: graphene: materials in the flatland", Reviews of Modern Physics **83**, 837–849 (2011) (cit. on pp. 53, 54, 80).

[75] H. Rao, Y. Yang, I. Abuduresule, W. Li, X. Hu, and C. Wang, "Proteomic identification of adhesive on a bone sculpture-inlaid wooden artifact from the Xiaohe Cemetery, Xinjiang, China", Journal of Archaeological Science **53**, 148–155 (2015) (cit. on p. 53).

[76] L. Ventolà, M. Vendrell, P. Giraldez, and L. Merino, "Traditional organic additives improve lime mortars: new old materials for restoration and building natural stone fabrics", Construction and Building Materials **25**, 3313–3318 (2011) (cit. on p. 53).

[77] J. M. F. Bassalo, "O prêmio nobel de física de 2010", Caderno Brasileiro de Ensino de Fısica **28**, `10.5007/2175-7941.2011v28n1p205` (2011) (cit. on pp. 54, 60).

[78] A. K. Geim, S. V. Dubonos, I. V. Grigorieva, K. S. Novoselov, A. A. Zhukov, and S. Y. Shapoval, "Microfabricated adhesive mimicking gecko foot-hair", Nature Materials **2**, 461–463 (2003) (cit. on p. 54).

[79] *Laboratório de material didático multimídia - LMDM.* `http://www.cienciadosmateriais.org/index.php?acao=exibir&cap=17&top=178`, 2019 (accessed April 1, 2019) (cit. on p. 55).

[80] *Comprehensive nanoscience and nanotechnology* (Elsevier Science Techn., Jan. 2019), 1886 pp. (cit. on p. 55).

[81] D. A. C. Brownson and C. E. Banks, *The handbook of graphene electrochemistry* (Springer London, 2014) (cit. on p. 57).

[82] R. Raccichini, A. Varzi, S. Passerini, and B. Scrosati, "The role of graphene for electrochemical energy storage", Nature Materials **14**, 271–279 (2014) (cit. on p. 58).

[83] Y. Zhong et al., "Review of mid-infrared plasmonic materials", J. Nanophotonics **9**, 093791 (2015) (cit. on pp. 58, 127, 143).

[84] R. A. Schultz, M. C. Jensen, and R. C. Bradt, "Single crystal cleavage of brittle materials", International Journal of Fracture **65**, 291–312 (1994) (cit. on p. 56).

[85] R. Romero, M. Robert, F. Elsass, and C. Garcia, "Evidence by transmission electron microscopy of weathering microsystems in soils developed from crystalline rocks", Clay Minerals **27**, 21–33 (1992) (cit. on p. 56).

[86] X. Lu, M. Yu, H. Huang, and R. S. Ruoff, "Tailoring graphite with the goal of achieving single sheets", Nanotechnology **10**, 269–272 (1999) (cit. on p. 56).

[87] O. M. Maragó, F. Bonaccorso, R. Saija, G. Privitera, P. G. Gucciardi, M. A. Iatì, G. Calogero, P. H. Jones, F. Borghese, P. Denti, V. Nicolosi, and A. C. Ferrari, "Brownian motion of graphene", ACS Nano **4**, 7515–7523 (2010) (cit. on p. 56).

[88] M. Lotya, Y. Hernandez, P. J. King, R. J. Smith, V. Nicolosi, L. S. Karlsson, F. M. Blighe, S. De, Z. Wang, I. T. McGovern, G. S. Duesberg, and J. N. Coleman, "Liquid phase production of graphene by exfoliation of graphite in surfactant/water solutions", Journal of the American Chemical Society **131**, 3611–3620 (2009) (cit. on p. 56).

[89] T. Hasan, F. Torrisi, Z. Sun, D. Popa, V. Nicolosi, G. Privitera, F. Bonaccorso, and A. C. Ferrari, "Solution-phase exfoliation of graphite for ultrafast photonics", physica status solidi (b) **247**, 2953–2957 (2010) (cit. on p. 56).

[90] J. Hassoun, F. Bonaccorso, M. Agostini, M. Angelucci, M. G. Betti, R. Cingolani, M. Gemmi, C. Mariani, S. Panero, V. Pellegrini, and B. Scrosati, "An advanced lithium-ion battery based on a graphene anode and a lithium iron phosphate cathode", Nano Letters **14**, 4901–4906 (2014) (cit. on p. 56).

[91] U. Khan, A. O'Neill, M. Lotya, S. De, and J. N. Coleman, "High-concentration solvent exfoliation of graphene", Small **6**, 864–871 (2010) (cit. on p. 56).

[92] F. Torrisi, T. Hasan, W. Wu, Z. Sun, A. Lombardo, T. S. Kulmala, G.-W. Hsieh, S. Jung, F. Bonaccorso, P. J. Paul, D. Chu, and A. C. Ferrari, "Inkjet-printed graphene electronics", ACS Nano **6**, 2992–3006 (2012) (cit. on p. 56).

[93] D. Wei, L. Grande, V. Chundi, R. White, C. Bower, P. Andrew, and T. Ryhänen, "Graphene from electrochemical exfoliation and its direct applications in enhanced energy storage devices", Chem. Commun. **48**, 1239–1241 (2012) (cit. on p. 56).

[94] K. R. Paton, E. Varrla, C. Backes, R. J. Smith, U. Khan, A. O'Neill, C. Boland, M. Lotya, O. M. Istrate, P. King, T. Higgins, S. Barwich, P. May, P. Puczkarski, I. Ahmed, M. Moebius, H. Pettersson, E. Long, J. Coelho, S. E. O'Brien, E. K. McGuire, B. M. Sanchez, G. S. Duesberg, N. McEvoy, T. J. Pennycook, C. Downing, A. Crossley, V. Nicolosi, and J. N. Coleman, "Scalable production of large quantities of defect-free few-layer graphene by shear exfoliation in liquids", Nature Materials **13**, 624–630 (2014) (cit. on p. 58).

[95] J. M. Tour, "Scaling up exfoliation", Nature Materials **13**, 545–546 (2014) (cit. on p. 58).

[96] Q. Yu, J. Lian, S. Siriponglert, H. Li, Y. P. Chen, and S.-S. Pei, “Graphene segregated on Ni surfaces and transferred to insulators”, Applied Physics Letters **93**, 113103 (2008) (cit. on p. 58).

[97] C. Mattevi, H. Kim, and M. Chhowalla, “A review of chemical vapour deposition of graphene on copper”, J. Mater. Chem. **21**, 3324–3334 (2011) (cit. on p. 58).

[98] W. Strupinski, K. Grodecki, A. Wysmolek, R. Stepniewski, T. Szkopek, P. E. Gaskell, A. Grüneis, D. Haberer, R. Bozek, J. Krupka, and J. M. Baranowski, “Graphene epitaxy by chemical vapor deposition on SiC”, Nano Letters **11**, 1786–1791 (2011) (cit. on p. 58).

[99] A. W. Weimer, ed., *Carbide, nitride and boride materials synthesis and processing* (Springer Netherlands, 1997) (cit. on p. 58).

[100] P. W. Sutter, J.-I. Flege, and E. A. Sutter, “Epitaxial graphene on ruthenium”, Nature Materials **7**, 406–411 (2008) (cit. on p. 58).

[101] T. Ohta, N. C. Bartelt, S. Nie, K. Thürmer, and G. L. Kellogg, “Role of carbon surface diffusion on the growth of epitaxial graphene on SiC”, Physical Review B **81**, 121411 (2010) (cit. on p. 59).

[102] E. Moreau, S. Godey, F. J. Ferrer, D. Vignaud, X. Wallart, J. Avila, M. C. Asensio, F. Bournel, and J.-J. Gallet, “Graphene growth by molecular beam epitaxy on the carbon-face of SiC”, Applied Physics Letters **97**, 241907 (2010) (cit. on p. 59).

[103] J. B. Hannon, M. Copel, and R. M. Tromp, “Direct measurement of the growth mode of graphene on SiC(0001) andSiC(0001¯)”, Physical Review Letters **107**, 166101 (2011) (cit. on p. 59).

[104] K. V. Emtsev, A. Bostwick, K. Horn, J. Jobst, G. L. Kellogg, L. Ley, J. L. McChesney, T. Ohta, S. A. Reshanov, J. Röhrl, E. Rotenberg, A. K. Schmid, D. Waldmann, H. B. Weber, and T. Seyller, “Towards wafer-size graphene layers by atmospheric pressure graphitization of silicon carbide”, Nature Materials **8**, 203–207 (2009) (cit. on p. 59).

[105] M. Ruan, Y. Hu, Z. Guo, R. Dong, J. Palmer, J. Hankinson, C. Berger, and W. A. de Heer, “Epitaxial graphene on silicon carbide: introduction to structured graphene”, MRS Bulletin **37**, 1138–1147 (2012) (cit. on p. 59).

[106] L. Colombo, R. M. Wallace, and R. S. Ruoff, “Graphene growth and device integration”, Proceedings of the IEEE **101**, 1536–1556 (2013) (cit. on p. 59).

[107] K. S. Novoselov et al., “Two-dimensional atomic crystals”, PNAS **102**, 10451–10453 (2005) (cit. on pp. 59, 70, 84, 126, 127, 142, 143).

[108] Y. Zhang, Y.-W. Tan, H. L. Stormer, and P. Kim, “Experimental observation of the quantum Hall effect and Berry’s phase in graphene”, Nature **438**, 201–204 (2005) (cit. on p. 60).

[109] A. F. Young and P. Kim, “Quantum interference and Klein tunnelling in graphene heterojunctions”, Nature Physics **5**, 222–226 (2009) (cit. on p. 60).

[110] C. Lee, X. Wei, J. W. Kysar, and J. Hone, "Measurement of the elastic properties and intrinsic strength of monolayer graphene", Science **321**, 385–388 (2008) (cit. on p. 60).

[111] F. Bonaccorso, Z. Sun, T. Hasan, and A. C. Ferrari, "Graphene photonics and optoelectronics", Nature Photonics **4**, 611–622 (2010) (cit. on pp. 61, 64, 65).

[112] R. R. Nair, P. Blake, A. N. Grigorenko, K. S. Novoselov, T. J. Booth, T. Stauber, N. M. R. Peres, and A. K. Geim, "Fine structure constant defines visual transparency of graphene", Science **320**, 1308–1308 (2008) (cit. on p. 61).

[113] F. Schwierz, "Graphene transistors", Nature Nanotechnology **5**, 487–496 (2010) (cit. on pp. 62, 63).

[114] L. Liao, Y.-C. Lin, M. Bao, R. Cheng, J. Bai, Y. Liu, Y. Qu, K. L. Wang, Y. Huang, and X. Duan, "High-speed graphene transistors with a self-aligned nanowire gate", Nature **467**, 305–308 (2010) (cit. on pp. 62, 63).

[115] R. Cheng, J. Bai, L. Liao, H. Zhou, Y. Chen, L. Liu, Y.-C. Lin, S. Jiang, Y. Huang, and X. Duan, "High-frequency self-aligned graphene transistors with transferred gate stacks", Proceedings of the National Academy of Sciences **109**, 11588–11592 (2012) (cit. on pp. 62, 63).

[116] D. Reddy, L. F. Register, G. D. Carpenter, and S. K. Banerjee, "Graphene field-effect transistors", Journal of Physics D: Applied Physics **44**, 313001 (2011) (cit. on p. 63).

[117] R. Liu et al., "Graphene plasmon enhanced photoluminescence in ZnO microwires", Nanoscale **5**, 5294 (2013) (cit. on pp. 63, 143).

[118] N. Petrone, I. Meric, J. Hone, and K. L. Shepard, "Graphene field-effect transistors with gigahertz-frequency power gain on flexible substrates", Nano Letters **13**, 121–125 (2012) (cit. on p. 63).

[119] I. Meric, C. R. Dean, N. Petrone, L. Wang, J. Hone, P. Kim, and K. L. Shepard, "Graphene field-effect transistors based on boron–nitride dielectrics", Proceedings of the IEEE **101**, 1609–1619 (2013) (cit. on p. 63).

[120] I. M. Derrington, T. Z. Butler, M. D. Collins, E. Manrao, M. Pavlenok, M. Niederweis, and J. H. Gundlach, "Nanopore DNA sequencing with MspA", Proceedings of the National Academy of Sciences **107**, 16060–16065 (2010) (cit. on pp. 63, 64).

[121] B. Y. Zhang, T. Liu, B. Meng, X. Li, G. Liang, X. Hu, and Q. J. Wang, "Broadband high photoresponse from pure monolayer graphene photodetector", Nature Communications **4**, `10.1038/ncomms2830` (2013) (cit. on pp. 63, 64).

[122] R. R. Johnson, *DNA translocation through graphene nanopores.* Retrieved from `http://www.physics.upenn.edu/~robertjo/gallery/graphene-nanopore-big.jpg`, 2010 (Accessed April 1, 2019) (cit. on p. 63).

[123] R. R. Johnson, *DNA-functionalized graphene field effect transistor for chemical sensing.* Retrieved from `http://www.physics.upenn.edu/~robertjo/gallery/graphene-device.jpg`, 2010 (Accessed April 1, 2019) (cit. on p. 63).

[124] Y. Liu, X. Dong, and P. Chen, "Biological and chemical sensors based on graphene materials", Chem. Soc. Rev. **41**, 2283–2307 (2012) (cit. on p. 64).

[125] P. Chen, T. Mitsui, D. B. Farmer, J. Golovchenko, R. G. Gordon, and D. Branton, "Atomic layer deposition to fine-tune the surface properties and diameters of fabricated nanopores", Nano Letters **4**, 1333–1337 (2004) (cit. on p. 64).

[126] Y. Lu, B. R. Goldsmith, N. J. Kybert, and A. T. C. Johnson, "DNA-decorated graphene chemical sensors", Applied Physics Letters **97**, 083107 (2010) (cit. on p. 64).

[127] C. A. Merchant, K. Healy, M. Wanunu, V. Ray, N. Peterman, J. Bartel, M. D. Fischbein, K. Venta, Z. Luo, A. T. C. Johnson, and M. Drndić, "DNA translocation through graphene nanopores", Nano Letters **10**, 2915–2921 (2010) (cit. on p. 64).

[128] F. Schedin, A. K. Geim, S. V. Morozov, E. W. Hill, P. Blake, M. I. Katsnelson, and K. S. Novoselov, "Detection of individual gas molecules adsorbed on graphene", Nature Materials **6**, 652–655 (2007) (cit. on p. 64).

[129] Y. Dan, Y. Lu, N. J. Kybert, Z. Luo, and A. T. C. Johnson, "Intrinsic response of graphene vapor sensors", Nano Letters **9**, 1472–1475 (2009) (cit. on p. 64).

[130] M. Pumera, "Graphene in biosensing", Materials Today **14**, 308–315 (2011) (cit. on p. 64).

[131] L. H. Hess, M. Jansen, V. Maybeck, M. V. Hauf, M. Seifert, M. Stutzmann, I. D. Sharp, A. Offenhäusser, and J. A. Garrido, "Graphene transistor arrays for recording action potentials from electrogenic cells", Advanced Materials **23**, 5045–5049 (2011) (cit. on p. 64).

[132] T. Nelson, B. Zhang, and O. V. Prezhdo, "Detection of nucleic acids with graphene nanopores: ab initio characterization of a novel sequencing device", Nano Letters **10**, 3237–3242 (2010) (cit. on p. 64).

[133] H. Kim, C. M. Gilmore, A. Piqué, J. S. Horwitz, H. Mattoussi, H. Murata, Z. H. Kafafi, and D. B. Chrisey, "Electrical, optical, and structural properties of indium–tin–oxide thin films for organic light-emitting devices", Journal of Applied Physics **86**, 6451–6461 (1999) (cit. on p. 64).

[134] S. Bae, S. J. Kim, D. Shin, J.-H. Ahn, and B. H. Hong, "Towards industrial applications of graphene electrodes", Physica Scripta **T146**, 014024 (2012) (cit. on pp. 64, 65).

[135] E. O. Polat, O. Balcı, and C. Kocabas, "Graphene based flexible electrochromic devices", Scientific Reports **4**, `10.1038/srep06484` (2014) (cit. on p. 64).

[136] J.-H. Ahn and B. H. Hong, "Graphene for displays that bend", Nature Nanotechnology **9**, 737–738 (2014) (cit. on pp. 64, 65).

[137] W. Ren and H.-M. Cheng, “The global growth of graphene”, Nature Nanotechnology **9**, 726–730 (2014) (cit. on pp. 64, 65).

[138] University of Surrey, *Nanotechnology and renewable energy*, `http://s3.amazonaws.com/digitaltrends-uploads-prod/2016/02/Moth-eye-solar-panels.jpg`, 2016 (Accessed April 1, 2019) (cit. on p. 65).

[139] A. C. Ferrari, F. Bonaccorso, V. Fal’Ko, K. S. Novoselov, S. Roche, P. Bøggild, S. Borini, F. H. Koppens, V. Palermo, N. Pugno, et al., “Science and technology roadmap for graphene, related two-dimensional crystals, and hybrid systems”, Nanoscale **7**, 4598–4810 (2015) (cit. on p. 64).

[140] J. Liu, Y. Xue, M. Zhang, and L. Dai, “Graphene-based materials for energy applications”, MRS Bulletin **37**, 1265–1272 (2012) (cit. on p. 64).

[141] Y.-P. Hsieh, B.-J. Hong, C.-C. Ting, and M. Hofmann, “Ultrathin graphene-based solar cells”, RSC Advances **5**, 99627–99631 (2015) (cit. on p. 64).

[142] E. Singh and H. S. Nalwa, “Stability of graphene-based heterojunction solar cells”, RSC Advances **5**, 73575–73600 (2015) (cit. on p. 64).

[143] H. Sung, N. Ahn, M. S. Jang, J.-K. Lee, H. Yoon, N.-G. Park, and M. Choi, “Transparent conductive oxide-free graphene-based perovskite solar cells with over 17% efficiency”, Advanced Energy Materials **6**, 1501873 (2015) (cit. on p. 64).

[144] K. J. Tielrooij, J. C. W. Song, S. A. Jensen, A. Centeno, A. Pesquera, A. Z. Elorza, M. Bonn, L. S. Levitov, and F. H. L. Koppens, “Photoexcitation cascade and multiple hot-carrier generation in graphene”, Nature Physics **9**, 248–252 (2013) (cit. on p. 64).

[145] H. Zhang, “Ultrathin two-dimensional nanomaterials”, ACS Nano **9**, 9451–9469 (2015) (cit. on pp. 66, 68, 70, 71, 126, 127, 130, 134, 142, 143).

[146] A. K. Geim and I. V. Grigorieva, “van der Waals heterostructures”, Nature **499**, 419–425 (2013) (cit. on pp. 65, 66, 68, 70, 71, 126, 127, 135, 142, 143).

[147] S. Manzeli, D. Ovchinnikov, D. Pasquier, O. V. Yazyev, and A. Kis, “2D transition metal dichalcogenides”, Nature Reviews Materials **2**, 17033 (2017) (cit. on pp. 67–70, 126, 127, 142, 143).

[148] Á. Coogan and Y. K. Gun’ko, “Solution-based “bottom-up” synthesis of group VI transition metal dichalcogenides and their applications”, Materials Advances **2**, 146–164 (2021) (cit. on pp. 67, 70).

[149] *Periodic Table of Chemical Elements*, (2020 (accessed April 1, 2020)) (cit. on p. 67).

[150] W. Choi, N. Choudhary, G. H. Han, J. Park, D. Akinwande, and Y. H. Lee, “Recent development of two-dimensional transition metal dichalcogenides and their applications”, Materials Today **20**, 116–130 (2017) (cit. on pp. 67, 69, 70).

[151] B. Radisavljevic, A. Radenovic, J. Brivio, V. Giacometti, and A. Kis, “Single-layer MoS_2 transistors”, Nature Nanotechnology **6**, 147–150 (2011) (cit. on p. 68).

[152]K. F. Mak et al., “Atomically thin MoS_2: a new direct-gap semiconductor”, Phys. Rev. Lett. **105**, 136805 (2010) (cit. on pp. 68, 70, 126, 127, 142, 143).

[153]A. Splendiani et al., “Emerging photoluminescence in monolayer MoS_2”, Nano Lett. **10**, 1271–1275 (2010) (cit. on pp. 68, 127, 143).

[154]Z. G. Yu et al., “Robust direct bandgap characteristics of one- and two-dimensional ReS2”, Sci. Reps **5**, 13783 (2015) (cit. on pp. 68, 126, 142).

[155]N. Ashcroft, *Solid state physics* (Holt, Rinehart and Winston, New York, 1976) (cit. on p. 68).

[156]K. S. Novoselov et al., “2D materials and van der Waals heterostructures”, Science **353**, aac9439 (2016) (cit. on pp. 68, 69, 143).

[157]Y. Liu et al., “Van der Waals heterostructures and devices”, Nat. Rev. Mater. **1**, 1–17 (2016) (cit. on pp. 68, 70, 127, 135, 143).

[158]Q. H. Wang et al., “Electronics and optoelectronics of two-dimensional transition metal dichalcogenides”, Nat. Nanotechnol **7**, 699–712 (2012) (cit. on pp. 68, 70, 71, 126, 127, 130, 135, 142, 143).

[159]T. Low and P. Avouris, “Graphene plasmonics for terahertz to mid-infrared applications”, ACS Nano **8**, 1086–1101 (2014) (cit. on pp. 68, 71, 126–128, 142, 143, 153).

[160]T. Low et al., “Polaritons in layered two-dimensional materials”, Nat. Mater **16**, 182–194 (2016) (cit. on pp. 68, 71, 126, 128, 130, 142).

[161]E. D. Ranieri, “Infrared silicon”, Nat. Nanotechnol **5**, 3011 (2014) (cit. on pp. 68, 71, 126, 142).

[162]D. Jariwala et al., “Emerging device applications for semiconducting two-dimensional transition metal dichalcogenides”, ACS Nano **8**, 1102–1120 (2014) (cit. on pp. 68, 71, 126, 127, 130, 135, 142, 143).

[163]L. Ju et al., “Graphene plasmonics for tunable terahertz metamaterials”, Nat. Nanotechnol **6**, 630–634 (2011) (cit. on pp. 68, 71, 126, 127, 130, 142, 143).

[164]G. Fiori et al., “Electronics based on two-dimensional materials”, Nat. Nanotechnol **9**, 768–779 (2014) (cit. on pp. 68, 71, 126, 142).

[165]K. F. Mak and J. Shan, “Photonics and optoelectronics of 2D semiconductor transition metal dichalcogenides”, Nat. Photonics **10**, 216–226 (2016) (cit. on pp. 68, 71, 126, 127, 135, 142, 143).

[166]L. Li, Y. Yu, G. J. Ye, Q. Ge, X. Ou, H. Wu, D. Feng, X. H. Chen, and Y. Zhang, “Black phosphorus field-effect transistors”, Nature Nanotechnology **9**, 372–377 (2014) (cit. on pp. 69–71, 73).

[167]F. Reale, K. Sharda, and C. Mattevi, “From bulk crystals to atomically thin layers of group VI-transition metal dichalcogenides vapour phase synthesis”, Applied Materials Today **3**, 11–22 (2016) (cit. on p. 69).

[168] U. Halim, C. R. Zheng, Y. Chen, Z. Lin, S. Jiang, R. Cheng, Y. Huang, and X. Duan, “A rational design of cosolvent exfoliation of layered materials by directly probing liquid-solid interaction”, Nature Communications **4**, 1 (2013) (cit. on p. 69).

[169] Y.-H. Lee, X.-Q. Zhang, W. Zhang, M.-T. Chang, C.-T. Lin, K.-D. Chang, Y.-C. Yu, J. T.-W. Wang, C.-S. Chang, L.-J. Li, and T.-W. Lin, “Synthesis of large-area MoS_2 atomic layers with chemical vapor deposition”, Advanced Materials **24**, 2320–2325 (2012) (cit. on p. 69).

[170] J. C. Shaw, H. Zhou, Y. Chen, N. O. Weiss, Y. Liu, Y. Huang, and X. Duan, “Chemical vapor deposition growth of monolayer $MoSe_2$ nanosheets”, Nano Research **7**, 511–517 (2014) (cit. on p. 69).

[171] D. Jariwala et al., “Mixed-dimensional van der Waals heterostructures”, Nat. Mater **16**, 170–181 (2016) (cit. on pp. 70, 127, 135, 143).

[172] V. O. Özcelik, J. G. Azadani, C. Yang, S. J. Koester, and T. Low, “Band alignment of two-dimensional semiconductors for designing heterostructures with momentum space matching”, Physical Review B **94**, 035125 (2016) (cit. on pp. 70, 127, 143).

[173] P. K. Sahoo et al., “One-pot growth of two-dimensional lateral heterostructures via sequential edge-epitaxy”, Nature **553**, 63–67 (2018) (cit. on pp. 70, 127, 143).

[174] X. Duan et al., “Lateral epitaxial growth of two-dimensional layered semiconductor heterojunctions”, Nat. Nanotechnol **9**, 1024–1030 (2014) (cit. on pp. 70, 127, 143).

[175] Y. Gong et al., “Vertical and in-plane heterostructures from WS_2/MoS_2 monolayers”, Nat. Mater **13**, 1135–1142 (2014) (cit. on pp. 70, 127, 143).

[176] Y. Gong et al., “Two-step growth of two-dimensional $WSe_2/MoSe_2$ heterostructures”, Nano Lett. **15**, 6135–6141 (2015) (cit. on pp. 70, 127, 143).

[177] C. Huang et al., “Lateral heterojunctions within monolayer $MoSe_2$–WSe_2 semiconductors”, Nat. Mater **13**, 1096–1101 (2014) (cit. on pp. 70, 127, 143).

[178] W. Zhao, Z. Ghorannevis, L. Chu, M. Toh, C. Kloc, P.-H. Tan, and G. Eda, “Evolution of electronic structure in atomically thin sheets of WS_2 and WSe_2”, ACS Nano **7**, 791–797 (2012) (cit. on p. 70).

[179] I. R. Lavor et al., “Probing the structure and composition of van der Waals heterostructures using the nonlocality of Dirac plasmons in the terahertz regime”, 2D Mater. **8**, 015014 (2020) (cit. on pp. 70, 148).

[180] S. Das, W. Zhang, M. Demarteau, A. Hoffmann, M. Dubey, and A. Roelofs, “Tunable transport gap in phosphorene”, Nano Letters **14**, 5733–5739 (2014) (cit. on p. 70).

[181] C. R. Dean, A. F. Young, I. Meric, C. Lee, L. Wang, S. Sorgenfrei, K. Watanabe, T. Taniguchi, P. Kim, K. L. Shepard, and J. Hone, “Boron nitride substrates for high-quality graphene electronics”, Nature Nanotechnology **5**, 722–726 (2010) (cit. on p. 70).

[182]S. Yamakoshi, T. Sanada, O. Wada, I. Umebu, and T. Sakurai, "Direct observation of electron leakage in InGaAsP/InP double heterostructure", Applied Physics Letters **40**, 144–146 (1982) (cit. on p. 73).

[183]F. Withers, O. D. Pozo-Zamudio, S. Schwarz, S. Dufferwiel, P. M. Walker, T. Godde, A. P. Rooney, A. Gholinia, C. R. Woods, P. Blake, S. J. Haigh, K. Watanabe, T. Taniguchi, I. L. Aleiner, A. K. Geim, V. I. Fal'ko, A. I. Tartakovskii, and K. S. Novoselov, "WSe_2 light-emitting tunneling transistors with enhanced brightness at room temperature", Nano Letters **15**, 8223–8228 (2015) (cit. on p. 73).

[184]M. I. Katsnelson, *Graphene: carbon in two dimensions* (Cambridge University Press, Cambridge New York, 2012) (cit. on pp. 74, 75, 77, 80, 81, 84).

[185]J. J. Sakurai, *Modern quantum mechanics* (Addison-Wesley Pub. Co, Reading, Mass, 1994) (cit. on pp. 75, 183).

[186]H. J. W. George B. Arfken, *Mathematical methods for physicists* (Elsevier LTD, Oxford, Feb. 2012), 1205 pp. (cit. on p. 76).

[187]A. H. C. Neto, F. Guinea, N. M. R. Peres, K. S. Novoselov, and A. K. Geim, "The electronic properties of graphene", Reviews of Modern Physics **81**, 109–162 (2009) (cit. on pp. 77, 80, 81).

[188]M. Zarenia, "Confined states in mono- and bi-layer graphene nanostructures", PhD thesis (University of Antwerp, 2013) (cit. on pp. 77, 78).

[189]D. W. Boukhvalov, M. I. Katsnelson, and A. I. Lichtenstein, "Hydrogen on graphene: electronic structure, total energy, structural distortions and magnetism from first-principles calculations", Physical Review B **77**, 035427 (2008) (cit. on pp. 77, 78).

[190]A. Bostwick, T. Ohta, T. Seyller, K. Horn, and E. Rotenberg, "Quasiparticle dynamics in graphene", Nature Physics **3**, 36–40 (2006) (cit. on pp. 77, 78).

[191]S. H. R. d. Sena, "Propriedades eletrônicas de tricamada de grafeno e nanofitas de carbono tensionadas", PhD thesis (Universidade Federal do Ceará, 2012) (cit. on p. 77).

[192]A. K. Geim and I. V. Grigorieva, "Van der Waals heterostructures", Nature **499**, 419–425 (2013) (cit. on p. 80).

[193]B. Partoens and F. M. Peeters, "From graphene to graphite: electronic structure around theKpoint", Phys. Rev. B **74**, 075404 (2006) (cit. on pp. 80, 86, 87, 137).

[194]A. L. Rakhmanov, A. V. Rozhkov, A. O. Sboychakov, and F. Nori, "Instabilities of the AA-stacked graphene bilayer", Physical Review Letters **109**, 206801 (2012) (cit. on pp. 80, 82).

[195]M. Koshino and E. McCann, "Parity and valley degeneracy in multilayer graphene", Physical Review B **81**, 115315 (2010) (cit. on p. 80).

[196]E. McCann and V. I. Fal'ko, "Landau-Level degeneracy and quantum Hall effect in a graphite bilayer", Phys. Rev. Lett. **96**, 086805 (2006) (cit. on pp. 80, 84).

[197] E. McCann and M. Koshino, "The electronic properties of bilayer graphene", Reports on Progress in Physics **76**, 056503 (2013) (cit. on pp. 80, 84, 87).

[198] A. Misu, E. E. Mendez, and M. S. Dresselhaus, "Near infrared reflectivity of graphite under hydrostatic pressure. I. Experiment", Journal of the Physical Society of Japan **47**, 199–207 (1979) (cit. on p. 81).

[199] J. Nilsson, A. H. C. Neto, N. M. R. Peres, and F. Guinea, "Electron-electron interactions and the phase diagram of a graphene bilayer", Physical Review B **73**, 214418 (2006) (cit. on p. 81).

[200] I. Snyman and C. W. J. Beenakker, "Ballistic transmission through a graphene bilayer", Physical Review B **75**, 045322 (2007) (cit. on p. 82).

[201] C. J. Tabert and E. J. Nicol, "Dynamical conductivity of AA-stacked bilayer graphene", Physical Review B **86**, 075439 (2012) (cit. on p. 82).

[202] R. Sensarma, E. H. Hwang, and S. D. Sarma, "Dynamic screening and low-energy collective modes in bilayer graphene", Physical Review B **82**, 195428 (2010) (cit. on p. 82).

[203] A. H. C. Neto et al., "The electronic properties of graphene", Rev. Mod. Phys. **81**, 109–162 (2009) (cit. on pp. 84, 91, 126, 129, 142, 146, 153).

[204] Y. Choi, J. Kemmer, Y. Peng, A. Thomson, H. Arora, R. Polski, Y. Zhang, H. Ren, J. Alicea, G. Refael, F. von Oppen, K. Watanabe, T. Taniguchi, and S. Nadj-Perge, "Electronic correlations in twisted bilayer graphene near the magic angle", Nat. Phys. **15**, 1174–1180 (2019) (cit. on p. 84).

[205] M. I. Katsnelson, "Zitterbewegung, chirality, and minimal conductivity in graphene", Eur. Phys. J. B **51**, 157–160 (2006) (cit. on p. 84).

[206] J. M. Pereira, F. M. Peeters, A. Chaves, and G. A. Farias, "Klein tunneling in single and multiple barriers in graphene", Semicond. Sci. Technol. **25**, 033002 (2010) (cit. on pp. 84, 90–92, 98).

[207] J. Cserti and G. Dávid, "Unified description of zitterbewegung for spintronic, graphene, and superconducting systems", Phys. Rev. B **74**, 172305 (2006) (cit. on p. 84).

[208] T. M. Rusin and W. Zawadzki, "Transient zitterbewegung of charge carriers in mono- and bilayer graphene, and carbon nanotubes", Phys. Rev. B **76**, 195439 (2007) (cit. on p. 84).

[209] B. Trauzettel, Y. M. Blanter, and A. F. Morpurgo, "Photon-assisted electron transport in graphene: scattering theory analysis", Phys. Rev. B **75**, 035305 (2007) (cit. on p. 84).

[210] T. M. Rusin and W. Zawadzki, "Zitterbewegung of electrons in graphene in a magnetic field", Phys. Rev. B **78**, 125419 (2008) (cit. on p. 84).

[211] H. Deng, F. Ye, B. A. Malomed, X. Chen, and N. C. Panoiu, “Optically and electrically tunable Dirac points and zitterbewegung in graphene-based photonic superlattices”, Phys. Rev. B **91**, 201402 (2015) (cit. on p. 84).

[212] E. Serna, I. Rodrıguez Vargas, R. Pérez-Álvarez, and L. Diago-Cisneros, “Pseudospin-dependent zitterbewegung in monolayer graphene”, J. Appl. Phys. **125**, 203902 (2019) (cit. on p. 84).

[213] P. Kim, “Graphene and relativistic quantum physics”, in *Progress in mathematical physics* (Springer International Publishing, 2017), pp. 1–23 (cit. on p. 84).

[214] P. Avouris, “Graphene: electronic and photonic properties and devices”, Nano Lett. **10**, 4285–4294 (2010) (cit. on p. 84).

[215] B. V. Duppen and F. M. Peeters, “Klein paradox for a pn junction in multilayer graphene”, EPL (Europhysics Letters) **102**, 27001 (2013) (cit. on pp. 86, 87).

[216] M. Nakamura and L. Hirasawa, “Electric transport and magnetic properties in multilayer graphene”, Physical Review B **77**, 045429 (2008) (cit. on p. 86).

[217] J. L. Mañes, F. Guinea, and M. A. H. Vozmediano, “Existence and topological stability of fermi points in multilayered graphene”, Phys. Rev. B **75**, 155424 (2007) (cit. on p. 86).

[218] S. B. Kumar and J. Guo, “Chiral tunneling in trilayer graphene”, Applied Physics Letters **100**, 163102 (2012) (cit. on pp. 86, 87).

[219] W. Prarokijjak and B. Soodchomshom, “Electron with arbitrary pseudo-spins in multilayer graphene”, Chin. Phys. B **24**, 048101 (2015) (cit. on pp. 86, 87).

[220] E. McCann, D. S. Abergel, and V. I. Fal’ko, “Electrons in bilayer graphene”, Solid State Commun. **143**, 110–115 (2007) (cit. on pp. 86, 87).

[221] B. Van Duppen, S. H. R. Sena, and F. M. Peeters, “Multiband tunneling in trilayer graphene”, Phys. Rev. B **87**, 195439 (2013) (cit. on p. 87).

[222] B. Partoens and F. M. Peeters, “Normal and Dirac fermions in graphene multilayers: tight-binding description of the electronic structure”, Phys. Rev. B **75**, 193402 (2007) (cit. on p. 87).

[223] G. Dávid and J. Cserti, “General theory of zitterbewegung”, Phys. Rev. B **81**, 121417 (2010) (cit. on p. 87).

[224] J. Cserti and G. Dávid, “Relation between zitterbewegung and the charge conductivity, Berry curvature, and the chern number of multiband systems”, Phys. Rev. B **82**, 201405 (2010) (cit. on p. 87).

[225] V. Y. Demikhovskii, G. M. Maksimova, and E. V. Frolova, “Wave packet dynamics in a two-dimensional electron gas with spin orbit coupling: splitting andzitterbewegung”, Physical Review B **78**, 115401 (2008) (cit. on p. 88).

[226] T. M. Rusin and W. Zawadzki, “Theory of electron zitterbewegung in graphene probed by femtosecond laser pulses”, Phys. Rev. B **80**, 045416 (2009) (cit. on pp. 89, 96, 105, 106).

[227] T. M. Rusin and W. Zawadzki, “Zitterbewegung of electrons in carbon nanotubes created by laser pulses”, J. Phys.: Condens. Matter **26**, 215301 (2014) (cit. on pp. 89, 96, 105).

[228] A. Chaves, G. A. Farias, F. M. Peeters, and R. Ferreira, “The split-operator technique for the study of spinorial wavepacket dynamics”, Comm. Comput. Phys. **17**, 850–866 (2015) (cit. on pp. 90–92, 98, 108, 110).

[229] K. Y. Rakhimov, A. Chaves, G. A. Farias, and F. M. Peeters, “Wavepacket scattering of Dirac and Schrödinger particles on potential and magnetic barriers”, J. Phys.: Condens. Matter **23**, 275801 (2011) (cit. on pp. 90, 92, 98).

[230] D. R. da Costa, A. Chaves, S. H. R. Sena, G. A. Farias, and F. M. Peeters, “Valley filtering using electrostatic potentials in bilayer graphene”, Phys. Rev. B **92**, 045417 (2015) (cit. on pp. 90, 92, 108, 110, 158).

[231] D. R. da Costa, A. Chaves, G. A. Farias, L. Covaci, and F. M. Peeters, “Wave-packet scattering on graphene edges in the presence of a pseudomagnetic field”, Phys. Rev. B **86**, 115434 (2012) (cit. on pp. 90, 92, 98).

[232] L. S. Cavalcante, A. Chaves, D. R. da Costa, G. A. Farias, and F. M. Peeters, “All-strain based valley filter in graphene nanoribbons using snake states”, Phys. Rev. B **94**, 075432 (2016) (cit. on pp. 90, 92, 98, 158).

[233] A. Chaves, D. R. da Costa, G. O. de Sousa, J. M. Pereira, and G. A. Farias, “Energy shift and conduction-to-valence band transition mediated by a time-dependent potential barrier in graphene”, Phys. Rev. B **92**, 125441 (2015) (cit. on pp. 90, 92, 98).

[234] D. R. da Costa, A. Chaves, G. Farias, and F. Peeters, “Valley filtering in graphene due to substrate-induced mass potential”, J. Phys. Condens. Matter **29**, 215502 (2017) (cit. on pp. 90, 92, 98).

[235] H. M. Abdullah, D. R. da Costa, H. Bahlouli, A. Chaves, F. M. Peeters, and B. Van Duppen, “Electron collimation at van der Waals domain walls in bilayer graphene”, Phys. Rev. B **100**, 045137 (2019) (cit. on pp. 90, 92).

[236] D. Lurié and S. Cremer, “Zitterbewegung of quasiparticles in superconductors”, Physica **50**, 224–240 (1970) (cit. on p. 96).

[237] J. Ibañez-Azpiroz, A. Eiguren, A. Bergara, G. Pettini, and M. Modugno, “Tight-binding models for ultracold atoms in honeycomb optical lattices”, Physical Review A **87**, 011602 (2013) (cit. on pp. 109, 192).

[238] X. Zang, S. Montangero, L. D. Carr, and M. T. Lusk, “Engineering and manipulating exciton wave packets”, Physical Review B **95**, 195423 (2017) (cit. on p. 111).

[239]J. Zipfel, M. Kulig, R. Perea-Causın, S. Brem, J. D. Ziegler, R. Rosati, T. Taniguchi, K. Watanabe, M. M. Glazov, E. Malic, and A. Chernikov, “Exciton diffusion in monolayer semiconductors with suppressed disorder”, Physical Review B **101**, 115430 (2020) (cit. on pp. 111, 113).

[240]R. Perea-Causın, S. Brem, R. Rosati, R. Jago, M. Kulig, J. D. Ziegler, J. Zipfel, A. Chernikov, and E. Malic, “Exciton propagation and halo formation in two-dimensional materials”, Nano Letters **19**, 7317–7323 (2019) (cit. on p. 111).

[241]M. Kulig, J. Zipfel, P. Nagler, S. Blanter, C. Schüller, T. Korn, N. Paradiso, M. M. Glazov, and A. Chernikov, “Exciton diffusion and halo effects in monolayer semiconductors”, Physical Review Letters **120**, 207401 (2018) (cit. on pp. 111, 113).

[242]D. Unuchek, A. Ciarrocchi, A. Avsar, Z. Sun, K. Watanabe, T. Taniguchi, and A. Kis, “Valley-polarized exciton currents in a van der Waals heterostructure”, Nature Nanotechnology **14**, 1104–1109 (2019) (cit. on p. 111).

[243]I. R. Lavor, D. R. da Costa, A. Chaves, S. H. R. Sena, G. A. Farias, B. V. Duppen, and F. M. Peeters, “Effect of zitterbewegung on the propagation of wave packets in ABC-stacked multilayer graphene: an analytical and computational approach”, Journal of Physics: Condensed Matter **33**, 095503 (2020) (cit. on p. 112).

[244]M. M. Glazov, “Phonon wind and drag of excitons in monolayer semiconductors”, Physical Review B **100**, 045426 (2019) (cit. on p. 113).

[245]A. Principi, G. Vignale, M. Carrega, and M. Polini, “Intrinsic lifetime of Dirac plasmons in graphene”, Physical Review B **88**, 195405 (2013) (cit. on pp. 119, 120).

[246]Ben Van Dupen, “Plasmonics in graphene and related materials”, PhD thesis (University of Antwerp, 2016) (cit. on pp. 119–125).

[247]K. W. .-K. Shung, “Dielectric function and plasmon structure of stage-1 intercalated graphite”, Physical Review B **34**, 979–993 (1986) (cit. on p. 119).

[248]T. Ando, “Screening effect and impurity scattering in monolayer graphene”, Journal of the Physical Society of Japan **75**, 074716 (2006) (cit. on p. 119).

[249]Y. Liu, G. Bian, T. Miller, and T.-C. Chiang, “Visualizing electronic chirality and Berry phases in graphene systems using photoemission with circularly polarized light”, Physical Review Letters **107**, 166803 (2011) (cit. on p. 120).

[250]B. Wunsch et al., “Dynamical polarization of graphene at finite doping”, New J. Phys. **8**, 318–318 (2006) (cit. on pp. 120, 121, 125, 129, 134, 145, 146).

[251]E. H. Hwang and S. D. Sarma, “Dielectric function, screening, and plasmons in two-dimensional graphene”, Phys. Rev. B **75**, 075418 (2007) (cit. on pp. 120, 121, 125, 129, 134, 145, 146).

[252]M. Gell-Mann and F. Low, “Bound states in quantum field theory”, Physical Review **84**, 350–354 (1951) (cit. on p. 124).

[253]D. Pines and D. Bohm, “A collective description of electron interactions: II. Collective *vs* Individual particle aspects of the interactions”, Physical Review **85**, 338–353 (1952) (cit. on p. 124).

[254]A. L. Fetter, *Quantum theory of many-particle systems* (Dover Publications Inc., May 26, 2003), 640 pp. (cit. on pp. 125, 129, 145).

[255]A. Principi et al., “Linear response of doped graphene sheets to vector potentials”, Phys. Rev. B **80**, 075418 (2009) (cit. on pp. 125, 129, 145).

[256]A. N. Grigorenko, M. Polini, and K. S. Novoselov, “Graphene plasmonics”, Nat. Photonics **6**, 749–758 (2012) (cit. on pp. 127, 128, 143).

[257]J. A. Schuller et al., “Plasmonics for extreme light concentration and manipulation”, Nat. Mater **9**, 193–204 (2010) (cit. on pp. 127, 143).

[258]M. Polini, “Tuning terahertz lasers via graphene plasmons”, Science **351**, 229–231 (2016) (cit. on pp. 127, 143).

[259]P. Alonso-González et al., “Acoustic terahertz graphene plasmons revealed by photocurrent nanoscopy”, Nat. Nanotechnol **12**, 31–35 (2016) (cit. on pp. 127, 128, 130, 143).

[260]Z. Li et al., “Active light control of the MoS_2 monolayer exciton binding energy”, ACS Nano **9**, 10158–10164 (2015) (cit. on pp. 127, 143).

[261]A. Chaves et al., “Bandgap engineering of two-dimensional semiconductor materials”, NPJ 2D Mater. Appl. **4**, 1–21 (2020) (cit. on p. 128).

[262]D. J. Griffiths, *Introduction to electrodynamics* (Cambridge University Press, Aug. 31, 2017) (cit. on pp. 128, 148).

[263]I. J. Luxmoore, C. H. Gan, P. Q. Liu, F. Valmorra, P. Li, J. Faist, and G. R. Nash, “Strong coupling in the far-infrared between graphene plasmons and the surface optical phonons of silicon dioxide”, ACS Photonics **1**, 1151–1155 (2014) (cit. on pp. 128, 130–133).

[264]Y. Wu et al., “Hybrid nonlinear surface-phonon-plasmon-polaritons at the interface of nolinear medium and graphene-covered hexagonal boron nitride crystal”, Opt. Express **24**, 2109 (2016) (cit. on p. 128).

[265]S. Dai et al., “Graphene on hexagonal boron nitride as a tunable hyperbolic metamaterial”, Nat. Nanotechnol **10**, 682–686 (2015) (cit. on pp. 128, 130, 133–135, 140, 143, 195).

[266]M. B. Lundeberg et al., “Tuning quantum nonlocal effects in graphene plasmonics”, Science **357**, 187–191 (2017) (cit. on pp. 128, 140, 143).

[267]M. B. Lundeberg et al., “Thermoelectric detection and imaging of propagating graphene plasmons”, Nat. Mater **16**, 204–207 (2016) (cit. on pp. 128, 140, 143).

[268] Z. Fei et al., "Gate-tuning of graphene plasmons revealed by infrared nano-imaging", Nature **487**, 82–85 (2012) (cit. on pp. 128, 130, 133, 140, 143).

[269] Z. Fei et al., "Tunneling plasmonics in bilayer graphene", Nano Lett. **15**, 4973–4978 (2015) (cit. on pp. 128, 130, 140, 143).

[270] S. Dai et al., "Tunable phonon polaritons in atomically thin van der Waals crystals of boron nitride", Science **343**, 1125–1129 (2014) (cit. on pp. 128, 130, 134, 135, 140, 143).

[271] K. Andersen et al., "Dielectric genome of van der Waals heterostructures", Nano Lett. **15**, 4616–4621 (2015) (cit. on pp. 128, 131, 145, 148).

[272] M. N. Gjerding et al., "Efficient Ab initio modeling of dielectric screening in 2D van der Waals materials: including phonons, substrates, and doping", J. Phys. Chem. **124**, 11609–11616 (2020) (cit. on pp. 128, 131, 132, 148).

[273] Y. Liu et al., "Plasmon-phonon strongly coupled mode in epitaxial graphene", Phys. Rev. B **81**, 081406 (2010) (cit. on p. 130).

[274] Z.-Y. Ong and M. V. Fischetti, "Theory of interfacial plasmon-phonon scattering in supported graphene", Phys. Rev. B **86**, 165422 (2012) (cit. on p. 130).

[275] Z. Fei et al., "Infrared nanoscopy of Dirac plasmons at the graphene–SiO_2 interface", Nano Lett. **11**, 4701–4705 (2011) (cit. on pp. 130, 133, 143).

[276] A. Principi et al., "Impact of disorder on Dirac plasmon losses", Phys. Rev. B **88**, 121405 (2013) (cit. on p. 131).

[277] T. Langer, J. Baringhaus, H. Pfnür, H. W. Schumacher, and C. Tegenkamp, "Plasmon damping below the Landau regime: the role of defects in epitaxial graphene", New J. Phys. **12**, 033017 (2010) (cit. on p. 131).

[278] L. S. R. Cavalcante et al., "Enhancing and controlling plasmons in Janus MoSSe–graphene based van der Waals heterostructures", J. Phys. Chem. C **123**, 16373–16379 (2019) (cit. on pp. 131, 148).

[279] R. Resta, "Macroscopic polarization in crystalline dielectrics: the geometric phase approach", Rev. Mod. Phys. **66**, 899–915 (1994) (cit. on p. 132).

[280] R. D. King-Smith and D. Vanderbilt, "Theory of polarization of crystalline solids", Phys. Rev. B **47**, 1651–1654 (1993) (cit. on p. 132).

[281] H. Yan et al., "Damping pathways of mid-infrared plasmons in graphene nanostructures", Nat. Photonics **7**, 394–399 (2013) (cit. on pp. 133, 143).

[282] J. McPherson et al., "Thermochemical description of dielectric breakdown in high dielectric constant materials", Appl. Phys. Lett. **82**, 2121–2123 (2003) (cit. on p. 134).

[283] E. Wagemann et al., "On the wetting translucency of hexagonal boron nitride", Phys. Chem. Chem. Phys. **22**, 7710–7718 (2020) (cit. on p. 134).

[284] Y. Cai et al., “Infrared reflectance spectrum of BN calculated from first principles”, Solid State Commun. **141**, 262–266 (2007) (cit. on pp. 135, 195).

[285] X. Zhang et al., “Phonon and Raman scattering of two-dimensional transition metal dichalcogenides from monolayer, multilayer to bulk material”, Chem. Soc. Rev. **44**, 2757–2785 (2015) (cit. on pp. 135, 138, 143, 148, 196).

[286] W. Zhao et al., “Lattice dynamics in mono- and few-layer sheets of WS_2 and WSe_2”, Nanoscale **5**, 9677 (2013) (cit. on pp. 138, 148, 196).

[287] A. Molina-Sánchez and L. Wirtz, “Phonons in single-layer and few-layer MoS_2 and WS_2”, Phys. Rev. B **84**, 155413 (2011) (cit. on pp. 138, 148, 196).

[288] B. Peng et al., “Thermal conductivity of monolayer MoS_2, $MoSe_2$, and WS_2: interplay of mass effect, interatomic bonding and anharmonicity”, RSC Advances **6**, 5767–5773 (2016) (cit. on pp. 138, 148, 196).

[289] A. Berkdemir et al., “Identification of individual and few layers of WS_2 using Raman spectroscopy”, Sci. Reps **3**, 1–8 (2013) (cit. on pp. 138, 148, 196).

[290] A. Sengupta et al., “Phonon scattering limited performance of monolayer MoS_2 and WSe_2 n-MOSFET”, AIP Advances **5**, 027101 (2015) (cit. on pp. 138, 148, 196).

[291] S. Z. Butler et al., “Progress, challenges, and opportunities in two-dimensional materials beyond graphene”, ACS Nano **7**, 2898–2926 (2013) (cit. on p. 142).

[292] M. Jablan et al., “Plasmonics in graphene at infrared frequencies”, Phys. Rev. B **80**, 245435 (2009) (cit. on p. 143).

[293] X. Cai et al., “Sensitive room-temperature terahertz detection via the photothermoelectric effect in graphene”, Nat. Nanotechnol **9**, 814–819 (2014) (cit. on p. 143).

[294] M. Hertzog et al., “Strong light–matter interactions: a new direction within chemistry”, Chem. Soc. Rev. **48**, 937–961 (2019) (cit. on pp. 143, 146).

[295] J. Xia et al., “Transition metal dichalcogenides: structural, optical and electronic property tuning via thickness and stacking”, FlatChem **4**, 1–19 (2017) (cit. on p. 143).

[296] L. Novotny, “Strong coupling, energy splitting, and level crossings: a classical perspective”, Am. J. Phys. **78**, 1199–1202 (2010) (cit. on pp. 143, 146, 147).

[297] P. Törmä and W. L. Barnes, “Strong coupling between surface plasmon polaritons and emitters: a review”, Rep. Prog. Phys. **78**, 013901 (2014) (cit. on pp. 143, 144, 146).

[298] O. Bitton et al., “Quantum dot plasmonics: from weak to strong coupling”, Nanophotonics **8**, 559–575 (2019) (cit. on p. 144).

[299] F. Yoshihara et al., “Superconducting qubit–oscillator circuit beyond the ultrastrong-coupling regime”, Nature Physics **13**, 44–47 (2016) (cit. on p. 144).

[300] A. F. Kockum et al., “Ultrastrong coupling between light and matter”, Nat. Rev. Phys. **1**, 19–40 (2019) (cit. on pp. 144, 145, 150, 151).

[301] S. Haastrup et al., “The computational 2D materials database: high-throughput modeling and discovery of atomically thin crystals”, 2D Mater. **5**, 042002 (2018) (cit. on p. 145).

[302] M. N. Gjerding, A. Taghizadeh, A. Rasmussen, S. Ali, F. Bertoldo, T. Deilmann, N. R. Knøsgaard, M. Kruse, A. H. Larsen, S. Manti, T. G. Pedersen, U. Petralanda, T. Skovhus, M. K. Svendsen, J. J. Mortensen, T. Olsen, and K. S. Thygesen, “Recent progress of the computational 2D materials database (C2DB)”, 2D Materials **8**, 044002 (2021) (cit. on p. 145).

[303] A. Tomadin et al., “Accessing phonon polaritons in hyperbolic crystals by angle-resolved photoemission spectroscopy”, Phys. Rev. Lett. **115**, 087401 (2015) (cit. on p. 146).

[304] A. Laturia et al., “Dielectric properties of hexagonal boron nitride and transition metal dichalcogenides: from monolayer to bulk”, NPJ 2D **2**, 6 (2018) (cit. on p. 146).

[305] L. S. R. Cavalcante et al., “Electrostatics of electron-hole interactions in van der Waals heterostructures”, Phys. Rev. B **97**, 125427 (2018) (cit. on p. 146).

[306] S. Ribeiro et al., “Quantum theory of multisubband plasmon– phonon coupling”, Photonics **7**, 19 (2020) (cit. on p. 147).

[307] S. N. Shirodkar et al., “Quantum plasmons with optical-range frequencies in doped few-layer graphene”, Phys. Rev. B **97**, 195435 (2018) (cit. on p. 148).

[308] H. C. Nerl et al., “Probing the local nature of excitons and plasmons in few-layer MoS_2”, NPJ 2D Mater. Appl. **1**, 2 (2017) (cit. on p. 148).

[309] Y. Jia et al., “Tunable plasmon–phonon polaritons in layered graphene–hexagonal boron nitride heterostructures”, ACS Photonics **2**, 907–912 (2015) (cit. on p. 150).

[310] C. Huck et al., “Strong coupling between phonon-polaritons and plasmonic nanorods”, Opt. Express **24**, 25528–25539 (2016) (cit. on p. 150).

[311] T. Low et al., “Novel midinfrared plasmonic properties of bilayer graphene”, Phys. Rev. Lett. **112**, 116801 (2014) (cit. on p. 150).

[312] I. S. Gradshteĭn, *Table of integrals, series and products* (Academic, Oxford, 2007) (cit. on pp. 167, 172, 182).

[313] I. S. Gradshteĭn, *Table of integrals, series and products* (Academic, Oxford, 2007) (cit. on p. 182).

[314] K. Wakabayashi, M. Fujita, H. Ajiki, and M. Sigrist, “Electronic and magnetic properties of nanographite ribbons”, Physical Review B **59**, 8271–8282 (1999) (cit. on p. 186).

[315] A. Chaves, “Dinâmica de pacotes de onda em semicondutores e grafeno e de vórtices em supercondutores”, PhD thesis (Universidade Federal do Ceará, 2010) (cit. on p. 187).

[316] Y. Wang, Z. Wang, W. Yao, G.-B. Liu, and H. Yu, “Interlayer coupling in commensurate and incommensurate bilayer structures of transition-metal dichalcogenides”, Physical Review B **95**, 115429 (2017) (cit. on p. 190).

[317] L. Zhang, Z. Zhang, F. Wu, D. Wang, R. Gogna, S. Hou, K. Watanabe, T. Taniguchi, K. Kulkarni, T. Kuo, S. R. Forrest, and H. Deng, "Twist-angle dependence of moiré excitons in $WS_2/MoSe_2$ heterobilayers", Nature Communications **11**, `10.1038/s41467-020-19466-6` (2020) (cit. on p. 192).

Index

ACS
Chemistry for Life®

PERIODIC TABLE OF ELEMENTS

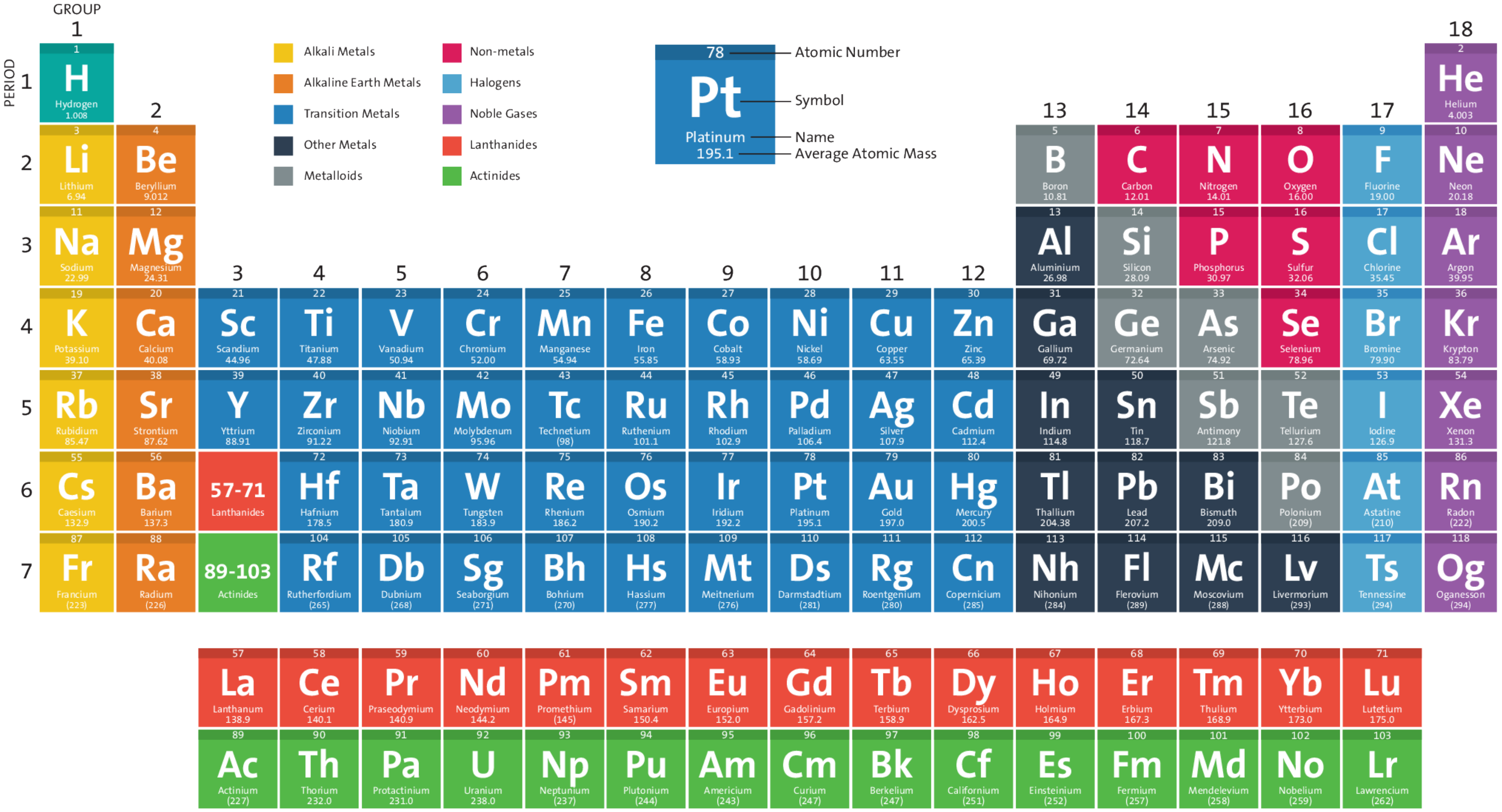

- 🟨 Alkali Metals
- 🟧 Alkaline Earth Metals
- 🟦 Transition Metals
- ⬛ Other Metals
- ⬜ Metalloids
- 🟥 Non-metals
- 🟦 Halogens
- 🟪 Noble Gases
- 🟥 Lanthanides
- 🟩 Actinides

78 — Atomic Number
Pt — Symbol
Platinum — Name
195.1 — Average Atomic Mass

PERIOD / GROUP	1	2	3	4	5	6	7	8	9	10	11	12	13	14	15	16	17	18
1	1 **H** Hydrogen 1.008																	2 **He** Helium 4.003
2	3 **Li** Lithium 6.94	4 **Be** Beryllium 9.012											5 **B** Boron 10.81	6 **C** Carbon 12.01	7 **N** Nitrogen 14.01	8 **O** Oxygen 16.00	9 **F** Fluorine 19.00	10 **Ne** Neon 20.18
3	11 **Na** Sodium 22.99	12 **Mg** Magnesium 24.31											13 **Al** Aluminium 26.98	14 **Si** Silicon 28.09	15 **P** Phosphorus 30.97	16 **S** Sulfur 32.06	17 **Cl** Chlorine 35.45	18 **Ar** Argon 39.95
4	19 **K** Potassium 39.10	20 **Ca** Calcium 40.08	21 **Sc** Scandium 44.96	22 **Ti** Titanium 47.88	23 **V** Vanadium 50.94	24 **Cr** Chromium 52.00	25 **Mn** Manganese 54.94	26 **Fe** Iron 55.85	27 **Co** Cobalt 58.93	28 **Ni** Nickel 58.69	29 **Cu** Copper 63.55	30 **Zn** Zinc 65.39	31 **Ga** Gallium 69.72	32 **Ge** Germanium 72.64	33 **As** Arsenic 74.92	34 **Se** Selenium 78.96	35 **Br** Bromine 79.90	36 **Kr** Krypton 83.79
5	37 **Rb** Rubidium 85.47	38 **Sr** Strontium 87.62	39 **Y** Yttrium 88.91	40 **Zr** Zirconium 91.22	41 **Nb** Niobium 92.91	42 **Mo** Molybdenum 95.96	43 **Tc** Technetium (98)	44 **Ru** Ruthenium 101.1	45 **Rh** Rhodium 102.9	46 **Pd** Palladium 106.4	47 **Ag** Silver 107.9	48 **Cd** Cadmium 112.4	49 **In** Indium 114.8	50 **Sn** Tin 118.7	51 **Sb** Antimony 121.8	52 **Te** Tellurium 127.6	53 **I** Iodine 126.9	54 **Xe** Xenon 131.3
6	55 **Cs** Caesium 132.9	56 **Ba** Barium 137.3	**57-71** Lanthanides	72 **Hf** Hafnium 178.5	73 **Ta** Tantalum 180.9	74 **W** Tungsten 183.9	75 **Re** Rhenium 186.2	76 **Os** Osmium 190.2	77 **Ir** Iridium 192.2	78 **Pt** Platinum 195.1	79 **Au** Gold 197.0	80 **Hg** Mercury 200.5	81 **Tl** Thallium 204.38	82 **Pb** Lead 207.2	83 **Bi** Bismuth 209.0	84 **Po** Polonium (209)	85 **At** Astatine (210)	86 **Rn** Radon (222)
7	87 **Fr** Francium (223)	88 **Ra** Radium (226)	**89-103** Actinides	104 **Rf** Rutherfordium (265)	105 **Db** Dubnium (268)	106 **Sg** Seaborgium (271)	107 **Bh** Bohrium (270)	108 **Hs** Hassium (277)	109 **Mt** Meitnerium (276)	110 **Ds** Darmstadtium (281)	111 **Rg** Roentgenium (280)	112 **Cn** Copernicium (285)	113 **Nh** Nihonium (284)	114 **Fl** Flerovium (289)	115 **Mc** Moscovium (288)	116 **Lv** Livermorium (293)	117 **Ts** Tennessine (294)	118 **Og** Oganesson (294)

57 **La** Lanthanum 138.9	58 **Ce** Cerium 140.1	59 **Pr** Praseodymium 140.9	60 **Nd** Neodymium 144.2	61 **Pm** Promethium (145)	62 **Sm** Samarium 150.4	63 **Eu** Europium 152.0	64 **Gd** Gadolinium 157.2	65 **Tb** Terbium 158.9	66 **Dy** Dysprosium 162.5	67 **Ho** Holmium 164.9	68 **Er** Erbium 167.3	69 **Tm** Thulium 168.9	70 **Yb** Ytterbium 173.0	71 **Lu** Lutetium 175.0
89 **Ac** Actinium (227)	90 **Th** Thorium 232.0	91 **Pa** Protactinium 231.0	92 **U** Uranium 238.0	93 **Np** Neptunium (237)	94 **Pu** Plutonium (244)	95 **Am** Americium (243)	96 **Cm** Curium (247)	97 **Bk** Berkelium (247)	98 **Cf** Californium (251)	99 **Es** Einsteinium (252)	100 **Fm** Fermium (257)	101 **Md** Mendelevium (258)	102 **No** Nobelium (259)	103 **Lr** Lawrencium (262)

American Chemical Society

www.acs.org/outreach

Ícaro Rodrigues Lavor

Curriculum Vitae

São Luís/MA - Brazil
✉ *icaro.lavor@ifma.edu.br*
Last update: August 16, 2021

Professional career

2017 – Present **Federal Institute of Education, Science and Technology of Maranhão (IFMA)**.
Occupation: Assistant Professor

Education

2016 – 2021 **Double PhD of Science in Physics**.
Double PhD obtained at the Condensed matter theory group, Department of physics, Universidade Federal do Ceará (CAPES 7), Brazil and at the Condensed matter theory group, Department of physics, University of Antwerp, Belgium.
Title of my Ph.D Thesis: *Plasmons and electronic transport in two-dimensional materials.*
Promotor: Prof. Dr. Andrey Chaves (Brazil) and Prof. Dr. François M. Peeters (Belgium).

2015 – 2016 **Master of Science in Solid State Physics**.
Condensed matter theory group, Department of physics, Universidade Federal do Ceará (CAPES 7), Brazil
Title of my Master Thesis: *Propagation of Gaussian Wave Pack in Graphene Monolayer and Bilayer*
Promotor: Prof. Dr. Andrey Chaves (Brazil) and Prof. Dr. François M. Peeters (Belgium).

2010 – 2014 **Bachelor of Science in Physics**.
Department of physics, Universidade Federal do Ceará, Brazil
Promotor: Prof. Dr. Andrey Chaves.

Skills & Abilities

Programming	Fortran, MATLAB
Packages	QEH, Mathematica, Origin, LATEX, CorelDRAW

Publications

I. R. Lavor, D. R. da Costa, L. Covaci, M. V. Milošević, F. M. Peeters and Andrey Chaves: *Zitterbewegung of moiré excitons in twisted MoS_2/WSe_2 hetero-bilayers*. Physical Review Letters (Accepted).

I. R. Lavor, L. S. R. Cavalcante, Andrey Chaves, F. M. Peeters and B. Van Duppen: *Probing the structure and composition of van der Waals heterostructures using the nonlocality of Dirac plasmons in the terahertz regime*. 2D Materials, **8** 015014 (2020)

I. R. Lavor, D. R. da Costa, Andrey Chaves, G. A. Farias, R. Macêdo and F. M. Peeters: *Magnetic field induced vortices in graphene quantum dots*. Journal Physics: Condensed Matter, **32**, 155501 (2020)

I. R. Lavor, D. R. da Costa, Andrey Chaves, S. H. R. Sena, G. A. Farias, B. Van Duppen and F. M. Peeters: *Effect of zitterbewegung on the propagation of wave packets in ABC-stacked multilayer graphene: an analytical and computational approach*. Journal Physics: Condensed Matter, **33**, 095503 (2020)

I. R. Lavor, Andrey Chaves, F. M. Peeters and B. Van Duppen: *Strong and ultra-strong plasmon-phonon coupling regime in graphene-based van der Waals heterostructures in the THz spectral range*. (Manuscript submitted)

Conferences and Workshops

2021 **ICFO Weizmann Schools on the frontier of light**, *New approaches to atom-light interactions. Barcelona, Spain (virtual).*

2020 **ICFO Schools on the frontier of light**, *Emergent phenomena in moiré materials. Barcelona, Spain (virtual).*

2018 **Graphene 2018**, *Dresden, Germany.*

2014 **XIV Brazilian School of Electronic Structure. 2014**, *Fortaleza, Ceará, Brazil.*

2014 **XXXVII National Condensed Matter Physics Meeting. 2014**, *Costa do Saupe, Bahia, Brazil.*

2013 **XXXI Meeting of North and Northeast Physicists**, *Campina Grade, Paraíba, Brazil.*

2012 **XXX Encontro de Física do Norte e Nordeste**, *Salvador, Bahia, Brazil.*

2010 **XV University Week**, *Ceará, Brazil.*

Posters

2018 **Ícaro R. Lavor**, D. R. da Costa, A. Chaves, G. A. Farias, R. Macêdo and F. M. Peeters, *Magnetic field induced vortices in graphene quantum dots*, Graphene 2018, Dresden, Germany.

2014 **Ícaro R. Lavor**, D. R. da Costa, A. Chaves, G. A. Farias, R. Macêdo and F. M. Peeters, *Magnetic field induced vortices in graphene quantum dots*, XXXVII National Condensed Matter Physics Meeting, Costa do Sauípe, Bahia, Brazil.

2014 **Ícaro R. Lavor**, G. O. de Sousa, A. Chaves, *Electronic states and transport properties in graphene nanostructures*, XXXIII Scientific Initiation Meeting – UFC, Fortaleza, Ceará, Brazil.

2014 **Ícaro R. Lavor**, D. R. da Costa, A. Chaves, G. A. Farias, R. Macêdo and F. M. Peeters, *Magnetic field induced vortices in graphene quantum dots*, XIV Brazilian School of Electronic Structure, Fortaleza, Ceará, Brazil.

2013 Irvile R. Lavor; **Ícaro R. Lavor**, R.C. da S. Gomes, *Simulation of an experiment to determine the acceleration of the local gravity: an activity for high school*, XXXI Meeting of North and Northeast Physicists, 2013, Campina Grande, Parabíba, Brazil.

2013 **Ícaro R. Lavor**, V. M. Nocrato, A. Chaves, *Simple pendulum oscillations studied using the accelerometer of a smartphone*, XXXI Meeting of North and Northeast Physicists, 2013, Campina Grande, Parabíba, Brazil.

2013 **Ícaro R. Lavor**, V. M. Nocrato, A. Chaves, *Spring-mass system and Hook's law studied using a smartphone accelerometer*, XXXI Meeting of North and Northeast Physicists, 2013, Campina Grande, Parabíba, Brazil.

2013 **Ícaro R. Lavor**, V. M. Nocrato, M. A. A. Silva, Josué M. Filho; Nildo L. Dias, *Teaching optics using the frustrated total internal reflection experiment*, XXXI Meeting of North and Northeast Physicists, 2013, Campina Grande, Parabíba, Brazil.

2014 **Ícaro R. Lavor**, C. R. Muniz; Ricardo C. S Gomes. Central force on particle following N-Leaved clover-shaped orbit. In: XV Semana Universitária - Universidade Estadual do Ceará, 2010, Fortaleza. XV Semana Universitária - Universidade Estadual do Ceará, 2010.

Awards

2020 One of the figures of my paper "*Magnetic field induced vortices in graphene quantum dots* ", J. Condens. Matter Phys. , **32**, 155501 (2020), was selected to be on the cover. JPCM. Click here to access.

2017 Approved in a public examination for Lecturer of Higher Education (DOU No. 90, Section 3, Page 60), *Federal Rural University of Amazônia - UFRA*.

2017 Approved in a public examination for Effective Lecturer (DOU No. 86, Section 3, Page 81), *Federal Institute of Education, Science and Technology of Maranhão*.

2016 Approved in public examination for Effective Lecturer (DOU No. 83, Section 3, Page 52), *Federal Institute of Education, Science and Technology of Sertão do Pernambuco - IF Sertão PE*.

Research interests

- Electronic properties of graphene
- Electronic transport in 2D materials
- Graphene plasmonic
- Plasmons in 2D materials
- Moiré excitons in twisted hetero-bilayers

Languages

- Portuguese: Native Speaker
- Spanish: Basic
- English: Advanced